

Combined Author Index

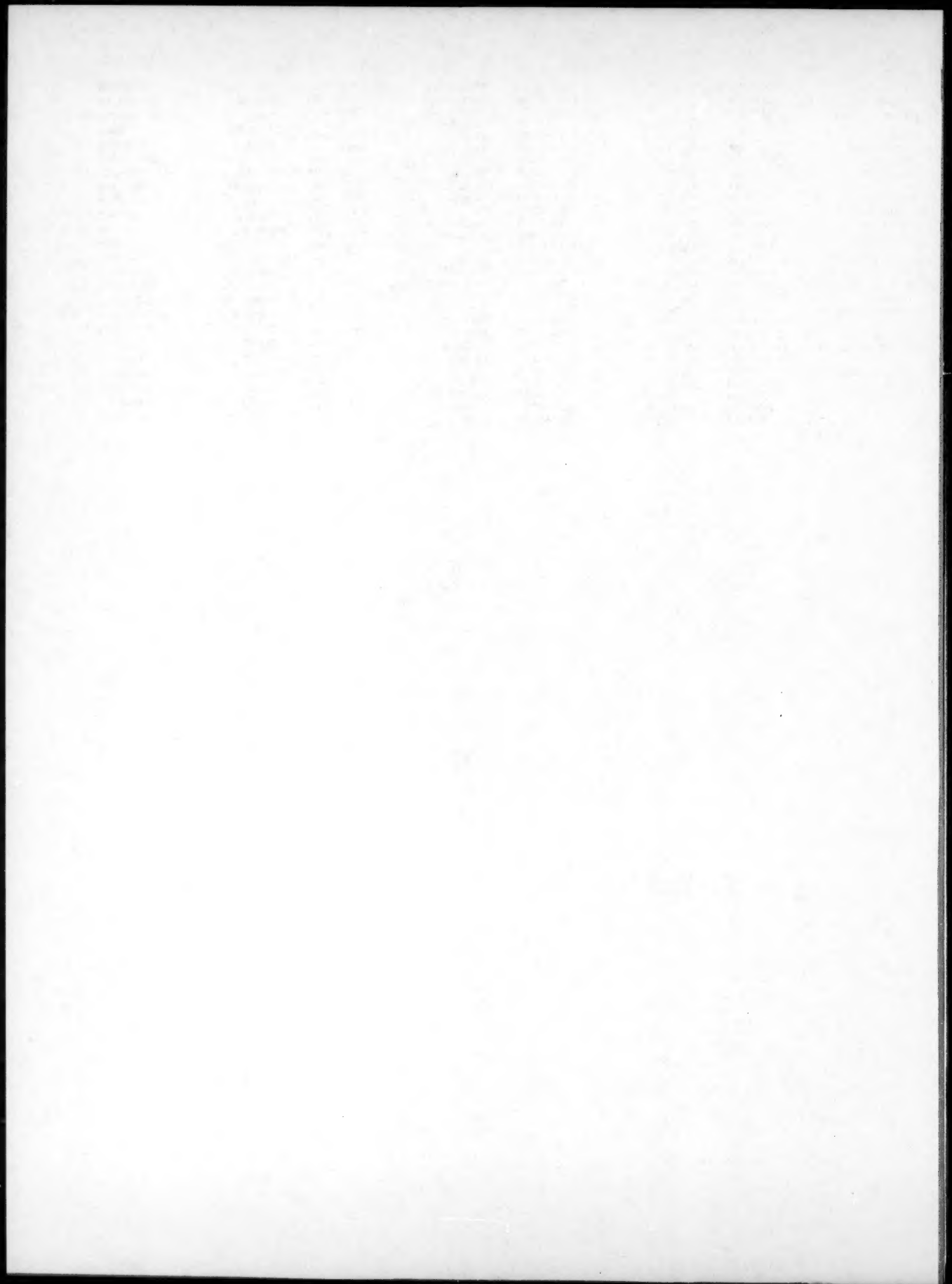
Abbaschian, R.	4049-4059A	Blackwell, P.L.	3747-3748A	Chou, Y.T.	3473-3477A	Durrant, G.	3612-3620A
Abe, T.	1585-1594A	Blakely, J.	2057-2061A	Choubey, R.	431-440A	4121-4132A	
Abraham, D.P.	2151-2159A	Blakely, B.C.	555-566B	Chrysanthou, A.	827-838B	567-576B	
Abuluwefia, H.	993-997B	Blue, C.A.	4011-4018A	Chu, Y.C.	165-182A	Dwarakadasa, E.S.	1283-1292A
Acoff, V.L.	2692-2703A	Blue, R.A.	4011-4018A	Chuang, T.H.	2617-2627A	Earthman, J.C.	863-872A
Aenoudt, E.	2347-2358A	Boettlinger, W.J.	657-669A		2653-2662A	Eckert, J.	2934-2946A
Agarwal, A.	2985-2993A	Boisson, M.	2904-2910A	Chun, B.S.	315-318B	Eggeler, G.	879-890A
Agren, J.	1073-1080A	Boivin, J.-A.	322-325B	Chung, T.-W.	29-34B	Eissa, M.M.	1693-1699A
Ahn, C.C.	2934-2946A	Bonnet, C.	371-379A	Clapp, P.C.	1476-1488A	Ekstrand, M.E.	1676-1682A
Ahn, S.	3881-3891A	Bordia, R.	839-849A	Clavel, M.	322-325B	El-Bealy, M.	689-693B
Ajersch, F.	993-997B	Borgenstam, A.	1499-1510A	Cockcroft, S.L.	3043-3058A	El-Eskandarany, M.S.	999-1014B
Akseisen, O.M.	3630-3638A	Bouchard, D.	101-113B		119-127B	El-Eskandarany, M.S.	2374-2382A
Albaran, J.L.	3601-3611A	Bourke, M.A.M.	2820-2836A		129-137B	4210-4213A	
Albers, M.	3569-3575A	Bracconi, P.	371-379A	Colvin, D.J.	1554-1568A	El-Magd, E.	747-758A
Ali, A.	1141-1147A	Braithwaite, N.S.J.	2495-2503A	Combeau, H.	2314-2327A	Elmer, J.W.	775-783A
Alonso, M.	801-807B	Bray, D.W.	3362-3370A	Coriell, S.R.	687-694A	Enomoto, M.	1489-1498A
Alpas, A.T.	3135-3148A	Brimacombe, J.K.	3371-3380A	Cortie, M.B.	2436-2444A	Escudero, M.L.	3809-3816A
Altunoglu, A.K.	2495-2503A	Bronson, A.	163-175B	Courtney, T.H.	1991-1997A	Eshelman, M.	2727-2739A
Altynova, M.	1837-1844A	Bryoles, S.E.	271-276B		1999-2004A	Eustathopoulos, N.	3181-3186A
Alvarez, L.F.	1799-1805A	Buchheit, T.E.	1217-1227A	Cox, A.	888-894B	Evangelista, E.	2916-2922A
Ananthasivan, K.	1919-1924A	Bul, R.T.	269-279A	Cramb, A.W.	717-730B	3871-3879A	
Anderson, K.R.	1217-1227A	Bronson, A.	1015-1023B	Cserhati, C.	59-69A	Evans, J.W.	19-27B
Andrews, S.	2023-2034A	Bryoles, S.E.	1217-1227A	Cul, Y.Y.	2221-2228A	Ewsuk, K.G.	2100-2104A
Ankem, S.	2366-2373A	Buchheit, T.E.	297-304B	Currier, P.A.	801-808A	2122-2129A	
Anthonyasamy, S.	1919-1924A	Bul, R.T.	1015-1023B	Czerwinski, F.	3649-3661A	Eylon, D.	4193-4204A
Antia, D.P.	1127-1132A	Buisson, L.	371-379A	Dash, G.S.	891-900A	Fahrenholtz, W.G.	2100-2104A
Anton, D.L.	3007-3018A	Byrne, J.G.	2383-2385A	Dahle, A.K.	2305-2313A	Fall, I.	2160-2177A
Araki, H.	1807-1814A	Cahn, J.W.	1431-1440A	Damodaran, A.D.	1283-1292A	Fang, H.-S.	1533-1543A
Ardell, A.J.	2888-2896A	Cantor, B.	4121-4132A	Dantzig, J.A.	707-717A	Farag, M.	747-758A
Arjuna Rao, A.	791-800A	Cardinale, A.M.	979-986B	Dao, M.	81-90A	Farber, L.	2140-2150A
Arberg, L.	2305-2313A	Carter, W.C.	1431-1440A	Darolja, R.	1229-1240A	Farouk, B.	911-920B
Arsenault, R.J.	995-1001A	Caruana, G.	3259-3266A	Das, S.	1618-1629A	Faulkner, R.G.	3381-3390A
Arvanitidis, I.	409-416B	Castello-Branco,		Datta, A.	4213-4216A	Feaugas, X.	3043-3058A
Arya, V.K.	3279-3291A	M.A.S.C.	231-239B	Datta, S.K.	3668-3674A	Fedotov, V.G.	2045-2064A
Asaro, R.J.	81-99A	Catalina, A.V.	4205-4210A	David, S.A.	783-774A	Feliner, P.	255-261B
Asundi, M.K.	757-761A	Cerri, E.	2916-2922A	Davidson, D.L.	2540-2556A	Feng, C.	1773-1778A
Atrens, A.	2686-2691A	Chakraborty, M.	3871-3879A	Davies, C.H.J.	3007-3018A	Fernández Navarro, J.M.	379-384B
Avery, S.	773-779B	Chakraborty, D.	791-800A	Davies, C.H.J.	4095-4111A	Ferro, R.	979-986B
Aramavio-Cingara, G.	3478-3490A	Chakraborty, D.	4213-4216A	Davignon, G.	4113-4120A	Fields, R.J.	923-928A
Ayensu, A.	901-907A	Chan, J.W.	3466-3472A	Davison, G.	3357-3361A	Fine, M.E.	1267-1271A
Ayer, R.	2510-2517A	Chan, K.S.	2518-2531A	Davis, C.L.	3019-3029A	2397-2418A	
Aziz, M.J.	671-688A		2540-2556A	Davis, S.H.	583-593A	Fitzgerald, T.J.	3700-3717A
	725-730A		3007-3018A	Davay, R.K.	2881-2887A	Flanagan, W.F.	819-821A
Babu, S.S.	763-774A	Chandramouli, V.	1919-1924A	Dayanandan, M.A.	2504-2509A	Flemings, M.C.	595-609A
Badrinarayanan, K.	3781-3792A	Chang, S.	2708-2721A	de Gregorio, P.	3773-3780A	863-868B	
Baek, E.-R.	3335-3340A	Chang, Y.	3162-3169A	de Groh, H.C., III	1095-1110A	2326-3240A	
Bahr, D.F.	3793-3800A	Chao, C.-G.	809-818A	De Schutter, F.	794-800B	Flewitt, P.E.J.	3381-3390A
Baik, W.-H.	3120-3125A	Chao, J.	3809-3816A	De Ardo, A.J.	951-960A	Flueury, E.	829-837A
Baker, T.N.	4039-4047A	Charette, A.	297-304B	Debroy, T.	43-50B	Foley, R.P.	1845-1859A
Balasubramaniam, R.	2985-2993A	Chatterjee, S.K.	503-505A	Decultieux, F.	81-99B	Forbes, K.R.	1229-1240A
Balich, D.K.	3700-3717A	Chattopadhyay, K.	2053-2057A	Dekeyser, J.C.	794-800B	Fournelle, R.A.	1293-1302A
Balzer, M.	3066-3073A	Chaturvedi, M.C.	785-790A	Deflino, S.	979-986B	Fraser, H.L.	2047-2050A
Banerjee, D.	2593-2604A	Chen, G.	1676-1682A	Demestral, B.	879-890A	Fray, D.J.	794-800B
Banerjee, R.	2047-2050A	Chen, H.	2429-2435A	Demopoulos, G.P.	585-594B	Fredriksson, H.	407-414A
Barbante, G.G.	3187-3191A	Chen, H.S.	745-756B	Dengel, D.	1333-1346A	999-1014B	
Barker, J.	923-928A	Chen, J.H.	1909-1917A	Dereball, R.	686-689B	Friedman, P.A.	1889-1898A
Barrett, C.A.	3279-3291A	Chen, J.K.	1676-1682A	Desbiolles, J.-L.	695-705A	3030-3042A	
Bartholomeusz, M.F.	127-134A	Chen, L.H.	1683-1686A	Deu, T.N.	839-845B	3827-3839A	
Bartlett, R.W.	2086-2093A	Chen, M.C.	1683-1686A	Diaz, C.	3259-3266A	Frisk, K.	2869-2880A
Bate, P.S.	3250-3258A	Chen, R.	3662-3668A	Diedrichs, R.	305-314B	Fröba, M.	775-783A
	3747-3748A	Chen, S.	29-40A	DiMelli, R.J.	467-469A	Froes, F.H.	41-48A
Bay, F.	81-99B	Chen, S.-W.	3391-3398A	Dimiduk, D.M.	1642-1654A	Fruhan, R.J.	717-730B
Beckermann, C.	2754-2764A	Chen, S.H.	1379-1394A	Ding, B.Z.	3903-3912A	Fujii, Y.	469-471A
	2765-2783A	Chen, S.R.	2994-3006A	Ding, D.	71-79B	Fukagawa, H.	846-851B
	2784-2795A	Chen, T.-R.	2923-2933A	Ding, W.	5-17B	Fukami-Ushiro, K.L.	183-191A
Belle, M.	81-99B	Chen, T.T.	567-576B	Divakar, M.	241-253B	193-203A	
Bencze, L.	3576-3590A	Chen, W.-C.	4113-4120A	Doan, R.	3126-3134A	Fukatsu, N.	929-935B
Bender, W.	2470-2478A	Chen, W.C.	4095-4111A	Dogan, C.	3126-3134A	Fukui, Y.	4145-4151A
Bennett, C.G.	3530-3541A	Chen, X.	4031-4038A	Donaki, J.R.	363-374B	Fukuoka, C.	3841-3851A
Berns, H.	1845-1859A	Cheng, X.	393-398B	Drew, R.A.L.	577-584B	Fultz, B.	2934-2946A
Bewlay, B.P.	3801-3808A		610-616B		585-594B	Funkenbusch, P.D.	1047-1053A
Bhaduri, A.	3718-3726A	Chenot, J.-L.	81-99B	Drezet, J.-M.	2314-2327A	Fuhara, T.	1630-1641A
Bhanu Sankara Rao, K.	255-267A	Chernov, A.A.	687-694A		3214-3225A	Gale, W.F.	363-369A
	851-861A	Chihara, T.	765-772B	Du, H.	1073-1080A	1925-1931A	
Bhargava, S.	2985-2993A	Cho, S.S.	315-318B				
Bhattacharyya, A.	2359-2365A	Choi, B.G.	1273-1281A	Dudek, H.J.	1403-1405A	Gall, K.	3491-3502A
Bhattacharyya, P.K.	139-141B	Choi, C.S.	923-928A		3318-3329A	Gallermeault, M.	4121-4132A
Biemann, H.	1003-1014A	Chokshi, A.H.	2532-2539A	Dulcy, J.	1823-1835A	Gandin, Ch.-A.	695-705A
Bilger, P.	1823-1835A	Choo, S.-H.	3335-3340A	Dunand, D.C.	183-191A	Gangli, P.	2179-2186A
Biswas, S.	5-17A		3881-3891A		193-203A	Gantois, M.	1823-1835A
	71-79A	Chopra, H.D.	1687-1692A		2820-2836A	Gao, M.	3391-3398A
Bitler, W.R.	146-148B	Chou, M.-C.	2005-2012A	DuPont, J.N.	481-489B	29-40A	

Gao, Z.	2293-2298A	Han, K.N.	355-361B	Iswaran, C.V.	3524-3529A	Kim, J.	2574-2582A
García de Andrés, C.	1799-1805A	Hänninen, H.	1815-1821A	Itoh, G.	3957-3962A	Kim, N.J.	1241-1250A
García, C.I.	951-960A		2796-2808A	Iwase, M.	3081-3088A		3881-3891A
Garg, A.	3170-3180A	Hansen, G.	569-581A		375-378B	Kim, S.	1889-1898A
Garrett, R.K., Jr.	737-745A	Hansen, P.N.	4085-4093A		385-392B	Kim, S.B.	493-496A
Gasior, W.	2419-2426A	Hanumanth, G.S.	663-671B		595-603B	Kim, Y.G.	493-496A
Gaskell, D.R.	139-141B	Hao, S.M.	2429-2435A	Izaki, M.	483-486A	King, J.E.	353-361A
	693-694B	Harlow, D.G.	3391-3398A	Jackson, J.A.	431-440A		363-369A
Gatica, J.E.	3669-3674A	Hashimoto, S.	317-326A	Jackson, M.R.	3801-3808A		3019-3029A
Gauthier, J.	1785-1798A	Hatta, T.	967-972B	Jacob, K.T.	647-651B	Kirkaldy, J.S.	101-113B
Gavriljuk, V.G.	1815-1821A	Hawbolt, E.B.	1544-1553A		1919-1924A		1606-1617B
Genin, J.-M.R.	2160-2177A		3399-3409A	Jacobus, K.	3066-3073A	Kishore, R.	757-761A
Gerberich, W.W.	3793-3800A		3410-3423A	Jakobsson, A.	318-322B		3340-3343A
German, R.M.	441-450A		4095-4111A	Järvstråt, N.	501-508B	Kivilahti, J.K.	59-69A
	901-909B		4113-4120A	Jeng, S.-C.	2722-2726A		2229-2238A
Ghosh, A.	3993-4002A	He, Z.	731-736A	Jeniski, R.A., Jr.	19-27A	Klaar, H.-J.	2285-2292A
	4003-4010A	Hegazy, M.M.	1693-1699A	Jha, A.	827-838B	Klam, H.-J.	879-890A
Ghosh, A.K.	1889-1898A	Hei, Z.	1347-1352A	Jiang, H.G.	71-79B	Kleff, J.	1845-1859A
	3030-3042A	Heilmair, M.	3861-3870A	Jiang, J.-Q.	3250-3258A	Kleppa, O.J.	417-422B
	3827-3839A	Helbert, A.L.	3043-3058A	Jiang, L.	2796-2808A	Kloc, L.	3871-3879A
Ghoshi, A.K.	909-921A	Hellawell, A.	229-232A	Jiang, X.-G.	863-872A	Klug, R.C.	1963-1978A
Giannuzzi, L.A.	146-148B	Hempstenmacher, J.	569-581A	Jiao, Y.	1026-1029B	Ko, S.K.	315-318B
Gibeling, J.C.	1217-1227A	Henager, C.H., Jr.	1403-1405A	Jiménez, J.A.	1799-1805A	Kobayashi, S.	945-949A
Glumelli, A.	3399-3409A	Henein, H.	839-849A		1881-1887A	Kobayashi, T.	652-657B
Gjønnes, L.	2338-2346A	Heo, N.-H.	1045-1056B	Jo, B.L.	490-493A		1979-1989A
Glass, S.J.	2122-2129A	Heo, N.H.	1015-1020A	Johari, G.P.	2461-2469A		2013-2021A
Glatzel, U.	1229-1240A	Heo, N.H.	3059-3065A	John, R.	3074-3080A		3825-3935A
Gleeson, B.	3761-3772A	Heuze, M.-C.	808-826B	Johnson, J.L.	441-450A	Kocak, D.	1015-1023B
Glicksman, M.E.	557-567A	Hillert, M.	480-483A		901-909B	Kocak, M.	2130-2139A
Gnanamoorthy, J.B.	1313-1325A		1499-1510A	Johnson, W.C.	1460-1475A	Kocak, M.J.	2140-2150A
	2881-2887A	Hilpert, K.	2673-2677A	Johnson, W.L.	2934-2946A	Kodentsov, A.A.	59-69A
Goetz, R.L.	1709-1720A		3569-3575A	Jonas, J.J.	155-164A		2229-2238A
	3903-3912A		3576-3590A		232-235A	Kohtoku, Y.	3307-3317A
Goldstein, J.I.	3192-3202A	Hines, A.L.	29-34B		1303-1312A	Komvopoulos, K.	381-390A
Goller, G.	3727-3738A	Hiral, T.	4210-4213A		1869-1876A	Konno, T.J.	4210-4213A
Gomanikov, V.I.	2045-2046A	Hirth, J.P.	1489-1498A		1877-1887A	Koo, Y.	3149-3161A
González, J.	281-290A	Hiskey, J.B.	393-398B		2178-2186A	Kooi, B.J.	1055-1061A
	291-304A		610-616B		2347-2358A		1063-1071A
González-Carrasco, J.L.		Hives, J.	255-261B		3346-3348A	Koseki, T.	3226-3240A
		Ho, N.-J.	2479-2494A		3963-3970A	Koster, J.N.	686-689B
		Ho, S.	3241-3249A		839-849A	Koty, D.P.	3727-3738A
González-Doncel, G.	1861-1867A	Honda, K.	2843-2851A	Jong, S.-H.	1951-1962A	Koursaris, A.	287-296B
	2837-2842A	Hong, J.W.	1273-1281A	Jong-Leng, L.	633-646B	Koyama, T.	945-949A
	3809-3816A	Hong, L.B.	2934-2946A	Jonsson, P.	2196-2208A	Krauss, G.	1554-1568A
Gooding, R.J.	1203-1216A	Hong, S.H.	493-496A	Jung, W.	51-55B		1569-1584A
Gopinathan, V.	3718-3726A	Hopkins, J.A.	477-480A	Justice, I.	486-490A		1845-1859A
Gotman, I.	2071-2079A	Hort, W.	1460-1475A	Kadioglu, Y.	3491-3502A		1963-1978A
	2130-2139A	Hoshino, H.	375-378B	Kagawa, Y.	2843-2851A	Kroupa, A.	1149-1165A
	2140-2150A		595-603B	Kainuma, R.	2187-2195A	Krüger, J.	1031-1044B
Gou, H.	195-201B	Hovland, R.	185-193B	Kar, R.N.	2445-2453A	Kuang, Z.	177-183B
Goulet, R.U.	3853-3860A	Howe, J.M.	1618-1629A		4153-4162A	Kuehmann, C.J.	937-943A
Govier, D.	3126-3134A		3362-3370A	Kakehi, K.	317-326A	Kumar, S.G.	1121-1128A
Gray, G.T., III	459-465A	Howell, P.R.	3371-3380A	Kallappan, I.	1919-1924A	Kuramoto, S.	3081-3088A
	2994-3006A	Hsiao, Y.-H.	146-148B	Kamara, A.B.	2888-2898A	Kuranaga, T.	35-41B
Gray, N.B.	3739-3746A	Hsieh, Y.M.	891-900A	Kang, C.G.	277-285B	Kurita, N.	929-935B
	221-230B	Hsu, F.-Y.	245-253A	Kang, C.Y.	4019-4029A	Kurz, W.	625-634A
	633-646B	Hsu, K.C.	2285-2292A	Kang, S.-J.L.	3120-3125A	Kuwata, M.	57-64B
Grebe, H.A.	1749-1759A	Hsu, K.C.	399-408B	Kannan, K.	2947-2957A	Kweon, Y.-G.	2557-2564A
Greenberg, R.R.	3682-3687A	Hu, C.	4039-4047A	Kanno, M.	3081-3088A	Kwon, D.	1241-1250A
Greer, A.L.	549-555A	Hu, X.	1837-1844A	Kao, W.H.	1363-1370A		3893-3901A
Griffiths, J.R.	115-118B	Hu, Z.	1025-1029B	Kapala, J.	2673-2677A	Kwon, H.	3343-3346A
Gronig, Ø.	3630-3638A	Hu, Z.Q.	71-79B	Kar, R.N.	351-354B	Lahiri, A.K.	695-697B
Gross, T.S.	3853-3860A		2221-2228A	Karjalainen, L.P.	4031-4038A		757-764B
Groza, J.R.	1217-1227A	Huang, J.C.	2479-2494A	Karjulber, S.	921-927B	Lakshminikantha, M.G.	981-972A
Gruzleski, J.E.	929-936A		2923-2933A	Karlsson, L.	2196-2208A	Lance, J.J.	3841-3851A
Gu, N.	719-724A		3095-3107A	Karma, A.	635-658A	Landry, K.	3181-3186A
	3108-3111A	Huang, W.	480-483A	Karwan-Baczewska, J.	2978-2984A	Langberg, D.E.	773-779B
Guan, H.	1327-1331A		3591-3600A	Kashyap, B.P.	2274-2284A		780-787B
Guan, Y.	3621-3629A	Huang, X.	617-632B	Kath, D.	2673-2677A	Langdon, T.G.	873-878A
Guan, Y.C.	355-361B		785-790A		3568-3575A		901-907A
Gülpén, J.H.	59-69A	Huhtala, T.	2196-2208A	Kaufman, M.J.	819-821A		2532-2539A
Gündel, D.B.	2035-2043A	Hunt, J.D.	611-623A		3524-3529A		3871-3879A
Guo, Q.	417-422B	Hwang, K.S.	203-211B	Kar, R.N.	3542-3557A	Larson, E.M.	775-783A
Guo, S.Q.	2843-2851A		245-253A		3957-3962A	Last, H.R.	737-745A
Gupta, D.	695-697B	Hwang, N.M.	2809-2819A	Kaukler, W.F.	801-808A	Lavemia, E.J.	2115-2121A
	757-764B	Iacocca, R.G.	145-153A	Kauppinen, V.	2796-2808A		3241-3249A
Guthrie, R.I.L.	993-997B	Ibáñez, J.	3809-3816A	Kawakami, N.	3925-3935A	Lee, B.J.	81-99A
Gutiérrez-Solana, F.	281-290A	Iguchi, M.	35-41B	Kaysser, W.A.	1700-1708A	Lee, D.N.	955-966B
	291-304A		765-772B	Ke, W.	1327-1331A	Lee, H.-C.	1015-1020A
Gutmanas, E.Y.	2071-2079A	Ilegbusi, O.J.	35-41B	Kestens, L.	155-164A	Lee, H.C.	3149-3161A
	2130-2139A	Ioku, S.	1668-1675A		2178-2186A	Lee, H.M.	3466-3472A
	2140-2150A	Irie, K.	929-935B		2347-2358A	Lee, J.-H.	1749-1759A
Haeberle, R.M.	493-496A	Irons, G.A.	195-201B	Khani, M.K.	1333-1346A	Lee, J.H.	3343-3346A
Hajra, J.P.	241-253B		663-671B	Khatak, H.S.	1313-1325A	Lee, J.K.	1449-1459A
Halford, G.R.	255-267A	Ishida, A.	3753-3759A	Khoobab, M.	3074-3080A	Lee, J.M.	1273-1281A
	851-861A	Ishida, K.	2187-2195A	Kiaki, A.A.	2297-2304A	Lee, K.N.	3279-3291A
	3279-3291A		2445-2453A	Kikuchi, A.	469-471A	Lee, K.R.	423-431B
Hall, M.G.	1517-1523A		4153-4162A	Kim, C.	1889-1898A	Lee, L.B.	3343-3346A
Hamano, R.	471-476A	Ishida, Y.	3925-3935A	Kim, C.K.	3203-3213A	Lee, M.S.	212-219B
Hamilton, C.H.	2947-2957A	Ishii, H.	2653-2662A	Kim, C.M.	3343-3346A	Lee, S.	1241-1250A
Hampel, F.G.	433-443B	Ishikuro, M.	4210-4213A	Kim, D.-Y.	51-55B		3149-3161A
Hampikian, J.M.	491-500B	Isono, N.	725-730A	Kim, H.-J.	2557-2564A		3335-3340A

3881-3891A	Mathews, C.K.	1919-1924A	Nagamori, M.	322-325B	Park, J.	2151-2159A
3893-3901A	Mathews, S.A.	2858-2860A	Nagarathnam, K.	381-390A	Park, J.S.	496-498A
391-400A	Matlock, C.A.	698-701B	Nagata, K.	658-662B		2328-2373A
111-118A	Matlock, D.K.	1251-1266A	Nagumo, M.	469-471A		2740-2753A
343-352A		1963-1978A		2574-2582A	Park, L.J.	493-496A
Leucht, R.	1403-1405A	Matson, D.M.	863-868B	Nagy, A.	Park, S.-H.	1241-1250A
Levaillant, C.	81-99B	Matsuda, A.	1363-1370A	Nakagawa, Y.G.	Park, S.W.	51-55B
Lewandowski, J.J.	3292-3306A	Matsuyama, Y.	3925-3935A	Nakai, H.	Park, Y.J.	2809-2819A
3937-3947A	Maurice, D.	1991-1997A	Nakanishi, N.	719-724A	Paro, J.	2796-2808A
Levens, C.	1700-1708A		1999-2004A	Nakano, H.	Pascotto, W.	2461-2469A
Li, B.J.	809-818A	Maziasz, P.J.	1655-1667A	Nakatsuka, T.	Pascual, L.	379-384B
Li, C.	2293-2296A	Mazumdar, D.	704-708B	Nam, S.W.	Patwardhan, A.K.	3513-3523A
Li, C.M.	1533-1543A	McCay, M.H.	477-480A		Paul, R.L.	3682-3687A
Li, C.X.	1533-1543A	McCay, T.D.	477-480A	Namjoshi, S.	Pedersen, A.S.	4085-4093A
Li, D.	2221-2228A	McClung, R.C.	2540-2556A	Nana, S.	Pehlke, R.D.	745-756B
Li, G.	509-525B	McDavid, R.M.	672-685B	Naohara, T.		852-862B
Li, J.B.	3662-3668A	McDeavitt, S.M.	2151-2159A		Pei, Y.T.	391-400A
Li, Q.C.	2221-2228A	McFadden, G.B.	687-694A	Narayana, K.L.	Peltion, A.D.	808-826B
Li, S.	135-143A	McGuire, S.M.	1267-1271A	Nastac, L.	Perla, M.	271-276B
Li, Y.	467-469A	McKelvey, A.L.	2704-2707A		Peng, G.-J.	2923-2933A
Li, Y.Z.	3473-3477A		3781-3792A	Neale, K.W.	Peng, H.	3108-3111A
Liang, J.	2293-2296A	McMahon, M.E.	2252-2262A	Nemat-Nasser, S.	Peng, Z.	41-48A
Lichter, B.D.	819-821A	McNelley, T.R.	2252-2262A	1739-1748A	Perezko, J.H.	
Lieblich, M.	3259-3266A	McNulty, J.C.	1899-1907A	Nes, E.	4133-4144A	509-824A
Lin, H.K.	157-162B	McQueen, H.J.	3478-3490A	Nethercott, R.B.	533-547A	
Lin, R.Y.	527-532B	Meadowcroft, T.R.	3399-3409A	Nicholas, T.	2239-2251A	1618-1629A
1379-1394A		Menai, M.	81-99B	Nicolaou, P.D.	1709-1720A	Perkins, C.A.
4011-4018A		Mendelsohn, D.A.	3853-3860A		3112-3119A	1251-1266A
Lindahl, K.A.	2958-2965A	Mendiratta, M.G.	2583-2592A		3675-3681A	Perovic, D.D.
Lindholm, M.	2897-2903A		3903-3912A	Nicolini, G.	297-304B	
Lindroos, V.K.	4171-4181A	Meng, L.	3089-3094A	Nilmini, M.	3025-3035A	
Lindstrom, R.M.	3682-3687A	Menon, E.S.K.	1642-1654A	Nilles, P.E.	541-553B	
Lipsitz, H.A.	3801-3808A	Meyer, W.W.	325-327B	Nilmani, M.	773-779B	
Liu, C.T.	3473-3477A	Michaud, V.J.	3700-3717A	Nilsson, J.-O.	780-787B	
Liu, G.	213-219A	Miki, T.	937-941B	Noebe, R.D.	327-341A	
Liu, Q.	1025-1029B	Mikula, A.	921-927B	32196-2208A	Potter, S.	
Liu, S.	1327-1331A	Miltzner, M.	1544-1553A	Nioui, C.-S.	229-232A	
Liu, W.	2293-2296A		3399-3409A	Nishida, Y.	509-921A	
Liu, W.-P.	1951-1962A	Miller, M.K.	763-774A	Nix, W.D.	3285-3294B	
	3558-3568A	Minamino, Y.	1807-1814A	Noebe, R.D.	1033-1041A	
Liu, X.J.	2429-2435A	Miodownik, A.P.	3718-3726A	3229-1240A	Pollcock, T.M.	
Liu, Z.	407-414A	Miracle, D.B.	2035-2043A	3170-3180A	Ponce, J.	
Liu, Z.B.	895-900B		2583-2592A	3268-2641A	2023-2034A	
Liu, Z.T.	2904-2910A	Mishra, R.S.	305-316A	3170-3180A	Potocnik, V.	
Llorca, J.	486-490A	Mitra, S.	3913-3923A	3542-3557A	297-304B	
Lloyd, D.J.	4113-4120A	Mittemeijer, E.J.	1055-1061A	Nourbakhsh, S.	Pilling, J.	
Loehman, R.E.	2100-2104A		1063-1071A	O'Hanley, R.C.	229-232A	
2122-2129A		Miller, M.K.	763-774A	327-341A		
Lombard, C.M.	3112-3119A	Miyamoto, S.	1807-1814A	Noebe, R.D.	1700-1708A	
Longton, R.J.	567-576B	Miyamoto, Y.	2035-2043A	327-341A		
López, F.A.	379-384B	Miyazaki, S.	3753-3759A	Nohmi, S.	Pickard, S.M.	
	801-807B	Miyazaki, T.	945-949A	Nomura, K.	909-921A	
López, H.F.	3601-3611A	Mo, A.	2314-2327A	3753-3759A	Pickles, C.A.	
López-Delgado, A.	379-384B	Miyamoto, S.	929-935B	Ohta, H.	363-374B	
Lou, B.Y.	3095-3107A	Mogilovskiy, P. DLR	1807-1814A	Ohtani, H.	498-502A	
Lu, J.	2565-2573A	Mohamed, F.A.	863-872A	Ohyu, K.	995-1001A	
Lu, S.-Z.	611-623A	Mohan, S.	1057-1060B	Oishi, T.	1283-1292A	
Lu, S.Z.	569-581A	Montemayor-Aldrete, J.	3330-3335A	Oikawa, K.	2035-2043A	
Lu, W.-K.	195-201B	Montheillet, F.	232-235A	Oikawa, K.	2057-2061A	
Lui, T.S.	1683-1686A		3346-3348A	Oishi, T.	2285-2292A	
Lum, J.W.	863-868B	Morgan, G.J.	163-175B	Oikawa, T.	2071-2079A	
Luo, Z.P.	1779-1784A	Morita, K.	652-657B	Oikawa, T.H.	2129-2140A	
Lynch, S.P.	3530-3541A		846-851B	Oikawa, T.H.	2141-2150A	
Lytle, M.T.	3503-3512A		937-941B	Oizumi, M.	2151-2160A	
Ma, Y.	873-878A	Morita, Z.-I.	345-41B	Oizumi, M.	2161-2170A	
Maccid, D.	979-986B		765-772B	Ohta, H.	2171-2180A	
Machmeier, P.M.	2510-2517A	Morris, J.W., Jr.	1187-1201A	Ohta, H.	2181-2190A	
Mackenbrock, A.	869-879B		3466-3472A	Ohta, H.	2191-2200A	
Mahajan, Y.R.	305-316A	Morita, K.	1063-1071A	Ohta, H.	2201-2210A	
Majumdar, B.	2053-2057A		595-609A	Ohta, H.	2211-2220A	
Majumdar, B.S.	2035-2043A	Mortensen, A.	3700-3717A	Ohta, H.	2221-2230A	
Maki, T.	1630-1641A		3214-3227A	Ohta, H.	2231-2240A	
Malakondiah, G.	2239-2251A	Mudali, U.K.	2881-2887A	Ohta, H.	2241-2250A	
Malik, M.K.	2274-2284A	Mughrabi, H.	1003-1014A	Ohta, H.	2251-2260A	
Mannan, S.L.	119-126A	Mukunthan, K.	3410-3423A	Ohta, H.	2261-2270A	
Manory, R.R.	135-143A	Mulazimoglu, M.H.	929-936A	Ohta, H.	2271-2280A	
Mao, X.	3817-3825A	Munir, Z.A.	475-480B	Ohta, H.	2281-2290A	
Marder, A.R.	481-489B		2080-2085A	Ohta, H.	2291-2300A	
	3192-3202A	Munitz, A.	4049-4059A	Ohta, H.	2301-2310A	
Margolin, H.	451-458A	Mutoz-Andrade, D.	3330-3335A	Ohta, H.	2311-2320A	
Marl, D.	183-191A	Munro, T.C.	3761-3772A	Ohta, H.	2321-2330A	
	2820-2836A	Muraleedharan, K.	2593-2604A	Ohta, H.	2331-2340A	
Marguis, F.	557-567A	Muralidhar, G.K.	1057-1060B	Ohta, H.	2341-2350A	
Marsh, S.P.		Murphy, W.H.	1081-1094A	Ohta, H.	2351-2360A	
Marthinsen, K.	4133-4144A	Murr, L.E.	1773-1778A	Ohta, H.	2361-2370A	
Martinez, E.	3330-3335A	Murray, B.T.	687-694A	Ohta, H.	2371-2380A	
Martinez, J.L.	486-490A	Murray, M.T.	115-118B	Ohta, H.	2381-2390A	
Martinez, L.	3801-3811A	Mury, B.S.	791-800A	Ohta, H.	2391-2400A	
Masamura, K.	385-392B	Musulin, I.	3530-3541A	Ohta, H.	2401-2410A	
Mataya, M.C.	1251-1266A	Mutharasan, R.	911-920B	Ohta, H.	2411-2420A	
Matera, S.	3773-3780A	Nabarro, F.R.N.	513-530A	Ohta, H.	2421-2430A	
				Ohta, H.	2431-2440A	
				Ohta, H.	2441-2450A	
				Ohta, H.	2451-2460A	
				Ohta, H.	2461-2470A	
				Ohta, H.	2471-2480A	
				Ohta, H.	2481-2490A	
				Ohta, H.	2491-2500A	
				Ohta, H.	2501-2510A	
				Ohta, H.	2511-2520A	
				Ohta, H.	2521-2530A	
				Ohta, H.	2531-2540A	
				Ohta, H.	2541-2550A	
				Ohta, H.	2551-2560A	
				Ohta, H.	2561-2570A	
				Ohta, H.	2571-2580A	
				Ohta, H.	2581-2590A	
				Ohta, H.	2591-2600A	
				Ohta, H.	2601-2610A	
				Ohta, H.	2611-2620A	
				Ohta, H.	2621-2630A	
				Ohta, H.	2631-2640A	
				Ohta, H.	2641-2650A	
				Ohta, H.	2651-2660A	
				Ohta, H.	2661-2670A	
				Ohta, H.	2671-2680A	
				Ohta, H.	2681-2690A	
				Ohta, H.	2691-2700A	
				Ohta, H.	2701-2710A	
				Ohta, H.	2711-2720A	
				Ohta, H.	2721-2730A	
				Ohta, H.	2731-2740A	
				Ohta, H.	2741-2750A	
				Ohta, H.	2751-2760A	
				Ohta, H.	2761-2770A	
				Ohta, H.	2771-2780A	
				Ohta, H.	2781-2790A	
				Ohta, H.	2791-2800A	
				Ohta, H.	2801-2810A	
				Ohta, H.	2811-2820A	
				Ohta, H.	2821-2830A	
				Ohta, H.	2831-2840A	
				Ohta, H.	2841-2850A	
				Ohta, H.	2851-2860A	
				Ohta, H.	2861-2870A	
				Ohta, H.	2871-2880A	
				Ohta, H.	2881-2890A	
				Ohta, H.	2891-2900A	
				Ohta, H.	2901-2910A	
				Ohta, H.	2911-2920A	
				Ohta, H.	2921-2930A	
				Ohta, H.	2931-2940A	
				Ohta, H.	2941-2950A	
				Ohta, H.	2951-2960A	
				Ohta, H.	2961-2970A	
				Ohta, H.	2971-2980A	
				Ohta, H.	2981-2990A	
				Ohta, H.	2991-3000A	
				Ohta, H.	3001-3010A	
				Ohta, H.	3011-3020A	
				Ohta, H.	3021-3030A	
				Ohta, H.	3031-3040A	
				Ohta, H.	3041-3050A	
				Ohta, H.	3051-3060A	
				Ohta, H.	3061-3070A	
				Ohta, H.	3071-3080A	
				Ohta, H.	3081-3090A	
				Ohta, H.	3091-3100A	
				Ohta, H.	3101-3110A	
				Ohta, H.	3111-3120A	
				Ohta, H.	3121-3130A	
				Ohta, H.	3131-3140A	
				Ohta, H.	3141-3150A	
				Ohta, H.	3151-3160A	
				Ohta, H.	3161-3170A	
				Ohta, H.	3171-3180A	
				Ohta, H.	3181-3190A	
				Ohta, H.	3191-3200A	
				Ohta, H.	3201-3210A	
				Ohta, H.	3211-3220A	
				Ohta, H.	3221-3230A	
				Ohta, H.	3231-3240A	
				Ohta, H.	3241-3250A	
				Ohta, H.	3251-3260A	
				Ohta, H.	3261-3270A	
				Ohta, H.	3271-3280A	
				Ohta, H.	3281-3290A	
				Ohta, H.	3291-3300A	
				Ohta, H.	3301-3310A	
				Ohta, H.	3311-3320A	
				Ohta, H.	3321-3330A	
				Ohta, H.	3331-3340A	
				Ohta, H.	3341-3350A	
				Ohta, H.	3351-3360A	
				Ohta, H.	3361-3370A	
				Ohta, H.	3371-3380A	
				Ohta, H.	3381-3390A	
				Ohta, H.	3391-3400A	
				Ohta, H.	3401-3410A	
				Ohta, H.	3411-3420A	
				Ohta, H.	3421-3430A	
				Ohta, H.	3431-3440A	
				Ohta, H.	3441-3450A	
				Ohta, H.	3451-3460A	
				Ohta, H.	3461-3470A	
				Ohta, H.	3471-3480A	
				Ohta, H.	3481-3490A	
				Ohta, H.	3491-3500A	
				Ohta, H.	3501-3510A	
				Ohta, H.	3511-3520A	
				Ohta, H.	3521-3530A	
				Ohta, H.	3531-3540A	
				Ohta, H.	3541-3550A	
				Ohta, H.	3551-3560A	
				Ohta, H.	3561-3570A	
		</				

Richards, N.L.	785-790A	Semeels, A.	3357-3361A	Sui, H.X.	1779-1784A	Trivedi, R.	509-824A
Richards, W.J.	3682-3687A	Seyhan, I.	2470-2478A	Sui, Z.T.	71-79B		625-634A
Rifkin, J.A.	1476-1488A	Sha, H.	305-314B	Suito, H.	57-64B		2727-2739A
Rigney, J.D.	3292-3306A	Shah, R.	1353-1362A		263-270B	Tsai, P.C.	399-408B
Rios, P.R.	1132-1134A	Shang, J.K.	205-211A		423-431B	Tsai, T.C.	2617-2627A
Ritchie, R.O.	3781-3792A		213-219A		351-354B	Tsubakino, H.	1668-1675A
Roberts, J.A.	2820-2836A		221-228A	Sukia, L.B.	943-953B	Tsukihashi, F.	967-972B
Robino, C.V.	65-69B	Shankar, P.	1175-1186A	Sukonnik, I.M.	2051-2053A	Tumbull, D.	725-730A
Rodriguez, P.	1313-1325A	Shao, Y.	1476-1488A	Sumin, V.V.	2045-2046A	Ueda, H.	35-41B
	2881-2887A	Sharivker, V.S.	788-793B	Sumiyama, K.	4210-4213A		765-772B
Rohatgi, P.K.	277-285B	Shaw, W.	923-928A	Sun, H.	852-862B	Uhlenius, B.	2869-2880A
Rokhlin, S.I.	165-182A	Shekhar, R.	19-27B	Sun, X.	355-361B	Ullakko, K.	1815-1821A
Rolseth, S.	177-183B	Shen, Y.-L.	3700-3717A	Sundararaman, D.	1175-1186A	Ulvensseen, J.H.	3630-3638A
	185-193B	Sherby, O.D.	111-118A		2966-2977A	Urao, R.	401-405A
	739-744B		2837-2842A	Sundman, B.	2897-2903A	Uttomark, M.J.	533-547A
Rönkä, K.J.	2229-2238A	Sherif El-Eskandarany, M.	3267-3278A	Suresh, S.	1045-1056B	Uwakweh, O.N.C.	2904-2910A
Root, J.H.	993-997B	Shi, N.	3739-3746A	Suryanarayana, C.	3700-3717A	Vaidya, R.U.	459-465A
Roy, N.	415-429A	Shiau, M.Y.	203-211B		41-48A	Valentini, R.	3773-3780A
Roy, T.	1167-1173A	Shiflet, G.J.	1595-1605A	Suzuki, K.	4210-4213A	Valiente, A.	291-304A
Roy, T.K.	3993-4002A	Shigematsu, T.	3431-3444A	Suzuki, M.	3307-3317A	Van Aken, D.C.	2565-2573A
	4003-4010A	Shih, H.-C.	719-724A	Svensson, I.	81-99B	Van Houtte, P.	2347-2358A
Royal, T.E.	1761-1771A	Shim, J.-H.	2479-2494A	Svensson, I.L.	2209-2220A	Van Loo, F.J.J.	59-69A
Roytburd, A.L.	1687-1692A	Shimizu, K.	955-966B	Swaminathan, S.	2047-2050A	Van Loon, P.J.J.	2229-2238A
Ruano, O.A.	1861-1867A	Shirayanagi, I.	719-724A	Swamy, K.M.	351-354B	Van Zyl, B.P.	1203-1216A
Rubin, J.B.	2297-2304A	Shitessel, V.E.	4163-4169A	Sweet, E.D.	3530-3541A	Vandermeer, R.A.	1511-1516A
Russell, K.C.	1441-1448A	Sichen, D.	2852-2858A	Swinbourne, D.R.	3187-3191A	Varghese, V.	847-851B
Ruuskanen, P.R.	2297-2304A		318-322B	Symons, D.M.	101-110A	Varin, R.A.	5-17A
Ryun, N.	2916-2922A		409-416B	Syn, C.K.	111-118A		71-79A
Saccone, A.	979-986B	Sikka, V.K.	4011-4018A	Szpunar, J.A.	3849-3861A	Varma, S.K.	2023-2034A
Sadoway, D.R.	839-845B	Simalai, N.	3669-3674A	Tacke, K.-H.	869-879B	Varona, J.M.	281-290A
Sagar, P.K.	2593-2604A	Singh, A.K.	1167-1173A	Tada, S.	1585-1594A		291-304A
Sahay, S.S.	2383-2385A	Singh, J.	3135-3148A	Tadaki, T.	719-724A	Vatne, H.E.	4133-4144A
Sahin, O.	451-458A	Singh, M.	3669-3674A	Tagami, M.	1686-1675A	Vecchio, K.S.	1739-1748A
Sáinz, E.	379-384B		3727-3738A	takada, K.	4210-4213A	Venkateswara Rao, K.T.	3781-3792A
	801-807B	Sinha, T.K.	3340-3343A	Takagi, S.	1630-1641A	Verugopal, S.	119-126A
Sekai, Y.	4163-4169A	Skrotzki, B.	3431-3444A	Takahashi, S.	2187-2195A	Verugopal, H.	43-50B
Sekaki, T.	317-326A	Skybakmoen, E.	738-744B	Takahashi, T.	1047-1053A	Verugopal, R.	731-738B
Salas, D.	2023-2034A	Smeltzer, W.W.	3649-3661A		1585-1594A	Verhoeven, J.D.	496-498A
Salvens, G.	3126-3134A	Smith, B.J.	3192-3202A	Takai, A.	3753-3759A	Verlinden, B.	2328-2337A
Samarasekera, I.V.	4095-4111A	Smith, P.M.	725-730A	Taleff, E.M.	43-50B	Verma, R.	2740-2753A
	4113-4120A	Smith, P.R.	3074-3080A	Talvitie, M.	4171-4181A	Vetrano, J.S.	2947-2957A
Samuel, A.M.	415-429A	Smouk, S.Yu.	1815-1821A	Tamura, M.	385-392B	Vijay, P.L.	731-738B
	1785-1798A	Soboyejo, W.O.	2263-2273A	Tanabe, J.	656-662B	Vijaya, H.S.	1057-1060B
Samuel, F.H.	415-429A	Sohn, H.Y.	213-219B	Tanaka, M.	2878-2885A	Vinokur, A.	2852-2858A
	1785-1798A	Solheim, A.	738-744B	Tang, S.	827-938B	Vinokur, B.B.	2852-2858A
Sanders, T.H., Jr.	19-27A	Solina, A.	3773-3780A	Tankala, K.	43-50B	Vinsand, T.	804-809B
Sano, N.	652-657B	Solis, M.	2023-2034A	Tarasenko, A.V.	1815-1821A	Visvesvaran, P.	973-980A
	846-851B	Solnordal, C.B.	221-230B	Tawara, E.	967-972B	Viswanathan, U.K.	757-761A
	937-941B	Somers, M.A.J.	1055-1061A	Tekin, A.	3727-3738A	Vitek, J.M.	763-774A
Saqib, M.	491-500B		1063-1071A	Terakado, K.	401-405A	Vives, C.	445-455B
Sarkissian, A.	635-656A	Sommer, F.	921-927B	Tewari, S.N.	1095-1110A	1111-1119A	457-464B
Sarma, B.	717-730B	Song, H.	51-55B		1111-1119A	Voorhees, P.W.	937-943A
Sarral-Mamoory, R.	577-584B		1095-1110A		1353-1362A	2470-2478A	
	585-594B		1111-1119A		3669-3674A	Voskamp, A.P.	3445-3465A
Sathiyamoorthy, D.	731-738B	Song, S.	3381-3390A		3727-3738A	Vrestal, J.	701-704B
Sato, F.	929-935B	Song, S.G.	459-465A		1749-1759A	Wadsworth, J.	343-352A
Sato, M.	3753-3759A		3739-3746A	Thadhani, N.N.	1761-1771A	Wagner, C.N.J.	2888-2896A
Saunders, F.I.	2605-2616A	Sopousek, J.	701-704B	Thakur, A.	1739-1748A	Wagoner, R.H.	2605-2616A
Sauthoff, G.	1395-1400A	Serie, M.	177-183B		2274-2284A	3971-3981A	
	2642-2652A	Sosnai, V.V.	2045-2046A	Thanaboonsutb, B.	19-27A	Waide, P.A.	775-783A
Savva, G.C.	1606-1617A	Spanos, G.	1517-1532A		695-705A	Waku, Y.	3307-3317A
Schaefler, M.	1293-1302A	Spencer, C.W.	1576-1682A	Thadani, N.N.	1761-1771A	Wallace, T.C., Sr.	141-146B
Schiffers, H.	255-267A	Spicarelli, S.	3871-3879A	Thévoz, Ph.	1781-1794A	Walls, D.P.	1899-1907A
Schmidt, P.	81-99B	Spooner, S.	2934-2946A	Thomas, B.G.	2274-2284A	Wan, C.C.	1363-1370A
Schoenway, J.M.	2115-2121A	Stackpole, M.M.	639-849A	Thompson, A.W.	101-110A	Wang, C.-C.	3162-3169A
Schulze, T.P.	583-593A	Starke, E.A., Jr.	3431-3444A	Thompson, R.G.	2692-2703A	Wang, C.Y.	2754-2764A
Schuster, H.	255-267A	Steele, J.H.	433-443B	Thompson, S.W.	1251-1266A	Wang, G.-X.	2765-2783A
	851-861A	Steele, J.K.	981-993A		1554-1568A	Wang, G.Z.	2784-2795A
Schwartz, D.S.	2263-2273A	Stefanescu, D.M.	2708-2721A	Thompson, A.W.	1001-110A	Wang, H.Z.	2285-2292A
Schwenker, S.W.	4193-4204A		4061-4074A	Thompson, R.G.	1251-1266A	Wang, J.-J.	2385-2389A
Schwerdtfeger, K.	231-239B		4075-4083A	Thompson, S.W.	1569-1584A	Wang, L.	1533-1543A
	305-314B		4205-4210A		1581-1594A	Wang, L.L.	1347-1352A
Schwitzgebel, G.	2419-2428A	Sterten, Å.	255-261B	Thonstad, J.	177-183B	Wang, L.	141-146B
Seetharaman, S.	318-322B		739-744B		185-193B	Wang, M.	819-821A
	409-416B	Steube, R.S.	569-581A		255-261B	Wang, R.	3108-3111A
	2105-2114A	Stiller, K.	327-341A	Tian, D.W.	4031-4038A	Wang, S.	3318-3329A
	2978-2984A	Stoen, L.	739-744B	Tiedje, N.	4085-4093A	Wang, X.-J.	3971-3981A
Seetharaman, V.	1933-1950A	Støre, T.	739-744B	Tjøn, S.C.	2385-2389A	Wang, Z.F.	2686-2691A
	2051-2053A	Strahan, A.	3187-3191A		2663-2672A	Wang, Z.G.	3662-3668A
Sehitoglu, H.	3068-3073A	Strehler, M.	1003-1014A	Tjøtta, S.	501-508B	Wang, Z.M.	1595-1605A
	3491-3502A	Stubergh, J.R.	604-609B	Toda, H.	2013-2021A	Warren, J.A.	657-669A
Sekhar, J.A.	981-972A		895-900B	Tomsett, A.	297-304B	Warrier, S.G.	527-532B
Semiatin, S.L.	1709-1720A	Su, Q.	2858-2860A	Tomeia, A.P.	2100-2104A	Watson, J.	1379-1394A
	1933-1950A	Subbanha, G.N.	1057-1060B	Tøndel, P.A.	2122-2129A	Watson, K.	2035-2043A
	2051-2053A	Subrahmanyam, J.	237-240A	Torchane, L.	2305-2313A	Watson, M.	1630-1641A
	3112-3119A	Subramanian, P.R.	1842-1854A	Toriyama, O.	1823-1835A	Watson, N.	1909-1917A
Sen, R.	3675-3681A	Subramanian, S.V.	1149-1165A	3925-3935A	1843-1855A	Watson, P.	1918-1926A
	503-505A	Subramanian, V.	961-972A	Torres-Villaseñor, G.	3330-3335A	Watson, R.	1927-1935A
Senkov, O.N.	1303-1312A	Sudhakar, V.	704-708B	Torvund, T.	3630-3638A	Watson, T.	1936-1944A
	1869-1876A	Sudhölter, S.	1031-1044B	Totemeier, T.C.	353-361A	Watson, W.	1945-1953A
	1877-1887A	Suh, D.	3149-3161A		363-369A	Watson, Z.	1954-1962A
	3963-3970A		3893-3901A	Trefny, J.U.	2958-2965A	Watson, Z.	1963-1971A

Watanebe, Y.	4145-4151A	Wolff, I.M.	1395-1400A	Yamamoto, A.	1668-1675A	Zelin, M.G.	1400-1403A
Watwe, A.S.	493-496A		2642-2652A	Yamamoto, T.	385-392B	Zeng, X.	2115-2121A
Weatherly, G.C.	1149-1165A		3688-3699A	Yamane, T.	1807-1814A	Zhang, D.L.	3983-3991A
Weaver, M.L.	1606-1617A	Won, C.W.	315-318B	Yamano-Uchi, N.	385-392B	Zhang, H.	891-900A
Webster, G.A.	3542-3557A	Wong, J.	775-783A	Yang, H.R.	3343-3346A	Zhang, J.	2094-2099A
Wei, B.	829-837A	Wu, D.	2293-2296A	Yang, J.-M.	1363-1370A		2293-2296A
Wei, R.P.	2293-2296A	Wu, L.-T.	3639-3648A	Yang, L.	2094-2099A		
Wei, S.	29-40A	Wu, S.K.	527-532B	Yang, S.T.	863-872A	Zhang, L.	794-800B
Wei, S.	3391-3398A		1379-1394A	Yang, Y.	1025-1029B	Zhang, P.	2105-2114A
Weinem, D.	973-978B	Wu, S.Q.	2385-2389A	Yang, Z.-G.	1533-1543A		2978-2984A
Wells, M.E.	1700-1708A	Wu, W.	3639-3648A	Ye, F.	2263-2273A	Zhang, S.Q.	1779-1784A
Weng, G.J.	598-701B	Wu, X.	157-162B	Yegneswaran, A.H.	3513-3523A	Zhang, Z.	205-211A
Wert, J.A.	317-326A	Wu, Y.	2115-2121A	Yeh, J.-W.	1951-1962A		221-228A
	2359-2365A	Wuttig, M.	1687-1692A		3558-3568A		2911-2915A
	269-279A		2858-2860A	Yin, F.	719-724A		
Wessén, M.	3503-3512A	Xiao, H.	185-193B	Yilitao, M.	49-57A	Zheng, L.	3983-3991A
Westwood, A.R.C.	2209-2220A	Xing, X.	973-978B	Yokoyama, K.	2574-2582A	Zheng, X.L.	3089-3094A
	337-350B	Xu, C.	2094-2099A	Yoo, C.H.	3466-3472A	Zheng, Y.K.	1533-1543A
Wheeler, R.	1413-1426A	Xu, D.M.	2221-2228A	Yoon, D.-Y.	3120-3125A	Zhigalina, O.M.	2045-2046A
Whittenberger, J.D.	2047-2050A	Xu, H.B.	3662-3668A	Yoon, D.Y.	2809-2819A		
	2628-2641A	Xu, L.Y.	2429-2435A	Yoon, Y.C.	1273-1281A	Zhou, Y.	1047-1053A
Wiezorek, J.M.K.	3170-3180A	Xu, P.	1187-1201A	Yu, D.P.	2911-2915A	Zhu, D.	2094-2099A
Wilson, A.	2047-2050A	Xu, R.	2221-2228A	Yu, S.Y.	2653-2662A	Zhu, M.	819-821A
Windisch, C.F., Jr.	2196-2208A	Xu, X.	1347-1352A	Yu, Z.	1347-1352A	Zhu, S.M.	2663-2672A
Wiskel, J.B.	839-849A	Xue, H.	475-480B	Zaki, M.	1043-1046A	Zhu, Z.	1327-1331A
	119-127B	Xue, X.M.	71-79B	Zakulski, W.	2419-2428A	Zok, F.W.	1899-1907A
	129-137B	Yamada, H.	1021-1031A	Zaluska, A.	929-936A	Zurek, A.K.	459-465A
		Yamada, S.	1979-1989A	Zbiral, J.	1371-1377A		



Combined Subject Index

Abrasion resistant coatings, Mechanical properties	
Correlation of microstructure and fracture toughness in high-chromium white iron hardfacing alloys.	3881-3891A
Abrasive wear	
The wear behavior between hardfacing materials.	3639-3648A
Influence of reinforcement volume fraction and size on the microstructure and abrasion wear resistance of hot isostatic pressed white iron matrix composites.	4171-4181A
Influence of matrix structure on the abrasion wear resistance and toughness of a hot isostatic pressed white iron matrix composites.	4183-4191A
Abrasive wear, Coating effects	
Wear-resistant coatings produced by shock-wave compaction of powders.	2297-2304A
Abrasives	
Fracture and crushing strength of micrometer-size diamond abrasives used in microgrinding of optical glass.	1047-1053A
Accuracy	
Solid-state contributions to densification during liquid-phase sintering.	901-909B
Studies of interface deformations in single- and multi-layered liquid baths due to an impinging gas jet.	911-920B
A thermodynamic evaluation of the Ti-Mo-C system.	955-966B
Plastic zone and pileup around large indentations.	3793-3800A
Measurement of friction under sheet forming conditions.	3971-3981A
High-temperature oxidation of Ti_3Al -based titanium aluminides in oxygen.	3993-4002A
Macrotransport-solidification kinetics modeling of equiaxed dendritic growth. II. Computation problems and validation on Inconel 718 superalloy casting.	4075-4083A
Modeling particle fracture during the extrusion of aluminum/alu-mina composites.	4113-4120A
Acid leaching	
Zinc reduction of Mo_3 in a self propagating high temperature synthesis process.	315-318B
Acoustic emission testing	
Creep deformation and damage in a continuous fiber-reinforced Ti-6Al-4V composite.	4193-4204A
Activated sintering	
Synthesis of RuAl by reactive powder processing.	3688-3699A
Activation	
Internal friction in hydrogen-charged CrNi and CrNiMn austenitic stainless steels.	1815-1821A
Activation energy	
Preparation of fine copper powders from organic media by reaction with hydrogen under pressure. II. The kinetics of particle nucleation, growth, and dispersion.	585-594B
Viscosity of superalloy 718 by the oscillating vessel technique.	698-701B
Recrystallization in oxide-dispersion strengthened mechanically alloyed sheet steel.	1983-1978A
Deformation behavior of an Al-3.37 wt. % Li alloy.	2274-2284A
Activity (chemical)	
Chemical potentials of components of the system $CaO+P_2O_5+Fe_2O_3$ at 1673K.	595-603B
Thermodynamics of sulfur in the $BaO-MnO-SiO_2$ flux system.	652-657B
Use of solid-electrolyte galvanic cells to determine the activity of CaO in the $CaO-ZrO_2$ system and the standard Gibbs free energies of formation of $CaZrO_3$ from CaO and ZrO_2 .	658-662B
Adsorption, Temperature effects	
Applicability of Butler's equation in interpreting the thermodynamic behavior of surfaces and adsorption in Fe-S-O melts.	241-253B
Aerospace	
Materials and society—impacts and responsibilities.	337-350B
Identification of precipitate phases in a mechanically alloyed rapidly solidified Al-Fe-Ce alloy.	1033-1041A
Aging (artificial)	
Carbide diagrams and precipitation of alloying elements during aging of low-alloy steels.	498-502A
Characterization of the formation of α_1 plates from the β_2 phase in a Cu-Zn-Au alloy.	719-724A
Mechanical properties and 95°C aging characteristics of zircon reinforced Zn-4Al-3Cu alloy.	809-818A
Microstructural stability on aging of an $\alpha+\beta$ titanium alloy: Ti-6Al-1.6Zr-3.3Mo-0.3Si.	1167-1173A
Heterogeneous nucleation of δ on dislocations in a dilute aluminum-lithium alloy.	1595-1605A
Dense CoAl-based alloys with improved ductility: solid-state synthesis and microstructure control.	2140-2150A
Mössbauer spectroscopy study of the aging and tempering of high nitrogen quenched Fe-N alloys: kinetics of formation of $Fe_{1-x}N_x$ nitride by interstitial ordering in martensite.	2160-2177A
Effects of low-temperature aging on the microstructure and soft magnetic properties of rapidly quenched Fe-Si-B alloys.	2454-2460A
Precipitation behaviors in Al-Cu-Mg and 2024 aluminum alloys.	2479-2494A
Atmospheric stress corrosion cracking of a superplastic 7475 aluminum alloy.	2617-2627A
Influence of thermal aging on the intergranular corrosion resistance of types 304LN and 316LN stainless steels.	2881-2887A
Low quench sensitivity of superplastic 8090 Al-Li thin sheets.	2923-2933A
On the effect of stress on nucleation and growth of precipitates in an Al-Cu-Mg-Ag alloy.	3431-3444A
The plastic anisotropy of an Al-Li-Cu-Zr alloy extrusion in unidirectional deformation.	3503-3512A
Effect of aging on shape memory behavior of Ti-51.3 at. % Ni thin films.	3753-3759A
Aging (natural), Alloying effects	
Effect of magnesium on the aging behavior of Al-Zn-Mg-Cu/ Al_2O_3 metal matrix composites.	2005-2012A
Air, Environment	
Hydrogen-induced cleavage fracture of Fe_3Al -based intermetallics.	3949-3956A
Aircraft components, Materials selection	
Tension characteristics of notched specimens for Al-Li-Cu-Zr alloys sheets with various cerium contents.	3089-3094A
Alkali metals, Impurities	
Effects of alkali-metal impurities on fracture toughness of 2090 Al-Li-Cu extrusions.	3530-3541A
Alkalies, Environment	
Stress corrosion cracking of pressure vessel steels in high-temperature caustic aluminate solutions.	1327-1331A
Alloy powders, Phase transformations	
Thermally assisted and mechanically driven solid-state reactions for formation of amorphous $Al_{33}Ta_{67}$ alloy powders.	3267-3278A
Alloy powders, Phases (state of matter)	
Kinetics of phase evolution of Zn-Fe intermetallics.	2904-2910A
Incipient chemical instabilities of nanophase Fe-Cu alloys prepared by mechanical alloying.	2934-2946A
Alloying	
The production of nickel-zinc alloys by powder injection.	780-787B
Aluminothermic reactions, Temperature effects	
Modeling of sequential reactions during micropyrotechnic synthesis.	961-972A
Aluminum, Alloying additive	
Retardation of intermetallic phase formation in experimental super ferritic stainless steels.	2436-2444A
Aluminum, Alloying elements	
Solubility of carbon in $CaO-Al_2O_3$ melts.	57-64B
Aluminum, Binary systems	
Critical evaluation and optimization of the thermodynamic properties of liquid tin solutions.	808-828B
Inverse melting in binary systems: morphology and microscopy of catactic alloys.	979-986B
Mechanistic processes influencing shock chemistry in powder mixtures of the Ti-Si, Ti-Al, and Ti-B systems.	1761-1771A
Aluminum, Bonding	
Microstructural development in NiAl/Ni-Si-B/Ni transient liquid phase bonds.	1925-1931A
Aluminum, Casting	
Thermomechanics of the cooling stage in casting processes: three-dimensional finite element analysis and experimental validation.	81-99B
Heat-flow-based analysis of surface crack formation during the start-up of the direct chill casting process. I. Development of the inverse heat-transfer model.	119-127B
Influence of chromium and impurities on the grain refining behavior of aluminum.	791-800A
Aluminum, Composite materials	
Subcritical crack growth at bimaterial interfaces. I. Flexural peel technique.	205-211A
Subcritical crack growth at bimaterial interfaces. III. Shear-enhanced fatigue crack growth resistance at polymer/metal interface.	221-228A
Reinforcement stresses during deformation of sphere- and particulate-reinforced aluminum-matrix composites.	486-490A
The Bauschinger effect in a SiC/Al composite.	995-1001A
A one-phase model of the mixing of Al-SiC composite melt.	1015-1023B

Theoretical analysis of the particle gradient distribution in centrifugal field during solidification.	1025-1029B	Aluminum base alloys, Casting	Scaling of intragranular dendritic microstructure in ingot solidification.	101-113B
Microstructure and properties of Al_2O_3 -Al(Si) and Al_2O_3 -Al(Si)-Si composites formed by in situ reaction of aluminum with aluminosilicate ceramics.	2122-2129A		Heat-flow-based analysis of surface crack formation during the start-up of the direct chill casting process. II. Experimental study of an AA5182 rolling ingot.	129-137B
The effect of volume percent and morphology of phases on the damping behavior of epoxy-aluminum composites.	2366-2373A		Porosity formation in Al-9 wt.% Si-3 wt.% Cu alloy systems: metallographic observations.	415-429A
Ni_3Al intermetallic particles as wear-resistant reinforcement for Al-base composites processed by powder metallurgy.	3259-3266A		Effects of forced electromagnetic vibrations during the solidification of aluminum alloys. I. Solidification in the presence of crossed alternating electric fields and stationary magnetic fields.	445-455B
Thermal expansion of metals reinforced with ceramic particles and microcellular foams.	3700-3717A		Effects of forced electromagnetic vibrations during the solidification of aluminum alloys. II. Solidification in the presence of colinear variable and stationary magnetic fields.	457-464B
Flow and fracture of bimaterial systems based on aluminum alloys.	3937-3947A		The improved microstructures and properties of 7075 alloys produced by a water-cooling centrifugal casting method.	1951-1962A
Infiltration of fibrous preform by molten aluminum in a centrifugal force field.	4163-4169A		Effect of grain refinement on the fluidity of two commercial Al-Si foundry alloys.	2305-2313A
Aluminum, Crystal growth			A model for macrosegregation and its application to Al-Cu castings.	2708-2721A
Crystallization of amorphous phase in sputter-deposited Ti-Al alloy thin films.	2047-2050A		Modeling of ingot distortions during direct chill casting of aluminum alloys.	3214-3225A
Determination of the solidification curves of commercial aluminum alloys.	2722-2726A		The squeeze casting of hypoeutectic binary Al-Cu.	4121-4132A
Aluminum, Diffusion				
Anomalous diffusion of iron in liquid aluminum measured by the pulsed laser technique.	725-730A	Aluminum base alloys, Composite materials	Probing the initial stage of synthesis of Al_2O_3 /Al composites by directed oxidation of Al-Mg alloys.	43-50B
Aluminum, Dopants			Subcritical crack growth at bimaterial interfaces. II. Microstructural effects on fracture resistance of metal/ceramic interfaces.	213-219A
Improved oxidation resistance of group VB refractory metals by Al^{+} ion implantation.	491-500B		Transient thermal analysis of solidification in a centrifugal casting for composite materials containing particle segregation.	277-285B
Aluminum, Electrical properties			Effect of a solid solution on the steady-state creep behavior of an aluminum matrix composite.	305-316A
Physical modeling studies of electrolyte flow due to gas evolution and some aspects of bubble behavior in advanced Hall cells. III. Predicting the performance of advanced Hall cells.	19-27B		Stacking faults in SiC particles and their effect on the fracture behavior of a 15 vol.% SiC/6061-Al matrix composite.	459-465A
Aluminum, Extraction			Effect of manganese dispersoid on the fatigue crack propagation of Al-Zn-Mg alloys.	490-493A
Studies on the corrosion and the behavior of inert anodes in aluminum electrolysis.	185-193B		The x-ray diffraction study of deformation in the composite matrix of Al-Mg-Zn and SiC.	503-505A
Electrical conductivity of molten cryolite based mixtures obtained with a tube type cell made of pyrolytic boron nitride.	255-261B		Solidification of binary hypoeutectic alloy matrix composite castings.	595-609A
Liquidus temperatures for primary crystallization of cryolite in molten salt systems of interest for aluminum electrolysis.	739-744B		Solidification of particle-reinforced metal-matrix composites.	663-671B
The transported entropy of Na^{+} in solid state cryolite.	788-793B		Effect of magnesium on the aging behavior of Al-Zn-Mg-Cu/ Al_2O_3 metal matrix composites.	2005-2012A
Reference electrode of simple galvanic cells for developing sodium sensors for use in molten aluminum.	794-800B		The control of grain size and distribution of particles in a (6061 alloy) _m /(Al_2O_3) _p composite by solutionizing treatment.	2023-2034A
Aluminum, Forming			On the role of magnesium and silicon in the formation of alumina from aluminum alloys by means of DIMOX processing.	2094-2099A
Reply: Dynamic materials model. Basis and principles.	235-236A		Wear behavior of aluminum-based metal matrix composites reinforced with a preform of aluminosilicate fiber.	2385-2389A
Aluminum, Mechanical properties			Corrosive wear of SiC whisker- and particulate-reinforced 6061 aluminum alloy composites.	2653-2662A
Communication: Mechanical deformation of dendrites by fluid flow.	229-232A		Tensile ductility and fracture of superplastic aluminum-SiC composites under thermal cycling conditions.	2837-2842A
Temperature dependence of the rate sensitivity and its effect on the activation energy for high-temperature flow.	3346-3348A		Failure characteristics of 6061/ $Al_2O_3/15_p$ and 2014/ $Al_2O_3/15_p$ composites as a function of loading rate.	3095-3107A
Plastic zones and fatigue-crack closure under plane-strain double slip.	3491-3502A		High-temperature wear and deformation processes in metal matrix composites.	3135-3148A
Aluminum, Oxidation			Thermal residual stresses in functionally graded and layered 6061 Al/SiC materials.	3241-3249A
Reoxidation of aluminum in Fe-Al-M (M=C, Mn, and Ti) melts with $CaO-Al_2O_3-FeO$ (3 mass%) slags.	423-431B		Structure of phases in the 6-Al ₂ O ₃ fiber studied by convergent beam electron diffraction.	3318-3329A
Aluminum, Physical properties			Microstructural changes in a mechanically alloyed Al-8.2Zn-2.5Mg-1.7Cu alloy (7010) with and without particulate SiC reinforcement.	3718-3726A
Variation of contact angles with temperature and time in the Al-Al ₂ O ₃ system.	51-55B		Reinforcement shape effects on the fracture behavior and ductility of particulate-reinforced 6061-Al matrix composites.	3739-3746A
Aluminum, Quaternary systems			Microstructure and fracture of SiC-particulate-reinforced cast A356 aluminum alloy composites.	3893-3901A
An isothermal section at 550°C in the Al-rich corner of the Al-Fe-Mn-Si system.	3357-3361A		Flow and fracture of bimaterial systems based on aluminum alloys.	3937-3947A
Aluminum, Rolling			Mathematical modeling of the extrusion of 6061/ $Al_2O_3/20_p$ composite.	4095-4111A
Quantitative characterization of the surface topography of rolled sheets by laser scanning microscopy and Fourier transformation.	2338-2346A		Modeling particle fracture during the extrusion of aluminum/alumina composites.	4113-4120A
Modeling recrystallization kinetics, grain sizes, and textures during multipass hot rolling.	4133-4144A		Analysis of thermal residual stress in a thick-walled ring of Dur-alcan-base Al-SiC functionally graded material.	4145-4151A
Aluminum, Ternary systems			Aluminum base alloys, Corrosion	
Evolution of microstructures in the nickel modified titanium tri-aluminides near the L_1 phase field.	5-17A		Atmospheric stress corrosion cracking of a superplastic 7475 aluminum alloy.	2617-2627A
Mechanical behavior of the in situ composite alloys in the Al-Ni-Ti system near the L_1 phase field.	71-79A			
Mechanical properties of Ru-Ni-Al alloys.	1395-1400A		Aluminum base alloys, Crystal growth	
Experimental study of the phase equilibria in the Fe-Mn-Al system.	2429-2435A		Modeling of microsegregation in macrosegregation computations.	2314-2327A
Thermodynamic activities and phase boundaries for the alloys of the Ni_3Al-Ni_3Ti pseudobinary section in the Ni-Al-Ti system.	2673-2677A		Determination of the solidification curves of commercial aluminum alloys.	2722-2726A
Thermodynamic activities and partial enthalpies of mixing in the solid solution of Fe in Ni_3Al .	3569-3575A		Equiaxed dendritic solidification with convection. I. Multiscale/multiphase modeling.	2754-2764A
Martensitic transformations in NiMnAl β phase alloys.	4153-4162A		Equiaxed dendritic solidification with convection. II. Numerical simulations for an Al-4 wt.% Cu alloy.	2765-2783A
Aluminum base alloys				
The improved microstructures and properties of 7075 alloys produced by a water-cooling centrifugal casting method.	1951-1962A			
Aluminum base alloys, Alloy development				
Formation of aluminum-silicon alloys from feldspars—determination of silicon, light, and heavy elements in silumin by scanning electron microscopy.	604-609B			

Equiaxed dendritic solidification with convection. III. Comparisons with $\text{NH}_4\text{Cl}-\text{H}_2\text{O}$ experiments.	2784-2795A	A high resolution transmission electron microscopy study of interfaces between the γ , B_2 , and α_2 phases in a Ti-Al-Mo alloy.	1618-1629A
Effects of alloy modification and thermomechanical processing on recrystallization of Al-Mg-Mn alloys.	2947-2957A	Microstructural aspects of the dissolution and melting of Al_2Cu phase in Al-Si alloys during solution heat treatment.	1785-1798A
Aluminum base alloys, Diffusion		High-resolution electron microscopy analysis of structural defects in a (2/1, 5/3)-type approximant of a decagonal quasicrystal of an Al-Pd-Mn alloy.	2911-2915A
Analysis on the amplitude of serrated flow associated with the Portevin-LeChatelier effect of substitutional fcc alloys.	1683-1686A		
Aluminum base alloys, Forming			
Reply: Dynamic materials model. Basis and principles.	235-236A	Aluminum base alloys, Rolling	
		Modeling recrystallization kinetics, grain sizes, and textures during multipass hot rolling.	4133-4144A
Aluminum base alloys, Heat treatment			
A process model for on-line quenching of aluminum extrusions. Low quench sensitivity of superplastic 8090 Al-Li thin sheets.	501-508B 2923-2933A	Aluminum base alloys, Structural hardening	
		Precipitation behaviors in Al-Cu-Mg and 2024 aluminum alloys. On the effect of stress on nucleation and growth of precipitates in an Al-Cu-Mg-Ag alloy.	2479-2494A
Aluminum base alloys, Mechanical properties			3431-3444A
Enhanced ductility in coarse-grained Al-Mg alloys.	343-352A	Aluminum base alloys, Surface properties	
Mechanical behavior and properties of mechanically alloyed aluminum alloys.	737-745A	Measurement of friction under sheet forming conditions.	3971-3981A
A study of the influence of mischmetal additions to Al-7Si-0.3Mg (LM 25/356) alloy.	1283-1292A	Aluminum compounds	
Effect of strontium modification on near-threshold fatigue crack growth in an Al-Si-Cu die cast alloy.	1293-1302A	Martensitic transformations in NiMnAl β phase alloys.	4153-4162A
On microsuperplasticity in AA7475 domes.	1400-1403A		
Increased ductility in high velocity electromagnetic ring expansion.	1837-1844A	Aluminum compounds, Alloying elements	
Characterization of superplastic deformation behavior of a fine grain 5083 Al alloy sheet.	1889-1898A	Notch fracture in γ -titanium aluminides.	3903-3912A
Growth behavior of microstructurally short cracks in the 6061 aluminum alloy with and without 22 vol.% SiC whiskers.	2013-2021A	Aluminum compounds, Coating	
Deformation behavior of an Al-3.37 wt.% Li alloy.	2274-2284A	The deposition of aluminide and silicide castings on $\gamma\text{-TiAl}$ using the halide-activated pack cementation method.	3761-3772A
Control of superplastic deformation rate during uniaxial tensile tests.	3030-3042A	Aluminum compounds, Coatings	
Intergranular fracture in some precipitation-hardened aluminum alloys at low temperatures.	3081-3088A	Isothermal fatigue of an aluminide-coated single-crystal superalloy. I.	353-361A
Tension characteristics of notched specimens for Al-Li-Cu-Zr alloys sheets with various carbon contents.	3089-3094A	Isothermal fatigue of an aluminide-coated single-crystal superalloy. II. Effects of brittle precracking.	363-369A
Simulation of the hot-tension test under cavitating conditions.	3112-3119A	Aluminum compounds, Composite materials	
Hot deformation mechanisms of a solution-treated Al-Li-Cu-Mg-Zr alloy.	3478-3490A	Investigation of the reaction zone between TiAl and molybdenum.	2285-2292A
The plastic anisotropy of an Al-Li-Cu-Zr alloy extrusion in unidirectional deformation.	3503-3512A	Ni_2Al intermetallic particles as wear-resistant reinforcement for Al-base composites processed by powder metallurgy.	3259-3266A
Effects of alkali-metal impurities on fracture toughness of 2090 Al-Li-Cu extrusions.	3530-3541A	Aluminum compounds, Joining	
The cracking mechanism of silicon particles in an A357 aluminum alloy.	3558-3568A	Transient liquid-phase bonding in the NiAl/Cu/Ni system—a microstructural investigation.	3621-3629A
Microstructural evolution and superplastic deformation behavior of fine grain 5083Al.	3827-3839A	Aluminum compounds, Mechanical properties	
Evidence of fracture surface interference for cracks loaded in shear detected by phase-shifted speckle interferometry.	3853-3860A	Non-Schmid effects on the behavior of polycrystals, with applications to Ni_3Al .	81-99A
An evaluation of the creep properties of two Al-Si alloys produced by rapid solidification processing.	3871-3879A	Effect of creep strain on microstructural stability and creep resistance of a TiAl/Ti ₂ Al lamellar alloy.	127-134A
Elevated temperature deformation behavior of a dispersion-strengthened Al-Fe, V, Si alloy.	3913-3923A	Rafting in superalloys.	513-530A
The quench sensitivity of cast Al-7 wt.% Si-0.4 wt.% Mg alloy.	3983-3991A	High-temperature deformation properties of NiAl single crystals.	1229-1240A
Aluminum base alloys, Metal working		Influence of temperature transients on the hot workability of a two-phase gamma titanium aluminide alloy.	1933-1950A
An investigation by interactive electron backscatter pattern analysis of processing and superplasticity in an aluminum-magnesium alloy.	2252-2262A	High-temperature low-cycle fatigue of a gamma titanium aluminide alloy Ti-46Al-2Nb-2Cr.	2239-2251A
Aluminum base alloys, Microstructure		High-temperature deformation processing of Ti-24Al-20Nb.	2593-2604A
The effect of iron and manganese on the recrystallization behavior of hot-rolled and solution-heat-treated aluminum alloy 6013.	19-27A	Elevated temperature compressive properties of zirconium-modified NiAl.	2628-2641A
Crystallization of amorphous alloys.	549-555A	Effect of thermomechanical treatments on the room-temperature mechanical behavior of iron aluminide Fe_3Al .	2985-2993A
Numerical modeling of cellular/dendritic array growth: spacing and structure predictions.	611-623A	Elevated temperature compressive properties of N-doped NiAl.	3170-3180A
Heterogeneous nucleation of 8 on dislocations in a dilute aluminum-lithium alloy.	1595-1605A	High-temperature deformation and failure of an orthorhombic titanium aluminide sheet material.	3675-3681A
Aluminum base alloys, Phase transformations		Shear ligament phenomena in Fe_3Al intermetallics and micro-mechanics of shear ligament toughening.	3817-3825A
Banded solidification microstructures.	625-634A	Hydrogen-induced cleavage fracture of Fe_3Al -based intermetallics.	3949-3956A
Computer simulation of ledge migration under elastic interaction.	1489-1498A	Aluminum compounds, Oxidation	
Phase transformations in condensed systems revisited: industrial applications.	2397-2418A	High-temperature oxidation of Ti_3Al -based titanium aluminides in oxygen.	3993-4002A
The relationship between microstructural and plastic instability in Al-4.0 wt.% Cu alloy.	2916-2922A	Effect of nitrogen on the oxidation behavior of Ti_3Al -based intermetallic alloys.	4003-4010A
Alloy phase analysis from measurements of bulk magnetic properties.	2958-2965A	Aluminum compounds, Phase transformations	
An isothermal section at 550°C in the Al-rich corner of the Al-Fe-Mn-Si system.	3357-3361A	Molecular dynamics simulation of martensitic transformations in NiAl.	1476-1488A
Aluminum base alloys, Phases (state of matter)		Effect of alloying elements on martensitic transformation in the binary NiAl(β) phase alloys.	2445-2453A
Mechanical alloying of Nb-Al powders.	41-48A	Aluminum compounds, Powder technology	
Nucleation controlled solidification kinetics.	533-547A	Mechanistic processes influencing shock chemistry in powder mixtures of the Ti-Si, Ti-Al, and Ti-B systems.	1761-1771A
Real time x-ray transmission microscopy of solidifying Al-In alloys.	801-808A	Pressure-assisted reactive synthesis of titanium aluminides from dense 50Al-50Ti elemental powder blends.	2130-2139A
Electron microscope study of Al-Fe-Si intermetallics in 6201 aluminum alloy.	929-936A	Dense CoAl-based alloys with improved ductility: solid-state synthesis and microstructure control.	2140-2150A
Identification of precipitate phases in a mechanically alloyed rapidly solidified Al-Fe-Ce alloy.	1033-1041A	Synthesis of RuAl by reactive powder processing.	3688-3699A
		Aluminum compounds, Reactions (chemical)	
		Thermodynamics of calcium and oxygen in molten titanium and titanium-aluminum alloy.	967-972B

Aluminum compounds, Structural hardening			
Manifestations of dynamic strain aging in soft-oriented NiAl single crystals.	3542-3557A	Transition between internal and external nitridation of Ni-Ti alloys.	1606-1617A
Aluminum compounds, Thermal properties			
Thermodynamic activities and partial enthalpies of mixing in the solid solution of Fe in Ni ₃ Al.	3569-3575A	Influence of long term annealing on tensile properties and fracture of near- α titanium alloy Ti-6Al-2.75Sn-4Zr-0.4Mo-0.45Si. An analysis of static recrystallization during continuous, rapid heat treatment.	1700-1708A
Aluminum killed steels, Crystal growth			
Austenite grain growth kinetics in Al-killed plain carbon steels.	3399-3409A	The role of coincident site lattice boundaries during selective growth in interstitial-free steels.	2051-2053A
Aluminum killed steels, Metal working			
Analysis and prevention of vertical cracking phenomena during deep drawing of hot-rolled SG295 steel strips.	1241-1250A	Orientation selective recrystallization of nonoriented electrical steels.	2178-2186A
Aluminum killed steels, Welding			
Forming of tailor-welded blanks.	2605-2616A	Anode sludge, Oxidation	2347-2358A
Aluminum oxide, Composite materials			
Probing the initial stage of synthesis of Al ₂ O ₃ /Al composites by directed oxidation of Al-Mg alloys.	43-50B	Influence of gold content on copper oxidation from silver-gold-copper alloys.	3187-3191A
Subcritical crack growth at bimaterial interfaces. II. Microstructural effects on fracture resistance of metal/ceramic interfaces.	213-219A	Anodes	
Transient thermal analysis of solidification in a centrifugal casting for composite materials containing particle segregation. Effect of a solid solution on the steady-state creep behavior of an aluminum matrix composite.	277-285B	An extended two-dimensional mathematical model of vertical ring furnaces.	297-304B
Microstructure of Al ₂ O ₃ fiber-reinforced superalloy (Inconel 718) composites.	305-316A	Fundamental studies of copper anode passivation during electrotrefining. II. Surface morphology.	610-616B
Solidification of binary hypoeutectic alloy matrix composite castings.	451-458A	Anodes, Corrosion	
Bridge toughening enhancement in double-notched MoSi ₂ /Nb model composites.	595-609A	Studies on the corrosion and the behavior of inert anodes in aluminum electrolysis.	185-193B
Creep deformation of dispersion-strengthened copper.	909-921A	Antimony, Impurities	
Effect of magnesium on the aging behavior of Al-Zn-Mg-Cu/Al ₂ O ₃ metal matrix composites.	1217-1227A	Behavior of antimony(III) during copper electrotwinning in chloride solutions.	157-162B
Control of grain size and distribution of particles in a (6061 alloy) _m /(Al ₂ O ₃) _p composite by solutionizing treatment.	2005-2012A	Armor, Mechanical properties	
On the role of magnesium and silicon in the formation of alumina from aluminum alloys by means of DIMOX processing. Formation of structural intermetallics by reactive metal penetration of titanium and nickel oxides and aluminates.	2023-2034A	Ballistic impact behavior of multilayered armor plates processed by hardfacing.	3335-3340A
Failure characteristics of 6061/Al ₂ O ₃ /15 _p and 2014/Al ₂ O ₃ /15 _p composites as a function of loading rate.	2094-2099A	Atmospheric corrosion, Heating effects	
High-temperature wear and deformation processes in metal matrix composites.	2100-2104A	Atmospheric stress corrosion cracking of a superplastic 7475 aluminum alloy.	2617-2627A
Structure of phases in the δ -Al ₂ O ₃ fiber studied by convergent beam electron diffraction.	3095-3107A	Atomic properties	
A model for coupled growth of reaction layers in reactive brazing of ZrO ₂ -toughened Al ₂ O ₃ .	3135-3148A	Atomistic Mechanisms of Nucleation and Growth in Solids.	
Reinforcement shape effects on the fracture behavior and ductility of particulate-reinforced 6061-Al matrix composites.	3318-3329A	Atomic structure	
Mathematical modeling of the extrusion of 6061/Al ₂ O ₃ /20p composite.	3630-3638A	A high resolution transmission electron microscopy study of interfaces between the γ , B ₂ , and α_2 phases in a Ti-Al-Mo alloy.	1618-1629A
Modeling particle fracture during the extrusion of aluminum/alumina composites.	3739-3746A	Atomic structure, Alloying effects	
Infiltration of fibrous preform by molten aluminum in a centrifugal force field.	4095-4111A	Thermodynamics and long-range order of nitrogen in γ -Fe ₄ N _{1-x} . Precipitation in lead-calcium alloys containing tin.	1055-1061A
Aluminum oxide, Physical properties		Atomic structure, Composition effects	
Variation of contact angles with temperature and time in the Al-Al ₂ O ₃ system.	4113-4120A	An evaluation of the Fe-N phase diagram considering long-range order of nitrogen atoms in γ -Fe ₄ N _{1-x} and ϵ -Fe ₂ N _{1-x} .	1668-1675A
Aluminum oxide, Reactions (chemical)		Atomic structure, Radiation effects	
Activities in CaO-SiO ₂ -Al ₂ O ₃ slags and deoxidation equilibria of silicon and aluminum.	4163-4169A	Sputter-induced pits on {100} nickel surfaces.	1063-1071A
Amorphization, Alloying effects		Theory of nucleation with cluster loss and injection: application to plastic deformation and irradiation.	981-993A
Mechanical alloying of Nb-Al powders.	51-55B	Atomic structure, Stress effects	
Amorphous structure		Stacking faults in SiC particles and their effect on the fracture behavior of a 15 vol.-% SiC/6061-Al matrix composite.	1441-1448A
Crystallization of amorphous phase in sputter-deposited Ti-Al alloy thin films.	943-953B	A study on coherency strain and precipitate morphology via a discrete atom method.	1449-1459A
Amorphous structure, Heating effects		Molecular dynamics simulation of martensitic transformations in NiAl.	1476-1488A
Effects of low-temperature aging on the microstructure and soft magnetic properties of rapidly quenched Fe-Si-B alloys.	2047-2050A	Atomizing	
Amorphous structure, Temperature effects		Characterization and mechanical properties of ultrahigh boron steels produced by powder metallurgy.	1861-1867A
Crystallization of amorphous alloys.	2454-2460A	Microstructural development of a gas-atomized and hot-pressed α_2 alloy.	2221-2228A
Amplitude		Austempering	
Multiple matrix cracking in a fiber-reinforced titanium matrix composite under high-cycle fatigue.	549-555A	Neutron diffraction study of austempered ductile iron.	923-928A
Anisotropy		Effect of bainite transformation and retained austenite on mechanical properties of austempered spheroidal graphite cast steel.	1585-1594A
Effect of phase composition and hydrogen level on the deformation behavior of titanium-hydrogen alloys.	1869-1876A	Effect of holding time in the (α - γ) temperature range on toughness of specially austempered ductile iron.	1979-1989A
Anisotropy, Heating effects		Austenite	
The plastic anisotropy of an Al-Li-Cu-Zr alloy extrusion in unidirectional deformation.	3503-3512A	NiTi and NiTi-TiC composites. II. Compressive mechanical properties.	183-191A
Annealing		Microstructure and tensile behavior of nitrogen-alloyed, dual-phase stainless steels.	1845-1859A
Effect of primary grain size on the secondary recrystallization of mechanically alloyed oxide dispersion strengthened nickel-based superalloy.	493-496A	Microstructure and phase identification in type 304 stainless steel-zirconium alloys.	2151-2159A
Austenite, Alloying effects		Austenite, Alloying effects	
The influence of niobium supersaturation in austenite on the static recrystallization behavior of low carbon microalloyed steels.		The influence of niobium supersaturation in austenite on the static recrystallization behavior of low carbon microalloyed steels.	951-960A
A study on morphology and plate mean dimensions in Fe-Ni and Fe-Ni-Cr alloys.		A study on morphology and plate mean dimensions in Fe-Ni and Fe-Ni-Cr alloys.	973-980A
Austenite, Cooling effects		Austenite, Cooling effects	
The role of grain corners in nucleation.		The role of grain corners in nucleation.	480-483A
Austenite decomposition during continuous cooling of an HSLA-80 plate steel.		Austenite decomposition during continuous cooling of an HSLA-80 plate steel.	1554-1568A

Copper precipitation during continuous cooling and isothermal aging of A710 type steels.	1569-1584A	Effect of holding time in the $(\alpha+\gamma)$ temperature range on toughness of specially austempered ductile iron.	1979-1989A
Austenite, Crystal growth		Autoclaves	
Austenite grain growth kinetics in Al-killed plain carbon steels.	3399-3409A	A study of solid-aqueous equilibria by the speciation approach in the hydronium alunite-sulfuric acid-water system at high temperatures.	555-566B
Austenite, Deformation effects		Automobiles	
Experimental investigation of the transformation texture in hot-rolled ferritic stainless steel using single orientation determination.	49-57A	Materials and society—impacts and responsibilities.	337-350B
Precipitation behavior in a medium carbon, Ti-V-N microalloyed steel.	1149-1165A	Automotive components	
Austenite, Heating effects		Materials and society—impacts and responsibilities.	337-350B
Pearlite in ultrahigh carbon steels: heat treatments and mechanical properties.	111-118A	Automotive components, Forming	
Neutron diffraction study of austempered ductile iron.	923-928A	Forming of tailor-welded blanks.	2605-2616A
Effect of bainite transformation and retained austenite on mechanical properties of austempered spheroidal graphite cast steel.	1585-1594A	Automotive components, Materials substitution	
Austenite, Phases (state of matter)		Microstructural evolution and superplastic deformation behavior of fine grain 5083Al.	3827-3839A
Ferrite nucleation and growth during continuous cooling.	1544-1553A	Axial stress	
Austenite, Temperature effects		Effect of multiaxial stresses on creep damage of 316 stainless steel weldments.	891-900A
Phase stability and atom probe field ion microscopy of type 308 CRE stainless steel weld metal.	763-774A	Effect of uniaxial stress on coarsening of precipitate clusters. The influence of stress triaxiality on the damage mechanisms in an equiaxed α/β Ti-6Al-4V alloy.	1480-1475A
The driving force for martensitic transformations in low alloy steels.	1127-1132A	Backscattering	
The formation mechanism(s), morphology, and crystallography of ferrite sideplates.	1517-1532A	The formation mechanism(s), morphology, and crystallography of ferrite sideplates.	1517-1532A
Austenitic stainless steels		Bacterial leaching	
Gibbs energies of formation of chromium carbides.	1919-1924A	Bioleaching of lateritic nickel ore by ultrasound.	351-354B
Austenitic stainless steels, Casting		Bainite	
Effect of superheat on the solidification structures of AISI 310S austenitic stainless steel.	287-296B	The effects of microstructure, strength level, and crack propagation mode on stress corrosion cracking behavior of 4135 steel.	281-290A
Austenitic stainless steels, Cladding		Formation of bainite in ferrous and nonferrous alloys through sympathetic nucleation and ledgewise growth mechanism.	1533-1543A
Ballistic impact behavior of multilayered armor plates processed by hardfacing.	3335-3340A	Bainite, Cooling effects	
Austenitic stainless steels, Coating		Bainite in the light of rapid continuous cooling information. Austenite decomposition during continuous cooling of an HSLA-80 plate steel.	1499-1510A
Microstructural analysis and oxidation behavior of laser-processed Fe-Cr-Al-Y alloy coatings.	381-390A	Bainite, Heating effects	
Austenitic stainless steels, Corrosion		Characterization of the formation of α_1 plates from the β_0 phase in a Cu-Zn-Au alloy.	719-724A
Studies on the influence of metallurgical variables on the stress corrosion behavior of AISI 304 stainless steel in sodium chloride solution using the fracture mechanics approach.	1313-1325A	Bainitic microstructures formed by split isothermal transformation in an Fe-C-Si-Mn-Mo steel.	1141-1147A
Influence of thermal aging on the intergranular corrosion resistance of types 304LN and 316LN stainless steels.	2881-2887A	Effect of bainite transformation and retained austenite on mechanical properties of austempered spheroidal graphite cast steel.	1585-1594A
Austenitic stainless steels, Machining		Baking	
Active wear and failure mechanisms of titanium nitride-coated high speed steel and titanium nitride-coated cemented carbide tools when machining powder metallurgically made stainless steels.	2796-2808A	An extended two-dimensional mathematical model of vertical ring furnaces.	297-304B
Austenitic stainless steels, Mechanical properties		Ball bearings, Microstructure	
Temperature and strain-rate effects on low-cycle fatigue behavior of alloy 800H.	255-267A	Crystallographic preferred orientation induced by cyclic rolling contact loading.	3445-3465A
Effect of multiaxial stresses on creep damage of 316 stainless steel weldments.	891-900A	Ball milling	
Prediction of fatigue crack formation in 304 stainless steel.	1267-1271A	Tensile properties of mechanically alloyed/milled ODS-Ni-based alloys.	1371-1377A
Internal friction in hydrogen-charged CrNi and CrNiMn austenitic stainless steels.	1815-1821A	Kinetics of phase evolution of Zn-Fe intermetallics.	2904-2910A
Temperature dependence of the rate sensitivity and its effect on the activation energy for high-temperature flow.	3346-3348A	Ballistic impact tests	
Fracture characteristics, microstructure, and tissue reaction of Ti-5Al-2.5Fe for orthopedic surgery.	3925-3935A	Ballistic impact behavior of multilayered armor plates processed by hardfacing.	3335-3340A
Austenitic stainless steels, Metal working		Banded structure	
Optimization of cold and warm workability in 304 stainless steel using instability maps.	119-126A	Microstructure and tensile behavior of nitrogen-alloyed, dual-phase stainless steels.	1845-1859A
Flow stress and microstructural evolution during hot working of alloy 22Cr-13Ni-5Mn-0.3N austenitic stainless steel.	1251-1266A	Banded structure, Temperature effects	
Austenitic stainless steels, Microstructure		Banded solidification microstructures.	625-634A
Electron microscopic study of Cr ₂ N formation in thermally aged 316LN austenitic stainless steels.	1175-1186A	Barium, Quaternary systems	
Austenitic stainless steels, Phase transformations		Thermodynamic properties of complex oxides in the Sm-Ba-Cu-O system.	973-978B
Hydride formation and decomposition in electrochemically charged metastable austenitic stainless steels.	29-40A	Bauschinger effect	
Austenitic stainless steels, Phases (state of matter)		Bauschinger effect in Haynes 230 alloy: influence of strain rate and temperature.	1739-1748A
Phase stability and atom probe field ion microscopy of type 308 CRE stainless steel weld metal.	763-774A	Bearing steels, Mechanical properties	
Austenitic stainless steels, Welding		High-temperature wear and deformation processes in metal matrix composites.	3135-3148A
Dilution in single pass arc welds.	481-489B	Bearing steels, Microstructure	
Austenitic stainless steels phases (state of matter)		Crystallographic preferred orientation induced by cyclic rolling contact loading.	3445-3485A
Microstructure and phase identification in type 304 stainless steel-zirconium alloys.	2151-2159A	Bend strength, Microstructural effects	
Austenitizing		Communication: Mechanical deformation of dendrites by fluid flow.	229-232A
Pearlite in ultrahigh carbon steels: heat treatments and mechanical properties.	111-118A	Temperature dependent deformation of polydomain phases in an In-22.5 at.% Ti shape memory alloy.	1887-1892A
		Microstructure and mechanical behavior of Cr-Cr ₂ Hf in situ intermetallic composites.	2583-2592A

Bend tests

Fracture characteristics, microstructure, and tissue reaction of Ti-5Al-2.5Fe for orthopedic surgery.	3925-3935A	Bottom blown converters	Water model experiment on the liquid flow behavior in a bottom blown bath with top layer.	35-41B
Bend tests			Model study of bubble and liquid-flow characteristics in a bottom blown bath under reduced pressure.	765-772B
Failure characteristics of 6061/Al ₂ O ₃ /15 _p and 2014/Al ₂ O ₃ /15 _p composites as a function of loading rate.	3095-3107A	Brasses, Composite materials	Nanoscale brass/steel multilayer composites produced by cold rolling.	2383-2385A
Bend tests, Development				
Measurement of friction under sheet forming conditions.	3971-3981A	Brasses, Phase transformations	Influence of training time and temperature on shape memory effect in Cu-Zn-Al alloys.	3108-3111A
Beryllium, Powder technology				
Physical chemistry of the powder metallurgy of beryllium: chemical characterization of the powder in relation to its granularity.	371-379A	Brasses, Surface properties	Measurement of friction under sheet forming conditions.	3971-3981A
Bimetals, Mechanical properties				
Flow and fracture of bimaterial systems based on aluminum alloys.	3937-3947A	Breeder reactors, Materials selection	Influence of thermal aging on the intergranular corrosion resistance of types 304LN and 316LN stainless steels.	2881-2887A
Binary systems, Crystal growth				
Effects of shear flow and anisotropic kinetics on the morphological stability of a binary alloy.	687-694A	Brinell hardness, Composition effects	A study of the influence of mischmetal additions to Al-7Si-0.3Mg (LM 25/356) alloy.	1283-1292A
Modeling of microsegregation in macrosegregation computations.	2314-2327A	Brittle fracture	Simulation of the hot-tension test under cavitating conditions.	3112-3119A
Binary systems, Phases (state of matter)				
Standard enthalpies of formation of dysprosium alloys, Dy+Me (Me=Ni, Ru, Rh, Pd, Ir, and Pt), by high-temperature direct synthesis calorimetry.	417-422B	Brittle fracture, Heating effects	Influence of long term annealing on tensile properties and fracture of near- α titanium alloy Ti-6Al-2.75Sn-4Zr-0.4Mo-0.45Si.	1700-1708A
Critical evaluation and optimization of the thermodynamic properties of liquid tin solutions.	808-826B	Brittle fracture, Welding effects	Microstructures relevant to brittle fracture initiation at the heat-affected zone of weldment of a low carbon steel.	2574-2582A
Generalized enthalpy method for multicomponent phase change.	869-879B	Brittleness	Flow and fracture of bimaterial systems based on aluminum alloys.	3937-3947A
Inverse melting in binary systems: morphology and microscopy of catactic alloys.	979-986B	Brittleness, Microstructural effects	Bridge toughening enhancement in double-notched MoSi ₂ /Nb model composites.	909-921A
Control of iron nitride layers growth kinetics in the binary Fe-N system.	1823-1835A	Bronzes, Crystal growth	Modeling of primary and secondary dendrites in a Cu-6 wt.% tin alloy.	4085-4093A
Thermodynamic studies and the phase diagram of the Li-Mg system.	2419-2428A	Bronzes, Mechanical properties	Characterization of the wear response of a modified zinc-based alloy vis-à-vis a conventional zinc-based alloy and a bearing bronze at a high sliding speed.	3513-3523A
A thermodynamic evaluation of the nickel-silicon system.	2897-2903A	Bubbles	Model study of bubble and liquid-flow characteristics in a bottom blown bath under reduced pressure.	765-772B
Thermochemistry of the Ni-Hf system—Intermetallic phases.	3576-3590A		Van der Waals approximation for potassium bubbles in tungsten.	987-992B
Thermodynamic assessment of the Nb-N system.	3591-3600A	Bubbling	The separation of the solids from the carrier gas during submerged powder injection.	773-779B
Binary systems, Powder technology				
Mechanistic processes influencing shock chemistry in powder mixtures of the Ti-Si, Ti-Al, and Ti-B systems.	1761-1771A	Bulk modulus, Alloying effects	Elastic moduli of titanium-hydrogen alloys in the temperature range 20°C to 1100°C.	3963-3970A
Binary systems, Reactions (chemical)				
Thermal decomposition of silicon carbides: discussion of "the effect of an electric field on self sustaining combustion synthesis, I and II", and author's reply.	322-325B	Cadmium base alloys, Phase transformations	Characterization of a massive transformation by microstructural analysis.	1511-1516A
Biocompatibility				
Fracture characteristics, microstructure, and tissue reaction of Ti-5Al-2.5Fe for orthopedic surgery.	3925-3935A	Calcium, Binary systems	Critical evaluation and optimization of the thermodynamic properties of liquid tin solutions.	808-826B
Biomedical materials				
Fracture characteristics, microstructure, and tissue reaction of Ti-5Al-2.5Fe for orthopedic surgery.	3925-3935A	Calcium, Chemical analysis	Formation of aluminum-silicon alloys from feldspars—determination of silicon, light, and heavy elements in silumin by scanning electron microscopy.	604-609B
Blast furnace chemistry				
Reaction equilibria in the production of manganese ferroalloys.	5-17B	Calorimetry	Standard enthalpies of formation of dysprosium alloys, Dy+Me (Me=Ni, Ru, Rh, Pd, Ir, and Pt), by high-temperature direct synthesis calorimetry.	417-422B
Reoxidation of aluminum in Fe-Al-M (M=C, Mn, and Ti) melts with CaO-Al ₂ O ₃ -FeO (3 mass%) slags.	423-431B		Thermodynamic investigations of the ternary Au-Sn-Zn system.	921-927B
Blast furnace slags				
Reaction equilibria in the production of manganese ferroalloys.	5-17B		Thermodynamic properties of complex oxides in the Sm-Ba-Cu-O system.	973-978B
Water model experiment on the liquid flow behavior in a bottom blown bath with top layer.	35-41B		Thermally assisted and mechanically driven solid-state reactions for formation of amorphous Al ₉₃ Ta ₆₇ alloy powders.	3267-3278A
The use of blast furnace slag and derived materials in the vitrification of electric arc furnace dust.	379-384B		Martensitic transformations in NiMnAl β phase alloys.	4153-4162A
A study of the thermal decomposition of BaCO ₃ .	409-416B	Carbide tools, Mechanical properties	Active wear and failure mechanisms of titanium nitride-coated high speed steel and titanium nitride-coated cemented carbide tools when machining powder metallurgically made stainless steels.	2796-2808A
Reoxidation of aluminum in Fe-Al-M (M=C, Mn, and Ti) melts with CaO-Al ₂ O ₃ -FeO (3 mass%) slags.	423-431B	Carbides	Effect of carbide precipitation on the creep behavior of alloy 800HT in the temperature range 700-900°C.	747-756A
Blast furnace slags, Reactions (chemical)				
Preparation of glass-forming materials from granulated blast furnace slag.	801-807B			
Blowing				
The separation of the solids from the carrier gas during submerged powder injection.	773-779B			
Bonding				
Microstructure of bonding zones in laser-clad nickel-alloy-based composite coatings reinforced with various ceramic powders.				
Microstructural development in NiAl/Ni-Si-B/Ni transient liquid phase bonds.	391-400A			
Bonding strength				
Microstructure of Al ₂ O ₃ fiber-reinforced superalloy (Inconel 718) composites.	451-458A			
Interface effects on the micromechanical response of a transversely loaded single fiber SCS-6/Ti-6Al-4V composite.	2035-2043A			
Borides, Composite materials				
Extending the compositional limit of combustion-synthesized B ₄ C-TiB ₂ composites by field activation.	475-480B			

Splitting phenomena occurring in the martensitic transformation of Cr13 and CrMoV14 stainless steels in the absence of carbide precipitation.	1799-1805A	Theoretical treatment of nitriding and nitrocarburizing of iron. <i>Corrosion fatigue in nitrocarburized quenched and tempered steels.</i>	1073-1080A 1333-1346A
A comparison of fracture behavior of low alloy steel with different sizes of carbide particles.	1909-1917A	Carbothermic reactions <i>A kinetic study of the reaction of zinc oxide with iron powder. Phase equilibria in the metal-sulfur-oxygen system and selective reduction of metal oxides and sulfides. I. The carbothermic reduction and calcination of complex mineral sulfides. Phase equilibria in the metal-sulfur-oxygen system and selective reduction of metal oxides and sulfides. I. The carbothermic reduction and calcination of complex mineral sulfides.</i>	363-374B 827-838B 827-838B
Carbides, Composite materials Extending the compositional limit of combustion-synthesized B_4C-TiB_2 composites by field activation.	475-480B	Carburizing <i>Simultaneous plasma treatment for carburizing and carbonitriding using hollow cathode discharge. High cycle fatigue behavior of gas-carburized medium carbon Cr-Mo steel.</i>	401-405A 2557-2564A
Carbides, Crystal growth Abnormal growth of faceted (WC) grains in a (Co) liquid matrix. M_2C precipitates in isothermal tempering of high Co-Ni secondary hardening steel.	2809-2819A 3466-3472A	Case depth <i>High cycle fatigue behavior of gas-carburized medium carbon Cr-Mo steel.</i>	2557-2564A
Carbides, High temperature effects Carbide diagrams and precipitation of alloying elements during aging of low-alloy steels.	498-502A	Cast Iron, Melting <i>Modeling and experimental study of gaseous oxidation of liquid iron alloys.</i>	852-862B
Carbon, Alloying elements Structural characterization of martensitic iron-carbon alloy films electrodeposited from an iron(II) sulfate solution. Influence of titanium and carbon contents on the hydrogen trapping of microalloyed steels.	483-486A 3773-3780A	Cast Iron, Microstructure <i>Transitions between type A flake, type D flake, and coral graphite eutectic structures in cast irons.</i>	2740-2753A
Carbon, Binary systems Thermal decomposition of silicon carbides: discussion of "the effect of an electric field on self sustaining combustion synthesis, I and II", and author's reply. Generalized enthalpy method for multicomponent phase change.	322-325B 869-879B	Castability <i>Effect of grain refinement on the fluidity of two commercial Al-Si foundry alloys.</i>	2305-2313A
Carbon, Composite materials Permeability of microporous carbon preforms. Wear and friction behavior of metal impregnated microporous carbon composites.	3669-3674A	Casting <i>Solidification of particle-reinforced metal-matrix composites. Prediction of dendrite arm spacing for low alloy steel casting processes.</i>	663-671B 689-693B
Carbon, Diffusion Modeling of ferrite growth in nodular cast iron. Annealing and aging of interstitial C in α -Fe, as measured by internal friction.	2209-2220A 2461-2469A	Casting alloys, Casting <i>Effect of grain refinement on the fluidity of two commercial Al-Si foundry alloys.</i>	2305-2313A
Carbon, End uses Permeability of microporous carbon preforms.	3669-3674A	Casting defects <i>A model for macrosegregation and its application to Al-Cu castings.</i>	2708-2721A
Carbon, Impurities Physical chemistry of the powder metallurgy of beryllium: chemical characterization of the powder in relation to its granularity.	371-379A	Casting defects, Cooling effects <i>Porosity formation in Al-9 wt.% Si-3 wt.% Cu alloy systems: metallographic observations. Macrotransport-solidification kinetics modeling of equiaxed dendritic growth. II. Computation problems and validation on Inconel 718 superalloy casting.</i>	415-429A 4075-4083A
Carbon, Quaternary systems An experimental study and thermodynamic calculations of phase equilibria in the Fe-Mo-C-N system.	2869-2880A	Casting defects, Temperature effects <i>Heat-flow-based analysis of surface crack formation during the start-up of the direct chill casting process. II. Experimental study of an AA1512 rolling ingot. Modeling of ingot distortions during direct chill casting of aluminum alloys.</i>	129-137B 3214-3225A
Carbon, Reactions (chemical) Reduction of FeO in smelting slags by solid carbon: experimental results.	717-730B	Castings, Crystal growth <i>A model for macrosegregation and its application to Al-Cu castings.</i>	2708-2721A
Carbon, Solubility Solubility of carbon in CaO-Al ₂ O ₃ melts.	57-64B	Castings, Heat treatment <i>Effect of bainite transformation and retained austenite on mechanical properties of austempered spheroidal graphite cast steel.</i>	1585-1594A
Carbon, Ternary systems M_2C carbide equilibria in the Fe-Cr-C system. A thermodynamic evaluation of the Ti-Mo-C system.	701-704B 955-966B	Castings, Mechanical properties <i>Mechanical properties and 95°C aging characteristics of zircon reinforced Zn-4Al-3Cu alloy. Effect of strontium modification on near-threshold fatigue crack growth in an Al-Si-Cu die cast alloy.</i>	809-818A 1293-1302A
Carbon dioxide, Reactions (chemical) Modeling and experimental study of gaseous oxidation of liquid iron alloys.	852-862B	Castings, Microstructure <i>Porosity formation in Al-9 wt.% Si-3 wt.% Cu alloy systems: metallographic observations. Effects of forced electromagnetic vibrations during the solidification of aluminum alloys. II. Solidification in the presence of collinear variable and stationary magnetic fields. Some consequences of thermosolutal convection: the grain structure of castings. Solidification of binary hypoeutectic alloy matrix composite castings. Prediction of grain structures in various solidification processes. Influence of chromium and impurities on the grain refining behavior of aluminum. Macrosegregation during dendritic arrayed growth of hypoeutectic Pb-Sn alloys: influence of primary arm spacing and mushy zone length. Phase transformations in condensed systems revisited: industrial applications.</i>	415-429A 457-464B 569-581A 595-609A 695-705A 791-800A 1353-1362A 2397-2418A
Carbon manganese steels, Irradiation A model describing neutron irradiation-induced segregation to grain boundaries in dilute alloys.	3381-3390A	Castings, Structural hardening <i>Effect of magnesium on the aging behavior of Al-Zn-Mg-Cu/Al₂O₃ metal matrix composites.</i>	2005-2012A
Carbon manganese steels, Mechanical properties A comparison of fracture behavior of low alloy steel with different sizes of carbide particles.	1909-1917A		
Carbon monoxide, Reactions (chemical) Modeling and experimental study of gaseous oxidation of liquid iron alloys.	852-862B		
Carbon steels, Casting Intermixing model of continuous casting during a grade transition.	617-632B		
Carbon steels, Corrosion Influence of microalloying on the corrosion resistance of steel in saturated calcium hydroxide.	1693-1699A		
Carbon steels, Phases (state of matter) Ferrite nucleation and growth during continuous cooling.	1544-1553A		
Carbonylides Nonuniform distribution of carbonitride particles and its effect on prior austenite grain size in the simulated coarse-grained heat-affected zone of thermomechanical control-processed steels.	4031-4038A		
Carbonitriding Surface morphology and compound layer pores of plasma nitrocarburized low carbon steel. Simultaneous plasma treatment for carburizing and carbonitriding using hollow cathode discharge.	135-143A 401-405A		

Cavitation	
The measurement of hydrogen activities in molten copper using an oxide protonic conductor.	929-935B
Characterization of superplastic deformation behavior of a fine grain 5083 Al alloy sheet.	1889-1898A
Deformation behavior of an Al-3.37 wt.% Li alloy.	2274-2284A
Simulation of the hot-tension test under cavitating conditions.	3112-3119A
Cavitation, Deformation effects	
High-temperature deformation and failure of an orthorhombic titanium aluminide sheet material.	3675-3681A
Cemented carbides, Coatings	
Wear-resistant coatings produced by shock-wave compaction of powders.	2297-2304A
Cemented carbides, Powder technology	
Abnormal growth of faceted (WC) grains in a (Co) liquid matrix.	2809-2819A
Cementite, Heating effects	
Pearlite in ultrahigh carbon steels: heat treatments and mechanical properties.	111-118A
Centrifugal casting	
Transient thermal analysis of solidification in a centrifugal casting for composite materials containing particle segregation.	277-285B
Theoretical analysis of the particle gradient distribution in centrifugal field during solidification.	1025-1029B
The improved microstructures and properties of 7075 alloys produced by a water-cooling centrifugal casting method.	1951-1962A
Centrifugal castings, Structural hardening	
Theoretical analysis of the particle gradient distribution in centrifugal field during solidification.	1025-1029B
Centrifugal force	
Theoretical analysis of the particle gradient distribution in centrifugal field during solidification.	1025-1029B
Infiltration of fibrous preform by molten aluminum in a centrifugal force field.	4163-4169A
Ceramic coatings	
Investigation of the temperature field developed by a spinning beam in laser processing.	4039-4047A
Ceramics, Composite materials	
Microstructure of bonding zones in laser-clad nickel-alloy-based composite coatings reinforced with various ceramic powders.	391-400A
Reinforcement stresses during deformation of sphere- and particulate-reinforced aluminum-matrix composites.	486-490A
Cerium, Alloying additive	
Tension characteristics of notched specimens for Al-Li-Cu-Zr alloys sheets with various cerium contents.	3089-3094A
Cerium, Binary systems	
Critical evaluation and optimization of the thermodynamic properties of liquid tin solutions.	808-826B
Inverse melting in binary systems: morphology and microscopy of catactic alloys.	979-986B
Cerium, Dopants	
The growth and structure of thin oxide films on cerium ion-implanted nickel.	3649-3661A
Chalcocite, Reduction (chemical)	
Kinetics of the flash converting of MK (chalcocite) concentrate.	163-175B
Chalcopyrite, Reactions (chemical)	
Kinetics of sulfation of chalcopyrite with steam and oxygen in the presence of ferric oxide.	465-474B
Charging	
Hydride formation and decomposition in electrolytically charged metastable austenitic stainless steels.	29-40A
Chemical composition	
Formation of aluminum-silicon alloys from feldspars—determination of silicon, light, and heavy elements in silumin by scanning electron microscopy.	604-609B
Intermixing model of continuous casting during a grade transition.	617-632B
On the role of magnesium and silicon in the formation of alumina from aluminum alloys by means of DIMOX processing.	2094-2099A
Structural stability of super duplex stainless steel weld metals and its dependence on tungsten and copper.	2196-2208A
Chemical equilibrium	
Reaction equilibria in the production of manganese ferroalloys.	5-17B
Representation of mixed reactive gases on free energy (Ellingham-Richardson) diagrams.	65-69B
Chemical equilibrium, Alloying effects	
Identification of precipitate phases in a mechanically alloyed rapidly solidified Al-Fe-Ce alloy.	1033-1041A
Chemical equilibrium, Cooling effects	
Vacuum evaporation of KCl-NaCl salts. II. Vaporization-rate model and experimental results.	433-443B
Chemical potential	
Thermodynamic properties of oxygen in yttrium-oxygen solid solutions.	839-845B
Chemical potential, Composition effects	
Thermodynamic activities and partial enthalpies of mixing in the solid solution of Fe in Ni ₃ Al.	3569-3575A
Chemical processing equipment, Corrosion	
Initiation of stress corrosion cracking for pipeline steels in a carbonate-bicarbonate solution.	2686-2691A
Chromium, Alloying elements	
A study on morphology and plate mean dimensions in Fe-Ni and Fe-Ni-Cr alloys.	973-980A
The effects on fracture toughness of ductile-phase composition and morphology in Nb-Cr-Ti and Nb-Si in situ composites.	3007-3018A
Chromium, Binary systems	
Critical evaluation and optimization of the thermodynamic properties of liquid tin solutions.	808-826B
Chromium, Diffusion	
Analysis of mean square penetration depth in grain boundary diffusion.	3473-3477A
Chromium, Impurities	
Influence of chromium and impurities on the grain refining behavior of aluminum.	791-800A
Chromium, Ternary systems	
M ₂ C ₆ carbide equilibria in the Fe-Cr-C system.	701-704B
Internal sulfide precipitation in low Cr-Fe alloys.	3192-3202A
Solidification of undercooled Fe-Cr-Ni alloys. II. Microstructural evolution.	3226-3240A
Chromium base alloys, Composite materials	
The fracture toughness of niobium-based, in situ composites.	2518-2531A
Chromium base alloys, Corrosion	
Internal sulfide precipitation in low Cr-Fe alloys.	3192-3202A
Chromium base alloys, Mechanical properties	
Microstructure and mechanical behavior of Cr-Cr ₂ Hf in situ intermetallic composites.	2583-2592A
Chromium carbide	
Correlation of microstructure and fracture toughness in high-chromium white iron hardfacing alloys.	3881-3891A
Chromium carbide, Physical properties	
Gibbs energies of formation of chromium carbides.	1919-1924A
Chromium molybdenum steels, Cladding	
Solidification of an alloy 625 weld overlay.	3612-3620A
The wear behavior between hardfacing materials.	3639-3648A
Chromium molybdenum steels, Corrosion	
The effects of microstructure, strength level, and crack propagation mode on stress corrosion cracking behavior of 4135 steel.	281-290A
A strain-based fracture model for stress corrosion cracking of low-alloy steels.	291-304A
Chromium molybdenum steels, Heat treatment	
Simultaneous plasma treatment for carburizing and carbonitriding using hollow cathode discharge.	401-405A
Corrosion fatigue in nitrocarburized quenched and tempered steels.	1333-1346A
Chromium molybdenum steels, Irradiation	
A model describing neutron irradiation-induced segregation to grain boundaries in dilute alloys.	3381-3390A
Chromium molybdenum steels, Mechanical properties	
High cycle fatigue behavior of gas-carburized medium carbon Cr-Mo steel.	2557-2564A
Analysis of the stress-strain curves of a modified 9Cr-1Mo steel by the Voce equation.	3340-3343A
Effect of alloying additions on fracture behavior of molybdenum-containing secondary hardening steels.	3343-3346A
Chromium molybdenum steels, Welding	
Effect of postweld treatment on the fatigue crack growth rate of electron-beam-welded AISI 4130 steel.	3162-3169A
Chromium molybdenum vanadium steels, Phases (state of matter)	
Carbide diagrams and precipitation of alloying elements during aging of low-alloy steels.	498-502A
Chromium steels, Mechanical properties	
High-temperature wear and deformation processes in metal matrix composites.	3135-3148A
Chromium steels, Microstructure	
Crystallographic preferred orientation induced by cyclic rolling contact loading.	3445-3465A
Circulation	
Studies of interface deformations in single- and multi-layered liquid baths due to an impinging gas jet.	911-920B
A one-phase model of the mixing of Al-SiC composite melt.	1015-1023B

Clad metals, Mechanical properties		
Ballistic impact behavior of multilayered armor plates processed by hardfacing.	3335-3340A	
Cladding		
Microstructure of bonding zones in laser-clad nickel-alloy-based composite coatings reinforced with various ceramic powders.	391-400A	
Cleavage		
Microstructure and tensile behavior of nitrogen-alloyed, dual-phase stainless steels.	1845-1859A	
The influence of stress triaxiality on the damage mechanisms in an equaxed α/β Ti-6Al-4V alloy.	3043-3058A	
Loading rate and test temperature effects on fracture of in situ niobium silicide-niobium composites.	3292-3306A	
Cleavage, Microstructural effects		
A comparison of fracture behavior of low alloy steel with different sizes of carbide particles.	1909-1917A	
Cleavage, Welding effects		
Cleavage initiation in the intercritically reheated coarse-grained heat affected zone. II. Failure criteria and statistical effects.	3019-3029A	
Coatings, Mechanical properties		
Structural characterization of martensitic iron-carbon alloy films electrodeposited from an iron(II) sulfate solution.	483-486A	
Cobalt, Binary systems		
Critical evaluation and optimization of the thermodynamic properties of liquid tin solutions.	808-826B	
Cobalt, Composite materials		
Abnormal growth of faceted (WC) grains in a (Co) liquid matrix.	2809-2819A	
Cobalt, Extraction		
A study of solid-aqueous equilibria by the speciation approach in the hydronium alunite-sulfuric acid-water system at high temperatures.	555-566B	
Phase equilibria in the metal-sulfur-oxygen system and selective reduction of metal oxides and sulfides. I. The carbothermic reduction and calcination of complex mineral sulfides.	827-838B	
Cobalt base alloys, Claddings		
The wear behavior between hardfacing materials.	3639-3648A	
Cobalt base alloys, Crystal growth		
Microstructure of Cu-Co alloys solidified at various supercoolings.	4049-4059A	
Cobalt base alloys, Magnetic properties		
Development of a magnetoelastic resonant sensor using iron-rich, nonzero magnetostrictive amorphous alloys.	3203-3213A	
Cobalt base alloys, Phase transformations		
High-resolution transmission electron microscopy investigation of the face-centered cubic/hexagonal close-packed martensite transformation in Co-31.8 wt.% Ni alloy. I. Plate interfaces and growth ledges.	3362-3370A	
High-resolution transmission electron microscopy investigation of the face-centered cubic/hexagonal close-packed martensite transformation in Co-31.8 wt.% Ni alloy. II. Plate intersections, extended defects, and nucleation mechanisms.	3371-3380A	
Cobalt compounds, Powder technology		
Dense CoAl-based alloys with improved ductility: solid-state synthesis and microstructure control.	2140-2150A	
Coercive force		
Development of a magnetoelastic resonant sensor using iron-rich, nonzero magnetostrictive amorphous alloys.	3203-3213A	
Coercive force, Heating effects		
Effects of low-temperature aging on the microstructure and soft magnetic properties of rapidly quenched Fe-Si-B alloys.	2454-2460A	
Cold rolling		
The role of coincident site lattice boundaries during selective growth in interstitial-free steels.	2178-2186A	
Orientation selective recrystallization of nonoriented electrical steels.	2347-2358A	
Nanoscale brass/steel multilayer composites produced by cold rolling.	2383-2385A	
Cold rolling, Quality control		
Quantitative characterization of the surface topography of rolled sheets by laser scanning microscopy and Fourier transformation.	2338-2346A	
Cold working		
Optimization of cold and warm workability in 304 stainless steel using instability maps.	119-126A	
Columnar structure, Temperature effects		
Some consequences of thermosolutal convection: the grain structure of castings.	569-581A	
Combustion		
Communication: On the in situ formation of TiC and Ti_2C reinforcements in combustion-assisted synthesis of titanium matrix composites.		237-240A
Thermal decomposition of silicon carbides: discussion of "the effect of an electric field on self sustaining combustion synthesis, I and II", and author's reply.		322-325B
Extending the compositional limit of combustion-synthesized B_2C-TiB_2 composites by field activation.		475-480B
Combustion, Temperature effects		
Modeling of sequential reactions during micropyretic synthesis.		961-972A
Compacting		
Microstructure and tensile properties of compacted, mechanically alloyed, nanocrystalline Fe-Al.		3126-3134A
Composite materials, Synthesis		
Microstructure and properties of $Al_2O_3-Al(Si)$ and $Al_2O_3-Al(Si)-Si$ composites formed by in situ reaction of aluminum with aluminosilicate ceramics.		2122-2129A
Compression tests		
The relationship between microstructural and plastic instability in $Al-4.0$ wt.% Cu alloy.		2916-2922A
Analysis of thermal residual stress in a thick-walled ring of Dur-alcan-base Al-SiC functionally graded material.		4145-4151A
Compressive strength		
Friability and crushing strength of micrometer-size diamond abrasives used in microgrinding of optical glass.		1047-1053A
Compressive strength, Alloying effects		
Elevated temperature compressive properties of zirconium-modified NiAl.		2628-2641A
Elevated temperature compressive properties of N-doped NiAl.		3170-3180A
Compressive strength, Microstructural effects		
$NiTi$ and $NiTi-TiC$ composites. II. Compressive mechanical properties.		183-191A
Compressive strength, Stress effects		
Prediction of fatigue crack formation in 304 stainless steel.		1267-1271A
Compressor blades, Nondestructive testing		
Determination of hydrogen in titanium alloys by cold neutron prompt gamma activation analysis.		3682-3687A
Computation		
A one-phase model of the mixing of Al-SiC composite melt.		1015-1023B
Computer simulation		
Materials and society—impacts and responsibilities.		337-350B
Nucleation controlled solidification kinetics.		533-547A
Viscosity of superalloy 718 by the oscillating vessel technique.		698-701B
Mathematical modeling of tundish operation and flow control to reduce transition slabs.		745-756B
Solid-state contributions to densification during liquid-phase sintering.		901-909B
A one-phase model of the mixing of Al-SiC composite melt.		1015-1023B
Computer simulation of reversible martensitic transformations.		1187-1201A
Computer simulation of ledge migration under elastic interaction.		1489-1498A
Orientation selective recrystallization of nonoriented electrical steels.		2347-2358A
Simulation of the hot-tension test under cavitating conditions.		3112-3119A
Concentrates (ores)		
The mineralogical department of germanium in the Clarksville electrolytic zinc plant of Savage Zinc Inc.		567-576B
Concentration (composition)		
Intermixing model of continuous casting during a grade transition.		617-632B
Splitting phenomena occurring in the martensitic transformation of Cr13 and CrMoV14 stainless steels in the absence of carbide precipitation.		1799-1805A
Thermodynamic and kinetic study of diffusion paths in the system Cu-Fe-Ni.		2229-2238A
Modeling of microsegregation in macrosegregation computations.		2314-2327A
Consolidation		
Dense CoAl-based alloys with improved ductility: solid-state synthesis and microstructure control.		2140-2150A
Contact angle, Temperature effects		
Variation of contact angles with temperature and time in the $Al-Al_2O_3$ system.		51-55B
Continuous annealing		
Modeling recovery and recrystallization kinetics in cold-rolled Ti-Nb stabilized interstitial-free steel.		3410-3423A
Continuous cast shapes, Crystal growth		
Analysis of shell thickness irregularity in continuously cast middle carbon steel slabs using mold thermocouple data.		1045-1056B
Continuous cast shapes, Diffusion		
Modeling of the peritectic reaction and macro-segregation in casting of low carbon steel.		999-1014B

Continuous casting

Effects of forced electromagnetic vibrations during the solidification of aluminum alloys. II. Solidification in the presence of colinear variable and stationary magnetic fields.
Intermixing model of continuous casting during a grade transition.
Flow and thermal behavior of the top surface flux/powder layers in continuous casting molds.
Prediction of grain structures in various solidification processes.
Cold model study of the surface profile in a continuous slab casting mold: effect of second phase.
Mathematical modeling of tundish operation and flow control to reduce transition slabs.
A water model study of the flow asymmetry inside a continuous slab casting mold.
Modeling of the peritectic reaction and macro-segregation in casting of low carbon steel.
Analysis of shell thickness irregularity in continuously cast mid-die carbon steel slabs using mold thermocouple data.

Convection

Some consequences of thermosolutal convection: the grain structure of castings.
Time dependence of tip morphology during cellular/dendritic arrayed growth.

Convection, Field effects

Convection during thermally unstable solidification of Pb-Sn in a magnetic field.

Cooling rate

Solidification of particle-reinforced metal-matrix composites.
Radioscopic visualization of isothermal solidification of eutectic Ga-In alloy.
Prediction of dendrite arm spacing for low alloy steel casting processes.
Modeling of the peritectic reaction and macro-segregation in casting of low carbon steel.
Ferrite nucleation and growth during continuous cooling.
Austenite decomposition during continuous cooling of an HSLA-60 plate steel.
The quench sensitivity of cast Al-7 wt.% Si-0.4 wt.% Mg alloy.
Macrotransport-solidification kinetics modeling of equiaxed dendritic growth. II. Computation problems and validation on Inconel 718 superalloy casting.

Cooling rate, Pressure effects

The squeeze casting of hypoeutectic binary Al-Cu.

Copper, Alloying additive

Retardation of intermetallic phase formation in experimental superferitic stainless steels.
The effect of metallic elements on the crystallization behavior of amorphous Fe-Si-B alloys.

Copper, Binary systems

Critical evaluation and optimization of the thermodynamic properties of liquid tin solutions.
Generalized enthalpy method for multicomponent phase change.

Copper, Composite materials

Creep deformation of dispersion-strengthened copper.
Thermal expansion of metals reinforced with ceramic particles and microcellular foams.

Copper, Crystal growth

Aspects of dynamic recrystallization in shaped charge and explosively formed projectile devices.

Copper, Diffusion

Anomalous diffusion of iron in liquid aluminum measured by the pulsed laser technique.
Incipient chemical instabilities of nanophase Fe-Cu alloys prepared by mechanical alloying.

Copper, Extraction

Kinetics of the flash converting of MK (chalcoite) concentrate.
Kinetics of sulfation of chalcopyrite with steam and oxygen in the presence of ferric oxide.
Phase equilibria in the metal-sulfur-oxygen system and selective reduction of metal oxides and sulfides. I. The carbothermic reduction and calcination of complex mineral sulfides.

Copper, Forming

Reply: Dynamic materials model. Basis and principles.

Copper, Mechanical properties

The inter-relationship between grain boundary sliding and cavitation during creep of polycrystalline copper.
Increased ductility in high velocity electromagnetic ring expansion.
Temperature dependence of the rate sensitivity and its effect on the activation energy for high-temperature flow.
Plastic zones and fatigue-crack closure under plane-strain double slip.

Copper, Oxidation

Oxidation-reduction equilibrium of $\text{Cu}^{2+}/\text{Cu}^+$ in binary alkaline sulfate melts.

385-392B

Copper, Powder technology

Preparation of fine copper powders from organic media by reaction with hydrogen under pressure. I. Experimental study.

577-584B

Preparation of fine copper powders from organic media by reaction with hydrogen under pressure. II. The kinetics of particle nucleation, growth, and dispersion.

585-594B

Milling dynamics. III. Integration of local and global modeling of mechanical alloying devices.

1999-2004A

Copper, Quaternary systems

Thermodynamic properties of complex oxides in the Sm-Ba-Cu-O system.

973-978B

Copper, Reactions (chemical)

Behavior of antimony(III) during copper electrotwinning in chloride solutions.

157-162B

Transient liquid-phase bonding in the NiAl/Cu/Ni system—a microstructural investigation.

3621-3629A

Copper, Refining

Fundamental studies of copper anode passivation during electrotrefining. I. Development of techniques.

393-398B

Fundamental studies of copper anode passivation during electrotrefining. II. Surface morphology.

610-616B

The measurement of hydrogen activities in molten copper using an oxide protonic conductor.

929-935B

Influence of gold content on copper oxidation from silver-gold-copper alloys.

3187-3191A

Copper, Solubility

Solid-state contributions to densification during liquid-phase sintering.

901-909B

Copper, Ternary systems

Thermodynamic and kinetic study of diffusion paths in the system Cu-Fe-Ni.

2229-2238A

Copper base alloys

Thermoelastic martensite and shape memory effect in ductile Cu-Al-Mn alloys.

2187-2195A

Copper base alloys, Composite materials

Transient thermal analysis of solidification in a centrifugal casting for composite materials containing particle segregation.

277-285B

Permeability of microporous carbon preforms.

3669-3674A

Wear and friction behavior of metal impregnated microporous carbon composites.

3727-3738A

Copper base alloys, Corrosion

Discussion of "a fully plastic microcracking model for transgranular stress corrosion cracking in planar slip materials" and reply.

819-821A

Copper base alloys, Crystal growth

Microstructure of Cu-Co alloys solidified at various supercoolings.

4049-4059A

Copper base alloys, Diffusion

Average effective interdiffusion coefficients and the Matano plane composition.

2504-2509A

Incipient chemical instabilities of nanophase Fe-Cu alloys prepared by mechanical alloying.

2934-2946A

Copper base alloys, Forming

Reply: Dynamic materials model. Basis and principles.

235-236A

Copper base alloys, Mechanical properties

Predicting the orientation-dependent stress-induced transformation and detwinning response of shape memory alloy single crystals.

269-279A

The characteristics of cavitation in superplastic metals and ceramics.

873-878A

A mode! study of cavity growth in superplasticity using single premachined holes.

2532-2539A

Copper base alloys, Microstructure

Prediction of grain structures in various solidification processes.

695-705A

Copper base alloys, Phase transformations

A new characterization method of the microstructure using the macroscopic composition gradient in alloys.

945-949A

Thermoelastic martensite and shape memory effect in ductile Cu-Al-Mn alloys.

2187-2195A

Copper base alloys, Phases (state of matter)

Characterization of the formation of α_1 plates from the β_3 phase in a Cu-Zn-Au alloy.

719-724A

Formation of bainite in ferrous and nonferrous alloys through sympathetic nucleation and ledgewise growth mechanism.

1533-1543A

Copper compounds, Synthesis

Synthesis of nanocrystalline Ni_3Cu by sol-gel route.

4213-4216A

Corrosion environments

On the transition of fatigue crack growth from stage I to stage II in a corrosive environment.
 Studies on the influence of metallurgical variables on the stress corrosion behavior of AISI 304 stainless steel in sodium chloride solution using the fracture mechanics approach.
 Stress corrosion cracking of pressure vessel steels in high-temperature caustic aluminate solutions.

Corrosion fatigue

The influence of aqueous environments on low ΔK and high ΔK fatigue crack propagation behavior in low carbon structural steels.

Corrosion fatigue, Heating effects

Corrosion fatigue in nitrocarburized quenched and tempered steels.

Corrosion potential, Alloying effects

Influence of microalloying on the corrosion resistance of steel in saturated calcium hydroxide.

Corrosion rate

Studies on the corrosion and the behavior of inert anodes in aluminum electrolysis.

Corrosion resistance

The improved microstructures and properties of 7075 alloys produced by a water-cooling centrifugal casting method.
 Corrosive wear of SiC whisker- and particulate-reinforced 6061 aluminum alloy composites.

Effects of the alumina scale on the room-temperature tensile behavior of preoxidized MA 956.

Corrosion resistance, Alloying effects

Influence of microalloying on the corrosion resistance of steel in saturated calcium hydroxide.

Corrosion resistance, Heating effects

Influence of thermal aging on the intergranular corrosion resistance of types 304LN and 316LN stainless steels.

Corrosion resistance, Microstructural effects

Retardation of intermetallic phase formation in experimental superferritic stainless steels.

Corrosion resistance, Welding effects

Microstructural aspects of sulfide stress cracking in an API X-80 pipeline steel.

Corrosion resistant steels

$M_{23}C_6$ carbide equilibria in the Fe-Cr-C system.

Corrosive wear

Corrosive wear of SiC whisker- and particulate-reinforced 6061 aluminum alloy composites.

Crack closure

Plastic zones and fatigue-crack closure under plane-strain double slip.

Crack closure, Composition effects

Growth behavior of microstructurally short cracks in the 6061 aluminum alloy with and without 22 vol.% SiC whiskers.

Crack initiation

An experimental and theoretical investigation of the rapid consolidation of continuously reinforced, metal-matrix composites.

Deformation behavior of an Al-3.37 wt. % Li alloy.

Copper-bearing high-strength low-alloy steels: the influence of microstructure on the initiation and growth of small fatigue cracks.

Observation of short fatigue crack-growth process in SiC-fiber-reinforced Ti-15-3 alloy composite.

Ballistic impact behavior of multilayered armor plates processed by hardfacing.

Crack initiation, Coating effects

Isothermal fatigue of an aluminide-coated single-crystal superalloy. I.

Crack initiation, Deformation effects

Analysis and prevention of vertical cracking phenomena during deep drawing of hot-rolled SG295 steel strips.

Crack initiation, Heating effects

A strain-based fracture model for stress corrosion cracking of low-alloy steels.

Effect of homogenization heat treatment on the microstructure and heat affected zone microfissuring in welded cast alloy 718.

Crack initiation, Impurity effects

The effect of hydrogen on the fracture of alloy X-750.

Crack initiation, Microstructural effects

Subcritical crack growth at bimaterial interfaces. II. Microstructural effects on fracture resistance of metal/ceramic interfaces.

Creep deformation and crack growth behavior of a single-crystal nickel-base superalloy.

829-837A

Crack initiation, Stress effects

Subcritical crack growth at bimaterial interfaces. I. Flexural peel technique.

205-211A

Temperature and strain-rate effects on low-cycle fatigue behavior of alloy 800H.

255-267A

Stacking faults in SiC particles and their effect on the fracture behavior of a 15 vol.% SiC/6061-Al matrix composite.

459-465A

Detecting stable crack onset at ductile-brittle transition in steels.

469-471A

Reinforcement stresses during deformation of sphere- and particulate-reinforced aluminum-matrix composites.

486-490A

Discussion of a "fully plastic microcracking model for transgranular stress corrosion cracking in planar slip materials" and reply.

819-821A

Mechanisms of high-temperature fatigue failure in alloy 800H. Prediction of fatigue crack formation in 304 stainless steel.

851-861A

1267-1271A

Crack initiation, Temperature effects

Heat-flow-based analysis of surface crack formation during the start-up of the direct chill casting process. I. Development of the inverse heat-transfer model.

119-127B

Heat-flow-based analysis of surface crack formation during the start-up of the direct chill casting process. II. Experimental study of an AA5182 rolling ingot.

129-137B

Isothermal fatigue of an aluminide-coated single-crystal superalloy. II. Effects of brittle precracking.

363-369A

Crack initiation, Welding effects

Cleavage initiation in the intercritically reheated coarse-grained heat affected zone. II. Failure criteria and statistical effects.

3019-3029A

Crack opening displacement

Effects of alkali-metal impurities on fracture toughness of 2090 Al-Li-Cu extrusions.

3530-3541A

Crack opening displacement, Welding effects

Cleavage initiation in the intercritically reheated coarse-grained heat affected zone. II. Failure criteria and statistical effects.

3019-3029A

Crack propagation

Copper-bearing high-strength low-alloy steels: the influence of microstructure on the initiation and growth of small fatigue cracks.

2540-2556A

Observation of short fatigue crack-growth process in SiC-fiber-reinforced Ti-15-3 alloy composite.

2843-2851A

The effects on fracture toughness of ductile-phase composition and morphology in Nb-Cr-Ti and Nb-Si in situ composites. Microstructure and tensile properties of compacted, mechanically alloyed, nanocrystalline Fe-Al.

3007-3018A

Plastic zones and fatigue-crack closure under plane-strain double slip.

3126-3134A

Effects of alkali-metal impurities on fracture toughness of 2090 Al-Li-Cu extrusions.

3491-3502A

The balance of mechanical and environmental properties of a multielement niobium-niobium silicide-based in situ composite.

3801-3808A

Conditioning monitoring by microstructural evaluation of cumulative fatigue damage.

3841-3851A

Crack propagation, Alloying effects

Effect of strontium modification on near-threshold fatigue crack growth in an Al-Si-Cu die cast alloy.

1293-1302A

Crack propagation, Composition effects

Effect of manganese dispersoid on the fatigue crack propagation of Al-Zn-Mg alloys.

490-493A

Growth behavior of microstructurally short cracks in the 6061 aluminum alloy with and without 22 vol.% SiC whiskers.

2013-2021A

Crack propagation, Deformation effects

Analysis and prevention of vertical cracking phenomena during deep drawing of hot-rolled SG295 steel strips.

1241-1250A

Crack propagation, Diffusion effects

Hydrogen-induced cleavage fracture of Fe_3Al -based intermetallics.

3949-3956A

Crack propagation, Environmental effects

On the transition of fatigue crack growth from stage I to stage II in a corrosive environment.

471-476A

Studies on the influence of metallurgical variables on the stress corrosion behavior of AISI 304 stainless steel in sodium chloride solution using the fracture mechanics approach.

1313-1325A

The influence of aqueous environments on low ΔK and high ΔK fatigue crack propagation behavior in low carbon structural steels.

2678-2685A

Microstructural aspects of sulfide stress cracking in an API X-80 pipeline steel.

3601-3611A

Crack propagation, Heating effects

A strain-based fracture model for stress corrosion cracking of low-alloy steels.

291-304A

Crack propagation, Impurity effects

The effect of hydrogen on the fracture of alloy X-750.

101-110A

Crack propagation, Microstructural effects

The effects of microstructure, strength level, and crack propagation mode on stress corrosion cracking behavior of 4135 steel.
 Creep deformation and crack growth behavior of a single-crystal nickel-base superalloy.
 Bridge toughening enhancement in double-notched MoSi_2/Nb model composites.
 Crystallographic preferred orientation induced by cyclic rolling contact loading.
 Fracture and fatigue-crack growth behavior in ductile-phase toughened molybdenum disilicide: effects of niobium wire vs. particulate reinforcements.

Crack propagation, Radiation effects

The effect of high-energy electron-beam irradiation on microstructural modification of a high-speed steel roll.

Crack propagation, Stress effects

Subcritical crack growth at bimaterial interfaces. I. Flexural peel technique.
 Subcritical crack growth at bimaterial interfaces. III. Shear-enhanced fatigue crack growth resistance at polymer/metal interface.
 Temperature and strain-rate effects on low-cycle fatigue behavior of alloy 800H.
 Stacking faults in SiC particles and their effect on the fracture behavior of a 15 vol-% SiC/6061-Al matrix composite.
 Detecting stable crack onset at ductile-brittle transition in steels.
 Reinforcement stresses during deformation of sphere- and particulate-reinforced aluminum-matrix composites.
 Time-dependent, environmentally assisted crack growth in Nicalon-fiber-reinforced SiC composites at elevated temperatures.
 Mechanisms of high-temperature fatigue failure in alloy 800H. Evidence of fracture surface interference for cracks loaded in shear detected by phase-shifted speckle interferometry.

Crack propagation, Temperature effects

Heat-flow-based analysis of surface crack formation during the start-up of the direct chill casting process. I. Development of the inverse heat-transfer model.
 Heat-flow-based analysis of surface crack formation during the start-up of the direct chill casting process. II. Experimental study of an AA5182 rolling ingot.
 Isothermal fatigue of an aluminum-coated single-crystal superalloy. II. Effects of brittle precracking.
 Temperature dependence of the intrinsic small fatigue crack growth behavior in nickel-base superalloys based on measurement of crack closure.

Crack propagation, Welding effects

Effect of postweld treatment on the fatigue crack growth rate of electron-beam-welded AISI 4130 steel.

Cracking (fracturing)

Multiple matrix cracking in a fiber-reinforced titanium matrix composite under high-cycle fatigue.
 Influence of temperature transients on the hot workability of a two-phase gamma titanium aluminate alloy.
 Solidification of an alloy 625 weld overlay.
 Mathematical modeling of the extrusion of 6061/ $\text{Al}_2\text{O}_3/20\%$ composite.
 Modeling particle fracture during the extrusion of aluminum/alumina composites.

Cracks

Thermal expansion of metals reinforced with ceramic particles and microcellular foams.

Creep (materials)

Tensile ductility and fracture of superplastic aluminum-SiC composites under thermal cycling conditions.
 Temperature dependence of the rate sensitivity and its effect on the activation energy for high-temperature flow.

Creep (materials), Microstructural effects

Creep deformation of dispersion-strengthened copper.
 Preferential coarsening of γ' precipitates in Inconel 718 during creep.

Creep (materials), Stress effects

Time-dependent, environmentally assisted crack growth in Nicalon-fiber-reinforced SiC composites at elevated temperatures.

Creep life

Prediction of creep-rupture life of unidirectional titanium matrix composites subjected to transverse loading.

Creep life, Microstructural effects

Creep deformation and crack growth behavior of a single-crystal nickel-base superalloy.
 The normalized Coffin-Manson plot in terms of a new damage function based on grain boundary cavitation under creep-fatigue condition.

Creep lifetime prediction of oxide-dispersion-strengthened nickel-base superalloys: a micromechanically based approach.

An evaluation of the creep properties of two Al-Si alloys produced by rapid solidification processing.

3861-3870A

3871-3879A

Creep life, Stress effects

Effect of carbide precipitation on the creep behavior of alloy 800HT in the temperature range 700-900°C.

Effect of multiaxial stresses on creep damage of 316 stainless steel weldments.

747-756A

891-900A

Creep rate

The balance of mechanical and environmental properties of a multielement niobium-niobium silicide-based *in situ* composite.

3801-3808A

Creep rate, Microstructural effects

Effect of creep strain on microstructural stability and creep resistance of a $\text{TiAl}/\text{Ti}_3\text{Al}$ lamellar alloy.

Creep deformation and crack growth behavior of a single-crystal nickel-base superalloy.

829-837A

Effect of iron on ductility and cavitation in the superplastic $\text{Al}-22\%$ Al eutectoid.

863-872A

On the influence of grain morphology on creep deformation and damage mechanisms in directionally solidified and oxide dispersion strengthened superalloys.

879-890A

Creep lifetime prediction of oxide-dispersion-strengthened nickel-base superalloys: a micromechanically based approach.

3861-3870A

An evaluation of the creep properties of two Al-Si alloys produced by rapid solidification processing.

3871-3879A

Creep rate, Stress effects

Effect of a solid solution on the steady-state creep behavior of an aluminum matrix composite.

305-316A

Effect of multiaxial stresses on creep damage of 316 stainless steel weldments.

891-900A

Creep deformation and damage in a continuous fiber-reinforced Ti-6Al-4V composite.

4193-4204A

Creep rupture strength

Prediction of creep-rupture life of unidirectional titanium matrix composites subjected to transverse loading.

3074-3080A

The balance of mechanical and environmental properties of a multielement niobium-niobium silicide-based *in situ* composite.

3801-3808A

Creep rupture strength, Microstructural effects

On the influence of grain morphology on creep deformation and damage mechanisms in directionally solidified and oxide dispersion strengthened superalloys.

879-890A

Creep lifetime prediction of oxide-dispersion-strengthened nickel-base superalloys: a micromechanically based approach.

3861-3870A

An evaluation of the creep properties of two Al-Si alloys produced by rapid solidification processing.

3871-3879A

Creep strength, Alloying effects

Elevated temperature compressive properties of N-doped NiAl.

3170-3180A

Creep strength, High temperature effects

High-temperature measurements of lattice parameters and internal stresses of a creep-deformed monocrystalline nickel-base superalloy.

1003-1014A

High-temperature deformation properties of NiAl single crystals.

1229-1240A

Creep strength, Microstructural effects

Effect of creep strain on microstructural stability and creep resistance of a $\text{TiAl}/\text{Ti}_3\text{Al}$ lamellar alloy.

127-134A

Phase stability and atom probe field ion microscopy of type 308 CRE stainless steel weld metal.

763-774A

The inter-relationship between grain boundary sliding and cavitation during creep of polycrystalline copper.

901-907A

Tensile properties of mechanically alloyed/milled ODS-Ni-based alloys.

1371-1377A

Creep strength, Stress effects

Effect of a solid solution on the steady-state creep behavior of an aluminum matrix composite.

305-316A

Rafting in superalloys.

513-530A

Effect of carbide precipitation on the creep behavior of alloy 800HT in the temperature range 700-900°C.

747-756A

Effect of multiaxial stresses on creep damage of 316 stainless steel weldments.

891-900A

Creep strength, Temperature effects

Enhanced ductility in coarse-grained Al-Mg alloys.

343-352A

Observations of secondary carbide precipitation and its relation to high-temperature flow and fracture in HT-9 stainless steel.

467-469A

Creep tests

An evaluation of the creep properties of two Al-Si alloys produced by rapid solidification processing.

3871-3879A

Creep deformation and damage in a continuous fiber-reinforced Ti-6Al-4V composite.

4193-4204A

Cryolite	Electrical conductivity of molten cryolite based mixtures obtained with a tube type cell made of pyrolytic boron nitride.	255-261B	Cutting tools, Materials selection	Synthesis of full-density nanocrystalline tungsten carbide by reduction of tungstic oxide at room temperature.	4210-4213A
Cryolite, Reactions (chemical)	Liquidus temperatures for primary crystallization of cryolite in molten salt systems of interest for aluminum electrolysis. The transported entropy of Na^+ in solid state cryolite.	739-744B 788-793B	Cyanidation	Electrochemical behavior of the dissolution of gold-silver alloys in cyanide solutions.	355-361B
Crystal defects	High-resolution electron microscopy analysis of structural defects in a (2/1, 53)-type approximant of a decagonal quasicrystal of an Al-Pd-Mn alloy.	2911-2915A	Cyclic loads	Crystallographic preferred orientation induced by cyclic rolling contact loading. Fracture and fatigue-crack growth behavior in ductile-phase toughened molybdenum disilicide: effects of niobium wire vs. particulate reinforcements.	3445-3465A 3781-3792A
Crystal growth	Time dependence of tip morphology during cellular/dendritic arrayed growth. Crystal shapes and phase equilibria: a common mathematical basis. The Rayleigh Instability and the origin of rows of droplets in the monotectic microstructure of zinc-bismuth alloys. Modeling of ferrite growth in nodular cast iron.	1111-1119A 1431-1440A 2053-2057A 2209-2220A	Damage	Conditioning monitoring by microstructural evaluation of cumulative fatigue damage.	3841-3851A
Crystal growth, Composition effects	Effects of shear flow and anisotropic kinetics on the morphological stability of a binary alloy.	687-694A	Damage, Stress effects	Creep deformation and damage in a continuous fiber-reinforced Ti-6Al-4V composite.	4193-4204A
Crystal growth, Field effects	Convection during thermally unstable solidification of Pb-Sn in a magnetic field.	1095-1110A	Damage tolerance	Conditioning monitoring by microstructural evaluation of cumulative fatigue damage.	3841-3851A
Crystal structure	Interdissolution kinetics in oxide powder mixture using high temperature x-ray diffraction technique. The inter-relationship between grain boundary sliding and cavitation during creep of polycrystalline copper. Crystal shapes and phase equilibria: a common mathematical basis. Crystallography of grain boundary α precipitates in a β titanium alloy. Microstructure and phase identification in type 304 stainless steel-zirconium alloys. Thermoelastic martensite and shape memory effect in ductile Cu-Al-Mn alloys. Lattice misfits in four binary Ni-base γ / γ' alloys at ambient and elevated temperatures.	318-322B 901-907A 1431-1440A 1630-1641A 2151-2159A 2187-2195A 2888-2896A	Damage tolerance, Stress effects	Effect of thermal cycling on the mechanical properties of 350 grade maraging steel. Effect of multiaxial stresses on creep damage of 316 stainless steel weldments.	757-761A 891-900A
Crystal structure, Alloying effects	Mechanical alloying of Nb-Al powders. Identification of precipitate phases in a mechanically alloyed rapidly solidified Al-Fe-Ce alloy.	41-48A 1033-1041A	Damping capacity	Analysis of damping in particle-reinforced superplastic zinc composites.	2565-2573A
Crystal structure, Coating effects	Microstructural analysis and oxidation behavior of laser-processed Fe-Cr-Al-Y alloy coatings.	381-390A	Damping capacity, Composition effects	The effect of volume percent and morphology of phases on the damping behavior of epoxy-aluminum composites.	2386-2373A
Crystal structure, Deformation effects	Effects of alloy modification and thermomechanical processing on recrystallization of Al-Mg-Mn alloys.	2947-2957A	Decomposition reactions	Hydride formation and decomposition in electrolytically charged metastable austenitic stainless steels.	29-40A
Crystal structure, Heating effects	Characterization of the formation of α_1 plates from the β phase in a Cu-Zn-Au alloy. Neutron diffraction study of austempered ductile iron.	719-724A 923-928A		A high-resolution transmission electron microscopy study of the precipitation process in a dilute Ti-N alloy.	2966-2977A
Crystal structure, Stress effects	On the effect of stress on nucleation and growth of precipitates in an Al-Cu-Mg-Ag alloy.	3431-3444A	Deep drawing	Analysis and prevention of vertical cracking phenomena during deep drawing of hot-rolled SG295 steel strips.	1241-1250A
Crystal structure, Temperature effects	Eutectoid decomposition in Ag-Ga.	1676-1682A	Deformation	Nanoscale brass/steel multilayer composites produced by cold rolling. Simulation of the hot-tension test under cavitating conditions. Hot deformation mechanisms of a solution-treated Al-Li-Cu-Mg-Zr alloy. Mathematical modeling of the extrusion of 6061/Al ₂ O ₃ /20% composite. Creep deformation and damage in a continuous fiber-reinforced Ti-6Al-4V composite.	2383-2385A 3112-3119A 3478-3490A 4095-4111A 4193-4204A
Crystallization	Liquidus temperatures for primary crystallization of cryolite in molten salt systems of interest for aluminum electrolysis. Crystallization of amorphous phase in sputter-deposited Ti-Al alloy thin films.	739-744B 2047-2050A	Deformation, High temperature effects	High-temperature deformation properties of NiAl single crystals.	1229-1240A
Crystallization, Alloying effects	The effect of metallic elements on the crystallization behavior of amorphous Fe-Si-B alloys.	3424-3430A	Deformation, Temperature effects	Elevated temperature deformation behavior of a dispersion-strengthened Al-Fe, V, Si alloy. An analysis of the flow stress of a two-phase alloy system, Ti-6Al-4V.	3913-3923A 3957-3962A
Crystallization, Temperature effects	Crystallization of amorphous alloys.	549-555A	Deformation mechanisms	Effect of phase composition and hydrogen level on the deformation behavior of titanium-hydrogen alloys. Characterization of superplastic deformation behavior of a fine grain 5083 Al alloy sheet. Deformation behavior of an Al-3.37 wt.% Li alloy. Hot deformation mechanisms of a solution-treated Al-Li-Cu-Mg-Zr alloy. Creep deformation and damage in a continuous fiber-reinforced Ti-6Al-4V composite.	1869-1876A 1889-1898A 2274-2284A 3478-3490A 4193-4204A
Crystals	An optical method for determining the surface orientation of crystals.	2057-2061A	Deformation resistance	Prediction of creep-rupture life of unidirectional titanium matrix composites subjected to transverse loading.	3074-3080A
Current density	Physical modeling studies of electrolyte flow due to gas evolution and some aspects of bubble behavior in advanced Hall cells. III. Predicting the performance of advanced Hall cells. Effect of baking temperature and anode current density on anode carbon consumption. Structural characterization of martensitic iron-carbon alloy films electrodeposited from an iron(II) sulfate solution.	19-27B 177-183B 483-486A	Deformation resistance, Microstructural effects	Van der Waals approximation for potassium bubbles in tungsten.	987-992B
Cutting tool materials, Synthesis	Synthesis of full-density nanocrystalline tungsten carbide by reduction of tungstic oxide at room temperature.	4210-4213A	Deformation resistance, Temperature effects	Influence of temperature transients on the hot workability of a two-phase gamma titanium aluminide alloy.	1933-1950A
			Dendritic structure	Communication: Mechanical deformation of dendrites by fluid flow. Microstructure of bonding zones in laser-clad nickel-alloy-based composite coatings reinforced with various ceramic powders.	229-232A 391-400A

Interface attachment kinetics in alloy solidification.	671-686A	Density	The effect of Mo addition on the liquid-phase sintering of W heavy alloy.	3120-3125A
Prediction of dendrite arm spacing for low alloy steel casting processes.	689-693B		Microstructure and tensile properties of compacted, mechanically alloyed, nanocrystalline Fe-Al.	3126-3134A
High-speed imaging and analysis of the solidification of undercooled nickel melts.	693-698B			
Generalized enthalpy method for multicomponent phase change.	869-879B	Density, Alloying effects	Solid-state contributions to densification during liquid-phase sintering.	901-909B
On the influence of grain morphology on creep deformation and damage mechanisms in directionally solidified and oxide dispersion strengthened superalloys.	879-890A	Deoxidizing	Activities in $MnO-SiO_2-Al_2O_3$ slags and deoxidation equilibria of manganese and silicon.	263-270B
Time dependence of tip morphology during cellular/dendritic arrayed growth.	1111-1119A		Use of solid-electrolyte galvanic cells to determine the activity of CaO in the $CaO-ZrO_2$ system and the standard Gibbs free energies of formation of $CaZrO_3$ from CaO and ZrO_2 .	658-662B
The Rayleigh Instability and the origin of rows of droplets in the monotectic microstructure of zinc-bismuth alloys.	2053-2057A		<i>Thermodynamic properties of oxygen in yttrium-oxygen solid solutions.</i>	839-845B
Effect of grain refinement on the fluidity of two commercial Al-Si foundry alloys.	2305-2313A		The measurement of hydrogen activities in molten copper using an oxide protonic conductor.	929-935B
Orientation dependence of primary dendrite spacing.	2727-2739A		Thermodynamics of calcium and oxygen in molten titanium and titanium-aluminum alloy.	967-972B
Equiaxed dendritic solidification with convection. I. Multiscale/multiphase modeling.	2754-2764A	Dephosphorizing	Thermodynamics of phosphorus in molten silicon.	937-941B
Equiaxed dendritic solidification with convection. II. Numerical simulations for an Al-4 wt.% Cu alloy.	2765-2783A			
Equiaxed dendritic solidification with convection. III. Comparisons with NH_4Cl-H_2O experiments.	2784-2795A	Deposition	Formation of aluminum-silicon alloys from feldspars—determination of silicon, light, and heavy elements in silumin by scanning electron microscopy.	604-609B
Microstructure of Cu-Co alloys solidified at various supercoolings.	4049-4059A			
Macrotransport-solidification kinetics modeling of equiaxed dendritic growth. I. Model development and discussion.	4061-4074A	Description	Physical chemistry of the powder metallurgy of beryllium: chemical characterization of the powder in relation to its granularity.	371-379A
Macrotransport-solidification kinetics modeling of equiaxed dendritic growth. II. Computation problems and validation on Inconel 718 superalloy casting.	4075-4083A	Description, Temperature effects	Applicability of Butler's equation in interpreting the thermodynamic behavior of surfaces and adsorption in Fe-S-O melts.	241-253B
Modeling of primary and secondary dendrites in a Cu-6 wt.% tin alloy.	4085-4093A	Desulfurizing	Thermodynamics of sulfur in the $BaO-MnO-SiO_2$ flux system. Use of solid-electrolyte galvanic cells to determine the activity of CaO in the $CaO-ZrO_2$ system and the standard Gibbs free energies of formation of $CaZrO_3$ from CaO and ZrO_2 .	652-657B
Dendritic structure, Alloying effects	19-27A			658-662B
The effect of iron and manganese on the recrystallization behavior of hot-rolled and solution-heat-treated aluminum alloy 6013.	1081-1094A	Diamond pyramid hardness	Plastic zone and pileup around large indentations.	3793-3800A
The breakdown of single-crystal solidification in high refractory nickel-base alloys.	101-113B		Diamond pyramid hardness, Alloying effects	3793-3800A
Dendritic structure, Cooling effects	415-429A		Effect of magnesium on the aging behavior of $Al-Zn-Mg-Cu/Al_2O_3$ metal matrix composites.	2005-2012A
Scaling of intragranular dendritic microstructure in ingot solidification.	477-480A	Diamond pyramid hardness, Composition effects	Structural characterization of martensitic iron-carbon alloy films electrodeposited from an iron(II) sulfate solution.	483-486A
Porosity formation in Al-9 wt.% Si-3 wt.% Cu alloy systems: metallographic observations.	595-609A	Diamond pyramid hardness, Microstructural effects	Mechanical behavior of the <i>in situ</i> composite alloys in the Al-Ni-Ti system near the L_1 phase field.	71-79A
The effect of bulk flow concentration on diffusion coupling between dendrites.	611-623A		Precipitation in lead-calcium alloys containing tin.	1668-1675A
Solidification of binary hypoeutectic alloy matrix composite castings.	695-705A		The effects on fracture toughness of ductile-phase composition and morphology in Nb-Cr-Ti and Nb-Si <i>in situ</i> composites.	3007-3018A
Numerical modeling of cellular/dendritic array growth: spacing and structure predictions.	1353-1362A	Diamond pyramid hardness, Radiation effects	The effect of high-energy electron-beam irradiation on microstructural modification of a high-speed steel roll.	3149-3161A
Prediction of grain structures in various solidification processes.	1149-1165A	Diamonds, Coatings	Quenching C60 fullerene into diamond in the Fe-C alloy system by laser treatment.	2293-2296A
Macrosegregation during dendritic arrayed growth of hypoeutectic Pb-Sn alloys: influence of primary arm spacing and mushy zone length.	1095-1110A	Die casting	The design of feed systems for thin-walled zinc high-pressure die castings.	115-118B
Dendritic structure, Deformation effects	287-296B	Die steels, Mechanical properties	The wear behavior between hardfacing materials.	3639-3648A
Precipitation behavior in a medium carbon, Ti-V-N microalloyed steel.	809-818A	Differential equations	Mathematical modeling of tundish operation and flow control to reduce transition slabs.	745-756B
Dendritic structure, Field effects	829-837A	Differential thermal analysis	A study of the thermal decomposition of $BaCO_3$. Thermally assisted and mechanically driven solid-state reactions for formation of amorphous $Al_{33}Ta_{67}$ alloy powders.	409-416B
Convection during thermally unstable solidification of Pb-Sn in a magnetic field.	557-567A		3267-3278A	
Dendritic structure, Heating effects	569-581A	Diffusion	Probing the initial stage of synthesis of Al_2O_3/Al composites by directed oxidation of $Al-Mg$ alloys.	43-50B
Effect of superheat on the solidification structures of AISI 310S austenitic stainless steel.	635-656A		Interdissolution kinetics in oxide powder mixture using high temperature x-ray diffraction technique.	318-322B
Mechanical properties and 95°C aging characteristics of zircon reinforced Zn-4Al-3Cu alloy.	657-669A		Theoretical modeling of densification during activated solid-state sintering.	441-450A
Dendritic structure, Stress effects	441-450A		Microstructure of Al_2O_3 fiber-reinforced superalloy (Inconel 718) composites.	451-458A
Creep deformation and crack growth behavior of a single-crystal nickel-base superalloy.	901-909B		Intermixing model of continuous casting during a grade transition.	617-632B
Dendritic structure, Temperature effects	2130-2139A		The characteristics of cavitation in superplastic metals and ceramics.	873-878A
Overview of geometric effects on coarsening of mushy zones. Some consequences of thermostolutal convection: the grain structure of castings.	2140-2150A			
Morphological instabilities of lamellar eutectics.	3688-3699A			
The phase field method: simulation of alloy dendritic solidification during recalescence.				
Densification				
Theoretical modeling of densification during activated solid-state sintering.				
Solid-state contributions to densification during liquid-phase sintering.				
Pressure-assisted reactive synthesis of titanium aluminides from dense 50Al-50Ti elemental powder blends.				
Dense CoAl-based alloys with improved ductility: solid-state synthesis and microstructure control.				
Densification, Pressure effects				
Synthesis of RuAl by reactive powder processing.				

Ostwald ripening in ternary alloys.	937-943A	Prediction of grain structures in various solidification processes.	695-705A
Creep deformation of dispersion-strengthened copper.	1217-1227A	Real time x-ray transmission microscopy of solidifying Al-In alloys.	801-808A
The mechanism of formation of a fine duplex microstructure in Ti-4Al-2Mn-2Nb alloys.	1655-1667A	Time dependence of tip morphology during cellular/dendritic arrayed growth.	1111-1119A
Internal friction in hydrogen-charged CrNi and CrNiMn austenitic stainless steels.	1815-1821A	Macrosegregation during dendritic arrayed growth of hypoeutectic Pb-Sn alloys: Influence of primary arm spacing and mushy zone length.	1353-1362A
Control of iron nitride layers growth kinetics in the binary Fe-N system.	1823-1835A	Directional solidification of white cast iron.	2328-2337A
Dense CoAl-based alloys with improved ductility: solid-state synthesis and microstructure control.	2140-2150A	Transitions between type A flake, type D flake, and coral graphite eutectic structures in cast irons.	2740-2753A
Modeling of ferrite growth in nodular cast iron.	2209-2220A		
Thermodynamic and kinetic study of diffusion paths in the system Cu-Fe-Ni.	2229-2238A		
Modeling of microsegregation in macrosegregation computations.	2314-2327A	Directional solidification, Field effects	
Infrared transient-liquid-phase joining of SCS-6/β21S titanium matrix composite.	4011-4018A	Convection during thermally unstable solidification of Pb-Sn in a magnetic field.	1095-1110A
Diffusion, Alloying effects			
Effects of nickel on the sintering behavior of Fe-Ni compacts made from composite and elemental powders.	203-211B	Directionally solidified eutectics, Mechanical properties	
Electron microscope study of Al-Fe-Si intermetallics in 6201 aluminum alloy.	929-936A	The fracture toughness of niobium-based, <i>in situ</i> composites. The effects on fracture toughness of ductile-phase composition and morphology in Nb-Cr-Ti and Nb-Si <i>in situ</i> composites. Loading rate and test temperature effects on fracture of <i>in situ</i> niobium silicide-niobium composites.	2518-2531A
		The balance of mechanical and environmental properties of a multielement niobium-niobium silicide-based <i>in situ</i> composite.	3007-3018A
			3292-3306A
Diffusion, Cooling effects			
Porosity formation in Al-9 wt.% Si-3 wt.% Cu alloy systems: metallographic observations.	415-429A	Dislocation density	
The effect of bulk flow concentration on diffusion coupling between dendrites.	477-480A	Creep deformation of dispersion-strengthened copper.	1217-1227A
Bainite in the light of rapid continuous cooling information.	1499-1510A	Tensile properties of mechanically alloyed/milled ODS-Ni-based alloys.	1371-1377A
Ferrite nucleation and growth during continuous cooling.	1544-1553A	The control of grain size and distribution of particles in a (6081 alloy) _n (Al ₂ O ₃) _p composite by solutionizing treatment.	2023-2034A
Diffusion, Deformation effects			
Analysis on the amplitude of serrated flow associated with the Portevin-LeChatelier effect of substitutional fcc alloys.	1683-1686A	Dislocation density, Composition effects	
		Electron microscopic study of Cr ₂ N formation in thermally aged 316LN austenitic stainless steels.	1175-1186A
Diffusion, Heating effects			
Characterization of the formation of α_1 plates from the β_1 phase in a Cu-Zn-Au alloy.	719-724A	Dislocation density, Deformation effects	
Anomalous diffusion of iron in liquid aluminum measured by the pulsed laser technique.	725-730A	Effect of creep strain on microstructural stability and creep resistance of a TiAl/Ti ₃ Al lamellar alloy.	127-134A
Heterogeneous nucleation of δ on dislocations in a dilute aluminum-lithium alloy.	1595-1605A	The x-ray diffraction study of deformation in the composite matrix of Al-Mg-Zn and SiC.	503-505A
Transition between internal and external nitridation of Ni-Ti alloys.	1606-1617A	Dislocation density, High temperature effects	
		High-temperature deformation properties of NiAl single crystals.	1229-1240A
Diffusion, High temperature effects			
Phase relations of a silicide/silica reaction couple at 2273K.	271-276B	Dislocation density, Radiation effects	
		A model describing neutron irradiation-induced segregation to grain boundaries in dilute alloys.	3381-3390A
Diffusion, Pressure effects			
Pressure dependence of anomalous diffusion of zirconium in β -titanium.	1807-1814A	Dislocation mobility	
		Deformation behavior of an Al-3.37 wt.% Li alloy.	2274-2284A
Diffusion, Radiation effects			
Transmission electron microscopy study on the cross-sectional microstructure of an ion-nitriding layer.	1347-1352A	Dislocation mobility, Temperature effects	
		RAFTING in superalloys.	513-530A
Diffusion, Stress effects			
A study on coherency strain and precipitate morphology via a discrete atom method.	1449-1459A	Dislocation pinning, Stress effects	
Computer simulation of ledge migration under elastic interaction.	1489-1498A	Elevated temperature deformation behavior of a dispersion-strengthened Al-Fe, V, Si alloy.	3913-3923A
Diffusion rate, Microstructural effects			
Influence of interstitials on the mechanical properties of metallic materials.	3524-3529A	Dislocations	
		NiTi and NiTi-TiC composites. II. Compressive mechanical properties.	183-191A
Diffusion welding		A high resolution transmission electron microscopy study of interfaces between the γ , B ₂ , and α_2 phases in a Ti-Al-Mo alloy.	1618-1629A
Microstructural development in NIAI/Ni-Si-B/NI transient liquid phase bonds.	1925-1931A	Crystallography of grain boundary α precipitates in a β titanium alloy.	1630-1641A
Diffusivity		Recrystallization in oxide-dispersion strengthened mechanically alloyed sheet steel.	1963-1978A
Average effective interdiffusion coefficients and the Matano plane composition.	2504-2509A	High-resolution transmission electron microscopy investigation of the face-centered cubic/hexagonal close-packed martensite transformation in Co-31.8 wt.% Ni alloy. I. Plate interfaces and growth ledges.	3362-3370A
Diffusivity, Heating effects			
Anomalous diffusion of iron in liquid aluminum measured by the pulsed laser technique.	725-730A	Dislocations, Deformation effects	
		Analysis on the amplitude of serrated flow associated with the Portevin-LeChatelier effect of substitutional fcc alloys.	1683-1686A
Direct chill casting			
Heat-flow-based analysis of surface crack formation during the start-up of the direct chill casting process. I. Development of the inverse heat-transfer model.	119-127B	Dislocations, Stress effects	
Heat-flow-based analysis of surface crack formation during the start-up of the direct chill casting process. II. Experimental study of an AA5182 rolling ingot.	129-137B	Stacking faults in SiC particles and their effect on the fracture behavior of a 15 vol.% SiC/6061-Al matrix composite.	459-465A
Modeling of ingot distortions during direct chill casting of aluminum alloys.	3214-3225A	Molecular dynamics simulation of martensitic transformations in NiAl.	1476-1488A
Directional solidification		Computer simulation of ledge migration under elastic interaction.	1489-1498A
Hydrogen effects on directional solidification of tellurium-doped cast irons.	496-498A		
Effects of flow on morphological stability during directional solidification.	583-593A	Dislocations, Temperature effects	
Solidification of binary hypoeutectic alloy matrix composite castings.	595-609A	A new characterization method of the microstructure using the macroscopic composition gradient in alloys.	945-949A
Effects of shear flow and anisotropic kinetics on the morphological stability of a binary alloy.	687-694A		

Dispersion hardening alloys, Crystal growth			
Recrystallization in oxide-dispersion strengthened mechanically alloyed sheet steel.	1963-1978A	Thermal stability of SiC-SCS-6 fiber-reinforced IMI834 alloys. The improved microstructures and properties of 7075 alloys produced by a water-cooling centrifugal casting method.	1403-1405A
Dispersion hardening alloys, Diffusion		Thermoelastic martensite and shape memory effect in ductile Cu-Al-Mn alloys.	1851-1962A
Hydrogen trapping and permeation in nickel thoria.	2495-2503A	Investigation of the reaction zone between TiAl and molybdenum.	2187-2195A
Dispersion hardening alloys, Mechanical properties		The fracture toughness of niobium-based, <i>in situ</i> composites.	2285-2292A
Creep lifetime prediction of oxide-dispersion-strengthened nickel-base superalloys: a micromechanically based approach.	3881-3870A	Tensile ductility and fracture of superplastic aluminum-SiC composites under thermal cycling conditions.	2518-2531A
Elevated temperature deformation behavior of a dispersion-strengthened Al-Fe, V, Si alloy.	3913-3923A	Simulation of the hot-tension test under cavitating conditions.	2837-2842A
Dispersions, High temperature effects		Fracture and fatigue-crack growth behavior in ductile-phase toughened molybdenum disilicide: effects of niobium wire vs. particulate reinforcements.	3112-3119A
Creep lifetime prediction of oxide-dispersion-strengthened nickel-base superalloys: a micromechanically based approach.	3881-3870A	Flow and fracture of bimaterial systems based on aluminum alloys.	3781-3792A
Dissimilar materials, Bonding		Mathematical modeling of the extrusion of 6061/Al ₂ O ₃ /20p composite.	3937-3947A
Flow and fracture of bimaterial systems based on aluminum alloys.	3937-3947A	Ductility, Alloying effects	4095-4111A
Dissimilar metals, Welding		Elevated temperature compressive properties of zirconium-modified NiAl.	2628-2641A
Forming of tailor-welded blanks.	2605-2616A	Tension characteristics of notched specimens for Al-Li-Cu-Zr alloys sheets with various cerium contents.	3089-3094A
Dissipation, Deformation effects		Elevated temperature compressive properties of N-doped NiAl.	3170-3180A
Communication: Discussion of "Modeling of dynamic materials behavior. A critical evaluation of the dissipator power co-constant approach".	232-235A	Ductility, Coating effects	
Dissolution		Isothermal fatigue of an aluminide-coated single-crystal superalloy, I.	353-361A
Interdissolution kinetics in oxide powder mixture using high temperature x-ray diffraction technique.	318-322B	Ductility, Composition effects	
Electrochemical behavior of the dissolution of gold-silver alloys in cyanide solutions.	355-361B	Structural characterization of martensitic iron-carbon alloy films electrodeposited from an iron(II) sulfate solution.	483-486A
Microstructure of bonding zones in laser-clad nickel-alloy-based composite coatings reinforced with various ceramic powders.	391-400A	Carbide diagrams and precipitation of alloying elements during aging of low-alloy steels.	498-502A
Interface characterization of ceramic fiber-reinforced titanium alloy composites manufactured by infrared processing.	1379-1394A	Mechanical properties of Ru-Ni-Al alloys.	1395-1400A
Splitting phenomena occurring in the martensitic transformation of Cr13 and CrMoV14 stainless steels in the absence of carbide precipitation.	1799-1805A	High-temperature behavior of precious metal base composites.	2642-2652A
Dissolution, Alloying effects		Ductility, Cooling effects	
Solubility of carbon in CaO-Al ₂ O ₃ melts.	57-64B	Rapid solidification processing of a Mg-Li-Si-Ag alloy.	1363-1370A
Effects of oxygen, selenium, and tellurium on the rate of nitrogen dissolution in molten iron.	846-851B	The quench sensitivity of cast Al-7 wt.% Si-0.4 wt.% Mg alloy.	3983-3991A
Dissolution, Coating effects		Ductility, Corrosion effects	
Microstructural analysis and oxidation behavior of laser-processed Fe-Cr-Al-Y alloy coatings.	381-390A	Shear ligament phenomena in Fe ₃ Al intermetallics and micro-mechanics of shear ligament toughening.	3817-3825A
Dissolution, Heating effects		Ductility, Deformation effects	
Microstructural aspects of the dissolution and melting of Al ₂ Cu phase in Al-Si alloys during solution heat treatment.	1785-1798A	Micronecking and fracture in cavitated superplastic materials.	1043-1046A
Distortion		Increased ductility in high velocity electromagnetic ring expansion.	1837-1844A
Modeling of ingot distortions during direct chill casting of aluminum alloys.	3214-3225A	Effect of thermomechanical treatments on the room-temperature mechanical behavior of iron aluminide Fe ₃ Al.	2985-2993A
Domain walls		Ductility, Heating effects	
Temperature dependent deformation of polydomain phases in an In-22.5 at.% Ti shape memory alloy.	1687-1692A	Influence of long term annealing on tensile properties and fracture of near- α titanium alloy Ti-6Al-2.75Sn-4Zr-0.4Mo-0.45Si.	1700-1708A
Dual phase steels, Mechanical properties		Ductility, Impurity effects	
Theoretical calculation of the stress-strain behavior of dual-phase metals with randomly oriented spheroidal inclusions.	2359-2365A	The effect of hydrogen on the fracture of alloy X-750.	101-110A
Ductile brittle transition		Ductility, Microstructural effects	
Nonequilibrium grain-boundary segregation and ductile-brittle-ductile transition in Fe-Mn-Ni-Ti age-hardening alloy.	3059-3065A	Mechanical behavior of the <i>in situ</i> composite alloys in the Al-Ni-Ti system near the L ₁ phase field.	71-79A
Ductile brittle transition, Corrosion effects		Pearlite in ultrahigh carbon steels: heat treatments and mechanical properties.	111-118A
Shear ligament phenomena in Fe ₃ Al intermetallics and micro-mechanics of shear ligament toughening.	3817-3825A	Communication: Mechanical deformation of dendrites by fluid flow.	229-232A
Ductile brittle transition, Welding effects		Mechanical behavior and properties of mechanically alloyed aluminum alloys.	737-745A
Microstructures relevant to brittle fracture initiation at the heat-affected zone of a low carbon steel.	2574-2582A	Effect of iron on ductility and cavitation in the superplastic Au-22% Al eutectoid.	863-872A
Cleavage initiation in the intercritically reheated coarse-grained heat affected zone. II. Failure criteria and statistical effects.	3019-3029A	Bridge toughening enhancement in double-notched MoSi ₂ /Nb model composites.	909-921A
Ductile fracture		The embrittlement and de-embrittlement of grain boundaries in an Fe-Mn-Ni alloy due to grain boundary segregation of manganese.	1015-1020A
Microstructure and properties of Al ₂ O ₃ -Al(Si) and Al ₂ O ₃ -Al(Si)-Si composites formed by <i>in situ</i> reaction of aluminum with aluminosilicate ceramics.	2122-2129A	On microsuperplasticity in AA7475 domes.	1400-1403A
The influence of stress triaxiality on the damage mechanisms in an equiaxed α / β Ti-6Al-4V alloy.	3043-3058A	Dense CoAl-based alloys with improved ductility: solid-state synthesis and microstructure control.	2140-2150A
Simulation of the hot-tension test under cavitating conditions.	3112-3119A	Deformation behavior of an Al-3.37 wt.% Li alloy.	2274-2284A
Ductile fracture, Microstructural effects		Microstructure and mechanical behavior of Cr-Cr ₂ Hf in <i>in situ</i> intermetallic composites.	2583-2592A
The cracking mechanism of silicon particles in an A357 aluminum alloy.	3558-3568A	Reinforcement shape effects on the fracture behavior and ductility of particulate-reinforced 6061-Al matrix composites.	3739-3746A
Ductile fracture, Stress effects		Microstructure and fracture of SiC-particulate-reinforced cast A356 aluminum alloy composites.	3893-3901A
Discussion of "a fully plastic microcracking model for transgranular stress corrosion cracking in planar slip materials" and reply.	819-821A	Ductility, Stress effects	
		Detecting stable crack onset at ductile-brittle transition in steels.	469-471A
		Effect of thermal cycling on the mechanical properties of 350 grade maraging steel.	757-761A
		Ductility, Temperature effects	
		Enhanced ductility in coarse-grained Al-Mg alloys.	343-352A

Ductility, Welding effects		
Effect of postweld treatment on the fatigue crack growth rate of electron-beam-welded AISI 4130 steel.	3162-3169A	
Duplex stainless steels		
Microstructure and tensile behavior of nitrogen-alloyed, dual-phase stainless steels.	1845-1859A	
Structural stability of super duplex stainless weld metals and its dependence on tungsten and copper.	2196-2208A	
Duplex stainless steels, Machining		
Active wear and failure mechanisms of titanium nitride-coated high speed steel and titanium nitride-coated cemented carbide tools when machining powder metallurgically made stainless steels.	2796-2808A	
Duplex stainless steels, Microstructure		
Microstructure and tensile behavior of nitrogen-alloyed, dual-phase stainless steels.	1845-1859A	
Duplex stainless steels, Welding		
Structural stability of super duplex stainless weld metals and its dependence on tungsten and copper.	2196-2208A	
Dynamics		
Dynamic Behavior of Materials. II.		
Milling dynamics. II. Dynamics of a SPEX mill and a one-dimensional mill.	1991-1997A	
Milling dynamics. III. Integration of local and global modeling of mechanical alloying devices.	1999-2004A	
Dysprosium, Binary systems		
Standard enthalpies of formation of dysprosium alloys, Dy+Me (Me=Ni, Ru, Rh, Pd, Ir, and Pt), by high-temperature direct synthesis calorimetry.	417-422B	
Economics		
Eco-techno-economic synthesis of process routes for the production of zinc using combinatorial optimization.	1031-1044B	
Edge dislocations, Heating effects		
Heterogeneous nucleation of δ on dislocations in a dilute aluminum-lithium alloy.	1595-1605A	
Elastic anisotropy		
The plastic anisotropy of an Al-Li-Cu-Zr alloy extrusion in unidirectional deformation.	3503-3512A	
Elastic constants		
A comprehensive dynamical study of nucleation and growth in a one-dimensional shear martensitic transition.	1203-1216A	
Elastic constants, Stress effects		
Computer simulation of reversible martensitic transformations. A study on coherency strain and precipitate morphology via a discrete atom method.	1187-1201A	
1449-1459A		
Elasticity, Deformation effects		
Communication: Discussion of "Modeling of dynamic materials behavior. A critical evaluation of the dissipator power co-constant approach".	232-235A	
Elasticity, Stress effects		
Effect of uniaxial stress on coarsening of precipitate clusters.	1460-1475A	
Electric fields		
Effects of forced electromagnetic vibrations during the solidification of aluminum alloys. I. Solidification in the presence of crossed alternating electric fields and stationary magnetic fields.	445-455B	
Electric potential		
Chemical potentials of components of the system $\text{CaO}+\text{P}_2\text{O}_5+\text{Fe}_2\text{O}_3$ at 1673K.	595-603B	
Controversy on the free energy of formation of CaO —additional evidence in support of thermochemical data.	647-651B	
Electrical steels, Rolling		
Orientation selective recrystallization of nonoriented electrical steels.	2347-2358A	
Electrochemistry		
Effect of baking temperature and anode current density on anode carbon consumption.	177-183B	
Electrochemical behavior of the dissolution of gold-silver alloys in cyanide solutions.	355-361B	
Chemical potentials of oxygen for mixtures of $\text{CaO}(s)+\text{Ca}_4\text{P}_2\text{O}_9(s)$ + $(\text{CaO}+\text{P}_2\text{O}_5+\text{Fe}_2\text{O}_3)$ melts and $\text{Ca}_4\text{P}_2\text{O}_9(s)+\text{Ca}_3\text{P}_2\text{O}_9(s)+\text{CaO}+\text{P}_2\text{O}_5+\text{Fe}_2\text{O}_3$ melts.	375-378B	
Fundamental studies of copper anode passivation during electrorefining. I. Development of techniques.	393-398B	
Electrodeposition		
Structural characterization of martensitic iron-carbon alloy films electrodeposited from an iron(II) sulfate solution.	483-486A	
Electrodeposition, Impurity effects		
Behavior of antimony(III) during copper electrowinning in chloride solutions.	157-162B	
Electrodes, Materials selection		
Reference electrode of simple galvanic cells for developing sodium sensors for use in molten aluminum.	794-800B	
Electrolysis		
Studies on the corrosion and the behavior of inert anodes in aluminum electrolysis.	185-193B	
Liquidus temperatures for primary crystallization of cryolite in molten salt systems of interest for aluminum electrolysis.	739-744B	
The transported entropy of Na^+ in solid state cryolite.	788-793B	
Reference electrode of simple galvanic cells for developing sodium sensors for use in molten aluminum.	794-800B	
Electrolysis, Temperature effects		
Electrical conductivity of molten cryolite based mixtures obtained with a tube type cell made of pyrolytic boron nitride.	255-261B	
Electrolytic cells		
Use of solid-electrolyte galvanic cells to determine the activity of CaO in the $\text{CaO}-\text{ZrO}_2$ system and the standard Gibbs free energies of formation of CaZrO_3 from CaO and ZrO_2 .	658-662B	
Preparation of pure silicon by electrowinning in a bytownite-cryolite melt.	895-900B	
Electrolytic cells, Development		
Application of centrifugal fields in fused salt electrowinning with a view to reducing electrolytic energy consumption.	889-894B	
Electromagnetic fields		
Increased ductility in high velocity electromagnetic ring expansion.	1837-1844A	
Electromagnetic testing		
Alloy phase analysis from measurements of bulk magnetic properties.	2958-2965A	
Electron beam welding		
Effect of homogenization heat treatment on the microstructure and heat affected zone microfissuring in welded cast alloy 718.	785-790A	
Effect of postweld treatment on the fatigue crack growth rate of electron-beam-welded AISI 4130 steel.	3162-3169A	
Electron diffraction		
Characterization of titanium thin films prepared by bias assisted magnetron sputtering.	1057-1060B	
Electron energy loss spectroscopy		
Incipient chemical instabilities of nanophase Fe-Cu alloys prepared by mechanical alloying.	2934-2946A	
Electron microscopy		
High-resolution electron microscopy analysis of structural defects in a (2/1, 5/3)-type approximant of a decagonal quasicrystal of an Al-Pd-Mn alloy.	2911-2915A	
Electronic structure, Composition effects		
Electron microscopic study of Cr_2N formation in thermally aged 316LN austenitic stainless steels.	1175-1186A	
Electronic structure, Radiation effects		
Sputter-induced pits on $\{100\}$ nickel surfaces.	981-993A	
Electroplating		
Characterization of titanium thin films prepared by bias assisted magnetron sputtering.	1057-1060B	
Electrorefining		
Fundamental studies of copper anode passivation during electrorefining. I. Development of techniques.	393-398B	
Fundamental studies of copper anode passivation during electrorefining. II. Surface morphology.	610-616B	
Influence of gold content on copper oxidation from silver-gold-copper alloys.	3187-3191A	
Electrowinning		
Application of centrifugal fields in fused salt electrowinning with a view to reducing electrolytic energy consumption.	889-894B	
Preparation of pure silicon by electrowinning in a bytownite-cryolite melt.	895-900B	
Electrowinning, Impurity effects		
Behavior of antimony(III) during copper electrotinning in chloride solutions.	157-162B	
Elongation		
Thermal stability of SiC-SCS-6 fiber-reinforced IMI834 alloys.	1403-1405A	
Characterization and mechanical properties of ultrahigh boron steels produced by powder metallurgy.	1861-1867A	
Characterization of superplastic deformation behavior of a fine grain 5083 Al alloy sheet.	1889-1898A	
Simulation of the hot-tension test under cavitating conditions.	3112-3119A	
Notch fracture in γ -titanium aluminides.	3903-3912A	
Elongation, Composition effects		
A study of the influence of mischmetal additions to Al-7Si-0.3Mg (LM 25/356) alloy.	1283-1292A	
Elongation, Deformation effects		
Analysis and prevention of vertical cracking phenomena during deep drawing of hot-rolled SG295 steel strips.	1241-1250A	

Elongation, Diffusion effects	
Hydrogen-induced cleavage fracture of Fe_3Al -based intermetallics.	3949-3956A
Elongation, Impurity effects	
The effect of hydrogen on the fracture of alloy X-750.	101-110A
Elongation, Microstructural effects	
Effect of iron ductility and cavitation in the superplastic $Al-22\%Fe$ eutectoid.	863-872A
The embrittlement and de-embrittlement of grain boundaries in an $Fe-Mn-Ni$ alloy due to grain boundary segregation of manganese.	1015-1020A
Tensile properties of mechanically alloyed/milled ODS-Ni-based alloys.	1371-1377A
Effect of bainite transformation and retained austenite on mechanical properties of austempered spheroidal graphite cast steel.	1585-1594A
Fracture characteristics, microstructure, and tissue reaction of $Ti-5Al-2.5Fe$ for orthopedic surgery.	3925-3935A
Elongation, Stress effects	
Effect of thermal cycling on the mechanical properties of 350 grade maraging steel.	757-761A
Elongation, Temperature effects	
Enhanced ductility in coarse-grained Al-Mg alloys.	343-352A
Embrittlement, Microstructural effects	
The embrittlement and de-embrittlement of grain boundaries in an $Fe-Mn-Ni$ alloy due to grain boundary segregation of manganese.	1015-1020A
End uses	
Materials and society: Impacts and responsibilities.	1413-1426A
Energy conservation	
Application of centrifugal fields in fused salt electrowinning with a view to reducing electrolytic energy consumption.	889-894B
Energy consumption	
The transported entropy of Na^+ in solid state cryolite.	788-793B
Energy consumption, Field effects	
Application of centrifugal fields in fused salt electrowinning with a view to reducing electrolytic energy consumption.	889-894B
Engine components	
Phase relations of a silicide/silica reaction couple at 2273K.	271-276B
Materials and society—Impacts and responsibilities.	337-350B
Engine components, Materials selection	
Wear behavior of aluminum-based metal matrix composites reinforced with a preform of aluminosilicate fiber.	2385-2389A
Prediction of creep-rupture life of unidirectional titanium matrix composites subjected to transverse loading.	3074-3080A
Engines, Materials selection	
Prediction of creep-rupture life of unidirectional titanium matrix composites subjected to transverse loading.	3074-3080A
Enthalpy	
Critical evaluation and optimization of the thermodynamic properties of liquid tin solutions.	808-826B
Generalized enthalpy method for multicomponent phase change.	869-879B
Thermodynamic properties of complex oxides in the $Sm-Ba-Cu-O$ system.	973-978B
Internal friction in hydrogen-charged $CrNi$ and $CrNiMn$ austenitic stainless steels.	1815-1821A
Modeling of microsegregation in macrosegregation computations.	2314-2327A
An analysis of the flow stress of a two-phase alloy system, $Ti-6Al-4V$.	3957-3962A
Enthalpy, Composition effects	
Thermodynamic activities and partial enthalpies of mixing in the solid solution of Fe in Ni_3Al .	3569-3575A
Entropy	
The transported entropy of Na^+ in solid state cryolite.	788-793B
Entropy, Composition effects	
Thermodynamic activities and partial enthalpies of mixing in the solid solution of Fe in Ni_3Al .	3569-3575A
Epoxy resins, Composite materials	
Subcritical crack growth at bimaterial interfaces. I. Flexural peel technique.	205-211A
Subcritical crack growth at bimaterial interfaces. III. Shear-enhanced fatigue crack growth resistance at polymer/metal interface.	221-228A
The effect of volume percent and morphology of phases on the damping behavior of epoxy-aluminum composites.	2366-2373A
Equiaxed structure	
Characterization of superplastic deformation behavior of a fine grain 5083 Al alloy sheet.	1889-1898A
The improved microstructures and properties of 7075 alloys produced by a water-cooling centrifugal casting method.	1951-1962A
Lamellar growth of eutectic equiaxed grains.	4205-4210A
Equilibrium	
Critical evaluation and optimization of the thermodynamic properties of liquid tin solutions.	808-826B
Phase equilibria in the metal-sulfur-oxygen system and selective reduction of metal oxides and sulfides. I. The carbothermic reduction and calcination of complex mineral sulfides.	827-838B
Thermodynamics of calcium and oxygen in molten titanium and titanium-aluminum alloy.	967-972B
Inverse melting in binary systems: morphology and microscopy of cataleptic alloys.	979-986B
An isothermal section at 550°C in the Al-rich corner of the $Al-Fe-Mn-Si$ system.	3357-3361A
Eutectic reactions	
Generalized enthalpy method for multicomponent phase change.	869-879B
Eutectics	
Radioscopic visualization of isothermal solidification of eutectic $Ga-In$ alloy.	686-689B
Microstructural aspects of the dissolution and melting of Al_2Cu phase in $Al-Si$ alloys during solution heat treatment.	1785-1798A
Directional solidification of white cast iron.	2328-2337A
Retrograde solubility in semiconductors.	2704-2707A
Transitions between type A flake, type D flake, and coral graphite eutectic structures in cast irons.	2740-2753A
Eutectics, Mechanical properties	
High-temperature behavior of precious metal base composites.	2642-2652A
Eutectics, Structural hardening	
Lamellar growth of eutectic equiaxed grains.	4205-4210A
Eutectoid decomposition, Temperature effects	
Eutectoid decomposition in $Ag-Ga$.	1676-1682A
Eutectoids	
Discussion of "Effects of tensile stress on microstructural change of eutectoid $Zn-Al$ alloy" and authors' reply.	3330-3335A
Evaporation, Cooling effects	
Vacuum evaporation of $KCl-NaCl$ salts. II. Vaporization-rate model and experimental results.	433-443B
Expansion	
Increased ductility in high velocity electromagnetic ring expansion.	1837-1844A
Explosive cladding	
Wear-resistant coatings produced by shock-wave compaction of powders.	2297-2304A
Explosive compacting	
Mechanistic processes influencing shock chemistry in powder mixtures of the $Ti-Si$, $Ti-Al$, and $Ti-B$ systems.	1761-1771A
Extrusion Ingots, Mechanical properties	
The plastic anisotropy of an $Al-Li-Cu-Zr$ alloy extrusion in unidirectional deformation.	3503-3512A
Extrusions, Heat treatment	
A process model for on-line quenching of aluminum extrusions.	501-508B
Extrusions, Mechanical properties	
Effects of alkali-metal impurities on fracture toughness of 2090 $Al-Li-Cu$ extrusions.	3530-3541A
Failure	
Failure characteristics of $6061/Al_2O_3/15_p$ and $2014/Al_2O_3/15_p$ composites as a function of loading rate.	3095-3107A
High-temperature deformation and failure of an orthorhombic titanium aluminide sheet material.	3675-3681A
Faraday effect	
Effect of baking temperature and anode current density on anode carbon consumption.	177-183B
Fast nuclear reactors, Materials selection	
Influence of thermal aging on the intergranular corrosion resistance of types 304LN and 316LN stainless steels.	2881-2887A
Fatigue (materials)	
The effects on fracture toughness of ductile-phase composition and morphology in $Nb-Cr-Ti$ and $Nb-Si$ in situ composites. Crystallographic preferred orientation induced by cyclic rolling contact loading.	3007-3018A
Plastic zones and fatigue-crack closure under plane-strain double slip.	3445-3465A
Fatigue (materials), Environmental effects	
On the transition of fatigue crack growth from stage I to stage II in a corrosive environment.	471-476A
Fatigue (materials), Stress effects	
Evidence of fracture surface interference for cracks loaded in shear detected by phase-shifted speckle interferometry.	3853-3860A
Fatigue failure	
Observation of short fatigue crack-growth process in SiC -fiber-reinforced $Ti-15-3$ alloy composite.	2843-2851A
Conditioning monitoring by microstructural evaluation of cumulative fatigue damage.	3841-3851A

Fatigue life

High-temperature low-cycle fatigue of a gamma titanium aluminide alloy Ti-46Al-2Nb-2Cr.
Copper-bearing high-strength low-alloy steels: the influence of microstructure on the initiation and growth of small fatigue cracks.
Conditioning monitoring by microstructural evaluation of cumulative fatigue damage.

2239-2251A
2540-2556A
3841-3851A

Austenite decomposition during continuous cooling of an HSLA-80 plate steel.

1554-1568A
1569-1584A

Ferrite, Heating effects

Neutron diffraction study of austempered ductile iron.
Bainitic microstructures formed by split isothermal transformation in an Fe-C-Si-Mn-Mo steel.

923-928A
1141-1147A

Fatigue life, Coating effects

Isothermal fatigue of an aluminide-coated single-crystal superalloy. I.

353-361A

Ferrite, Temperature effects

Phase stability and atom probe field ion microscopy of type 308 CRE stainless steel weld metal.
The formation mechanism(s), morphology, and crystallography of ferrite sideplates.

763-774A
1517-1532A

Fatigue life, Environmental effects

The influence of aqueous environments on low ΔK and high ΔK fatigue crack propagation behavior in low carbon structural steels.

2678-2685A

Ferritic stainless steels, Corrosion

Retardation of intermetallic phase formation in experimental superferitic stainless steels.

2436-2444A

Fatigue life, Heating effects

Corrosion fatigue in nitrocarburized quenched and tempered steels.

1333-1346A

Ferritic stainless steels, Mechanical properties

Effects of nitrogen implantation on low cycle fatigue behavior of ferritic Fe-24Cr-4Al stainless alloy.

2663-2672A

Fatigue life, Microstructural effects

The normalized Coffin-Manson plot in terms of a new damage function based on grain boundary cavitation under creep-fatigue condition.

1273-1281A

Ferritic stainless steels, Rolling

Experimental investigation of the transformation texture in hot-rolled ferritic stainless steel using single orientation determination.

49-57A

Fatigue life, Stress effects

Mechanisms of high-temperature fatigue failure in alloy 800H.
Prediction of fatigue crack formation in 304 stainless steel.

851-861A
1267-1271A

Ferromanganese

Reaction equilibria in the production of manganese ferroalloys.

5-17B

Fatigue life, Temperature effects

Isothermal fatigue of an aluminide-coated single-crystal superalloy. II. Effects of brittle precracking.

363-369A

Ferrous alloys

Recrystallization in oxide-dispersion strengthened mechanically alloyed sheet steel.

1963-1978A

Fatigue limit, Heating effects

High cycle fatigue behavior of gas-carburized medium carbon Cr-Mo steel.

2557-2564A

Ferrous alloys, Atomic properties

Thermodynamics and long-range order of nitrogen in γ -Fe₃N.
Effects of low-temperature aging on the microstructure and soft magnetic properties of rapidly quenched Fe-Si-B alloys.

1055-1061A
2454-2460A

Fatigue strength

Copper-bearing high-strength low-alloy steels: the influence of microstructure on the initiation and growth of small fatigue cracks.

2540-2556A

Ferrous alloys, Coatings

Microstructural analysis and oxidation behavior of laser-processed Fe-Cr-Al-V alloy coatings.

381-390A

Observation of short fatigue crack-growth process in SiC-fiber-reinforced Ti-15-3 alloy composite.

2843-2851A

Ferrous alloys, Composite materials

Kinetics of cyclic oxidation and cracking and finite element analysis of MA956 and sapphire/MA956 composite system.

3279-3291A

Fatigue strength, Alloying effects

Effect of strontium modification on near-threshold fatigue crack growth in an Al-Si-Cu die cast alloy.

1293-1302A

Ferrous alloys, Corrosion

Internal sulfide precipitation in low Cr-Fe alloys.

3192-3202A

Fatigue strength, Composition effects

Effect of manganese dispersoid on the fatigue crack propagation of Al-Zn-Mg alloys.

490-493A

Ferrous alloys, Crystal growth

Recrystallization in oxide-dispersion strengthened mechanically alloyed sheet steel.
The effect of metallic elements on the crystallization behavior of amorphous Fe-Si-B alloys.

1963-1978A
3424-3430A

Fatigue strength, Heating effects

High cycle fatigue behavior of gas-carburized medium carbon Cr-Mo steel.

2557-2564A

Ferrous alloys, Diffusion

Average effective interdiffusion coefficients and the Matano plane composition.
Incipient chemical instabilities of nanophase Fe-Cu alloys prepared by mechanical alloying.

2504-2509A
2934-2946A

Fatigue strength, Microstructural effects

Fracture characteristics, microstructure, and tissue reaction of Ti-5Al-2.5Fe for orthopedic surgery.

3925-3935A

Ferrous alloys, Heat treatment

Mössbauer spectroscopy study of the aging and tempering of high nitrogen quenched Fe-N alloys: kinetics of formation of Fe₁₈N₂ nitride by interstitial ordering in martensite.

2160-2177A

Fatigue strength, Stress effects

Subcritical crack growth at bimaterial interfaces. III. Shear-enhanced fatigue crack growth resistance at polymer/metal interface.

221-228A

Ferrous alloys, Magnetic properties

Development of a magnetoelastic resonant sensor using iron-rich, nonzero magnetostrictive amorphous alloys.

3203-3213A

Temperature dependence of the intrinsic small fatigue crack growth behavior in nickel-base superalloys based on measurement of crack closure.

1021-1031A
1267-1271A

Ferrous alloys, Mechanical properties

Structural characterization of martensitic iron-carbon alloy films electrodeposited from an iron(II) sulfate solution.
Effect of carbide precipitation on the creep behavior of alloy 800HT in the temperature range 700-900°C.

483-486A

Prediction of fatigue crack formation in 304 stainless steel.

3162-3169A

Mechanism of high-temperature fatigue failure in alloy 800H.
The embrittlement and de-embrittlement of grain boundaries in an Fe-Mn-Ni alloy due to grain boundary segregation of manganese.

747-756A
851-861A

Fatigue strength, Welding effects

Effect of postweld treatment on the fatigue crack growth rate of electron-beam-welded AISI 4130 steel.

2057-2061A

Ferrous alloys, Heat treatment

Effect of thermomechanical treatments on the room-temperature mechanical behavior of iron aluminide Fe₃Al.
Nonequilibrium grain-boundary segregation and ductile-brittle transition in Fe-Mn-Ni-Ti age-hardening alloy.

1015-1020A
2985-2993A

Effect of postweld treatment on the fatigue crack growth rate of electron-beam-welded AISI 4130 steel.

3162-3169A

Effects of the alumina scale on the room-temperature tensile behavior of preoxidized MA 956.

3059-3065A
3809-3816A

FCC metals, Metallurgy

An optical method for determining the surface orientation of crystals.

115-118B

Ferrous alloys, Microstructure

The role of grain corners in nucleation.
Crystallization of amorphous alloys.

480-483A
549-555A

The design of feed systems for thin-walled zinc high-pressure die castings.

281-290A

Ferrous alloys, Phase transformations

A study on morphology and plate mean dimensions in Fe-Ni and Fe-Ni-Cr alloys.

973-980A

Ferrite

The effects of microstructure, strength level, and crack propagation mode on stress corrosion cracking behavior of 4135 steel.

1979-1989A

Ferrous alloys, Phases (state of matter)

Nucleation controlled solidification kinetics.

533-547A

Effect of holding time in the $(\alpha+\gamma)$ temperature range on toughness of specially austempered ductile iron.

2151-2159A
2209-2220A

Microstructure and phase identification in type 304 stainless steel-zirconium alloys.

480-483A

Modeling of ferrite growth in nodular cast iron.

1544-1553A

The role of grain corners in nucleation.

1544-1553A

Ferrite nucleation and growth during continuous cooling.

An evaluation of the Fe-N phase diagram considering long-range order of nitrogen atoms in γ -Fe _{1-x} N _x and ϵ -Fe ₂ N _{1-x} . The formation mechanism(s), morphology, and crystallography of ferrite sideplates.	1063-1071A	Filaments, Mechanical properties	Van der Waals approximation for potassium bubbles in tungsten.	987-992B
Formation of bainite in ferrous and nonferrous alloys through sympathetic nucleation and ledgewise growth mechanism.	1517-1532A	Finite element method	Thermomechanics of the cooling stage in casting processes: three-dimensional finite element analysis and experimental validation.	81-99B
Ferrous alloys, Powder technology	1533-1543A		Heat-flow-based analysis of surface crack formation during the start-up of the direct chill casting process. II. Experimental study of an AA5182 rolling ingot.	129-137B
Effects of nickel on the sintering behavior of Fe-Ni compacts made from composite and elemental powders.	203-211B		Subcritical crack growth at bimaterial interfaces. I. Flexural peel technique.	205-211A
Characterization and mechanical properties of ultrahigh boron steels produced by powder metallurgy.	1861-1867A		A process model for on-line quenching of aluminum extrusions. Flow and thermal behavior of the top surface flux/powder layers in continuous casting molds.	501-508B
Microstructure and tensile properties of compacted, mechanically alloyed, nanocrystalline Fe-Al.	3126-3134A		Prediction of grain structures in various solidification processes.	872-885B
Ferrous alloys, Solubility	57-64B		Effect of multiaxial stresses on creep damage of 316 stainless steel weldments.	895-705A
Solubility of carbon in CaO-Al ₂ O ₃ melts.	71-79B		Modeling of ingot distortions during direct chill casting of aluminum alloys.	891-900A
Ferrous alloys, Steel making			Thermal residual stresses in functionally graded and layered 6061 Al/SiC materials.	3214-3225A
Influence of phosphorus addition on the surface tension of liquid iron and segregation of phosphorus on the surface of Fe-P alloy.			Kinetics of cyclic oxidation and cracking and finite element analysis of MA956 and sapphire/MA956 composite system. Plastic zones and fatigue-crack closure under plane-strain double slip.	3241-3249A
Ferrous alloys, Welding			Thermal expansion of metals reinforced with ceramic particles and microcellular foams.	3279-3291A
Microstructural features of friction welded MA 956 superalloy material.	4019-4028A		Notch fracture in γ -titanium aluminides.	3491-3502A
Fiber composites, Casting			Flow and fracture of bimaterial systems based on aluminum alloys.	3700-3717A
Solidification of binary hypoeutectic alloy matrix composite castings.	595-609A		Measurement of friction under sheet forming conditions.	3903-3912A
Infiltration of fibrous preform by molten aluminum in a centrifugal force field.	4163-4169A		Mathematical modeling of the extrusion of 6061/Al ₂ O ₃ /20p composite.	3937-3947A
Fiber composites, Fabrication				3971-3981A
Liquid state infrared processing of SCS-6/Ti-6Al-4V composites.	527-532B			4095-4111A
An experimental and theoretical investigation of the rapid consolidation of continuously reinforced, metal-matrix composites.	1709-1720A			
Fiber composites, Joining			Flash smelting	
Infrared transient-liquid-phase joining of SCS-6/B21S titanium matrix composite.	4011-4018A		Kinetics of the flash converting of MK (chalocite) concentrate. Experimental study of splash generation in a flash smelting furnace.	163-175B
Fiber composites, Mechanical properties				633-646B
Effective elastic moduli of fiber-matrix interphases in high-temperature composites.	165-182A		Fluid dynamics	
Time-dependent, environmentally assisted crack growth in Niobium-fiber-reinforced SiC composites at elevated temperatures.	839-849A		A water model study of the flow asymmetry inside a continuous slab casting mold.	757-764B
Bridge toughening enhancement in double-notched MoSi ₂ /Nb model composites.	909-921A		Model study of bubble and liquid-flow characteristics in a bottom blown bath under reduced pressure.	765-772B
The Bauschinger effect in a SiC/Al composite.	995-1001A		A one-phase model of the mixing of Al-SiC composite melt.	1015-1023B
Thermal stability of SIC-SCS-6 fiber-reinforced IMI834 alloys. Multiple matrix cracking in a fiber-reinforced titanium matrix composite under high-cycle fatigue.	1403-1405A			
Interface effects on the micromechanical response of a transversely loaded single fiber SCS-6/Ti-6Al-4V composite.	1899-1907A		Flow and thermal behavior of the top surface flux/powder layers in continuous casting molds.	672-685B
The effect of volume percent and morphology of phases on the damping behavior of epoxy-aluminum composites.	2035-2043A		Cold model study of the surface profile in a continuous slab casting mold: effect of second phase.	695-697B
Wear behavior of aluminum-based metal matrix composites reinforced with a preform of aluminosilicate fiber.	2366-2373A		A water model study of the flow asymmetry inside a continuous slab casting mold.	757-764B
Observation of short fatigue crack-growth process in SiC-fiber-reinforced Ti-15-3 alloy composite.	2385-2389A		Model study of bubble and liquid-flow characteristics in a bottom blown bath under reduced pressure.	765-772B
Prediction of creep-rupture life of unidirectional titanium matrix composites subjected to transverse loading.	2843-2851A			
Fracture and fatigue-crack growth behavior in ductile-phase toughened molybdenum disilicide: effects of niobium wire vs. particulate reinforcements.	3074-3080A		Fluidized bed reduction	
Creep deformation and damage in a continuous fiber-reinforced Ti-6Al-4V composite.	3781-3792A		Preoxidation and hydrogen reduction of ilmenite in a fluidized bed reactor.	731-738B
Fiber composites, Oxidation				
Kinetics of cyclic oxidation and cracking and finite element analysis of MA956 and sapphire/MA956 composite system.	3279-3291A		Flux core wire welding	
Fiber composites, Phases (state of matter)			Correlation of microstructure and fracture toughness in high-chromium white iron hardfacing alloys.	3881-3891A
Microstructure of Al ₂ O ₃ fiber-reinforced superalloy (Inconel 718) composites.	451-458A			
Fiber composites, Reactions (chemical)			Fluxes	
Interface characterization of ceramic fiber-reinforced titanium alloy composites manufactured by infrared processing.	1379-1394A		Controversy on the free energy of formation of CaO—additional evidence in support of thermochemical data.	647-651B
Investigation of the reaction zone between TiAl and molybdenum.	2285-2292A			
Structure of phases in the δ -Al ₂ O ₃ fiber studied by convergent beam electron diffraction.	3318-3329A		Fluxes, Physical properties	
Fiber composites, Structural hardening			Thermodynamics of sulfur in the BaO-MnO-SiO ₂ flux system.	652-657B
Effect of magnesium on the aging behavior of Al-Zn-Mg-Cu/Al ₂ O ₃ metal matrix composites.	2005-2012A			
Fiber composites, Synthesis			Foams, Composite materials	
Extending the compositional limit of combustion-synthesized B ₄ C-TiB ₂ composites by field activation.	475-480B		Thermal expansion of metals reinforced with ceramic particles and microcellular foams.	3700-3717A
Fibers, Phases (state of matter)				
Structure of phases in the δ -Al ₂ O ₃ fiber studied by convergent beam electron diffraction.	3318-3329A		Forging	
			An experimental and theoretical investigation of the rapid consolidation of continuously reinforced, metal-matrix composites.	1709-1720A
			Formability	
			Analysis and prevention of vertical cracking phenomena during deep drawing of hot-rolled SG295 steel strips.	1241-1250A
			Increased ductility in high velocity electromagnetic ring expansion.	1837-1844A
			High-temperature deformation processing of Ti-24Al-20Nb.	2593-2604A
			Forming of tailor-welded blanks.	2605-2616A
			Measurement of friction under sheet forming conditions.	3971-3981A
			Formability, Microstructural effects	
			Microstructural evolution and superplastic deformation behavior of fine grain 5083Al.	3827-3839A

Fourier analysis

Analysis of shell thickness irregularity in continuously cast middle carbon steel slabs using mold thermocouple data.
Quantitative characterization of the surface topography of rolled sheets by laser scanning microscopy and Fourier transformation.

Fractography

Loading rate and test temperature effects on fracture of in situ niobium silicide-niobium composites.
Effect of alloying additions on fracture behavior of molybdenum-containing secondary hardening steels.
Shear ligament phenomena in Fe_3Al intermetallics and micro-mechanics of shear ligament toughening.
Correlation of microstructure and fracture toughness in high-chromium white iron hardfacing alloys.
Microstructure and fracture of SiC-particulate-reinforced cast A356 aluminum alloy composites.
Notch fracture in γ -titanium aluminides.
Flow and fracture of bimaterial systems based on aluminum alloys.
Hydrogen-induced cleavage fracture of Fe_3Al -based intermetallics.

Fracture mechanics

Subcritical crack growth at bimaterial interfaces. I. Flexural peel technique.
High Temperature Fracture Mechanisms in Advanced Materials. 825-1136, 8 1/2 in. x 11 in., IllustratedA
Studies on the influence of metallurgical variables on the stress corrosion behavior of AISI 304 stainless steel in sodium chloride solution using the fracture mechanics approach.
Cleavage initiation in the intercritically reheated coarse-grained heat affected zone. II. Failure criteria and statistical effects.
Loading rate and test temperature effects on fracture of in situ niobium silicide-niobium composites.
Effect of alloying additions on fracture behavior of molybdenum-containing secondary hardening steels.
Evidence of fracture surface interference for cracks loaded in shear detected by phase-shifted speckle interferometry.
Correlation of microstructure and fracture toughness in high-chromium white iron hardfacing alloys.

Fracture strength

Failure characteristics of 6061/ $\text{Al}_2\text{O}_3/15$, and 2014/ $\text{Al}_2\text{O}_3/15$, composites as a function of loading rate.
Loading rate and test temperature effects on fracture of in situ niobium silicide-niobium composites.

Fracture strength, Composition effects

A study of the influence of mischmetal additions to Al-7Si-0.3Mg (LM 25/35) alloy.

Fracture strength, Deformation effects

Effect of thermomechanical treatments on the room-temperature mechanical behavior of iron aluminide Fe_3Al .

Fracture strength, Diffusion effects

Nonequilibrium grain-boundary segregation and ductile-brittle-ductile transition in Fe-Mn-Ni-Ti age-hardening alloy.

Fracture strength, Microstructural effects

Mechanical behavior and properties of mechanically alloyed aluminum alloys.
Phase stability and atom probe field ion microscopy of type 308 CRE stainless steel weld metal.
The embrittlement and de-embrittlement of grain boundaries in an Fe-Mn-Ni alloy due to grain boundary segregation of manganese.
Creep deformation of dispersion-strengthened copper.

Fracture strength, Stress effects

Reinforcement stresses during deformation of sphere- and particulate-reinforced aluminum-matrix composites.

Fracture strength, Temperature effects

Observations of secondary carbide precipitation and its relation to high-temperature flow and fracture in HT-9 stainless steel.

Fracture toughness

Microstructure and properties of $\text{Al}_2\text{O}_3\text{-Al}(\text{Si})$ and $\text{Al}_2\text{O}_3\text{-Al}(\text{Si})\text{-Si}$ composites formed by in situ reaction of aluminum with aluminosilicate ceramics.
The fracture toughness of niobium-based, in situ composites.
Loading rate and test temperature effects on fracture of in situ niobium silicide-niobium composites.
The balance of mechanical and environmental properties of a multielement niobium-niobium silicide-based in situ composite.
Notch fracture in γ -titanium aluminides.

Fracture toughness, Alloying effects

Effect of alloying additions on fracture behavior of molybdenum-containing secondary hardening steels.

Fracture toughness, Composition effects

Effect of manganese dispersoid on the fatigue crack propagation of Al-Zn-Mg alloys.

1045-1056B

2338-2346A

3292-3306A

3343-3346A

3817-3825A

3881-3891A

3893-3901A

3903-3912A

3937-3947A

3949-3956A

205-211A

1313-1325A

3019-3029A

3292-3306A

3343-3346A

3853-3860A

3881-3891A

3095-3107A

3292-3306A

1283-1292A

2985-2993A

3059-3065A

737-745A

763-774A

1015-1020A

1217-1227A

486-490A

467-469A

3292-3306A

3801-3808A

3903-3912A

3343-3346A

490-493A

Fracture toughness, Corrosion effects

Shear ligament phenomena in Fe_3Al intermetallics and micro-mechanics of shear ligament toughening.

3817-3825A

Fracture toughness, Heating effects

Microstructural basis for the effect of chromium on the strength and toughness of AF1410-based high performance steels.

2510-2517A

Fracture toughness, Impurity effects

Microsegregation of oxygen in Zr-2.5Nb alloy materials.
Effects of alkali-metal impurities on fracture toughness of 2090 Al-Li-Cu extrusions.

3530-3541A

Fracture toughness, Microstructural effects

Subcritical crack growth at bimaterial interfaces. II. Microstructural effects on fracture resistance of metal/ceramic interfaces.

213-219A

A comparison of fracture behavior of low alloy steel with different sizes of carbide particles.

1909-1917A

Microstructure and mechanical behavior of Cr-Cr₂Hf in situ intermetallic composites.

2583-2592A

The effects on fracture toughness of ductile-phase composition and morphology in Nb-Cr-Ti and Nb-Si in situ composites.

3007-3018A

Fracture and fatigue-crack growth behavior in ductile-phase toughened molybdenum disilicide: effects of niobium wire vs. particulate reinforcements.

3781-3792A

Correlation of microstructure and fracture toughness in high-chromium white iron hardfacing alloys.

3881-3891A

Microstructure and fracture of SiC-particulate-reinforced cast A356 aluminum alloy composites.

3893-3901A

Fracture characteristics, microstructure, and tissue reaction of Ti-5Al-2.5Fe for orthopedic surgery.

3925-3935A

Fracture toughness, Radiation effects

The effect of high-energy electron-beam irradiation on microstructural modification of a high-speed steel roll.

3149-3161A

Fracture toughness, Stress effects

Detecting stable crack onset at ductile-brittle transition in steels.

469-471A

Fracture toughness, Welding effects

Microstructures relevant to brittle fracture initiation at the heat-affected zone of weldment of a low carbon steel.

2574-2582A

Fracturing

High-temperature low-cycle fatigue of a gamma titanium aluminide alloy Ti-46Al-2Nb-2Cr.

2239-2251A

The influence of stress triaxiality on the damage mechanisms in an equiaxed α/β Ti-6Al-4V alloy.

3043-3058A

Microstructure and tensile properties of compacted, mechanically alloyed, nanocrystalline Fe-Al.

3126-3134A

Fracturing, Microstructural effects

Reinforcement shape effects on the fracture behavior and ductility of particulate-reinforced 6061-Al matrix composites.

3739-3746A

Free energy

Controversy on the free energy of formation of CaO—additional evidence in support of thermochemical data.

647-651B

Use of solid-electrolyte galvanic cells to determine the activity of CaO in the CaO-ZrO₂ system and the standard Gibbs free energies of formation of CaZrO₃ from CaO and ZrO₂.

658-662B

Discussion of "Representation of mixed reactive gases on free energy (Ellingham-Richardson) diagrams" and reply.

693-694B

Critical evaluation and optimization of the thermodynamic properties of liquid tin solutions.

808-826B

Phase equilibria in the metal-sulfur-oxygen system and selective reduction of metal oxides and sulfides. I. The carbothermic reduction and calcination of complex mineral sulfides.

827-838B

Thermodynamics of phosphorus in molten silicon.

937-941B

A thermodynamic evaluation of the Ti-Mo-C system.

955-968B

Thermodynamic properties of complex oxides in the Sm-Ba-Cu-O system.

967-972B

Gibbs energies of formation of chromium carbides.

1919-1924A

Formation of structural intermetallics by reactive metal penetration of titanium and nickel oxides and aluminates.

2100-2104A

Free energy, Temperature effects

Representation of mixed reactive gases on free energy (Ellingham-Richardson) diagrams.

85-89B

Freezing

An adaptive mesh refinement scheme for solidification problems.

707-717A

Fractility

Fractility and crushing strength of micrometer-size diamond abrasives used in microgrinding of optical glass.

1047-1053A

Friction

Measurement of friction under sheet forming conditions.

3971-3981A

Friction welding

Microstructural features of friction welded MA 956 superalloy material.

4019-4029A

Frictional wear

Frictional wear

High-temperature wear and deformation processes in metal matrix composites.
 Ni_3Al intermetallic particles as wear-resistant reinforcement for Al-base composites processed by powder metallurgy.
 Characterization of the wear response of a modified zinc-based alloy vis-à-vis a conventional zinc-based alloy and a bearing bronze at a high sliding speed.
 The wear behavior of hardfacing materials.
 Wear and friction behavior of metal impregnated microporous carbon composites.

Functionally gradient materials, Mechanical properties

Thermal residual stresses in functionally graded and layered 6061 Al/SiC materials.
 Analysis of thermal residual stress in a thick-walled ring of Dur-alcan-base Al-SiC functionally graded material.

Functionally gradient materials, Structural hardening

Theoretical analysis of the particle gradient distribution in centrifugal field during solidification.

Fused salt electrolysis

Application of centrifugal fields in fused salt electrowinning with a view to reducing electrolytic energy consumption.

Gadolinium, Binary systems

Inverse melting in binary systems: morphology and microscopy of catactic alloys.

Gallium base alloys, Melting

Radioscopic visualization of isothermal solidification of eutectic Ga-In alloy.

Galvanized steels

Modeling iron enrichment in hot-dip galvanneal coatings on interstitial-free steels.

Galvanized steels, Surface properties

Measurement of friction under sheet forming conditions.

Galvanizing

Discussion of "The effect of steel chemistry on the formation of Fe-Zn intermetallic compounds of galvanneal-coated steel sheets" and authors' reply.

Kinetics of phase evolution of Zn-Fe intermetallics.

Gas metal arc welding

Dilution in single pass arc welds.
 Solidification of an alloy 625 weld overlay.

Gas phases

Reaction equilibria in the production of manganese ferroalloys.

Gas phases, Cooling effects

Vacuum evaporation of $\text{KCl}-\text{NaCl}$ salts. II. Vaporization-rate model and experimental results.

Gas phases, Temperature effects

A study of the thermal decomposition of BaCO_3 .

Gas pipelines, Corrosion

Initiation of stress corrosion cracking for pipeline steels in a carbonate-bicarbonate solution.

Gas tungsten arc welding

Analysis of heat affected zone phase transformations using in situ spatially resolved x-ray diffraction with synchrotron radiation.

Gas turbine engines, Materials selection

Microstructural stability on aging of an $\alpha+\beta$ titanium alloy: Ti-6Al-1.6Zr-3.3Mo-0.30Si.

The fracture toughness of niobium-based, in situ composites.

Gases

Experimental study of splash generation in a flash smelting furnace.
 Discussion of "Representation of mixed reactive gases on free energy (Ellingham-Richardson) diagrams" and reply.

A unified representation of the two-phase plume characteristics in gas-stirred ladle systems.

Germanium, Binary systems

Effect of shear flow and anisotropic kinetics on the morphological stability of a binary alloy.

Germanium, Extraction

The mineralogical deportment of germanium in the Clarksville electrolytic zinc plant of Savage Zinc Inc.

Glow discharges

Simultaneous plasma treatment for carburizing and carbonitriding using hollow cathode discharge.

Gold, Binary systems

Inverse melting in binary systems: morphology and microscopy of catactic alloys.

Gold, Extraction

Electrochemical behavior of the dissolution of gold-silver alloys in cyanide solutions.

Gold, Recovering

Influence of gold content on copper oxidation from silver-gold-copper alloys.

3187-3191A

Gold, Ternary systems

Thermodynamic investigations of the ternary Au-Sn-Zn system.

921-927B

Grain boundaries

Modeling texture change during the static recrystallization of interstitial free steels.

155-164A

The effects of microstructure, strength level, and crack propagation mode on stress corrosion cracking behavior of 4135 steel.

281-290A

Structure, chemistry, and stress corrosion cracking of grain boundaries in alloys 600 and 690.

327-341A

Theoretical modeling of densification during activated solid-state sintering.

441-450A

Effect of iron on ductility and cavitation in the superplastic $\text{Al}-22\%$ Al eutectoid.

863-872A

The embrittlement and de-embrittlement of grain boundaries in an Fe-Mn-Ni alloy due to grain boundary segregation of manganese.

1015-1020A

Crystallography of grain boundary α precipitates in a β titanium alloy.

1630-1641A

An investigation by interactive electron backscatter pattern analysis of processing and superplasticity in an aluminum-magnesium alloy.

2252-2262A

Orientation selective recrystallization of nonoriented electrical steels.

2347-2358A

Grain boundaries, Diffusion

Analysis of mean square penetration depth in grain boundary diffusion.

3473-3477A

Grain boundaries, Heating effects

Evolution of microstructures in the nickel modified titanium tri-aluminides near the L_12 phase field.

5-17A

Surface morphology and compound layer pores of plasma nitrocarburized low carbon steel.

135-143A

Effect of homogenization heat treatment on the microstructure and heat affected zone microflourishing in welded cast alloy 718.

785-790A

Characterization of constitutional liquid film migration in nickel-base alloy 718.

2692-2703A

Grain boundaries, Radiation effects

A model describing neutron irradiation-induced segregation to grain boundaries in dilute alloys.

3381-3390A

Grain boundaries, Stress effects

Temperature and strain-rate effects on low-cycle fatigue behavior of alloy 800H.

255-267A

Grain boundaries, Temperature effects

The formation mechanism(s), morphology, and crystallography of ferrite sideplates.

1517-1532A

Grain boundary migration

Characterization of constitutional liquid film migration in nickel-base alloy 718.

2692-2703A

Grain boundary sliding

The inter-relationship between grain boundary sliding and cavitation during creep of polycrystalline copper.

901-907A

Grain growth

Microstructure of Al_2O_3 fiber-reinforced superalloy (Inconel 718) composites.

451-458A

High-speed imaging and analysis of the solidification of under-cooled nickel melts.

863-868B

Generalized enthalpy method for multicomponent phase change.

869-879B

The normalized Coffin-Manson plot in terms of a new damage function based on grain boundary cavitation under creep-fatigue condition.

1273-1281A

Characterization of superplastic deformation behavior of a fine grain 5083 Al alloy sheet.

1889-1898A

Austenite grain growth kinetics in Al-killed plain carbon steels.

3399-3409A

Lamellar growth of eutectic equiaxed grains.

4205-4210A

Grain growth, Alloying effects

Effects of nickel on the sintering behavior of Fe-Ni compacts made from composite and elemental powders.

203-211B

Grain growth, Coating effects

Microstructural analysis and oxidation behavior of laser-processed Fe-Cr-Al-Y alloy coatings.

381-390A

Grain growth, Cooling effects

Prediction of grain structures in various solidification processes.

695-705A

Grain growth, Deformation effects

Microstructural evolution and superplastic deformation behavior of fine grain 5083Al.

3827-3839A

Grain growth, Heating effects

Effect of primary grain size on the secondary recrystallization of mechanically alloyed oxide dispersion strengthened nickel-based superalloy.
The control of grain size and distribution of particles in a (6061 alloy)_m(Al₂O₃)_p composite by solutionizing treatment.

493-496A
2023-2034A

Grain orientation

An investigation by interactive electron backscatter pattern analysis of processing and superplasticity in an aluminum-magnesium alloy.

Grain refinement

The improved microstructures and properties of 7075 alloys produced by a water-cooling centrifugal casting method.
Effect of grain refinement on the fluidity of two commercial Al-Si foundry alloys.

Grain refinement, Impurity effects

Influence of chromium and impurities on the grain refining behavior of aluminum.

Grain size

The effects of microstructure, strength level, and crack propagation mode on stress corrosion cracking behavior of 4135 steel.
Theoretical modeling of densification during activated solid-state sintering.
Microstructure of Al₂O₃ fiber-reinforced superalloy (Inconel 718) composites.
Mechanical behavior and properties of mechanically alloyed aluminum alloys.
Effect of iron on ductility and cavitation in the superplastic Al-22% Al eutectoid.
Creep deformation of dispersion-strengthened copper.
The improved microstructures and properties of 7075 alloys produced by a water-cooling centrifugal casting method.
Effect of grain refinement on the fluidity of two commercial Al-Si foundry alloys.
Microstructure and tensile properties of compacted, mechanically alloyed, nanocrystalline Fe-Al.
Influence of titanium and carbon contents on the hydrogen trapping of microalloyed steels.
Microstructure of Cu-Co alloys solidified at various supercoolings.
Modeling recrystallization kinetics, grain sizes, and textures during multipass hot rolling.

Grain size, Alloying effects

Solid-state contributions to densification during liquid-phase sintering.

2252-2262A

Grain size, Cooling effects

Ferrite nucleation and growth during continuous cooling.
Austenite decomposition during continuous cooling of an HSLA-80 plate steel.
Macrotransport-solidification kinetics modeling of equiaxed dendritic growth. II. Computation problems and validation on Inconel 718 superalloy casting.

1951-1962A
2305-2313A
791-800A

Grain size, Deformation effects

Flow stress and microstructural evolution during hot working of alloy 22Cr-13Ni-5Mn-0.3N austenitic stainless steel.
Analysis on the amplitude of serrated flow associated with the Portevin-LeChatelier effect of substitutional fcc alloys.
Effects of alloy modification and thermomechanical processing on recrystallization of Al-Mg-Mn alloys.
Microstructural evolution and superplastic deformation behavior of fine grain 5083Al.

1401-4029A
4031-4038A

Grain size, Field effects

Characterization of titanium thin films prepared by bias assisted magnetron sputtering.

1057-1060B

Grain size, Heating effects

Effect of primary grain size on the secondary recrystallization of mechanically alloyed oxide dispersion strengthened nickel-based superalloy.
Analysis of heat affected zone phase transformations using in situ spatially resolved x-ray diffraction with synchrotron radiation.
The control of grain size and distribution of particles in a (6061 alloy)_m(Al₂O₃)_p composite by solutionizing treatment.
An analysis of static recrystallization during continuous, rapid heat treatment.

4031-4038A

Grain size, Impurity effects

Microsegregation of oxygen in Zr-2.5Nb alloy materials.
Influence of chromium and impurities on the grain refining behavior of aluminum.

2252-2262A
1951-1962A
2305-2313A
791-800A

Grain size, Vibration effects

Effects of forced electromagnetic vibrations during the solidification of aluminum alloys. II. Solidification in the presence of colinear variable and stationary magnetic fields.

1401-4029A
213-219A
327-341A
731-736A

Grain structure

Mechanical behavior of the in situ composite alloys in the Al-Ni-Ti system near the L₁ phase field.
Subcritical crack growth at bimaterial interfaces. II. Microstructural effects on fracture resistance of metal/ceramic interfaces.
Structure, chemistry, and stress corrosion cracking of grain boundaries in alloys 600 and 690.
A study of typical yields of metals.
On the influence of grain morphology on creep deformation and damage mechanism in directionally solidified and oxide dispersion strengthened superalloys.
The normalized Coffin-Manson plot in terms of a new damage function based on grain boundary cavitation under creep-fatigue condition.
On microsuperplasticity in AA7475 domes.
The mechanism of formation of a fine duplex microstructure in Ti-48Al-2Mn-2Nb alloys.
Modeling recrystallization kinetics, grain sizes, and textures during multipass hot rolling.

1273-1281A
1400-1403A
1655-1667A
4133-4144A

Grain structure, Alloying effects

The effect of iron and manganese on the recrystallization behavior of hot-rolled and solution-heat-treated aluminum alloy 6013.

281-290A

Grain structure, Coating effects

Microstructural analysis and oxidation behavior of laser-processed Fe-Cr-Al-Y alloy coatings.

441-450A

Grain structure, Cooling effects

The role of grain corners in nucleation.
Prediction of grain structures in various solidification processes.

451-458A

Grain structure, Deformation effects

Experimental investigation of the transformation texture in hot-rolled ferritic stainless steel using single orientation determination.

737-745A

Grain structure, Field effects

Precipitation behavior in a medium carbon, Ti-V-N microalloyed steel.

1217-1227A

Grain structure, Heating effects

Flow stress and microstructural evolution during hot working of alloy 22Cr-13Ni-5Mn-0.3N austenitic stainless steel.

1951-1962A

Grain structure, Impurity effects

Flow stress and microstructural evolution during hot working of alloy 22Cr-13Ni-5Mn-0.3N austenitic stainless steel.

2305-2313A

Grain structure, Stress effects

Effects of forced electromagnetic vibrations during the solidification of aluminum alloys. I. Solidification in the presence of crossed alternating electric fields and stationary magnetic fields.

3126-3134A

Grain structure, Temperature effects

Effects of forced electromagnetic vibrations during the solidification of aluminum alloys. II. Solidification in the presence of colinear variable and stationary magnetic fields.

3773-3780A

Graphite, Composite materials

Crystallization of amorphous alloys.
Some consequences of thermosolutal convection: the grain structure of castings.

4049-4059A

Graphitic structure, Cooling effects

Transient thermal analysis of solidification in a centrifugal casting for composite materials containing particle segregation.

4133-4144A

Graphitic structure, Heating effects

Transitions between type A flake, type D flake, and coral graphite eutectic structures in cast irons.

19-27A

Graphitic structure, Vibration effects

Effects of forced electromagnetic vibrations during the solidification of aluminum alloys. III. Solidification in the presence of colinear variable and stationary magnetic fields.

457-464B

Graphitic structure, Cooling effects

Transitions between type A flake, type D flake, and coral graphite eutectic structures in cast irons.

951-960A

Graphitic structure, Heating effects

Transitions between type A flake, type D flake, and coral graphite eutectic structures in cast irons.

1081-1094A

Graphitic structure, Stress effects

Transitions between type A flake, type D flake, and coral graphite eutectic structures in cast irons.

3170-3180A

Graphitic structure, Deformation effects

Aspects of dynamic recrystallization in shaped charge and explosively formed projectile devices.

19-27A

Graphitic structure, Field effects

Effects of forced electromagnetic vibrations during the solidification of aluminum alloys. IV. Solidification in the presence of crossed alternating electric fields and stationary magnetic fields.

445-455B

Graphitic structure, Temperature effects

Effects of superheat on the solidification structures of AISI 310S austenitic stainless steel.

287-296B

Graphitic structure, Impurity effects

Microsegregation of oxygen in Zr-2.5Nb alloy materials.

431-440A

Graphitic structure, Stress effects

Effect of carbide precipitation on the creep behavior of alloy 800HT in the temperature range 700-900°C.

49-57A

Graphitic structure, Field effects

Creep deformation and crack growth behavior of a single-crystal nickel-base superalloy.

1149-1165A

Graphitic structure, Temperature effects

Effect of multiaxial stresses on creep damage of 316 stainless steel weldments.

1251-1266A

Graphitic structure, Deformation effects

Aspects of dynamic recrystallization in shaped charge and explosively formed projectile devices.

1773-1778A

Graphitic structure, Field effects

Effects of forced electromagnetic vibrations during the solidification of aluminum alloys. V. Solidification in the presence of crossed alternating electric fields and stationary magnetic fields.

480-483A

Graphitic structure, Stress effects

The squeeze casting of hypoeutectic binary Al-Cu.

695-705A

Graphitic structure, Field effects

The role of grain corners in nucleation.

4121-4132A

Graphitic structure, Temperature effects

Prediction of grain structures in various solidification processes.

695-705A

Graphitic structure, Deformation effects

The squeeze casting of hypoeutectic binary Al-Cu.

4121-4132A

Graphitic structure, Field effects

The influence of niobium supersaturation in austenite on the static recrystallization behavior of low carbon microalloyed steels.

951-960A

Graphitic structure, Stress effects

The breakdown of single-crystal solidification in high refractory nickel-base alloys.

1081-1094A

Graphitic structure, Field effects

Elevated temperature compressive properties of N-doped NIAI.

3170-3180A

Graphitic structure, Temperature effects

The squeeze casting of hypoeutectic binary Al-Cu.

480-483A

Graphitic structure, Deformation effects

The breakdown of single-crystal solidification in high refractory nickel-base alloys.

695-705A

Graphitic structure, Field effects

The influence of niobium supersaturation in austenite on the static recrystallization behavior of low carbon microalloyed steels.

1149-1165A

Graphitic structure, Stress effects

The squeeze casting of hypoeutectic binary Al-Cu.

1251-1266A

Graphitic structure, Field effects

The influence of niobium supersaturation in austenite on the static recrystallization behavior of low carbon microalloyed steels.

1773-1778A

Graphitic structure, Temperature effects

The squeeze casting of hypoeutectic binary Al-Cu.

445-455B

Graphitic structure, Deformation effects

The squeeze casting of hypoeutectic binary Al-Cu.

287-296B

Graphitic structure, Field effects

The influence of niobium supersaturation in austenite on the static recrystallization behavior of low carbon microalloyed steels.

431-440A

Graphitic structure, Stress effects

The squeeze casting of hypoeutectic binary Al-Cu.

431-440A

Graphitic structure, Field effects

The influence of niobium supersaturation in austenite on the static recrystallization behavior of low carbon microalloyed steels.

431-440A

Graphitic structure, Temperature effects

The squeeze casting of hypoeutectic binary Al-Cu.

431-440A

Graphitic structure, Deformation effects

The squeeze casting of hypoeutectic binary Al-Cu.

431-440A

Graphitic structure, Field effects

The influence of niobium supersaturation in austenite on the static recrystallization behavior of low carbon microalloyed steels.

431-440A

Graphitic structure, Stress effects

The squeeze casting of hypoeutectic binary Al-Cu.

431-440A

Graphitic structure, Field effects

The influence of niobium supersaturation in austenite on the static recrystallization behavior of low carbon microalloyed steels.

431-440A

Graphitic structure, Temperature effects

The squeeze casting of hypoeutectic binary Al-Cu.

431-440A

Graphitic structure, Deformation effects

The squeeze casting of hypoeutectic binary Al-Cu.

431-440A

Graphitic structure, Field effects

The influence of niobium supersaturation in austenite on the static recrystallization behavior of low carbon microalloyed steels.

431-440A

Graphitic structure, Stress effects

The squeeze casting of hypoeutectic binary Al-Cu.

431-440A

Graphitic structure, Field effects

The influence of niobium supersaturation in austenite on the static recrystallization behavior of low carbon microalloyed steels.

431-440A

Graphitic structure, Temperature effects

The squeeze casting of hypoeutectic binary Al-Cu.

431-440A

Graphitic structure, Deformation effects

The squeeze casting of hypoeutectic binary Al-Cu.

431-440A

Graphitic structure, Field effects

The influence of niobium supersaturation in austenite on the static recrystallization behavior of low carbon microalloyed steels.

431-440A

Graphitic structure, Stress effects

The squeeze casting of hypoeutectic binary Al-Cu.

431-440A

Graphitic structure, Field effects

The influence of niobium supersaturation in austenite on the static recrystallization behavior of low carbon microalloyed steels.

431-440A

Graphitic structure, Temperature effects

The squeeze casting of hypoeutectic binary Al-Cu.

431-440A

Graphitic structure, Deformation effects

The squeeze casting of hypoeutectic binary Al-Cu.

431-440A

Graphitic structure, Field effects

The influence of niobium supersaturation in austenite on the static recrystallization behavior of low carbon microalloyed steels.

431-440A

Graphitic structure, Stress effects

The squeeze casting of hypoeutectic binary Al-Cu.

431-440A

Graphitic structure, Field effects

The influence of niobium supersaturation in austenite on the static recrystallization behavior of low carbon microalloyed steels.

431-440A

Graphitic structure, Temperature effects

The squeeze casting of hypoeutectic binary Al-Cu.

431-440A

Graphitic structure, Deformation effects

The squeeze casting of hypoeutectic binary Al-Cu.

431-440A

Graphitic structure, Field effects

The influence of niobium supersaturation in austenite on the static recrystallization behavior of low carbon microalloyed steels.

431-440A

Graphitic structure, Stress effects

The squeeze casting of hypoeutectic binary Al-Cu.

431-440A

Graphitic structure, Field effects

The influence of niobium supersaturation in austenite on the static recrystallization behavior of low carbon microalloyed steels.

431-440A

Graphitic structure, Temperature effects

The squeeze casting of hypoeutectic binary Al-Cu.

431-440A

Graphitic structure, Deformation effects

The squeeze casting of hypoeutectic binary Al-Cu.

431-440A

Graphitic structure, Field effects

The influence of niobium supersaturation in austenite

Graphitic structure, Heating effects		
Effect of bainite transformation and retained austenite on mechanical properties of austempered spheroidal graphite cast steel.	1585-1594A	775-783A
Gravitation		
On the reaction between Fe-Ti and Fe-C liquids under microgravity.	407-414A	785-790A
Gray iron, Casting		
Hydrogen effects on directional solidification of tellurium-doped cast irons.	496-498A	891-900A
Grinding		
Friability and crushing strength of micrometer-size diamond abrasives used in microgrinding of optical glass.	1047-1053A	2574-2582A
Grinding mills		
Milling dynamics. II. Dynamics of a SPEX mill and a one-dimensional mill.	1991-1997A	3019-3029A
Milling dynamics. III. Integration of local and global modeling of mechanical alloying devices.	1999-2004A	4031-4038A
Growth rate		
Orientational dependence of primary dendrite spacing.	2727-2739A	3267-3278A
Abnormal growth of faceted (WC) grains in a (Co) liquid matrix.	2809-2819A	
M_2C precipitates in isothermal tempering of high Co-Ni secondary hardening steel.	3466-3472A	417-422B
Modeling of primary and secondary dendrites in a Cu-6 wt.% tin alloy.	4085-4093A	647-651B
Guinier Preston zone		
Low quench sensitivity of superplastic 8090 Al-Li thin sheets.	2923-2933A	658-662B
Alloy phase analysis from measurements of bulk magnetic properties.	2958-2965A	1919-1924A
Guinier Preston zone, Alloying effects		
Effect of magnesium on the aging behavior of Al-Zn-Mg-Cu/ Al_2O_3 metal matrix composites.	2005-2012A	2100-2104A
Hafnium, Binary systems		
Thermochemistry of the Ni-Hf system—intermetallic phases.	3576-3590A	2100-2104A
Hall effect		
Physical modeling studies of electrolyte flow due to gas evolution and some aspects of bubble behavior in advanced Hall cells. III. Predicting the performance of advanced Hall cells.	19-27B	701-704B
Hall Heroult process		
Physical modeling studies of electrolyte flow due to gas evolution and some aspects of bubble behavior in advanced Hall cells. III. Predicting the performance of advanced Hall cells.	19-27B	81-99B
Effect of baking temperature and anode current density on anode carbon consumption.	177-183B	221-230B
Studies on the corrosion and the behavior of inert anodes in aluminum electrolysis.	185-193B	663-671B
Hard surfacing		
Correlation of microstructure and fracture toughness in high-chromium white iron hardfacing alloys.	3881-3891A	672-685B
Hardening, Composition effects		
Mechanical properties of Ru-Ni-Al alloys.	1395-1400A	869-879B
Hardness		
Microstructure and properties of Al_2O_3 -Al(Si) and Al_2O_3 -Al(Si)-Si composites formed by in situ reaction of aluminum with aluminosilicate ceramics.	2122-2129A	119-127B
Investigation of the reaction zone between TiAl and molybdenum.	2285-2292A	
Microstructure and tensile properties of compacted, mechanically alloyed, nanocrystalline Fe-Al.	3126-3134A	
Analysis of the stress-strain curves of a modified 9Cr-1Mo steel by the Voce equation.	3340-3343A	
Hardness, Alloying effects		
Effect of alloying additions on fracture behavior of molybdenum-containing secondary hardening steels.	3343-3348A	480-483A
Hardness, Composition effects		
Mechanical properties of Ru-Ni-Al alloys.	1395-1400A	1167-1173A
Hardness, Heating effects		
Low quench sensitivity of superplastic 8090 Al-Li thin sheets.	2923-2933A	1595-1605A
M_2C precipitates in isothermal tempering of high Co-Ni secondary hardening steel.	3466-3472A	
Hardness, Microstructural effects		
The cracking mechanism of silicon particles in an A357 aluminum alloy.	3558-3568A	533-547A
An evaluation of the creep properties of two Al-Si alloys produced by rapid solidification processing.	3871-3879A	635-656A
Correlation of microstructure and fracture toughness in high-chromium white iron hardfacing alloys.	3881-3891A	
Influence of matrix structure on the abrasion wear resistance and toughness of a hot isostatic pressed white iron matrix composites.	4183-4191A	2510-2517A
Heat affected zone		
Analysis of heat affected zone phase transformations using in situ spatially resolved x-ray diffraction with synchrotron radiation.		
Effect of homogenization heat treatment on the microstructure and heat affected zone microfissuring in welded cast alloy 718.		
Effect of multiaxial stresses on creep damage of 316 stainless steel weldments.		
Heat affected zone, Mechanical properties		
Microstructures relevant to brittle fracture initiation at the heat-affected zone of weldment of a low carbon steel.		
Cleavage initiation in the intercritically reheated coarse-grained heat affected zone. II. Failure criteria and statistical effects.		
Heat affected zone, Microstructure		
Nonuniform distribution of carbonitride particles and its effect on prior austenite grain size in the simulated coarse-grained heat-affected zone of thermomechanical control-processed steels.		
Heat of crystallization		
Thermally assisted and mechanically driven solid-state reactions for formation of amorphous Al_3Ta_7 alloy powders.		
Heat of formation		
Standard enthalpies of formation of dysprosium alloys, Dy+Me (Me=Ni, Ru, Rh, Pd, Ir, and Pt), by high-temperature direct synthesis calorimetry.		
Controversy on the free energy of formation of CaO —additonal evidence in support of thermochemical data.		
Use of solid-electrolyte galvanic cells to determine the activity of CaO in the $CaO-ZrO_2$ system and the standard Gibbs free energies of formation of $CaZrO_3$ from CaO and ZrO_2 .		
Gibbs energies of formation of chromium carbides.		
Formation of structural intermetallics by reactive metal penetration of titanium and nickel oxides and aluminates.		
Heat of reaction		
Formation of structural intermetallics by reactive metal penetration of titanium and nickel oxides and aluminates.		
Heat resistant steels		
M_2C_6 carbide equilibria in the Fe-Cr-C system.		
Heat transfer		
Thermomechanics of the cooling stage in casting processes: three-dimensional finite element analysis and experimental validation.		
Heat transfer and pressure drop considerations in the design of Siros melt lances.		
Solidification of particle-reinforced metal-matrix composites.		
Flow and thermal behavior of the top surface flux/powder layers in continuous casting molds.		
Generalized enthalpy method for multicomponent phase change.		
Heat transfer, Cooling effects		
Vacuum evaporation of KCl-NaCl salts. II. Vaporization-rate model and experimental results.		433-443B
Heat transfer, Temperature effects		
Heat-flow-based analysis of surface crack formation during the start-up of the direct chill casting process. I. Development of the inverse heat-transfer model.		
Heat transmission, Temperature effects		
Heat-flow-based analysis of surface crack formation during the start-up of the direct chill casting process. II. Development of the inverse heat-transfer model.		
Heat-flow-based analysis of surface crack formation during the start-up of the direct chill casting process. III. Experimental study of an AA5182 rolling ingot.		
Heterogeneous structure, Cooling effects		
The role of grain corners in nucleation.		
Heterogeneous structure, Heating effects		
Microstructural stability on aging of an $\alpha+\beta$ titanium alloy: Ti-6Al-1.6Zr-3.3Mo-0.3Si.		
Heterogeneous nucleation of δ on dislocations in a dilute aluminum-lithium alloy.		
Heterogeneous structure, Temperature effects		
Nucleation controlled solidification kinetics.		
Morphological instabilities of lamellar eutectics.		
High alloy steels, Mechanical properties		
Microstructural basis for the effect of chromium on the strength and toughness of AF1410-based high performance steels.		
High alloy steels, Microstructure		
M_2C precipitates in isothermal tempering of high Co-Ni secondary hardening steel.		
High carbon steels, Crystal growth		
Austenite grain growth kinetics in Al-killed plain carbon steels.		

High carbon steels, Mechanical properties Pearlite in ultrahigh carbon steels: heat treatments and mechanical properties.	111-118A	Tensile properties of mechanically alloyed/milled ODS-Ni-based alloys. 1371-1377A
High cycle fatigue Multiple matrix cracking in a fiber-reinforced titanium matrix composite under high-cycle fatigue.	1899-1907A	Homogeneous structure, Cooling effects Solidification of binary hypoeutectic alloy matrix composite castings. 595-609A
High speed steel tools, Mechanical properties Active wear and failure mechanisms of titanium nitride-coated high speed steel and titanium nitride-coated cemented carbide tools when machining powder metallurgically made stainless steels.	2796-2808A	Homogeneous structure, Field effects Effects of forced electromagnetic vibrations during the solidification of aluminum alloys. I. Solidification in the presence of crossed alternating electric fields and stationary magnetic fields. 445-455B
High speed tool steels, Irradiation The effect of high-energy electron-beam irradiation on microstructural modification of a high-speed steel roll.	3149-3161A	Homogenizing Evolution of microstructures in the nickel modified titanium tri-aluminides near the L_1 phase field. 5-17A
High strength low alloy steels, Cladding Ballistic impact behavior of multilayered armor plates processed by hardfacing.	3335-3340A	The effect of thermal cycle on the microstructural development of a powder metallurgy superalloy braze material. 145-153A
High strength low alloy steels, Corrosion Initiation of stress corrosion cracking for pipeline steels in a carbonate-bicarbonate solution. Microstructural aspects of sulfide stress cracking in an API X-80 pipeline steel.	2686-2691A 3601-3611A	Effect of homogenization heat treatment on the microstructure and heat affected zone microfissuring in welded cast alloy 718. 785-790A
High strength low alloy steels, Mechanical properties Copper-bearing high-strength low-alloy steels: the influence of microstructure on the initiation and growth of small fatigue cracks. Hydrogen-induced cleavage fracture of Fe_3Al -based intermetallics.	2540-2556A 3949-3956A	Hot bonding Transient liquid-phase bonding in the NiAl/Cu/Ni system—a microstructural investigation. 3621-3629A
High strength low alloy steels, Phases (state of matter) Austenite decomposition during continuous cooling of an HSLA-80 plate steel. Copper precipitation during continuous cooling and isothermal aging of A710 type steels.	1554-1568A 1569-1584A	Hot dip galvanizing The production of nickel-zinc alloys by powder injection. Modeling iron enrichment in hot-dip galvanal coatings on interstitial-free steels. 1132-1134A
High strength low alloy steels, Welding Dilution in single pass arc welds. Microstructures relevant to brittle fracture initiation at the heat-affected zone of weldment of a low carbon steel. Forming of tailor-welded blanks. Cleavage initiation in the intercritically reheated coarse-grained heat affected zone. II. Failure criteria and statistical effects. Nonuniform distribution of carbonitride particles and its effect on prior austenite grain size in the simulated coarse-grained heat-affected zone of thermomechanical control-processed steels.	481-489B 2574-2582A 2605-2616A 3019-3029A 4031-4038A	Hot extrusion Microsegregation of oxygen in Zr-2.5Nb alloy materials. 431-440A
High strength low alloy steels, Welding The wear behavior between hardfacing materials.	3639-3648A	Hot forming Communication: Discussion of "Modeling of dynamic materials behavior. A critical evaluation of the dissipator power co-tent approach". Reply: Dynamic materials model. Basis and principles. Micronecking and fracture in cavitated superplastic materials. 1043-1046A
High strength low alloy steels mech p The influence of aqueous environments on low ΔK and high ΔK fatigue crack propagation behavior in low carbon structural steels.	2678-2685A	Hot isostatic pressing Characterization and mechanical properties of ultrahigh boron steels produced by powder metallurgy. Synthesis of RuAl by reactive powder processing. Influence of reinforcement volume fraction and size on the microstructure and abrasion wear resistance of hot isostatic pressed white iron matrix composites. Influence of matrix structure on the abrasion wear resistance and toughness of a hot isostatic pressed white iron matrix composites. 1861-1867A 3688-3699A 4171-4181A 4183-4191A
High strength steels, Cladding The wear behavior between hardfacing materials.	3639-3648A	Hot pressing Microstructure and properties of $Al_2O_3-Al(Si)$ and $Al_2O_3-Al(Si)-Si$ composites formed by in situ reaction of aluminum with aluminosilicate ceramics. Microstructural development of a gas-atomized and hot-pressed super- α_2 alloy. The use of microstructural gradients in hot gas-pressure forming of Zn-Al sheet. 2122-2129A 2221-2228A 3250-3258A
High strength steels, Mechanical properties Microstructural basis for the effect of chromium on the strength and toughness of AF1410-based high performance steels.	2510-2517A	Hot pressing, Pressure effects Pressure-assisted reactive synthesis of titanium aluminides from dense 50Al-50Ti elemental powder blends. 2130-2139A
High strength steels, Microstructure M_2C precipitates in isothermal tempering of high Co-Ni secondary hardening steel.	3466-3472A	Hot rolling Experimental investigation of the transformation texture in hot-rolled ferritic stainless steel using single orientation determination. Austenite grain growth kinetics in Al-killed plain carbon steels. Modeling recrystallization kinetics, grain sizes, and textures during multipass hot rolling. 49-57A 3399-3409A 4133-4144A
High strength steels, Surface properties Measurement of friction under sheet forming conditions.	3971-3981A	Hot strip mills Austenite grain growth kinetics in Al-killed plain carbon steels. 3399-3409A
High temperature A study of solid-aqueous equilibria by the speciation approach in the hydronium alumite-sulfuric acid-water system at high temperatures.	555-566B	Hot workability, Temperature effects Influence of temperature transients on the hot workability of a two-phase gamma titanium aluminide alloy. 1933-1950A
A unified representation of the two-phase plume characteristics in gas-stirred ladle systems.	704-708B	
On the stable Mg-Zn-Y quasicrystals.	1779-1784A	
Characterization and mechanical properties of ultrahigh boron steels produced by powder metallurgy.	1861-1867A	Hot working Flow stress and microstructural evolution during hot working of alloy 22Cr-13Ni-5Mn-0.3N austenitic stainless steel. 1251-1266A
High-temperature low-cycle fatigue of a gamma titanium aluminide alloy Ti-46Al-2Nb-2Cr.	2239-2251A	
High temperature effects High Temperature Fracture Mechanisms in Advanced Materials. 825-1136, 8 1/2 in. x 11 in., IllustratedA		Hydrides Hydride formation and decomposition in electrolytically charged metastable austenitic stainless steels. 29-40A
Holes The measurement of hydrogen activities in molten copper using an oxide protonic conductor.	929-935B	Hydrodynamics Characteristics of eccentric bubble plumes in liquids. 231-239B
Homogeneity Microstructure and tensile behavior of nitrogen-alloyed, dual-phase stainless steels.	1845-1859A	Hydrogen, Alloying additive Effect of strain rate and temperature on the flow stress of β -phase titanium-hydrogen alloys. 1303-1312A
On the role of magnesium and silicon in the formation of alumina from aluminum alloys by means of DIMOX processing.	2094-2099A	Effect of phase composition and hydrogen level on the deformation behavior of titanium-hydrogen alloys. 1869-1876A
Homogeneous structure Microstructure of Al_2O_3 fiber-reinforced superalloy (Inconel 718) composites.	451-458A	Dynamic strain aging and hydrogen-induced softening in alpha titanium. 1877-1887A
		Elastic moduli of titanium-hydrogen alloys in the temperature range 20°C to 1100°C. 3963-3970A

Hydrogen, Binary systems		Hypereutectic structures	
Critical evaluation and optimization of the thermodynamic properties of liquid tin solutions.	808-826B	Correlation of microstructure and fracture toughness in high-chromium white iron hardfacing alloys.	3881-3891A
Hydrogen, Chemical analysis		Hysteresis	
Determination of hydrogen in titanium alloys by cold neutron prompt gamma activation analysis.	3682-3687A	Internal friction in hydrogen-charged CrNi and CrNiMn austenitic stainless steels.	1815-1821A
Hydrogen, Diffusion		Multiple matrix cracking in a fiber-reinforced titanium matrix composite under high-cycle fatigue.	1899-1907A
Internal friction in hydrogen-charged CrNi and CrNiMn austenitic stainless steels.	1815-1821A	High-temperature low-cycle fatigue of a gamma titanium aluminide alloy Ti-46Al-2Nb-2Cr.	2239-2251A
Hydrogen trapping and permeation in nickel thoria.	2495-2503A		
Influence of titanium and carbon contents on the hydrogen trapping of microalloyed steels.	3773-3780A	Ilmenite, Reduction (chemical)	
Hydrogen-induced cleavage fracture of Fe_3Al -based intermetallics.	3949-3956A	Preoxidation and hydrogen reduction of ilmenite in a fluidized bed reactor.	731-738B
Hydrogen, Dopants		Impact strength	
Hydride formation and decomposition in electrolytically charged metastable austenitic stainless steels.	29-40A	Failure characteristics of 6061/Al ₂ O ₃ /15 _p and 2014/Al ₂ O ₃ /15 _p composites as a function of loading rate.	3095-3107A
Hydrogen, Environment		Ballistic impact behavior of multilayered armor plates processed by hardfacing.	3335-3340A
Hydrogen effects on directional solidification of tellurium-doped cast irons.	496-498A	Impact strength, Alloying effects	
Hydrogen, Impurities		Effect of alloying additions on fracture behavior of molybdenum-containing secondary hardening steels.	3343-3346A
The effect of hydrogen on the fracture of alloy X-750.	101-110A	Impact strength, Heating effects	
Physical chemistry of the powder metallurgy of beryllium: chemical characterization of the powder in relation to its granularity.	371-379A	Microstructural basis for the effect of chromium on the strength and toughness of AF1410-based high performance steels.	2510-2517A
Hydrogen, Reactions (chemical)		Impact strength, Microstructural effects	
The measurement of hydrogen activities in molten copper using an oxide protonic conductor.	929-935B	Effect of bainite transformation and retained austenite on mechanical properties of austempered spheroidal graphite cast steel.	1585-1594A
Hydrogen embrittlement		Influence of matrix structure on the abrasion wear resistance and toughness of a hot isostatic pressed white iron matrix composites.	4183-4191A
The influence of aqueous environments on low ΔK and high ΔK fatigue crack propagation behavior in low carbon structural steels.	2678-2685A	Impact strength, Stress effects	
Initiation of stress corrosion cracking for pipeline steels in a carbonate-bicarbonate solution.	2686-2691A	Effect of thermal cycling on the mechanical properties of 350 grade maraging steel.	757-761A
Determination of hydrogen in titanium alloys by cold neutron prompt gamma activation analysis.	3682-3687A	Impact tests	
Shear ligament phenomena in Fe_3Al intermetallics and micro-mechanics of shear ligament toughening.	3817-3825A	Cleavage initiation in the intercritically reheated coarse-grained heat affected zone. II. Failure criteria and statistical effects.	3019-3029A
Hydrogen-induced cleavage fracture of Fe_3Al -based intermetallics.	3949-3956A	Failure characteristics of 6061/Al ₂ O ₃ /15 _p and 2014/Al ₂ O ₃ /15 _p composites as a function of loading rate.	3095-3107A
Hydrogen embrittlement, Composition effects		Impurities, Chemical analysis	
Influence of titanium and carbon contents on the hydrogen trapping of microalloyed steels.	3773-3780A	Physical chemistry of the powder metallurgy of beryllium: chemical characterization of the powder in relation to its granularity.	371-379A
Hydrogen embrittlement, Deformation effects		Inclusions	
Effect of thermomechanical treatments on the room-temperature mechanical behavior of iron aluminide Fe_3Al .	2985-2993A	Activities in Mn-O-SiO ₂ -Al ₂ O ₃ slags and deoxidation equilibria of manganese and silicon.	263-270B
Hydrogen embrittlement, Environmental effects		The improved microstructures and properties of 7075 alloys produced by a water-cooling centrifugal casting method.	1951-1962A
Studies on the influence of metallurgical variables on the stress corrosion behavior of AISI 304 stainless steel in sodium chloride solution using the fracture mechanics approach.	1313-1325A	Theoretical calculation of the stress-strain behavior of dual-phase metals with randomly oriented spheroidal inclusions.	2359-2365A
Hydrogen embrittlement, Heating effects		Indentation	
A strain-based fracture model for stress corrosion cracking of low-alloy steels.	291-304A	Plastic zone and pileup around large indentations.	3793-3800A
Hydrogen embrittlement, Impurity effects		Indium base alloys, Mechanical properties	
The effect of hydrogen on the fracture of alloy X-750.	101-110A	Temperature dependent deformation of polydomain phases in an In-22.5 at.% Ti shape memory alloy.	1687-1692A
Hydrogen reduction		Industrial wastes	
Preparation of fine copper powders from organic media by reaction with hydrogen under pressure. I. Experimental study.	577-584B	Materials and society—impacts and responsibilities.	337-350B
Preparation of fine copper powders from organic media by reaction with hydrogen under pressure. II. The kinetics of particle nucleation, growth, and dispersion.	585-594B	The use of blast furnace slag and derived materials in the vitrification of electric arc furnace dust.	379-384B
Discussion of "Representation of mixed reactive gases on free energy (Ellingham-Richardson) diagrams" and reply.	693-694B	Industrial wastes, Reactions (chemical)	
Preoxidation and hydrogen reduction of ilmenite in a fluidized bed reactor.	731-738B	Preparation of glass-forming materials from granulated blast furnace slag.	801-807B
Hydrogen storage		Industrial wastes, Recovering	
Hydrogen trapping and permeation in nickel thoria.	2495-2503A	A kinetic study of the reaction of zinc oxide with iron powder.	363-374B
Hydrogen sulfide, Environment		Infiltration	
Microstructural aspects of sulfide stress cracking in an API X-80 pipeline steel.	3601-3611A	Microstructure and properties of Al ₂ O ₃ -Al(Si) and Al ₂ O ₃ -Al(Si)-Si composites formed by in situ reaction of aluminum with aluminosilicate ceramics.	2122-2129A
Hydrogenation		Permeability of microporous carbon preforms.	3689-3674A
Hydride formation and decomposition in electrolytically charged metastable austenitic stainless steels.	29-40A	Infiltration of fibrous preform by molten aluminum in a centrifugal force field.	4163-4169A
Hydrometallurgy		Infrared brazing	
Zinc reduction of MoO_3 in a self propagating high temperature synthesis process.	315-318B	Infrared transient-liquid-phase joining of SCS-6/B21S titanium matrix composite.	4011-4018A
A study of solid-aqueous equilibria by the speciation approach in the hydronium alunite-sulfuric acid-water system at high temperatures.	555-566B	Infrared heating	
The mineralogical deportment of germanium in the Clarksville electrolytic zinc plant of Savage Zinc Inc.	567-576B	Liquid state infrared processing of SCS-6/Ti-6Al-4V composites.	527-532B
		Infrared radiation	
		Liquid state infrared processing of SCS-6/Ti-6Al-4V composites.	527-532B

Ingots

Heat-flow-based analysis of surface crack formation during the start-up of the direct chill casting process. II. Experimental study of an AA5182 rolling ingot.

129-137B

Ingots, Dimensional analysis

Modeling of ingot distortions during direct chill casting of aluminum alloys.

3214-3225A

Ingots, Microstructure

The effect of iron and manganese on the recrystallization behavior of hot-rolled and solution-heat-treated aluminum alloy 6013.

19-27A

Scaling of intragranular dendritic microstructure in ingot solidification.

101-113B

Effect of superheat on the solidification structures of AISI 310S austenitic stainless steel.

287-296B

Effects of forced electromagnetic vibrations during the solidification of aluminum alloys. I. Solidification in the presence of crossed alternating electric fields and stationary magnetic fields.

445-455B

Ingots, Phases (state of matter)

Electron microscope study of Al-Fe-Si intermetallics in 6201 aluminum alloy.

929-936A

Injection

Experimental study of splash generation in a flash smelting furnace.

633-646B

A unified representation of the two-phase plume characteristics in gas-stirred ladle systems.

704-708B

The separation of the solids from the carrier gas during submerged powder injection.

773-779B

The production of nickel-zinc alloys by powder injection.

780-787B

Injection molding

Comparative study of pore structure evolution during solvent and thermal debinding of powder injection molded parts.

245-253A

A statistical analysis of the effect of a mixture component on the rheology of alumina feedstocks.

399-408B

Interface reactions

Interface characterization of ceramic fiber-reinforced titanium alloy composites manufactured by infrared processing.

1379-1394A

Investigation of the reaction zone between TiAl and molybdenum.

2285-2292A

Structure of phases in the δ -Al₂O₃ fiber studied by convergent beam electron diffraction.

3318-3329A

Interface reactions, High temperature effects

Phase relations of a silicide/silica reaction couple at 2273K.

271-276B

Interface reactions, Pressure effects

Mechanistic processes influencing shock chemistry in powder mixtures of the Ti-Si, Ti-Al, and Ti-B systems.

1761-1771A

Interfaces

Interface effects on the micromechanical response of a transversely loaded single fiber SCS-6/Ti-6Al-4V composite.

2035-2043A

Interferometry

Evidence of fracture surface interference for cracks loaded in shear detected by phase-shifted speckle interferometry.

3853-3860A

Intergranular corrosion, Heating effects

Influence of thermal aging on the intergranular corrosion resistance of types 304LN and 316LN stainless steels.

2881-2887A

Intergranular corrosion, Microstructural effects

Structure, chemistry, and stress corrosion cracking of grain boundaries in alloys 600 and 690.

327-341A

Intergranular fracture, Diffusion effects

Nonequilibrium grain-boundary segregation and ductile-brittle-ductile transition in Fe-Mn-Ni-Ti age-hardening alloy.

3059-3065A

Intergranular fracture, Heating effects

A strain-based fracture model for stress corrosion cracking of low-alloy steels.

291-304A

Intergranular fracture, Microstructural effects

Intergranular fracture in some precipitation-hardened aluminum alloys at low temperatures.

3081-3088A

Intergranular structure, High temperature effects

Creep lifetime prediction of oxide-dispersion-strengthened nickel-base superalloys: a micromechanically based approach.

3861-3870A

Interlayers

Microstructural development in NiAl/Ni-Si-B/Ni transient liquid phase bonds.

1925-1931A

Intermetallics phases

Mechanical behavior of the *in situ* composite alloys in the Al-Ni-Ti system near the L₁ phase field.

71-79A

Discussion of "The effect of steel chemistry on the formation of Fe-Zn intermetallic compounds of galvannealed-coated steel sheets" and authors' reply.

146-148B

Physical chemistry of the powder metallurgy of beryllium: chemical characterization of the powder in relation to its granularity.

371-379A

Microstructure of Al₂O₃ fiber-reinforced superalloy (Inconel 718) composites.

451-458A

Interface attachment kinetics in alloy solidification.

671-686A

Interface characterization of ceramic fiber-reinforced titanium alloy composites manufactured by infrared processing.

1379-1394A

Mechanical properties of Ru-Ni-Al alloys.

1395-1400A

A high resolution transmission electron microscopy study of interfaces between the γ , B₂, and α_2 phases in a Ti-Al-Mo alloy.

1618-1629A

Microstructure and phase identification in type 304 stainless steel-zirconium alloys.

2151-2159A

Structural stability of super duplex stainless weld metals and its dependence on tungsten and copper.

2196-2208A

Microstructural development of a gas-atomized and hot-pressed super- α_2 alloy.

2221-2228A

Investigation of the reaction zone between TiAl and molybdenum.

2285-2292A

Retardation of intermetallic phase formation in experimental superferritic stainless steels.

2436-2444A

Thermodynamic activities and phase boundaries for the alloys of the Ni₃Al-Ni₃Ti pseudobinary section in the Ni-Al-Ti system.

2673-2677A

Lattice misfits in four binary Ni-base γ ' alloys at ambient and elevated temperatures.

2888-2896A

A thermodynamic evaluation of the nickel-silicon system.

2897-2903A

Kinetics of phase evolution of Zn-Fe intermetallics.

2904-2910A

Low quench sensitivity of superplastic 8090 Al-Li thin sheets.

2923-2933A

Thermodynamic activities and partial enthalpies of mixing in the solid solution of Fe in Ni₃Al.

3569-3575A

Thermochemistry of the Ni-H system—intermetallic phases.

3576-3590A

The balance of mechanical and environmental properties of a multielement niobium-niobium silicide-based *in situ* composite.

3801-3808A

Martensitic transformations in NiMnAl β phase alloys.

4153-4162A

Intermetallic phases, Alloying effects

Mechanical alloying of Nb-Al powders.

41-48A

Electron microscope study of Al-Fe-Si intermetallics in 6201 aluminum alloy.

929-936A

Identification of precipitate phases in a mechanically alloyed rapidly solidified Al-Fe-Ce alloy.

1033-1041A

Intermetallic phases, Cooling effects

Porosity formation in Al-9 wt.% Si-3 wt.% Cu alloy systems: metallographic observations.

415-429A

Rapid solidification processing of a Mg-Li-Si-Ag alloy.

1363-1370A

Intermetallic phases, Deformation effects

The relationship between microstructural and plastic instability in Al-4.0 wt.% Cu alloy.

2916-2922A

Preferential coarsening of γ' precipitates in Inconel 718 during creep.

3391-3398A

Intermetallic phases, Heating effects

Evolution of microstructures in the nickel modified titanium tri-aluminides near the L₁ phase field.

5-17A

Effect of homogenization heat treatment on the microstructure and heat affected zone microfissuring in welded cast alloy 718.

785-790A

Phase transformations in Nb-Al-Ti alloys.

1642-1654A

Microstructural aspects of the dissolution and melting of Al₂Cu phase in Al-Si alloys during solution heat treatment.

1785-1798A

Intermetallic phases, High temperature effects

Standard enthalpies of formation of dysprosium alloys, Dy-Me (Me=Ni, Ru, Rh, Pd, Ir, and Pt), by high-temperature direct synthesis calorimetry.

417-422B

Intermetallic phases, Radiation effects

Improved oxidation resistance of group VB refractory metals by Al⁺ ion implantation.

491-500B

Intermetallics, Stress effects

On the effect of stress on nucleation and growth of precipitates in an Al-Cu-Mg-Al alloy.

3431-3444A

Intermetallics, Temperature effects

Nucleation controlled solidification kinetics.

533-547A

Intermetallics

Thermodynamic activities and phase boundaries for the alloys of the Ni₃Al-Ni₃Ti pseudobinary section in the Ni-Al-Ti system.

2673-2677A

Intermetallics, Alloying elements

Notch fracture in γ -titanium aluminides.

3903-3912A

Intermetallics, Bonding

Microstructural development in NiAl/Ni-Si-B/Ni transient liquid phase bonds.

1925-1931A

Intermetallics, Coating

The deposition of aluminide and silicide castings on γ -TiAl using the halide-activated pack cementation method.

3761-3772A

Intermetallics, Coatings

Isothermal fatigue of an aluminide-coated single-crystal superalloy. I.
Isothermal fatigue of an aluminide-coated single-crystal superalloy. II. Effects of brittle precracking.

353-361A
363-369A

Intermetallics, Structural hardening

Manifestations of dynamic strain aging in soft-oriented NiAl single crystals.

3542-3557A

Intermetallics, Composite materials

Effective elastic moduli of fiber-matrix interphases in high-temperature composites.
Bridge toughening enhancement in double-notched $MoSi_2/Nb$ model composites.
Formation of structural intermetallics by reactive metal penetration of titanium and nickel oxides and aluminates.
Investigation of the reaction zone between TiAl and molybdenum.
NiTi and NiTi-TiC composites. IV. Neutron diffraction study of twinning and shape-memory recovery.
Ni₃Al intermetallic particles as wear-resistant reinforcement for Al-base composites processed by powder metallurgy.
Fracture and fatigue-crack growth behavior in ductile-phase toughened molybdenum disilicide: effects of niobium wire vs. particulate reinforcements.
The balance of mechanical and environmental properties of a multielement niobium-niobium silicide-based *in situ* composite.

165-182A
909-921A
2100-2104A
2285-2292A
2820-2836A
3259-3266A
3781-3792A
3801-3808A

Intermetallics, Synthesis

Synthesis of nanocrystalline Ni₃Cu by sol-gel route.

4213-4216A

Intermetallics, Thermal properties

Thermodynamic activities and partial enthalpies of mixing in the solid solution of Fe in Ni₃Al.

3569-3575A

Internal friction

Internal friction in hydrogen-charged CrNi and CrNiMn austenitic stainless steels.

1815-1821A

Interstitial impurities

The role of coincident site lattice boundaries during selective growth in interstitial-free steels.

2178-2186A

Influence of interstitials on the mechanical properties of metallic materials.

3524-3529A

Interstitial solutions

Annealing and aging of interstitial C in α -Fe, as measured by internal friction.

2461-2469A

Intragranular structure, Cooling effects

Scaling of intragranular dendritic microstructure in ingot solidification.

101-113B

Investment casting

Prediction of grain structures in various solidification processes.

695-705A

Viscosity of superalloy 718 by the oscillating vessel technique.

698-701B

Ion implantation

Improved oxidation resistance of group VB refractory metals by Al⁺ ion implantation.

491-500B

Effects of nitrogen implantation on low cycle fatigue behavior of ferric Fe-24Cr-4Al stainless alloy.

2663-2672A

The growth and structure of thin oxide films on cerium ion-implanted nickel.

3649-3661A

Ion nitriding

Transmission electron microscopy study on the cross-sectional microstructure of an ion-nitriding layer.

1347-1352A

Effects of nitrogen implantation on low cycle fatigue behavior of ferric Fe-24Cr-4Al stainless alloy.

2663-2672A

Iridium, Binary systems

Standard enthalpies of formation of dysprosium alloys, Dy+Me (Me=Ni, Ru, Rh, Pd, Ir, and Pt), by high-temperature direct synthesis calorimetry.

417-422B

Iron, Alloying elements

The effect of iron and manganese on the recrystallization behavior of hot-rolled and solution-heat-treated aluminum alloy 6013.

19-27A

Iron, Binary systems

Critical evaluation and optimization of the thermodynamic properties of liquid tin solutions.

808-826B

Generalized enthalpy method for multicomponent phase change.

869-879B

Control of iron nitride layers growth kinetics in the binary Fe-N system.

1823-1835A

Iron, Chemical analysis

Formation of aluminum-silicon alloys from feldspars—determination of silicon, light, and heavy elements in silumin by scanning electron microscopy.

604-609B

Iron, Diffusion

Anomalous diffusion of iron in liquid aluminum measured by the pulsed laser technique.

725-730A

Iron, Extraction

Phase equilibria in the metal-sulfur-oxygen system and selective reduction of metal oxides and sulfides. I. The carbothermic reduction and calcination of complex mineral sulfides.

827-838B

Iron, Impurities

Influence of chromium and impurities on the grain refining behavior of aluminum.

791-800A

Iron, Irradiation

Theoretical treatment of nitriding and nitrocarburizing of iron. A model describing neutron irradiation-induced segregation to grain boundaries in dilute alloys.

1073-1080A

Iron, Phase transformations

Bainite in the light of rapid continuous cooling information.

1499-1510A

Iron, Quaternary systems

An experimental study and thermodynamic calculations of phase equilibria in the Fe-Mo-C-N system.

2869-2880A

An isothermal section at 550°C in the Al-rich corner of the Al-Fe-Mn-Si system.

3357-3361A

Iron, Solubility

Effects of oxygen, selenium, and tellurium on the rate of nitrogen dissolution in molten iron.

846-851B

Intermetallics, Phase transformations

Molecular dynamics simulation of martensitic transformations in NiAl.
Effect of alloying elements on martensitic transformation in the binary NiAl(B) phase alloys.
The effect of substrate constraint on the martensitic transformation of Ni-Ti thin films.

271-276B
3993-4002A

Intermetallics, Phases (state of matter)

Stable and metastable ordered phases in microcrystalline alloys Ni (Fe, Mn, Ti).

4003-4010A

Intermetallics, Powder technology

Mechanistic processes influencing shock chemistry in powder mixtures of the Ti-Si, Ti-Al, and Ti-B systems.
Pressure-assisted reactive synthesis of titanium aluminides from dense 50Al-50Ti elemental powder blends.
Dense CoAl-based alloys with improved ductility: solid-state synthesis and microstructure control.
Kinetics of phase evolution of Zn-Fe intermetallics.
Synthesis of RuAl by reactive powder processing.

1476-1488A
2445-2453A

Intermetallics, Reactions (chemical)

Modeling of sequential reactions during micropyretic synthesis.
Thermodynamics of calcium and oxygen in molten titanium and titanium-aluminum alloy.

2858-2860A

Intermetallics, Reactions (chemical)

Modeling of sequential reactions during micropyretic synthesis.

2045-2046A

Intermetallics, Reactions (chemical)

Thermodynamics of calcium and oxygen in molten titanium and titanium-aluminum alloy.

1761-1771A

Intermetallics, Reactions (chemical)

Modeling of sequential reactions during micropyretic synthesis.

2130-2139A

Intermetallics, Reactions (chemical)

Thermodynamics of calcium and oxygen in molten titanium and titanium-aluminum alloy.

2140-2150A
2904-2910A
3688-3699A

Intermetallics, Reactions (chemical)

Modeling of sequential reactions during micropyretic synthesis.

961-972A

Intermetallics, Reactions (chemical)

Thermodynamics of calcium and oxygen in molten titanium and titanium-aluminum alloy.

967-972B

Iron, Ternary systems

Applicability of Butler's equation in interpreting the thermodynamic behavior of surfaces and adsorption in Fe-S-O melts. $M_{23}C_6$ carbide equilibria in the Fe-Cr-C system. Thermodynamic and kinetic study of diffusion paths in the system Cu-Fe-Ni. Experimental study of the phase equilibria in the Fe-Mn-Al system. Internal sulfide precipitation in low Cr-Fe alloys. Solidification of undercooled Fe-Cr-Ni alloys. II. Microstructural evolution. Thermodynamic activities and partial enthalpies of mixing in the solid solution of Fe in Ni_3Al .

Iron and steel making

Modeling and experimental study of gaseous oxidation of liquid iron alloys.

Iron compounds, Mechanical properties

Effect of thermomechanical treatments on the room-temperature mechanical behavior of iron aluminide Fe_3Al . Shear ligament phenomena in Fe_3Al intermetallics and micro-mechanics of shear ligament toughening. Hydrogen-induced cleavage fracture of Fe_3Al -based intermetallics.

Iron compounds, Powder technology

Kinetics of phase evolution of Zn-Fe intermetallics.

Iron oxides, Metallography

Real-time observations of the oxidation of mild steel at high temperature by neutron diffraction.

Iron oxides, Ternary systems

Chemical potentials of components of the system $CaO-P_2O_5-Fe_2O_3$ at 1673K.

Ironmaking

A multiphase fluid mechanics approach to gas holdup in bath smelting processes. A study of the thermal decomposition of $BaCO_3$. Alternative technologies in iron and steelmaking. Reduction of FeO in smelting slags by solid carbon: experimental results. Preparation of glass-forming materials from granulated blast furnace slag.

Isothermal annealing

Modeling recovery and recrystallization kinetics in cold-rolled Ti-Nb stabilized interstitial-free steel.

Isothermal treatment

The control of grain size and distribution of particles in a $(6061 \text{ alloy})_m/(Al_2O_3)_n$ composite by solutionizing treatment. An analysis of static recrystallization during continuous, rapid heat treatment. M_2C precipitates in isothermal tempering of high Co-Ni secondary hardening steel.

Joints, Microstructure

Transient liquid-phase bonding in the NiAl/Cu/Ni system—a microstructural investigation.

Killed steels, Steel making

Activities in $Mn-SiO_2-Al_2O_3$ slags and deoxidation equilibria of manganese and silicon.

Kinetics

Recrystallization in oxide-dispersion strengthened mechanically alloyed sheet steel. An analysis of static recrystallization during continuous, rapid heat treatment. Thermodynamic and kinetic study of diffusion paths in the system Cu-Fe-Ni. Modeling recrystallization kinetics, grain sizes, and textures during multipass hot rolling.

Ladle metallurgy

Characteristics of eccentric bubble plumes in liquids. A unified representation of the two-phase plume characteristics in gas-stirred ladle systems. Activities in $CaO-SiO_2-Al_2O_3$ slags and deoxidation equilibria of silicon and aluminum.

Lamellar structure

Microstructure and phase relations in a powder-processed Ti-22Al-12Nb alloy. A high resolution transmission electron microscopy study of interfaces between the γ , B2, and α_2 phases in a Ti-Al-Mo alloy. High-temperature low-cycle fatigue of a gamma titanium aluminide alloy Ti-46Al-2Nb-2Cr. Directional solidification of white cast iron.

Lamellar structure, Deformation effects

Effect of creep strain on microstructural stability and creep resistance of a TiAl/Ti₃Al lamellar alloy.

Lamellar structure, Heating effects

The use of microstructural gradients in hot gas-pressure forming of Zn-Al sheet. Discussion of "Effects of tensile stress on microstructural change of eutectoid Zn-Al alloy" and authors' reply.

Lamellar structure, Temperature effects

Morphological instabilities of lamellar eutectics. Eutectoid decomposition in Ag-Ga.

Laminates, Mechanical properties

Subcritical crack growth at bimaterial interfaces. I. Flexural peel technique. Subcritical crack growth at bimaterial interfaces. III. Shear-enhanced fatigue crack growth resistance at polymer/metal interface. Bridge toughening enhancement in double-notched $MoSi_2/Nb$ model composites.

Laminates, Reactions (chemical)

Investigation of the reaction zone between TiAl and molybdenum.

Laminates, Rolling

Nanoscale brass/steel multilayer composites produced by cold rolling.

Lances

Heat transfer and pressure drop considerations in the design of Siros melt lances.

Lanthanum, Binary systems

Inverse melting in binary systems: morphology and microscopy of catactic alloys.

Laser beam heating

Quenching C60 fullerene into diamond in the Fe-C alloy system by laser treatment.

Laser beam melting

Prediction of grain structures in various solidification processes. Anomalous diffusion of iron in liquid aluminum measured by the pulsed laser technique. Investigation of the temperature field developed by a spinning beam in laser processing.

Laser beam welding

Prediction of grain structures in various solidification processes. Forming of tailor-welded blanks.

Laser processing

Quantitative characterization of the surface topography of rolled sheets by laser scanning microscopy and Fourier transformation.

Latent heat

Modeling of ingot distortions during direct chill casting of aluminum alloys.

Lattice parameters

Dense CoAl-based alloys with improved ductility: solid-state synthesis and microstructure control. Microstructural development of a gas-atomized and hot-pressed super- α_2 alloy. Lattice misfits in four binary Ni-base γ/γ' alloys at ambient and elevated temperatures.

Lattice parameters, Alloying effects

Identification of precipitate phases in a mechanically alloyed rapidly solidified Al-Fe-Ce alloy.

Lattice parameters, Composition effects

An evaluation of the Fe-N phase diagram considering long-range order of nitrogen atoms in $\gamma-Fe_4N_{1-x}$ and $\epsilon-Fe_2N_{1-x}$.

Lattice parameters, Deformation effects

The x-ray diffraction study of deformation in the composite matrix of Al-Mg-Zn and SiC.

Lattice parameters, Heating effects

Microstructural stability on aging of an $\alpha+\beta$ titanium alloy: Ti-6Al-1.6Zr-3.3Mo-0.30Si.

Lattice parameters, High temperature effects

High-temperature measurements of lattice parameters and internal stresses of a creep-deformed monocrystalline nickel-base superalloy.

Lattice parameters, Stress effects

Predicting the orientation-dependent stress-induced transformation and detwinning response of shape memory alloy single crystals.

Lattice parameters, Temperature effects

Rafting in superalloys.

Lattice vacancies

The characteristics of cavitation in superplastic metals and ceramics. Creep deformation of dispersion-strengthened copper.

Lattice vacancies, Deformation effects			
Analysis on the amplitude of serrated flow associated with the Portevin-LeChatelier effect of substitutional fcc alloys.	1683-1636A	Liquid phases, Pressure effects	
Theory of nucleation with cluster loss and injection: application to plastic deformation and irradiation.	1441-1448A	Vacuum evaporation of KCl-NaCl salts. I. Thermodynamic modeling of vapor pressures of solid and liquid solutions.	141-146B
Lattice vacancies, Radiation effects		Liquid phases, Temperature effects	
Microstructure of Al_2O_3 fiber-reinforced superalloy (Inconel 718) composites.	451-458A	A study of the thermal decomposition of $CaCO_3$. Overview of geometric effects on coarsening of mushy zones. The phase field method: simulation of alloy dendritic solidification during recalescence.	409-416B 557-567A 657-669A
Microstructure and phase identification in type 304 stainless steel-zirconium alloys.	2151-2159A	Liquidus	
Laves phase		Liquidus temperatures for primary crystallization of cryolite in molten salt systems of interest for aluminum electrolysis.	739-744B
Microstructure of Al_2O_3 fiber-reinforced superalloy (Inconel 718) composites.	451-458A	Lithium, Alloying elements	
Microstructure and phase identification in type 304 stainless steel-zirconium alloys.	2151-2159A	Low quench sensitivity of superplastic 8090 Al-Li thin sheets. Tension characteristics of notched specimens for Al-Li-Cu-Zr alloy sheets with various cerium contents.	2923-2933A 3089-3094A
Laves phase, Heating effects		Lithium, Binary systems	
Effect of homogenization heat treatment on the microstructure and heat affected zone microfissuring in welded cast alloy 718.	785-790A	Thermodynamic studies and the phase diagram of the Li-Mg system.	2419-2428A
Leaching		Loads (forces)	
The mineralogical deportment of germanium in the Clarksville electrolytic zinc plant of Savage Zinc Inc.	567-576B	Time-dependent, environmentally assisted crack growth in Nicalon-fiber-reinforced SiC composites at elevated temperatures.	839-849A 851-861A 4095-4111A
Lead base alloys, Casting		Mechanisms of high-temperature fatigue failure in alloy 800H. Mathematical modeling of the extrusion of 6061/ Al_2O_3 /20p composite.	
Macrosegregation during dendritic arrayed growth of hypoeutectic Pb-Sn alloys: Influence of primary arm spacing and mushy zone length.	1353-1362A	Long range order	
Lead base alloys, Crystal growth		Interface attachment kinetics in alloy solidification. Stable and metastable ordered phases in microcrystalline alloys Ni (Fe, Mn, Ti).	671-686A 2045-2046A
Convection during thermally unstable solidification of Pb-Sn in a magnetic field.	1095-1110A	Long range order, Alloying effects	
Ostwald ripening of solid-liquid Pb-Sn dispersions.	2470-2478A	Thermodynamics and long-range order of nitrogen in γ - Fe_4N_1 .	1055-1061A
Lead base alloys, Phase transformations			
Banded solidification microstructures.	625-634A	Long range order, Composition effects	
Precipitation in lead-calcium alloys containing tin.	1668-1675A	An evaluation of the Fe-N phase diagram considering long-range order of nitrogen atoms in γ - Fe_4N_{1-x} and c- Fe_2N_{1-z} .	1063-1071A
Lime, Physical properties		Low alloy steels, Casting	
Controversy on the free energy of formation of CaO —additional evidence in support of thermochemical data.	647-651B	Prediction of dendrite arm spacing for low alloy steel casting processes.	689-693B
Lime, Reactions (chemical)		Low alloy steels, Coating	
Use of solid-electrolyte galvanic cells to determine the activity of CaO in the $CaO-ZrO_2$ system and the standard Gibbs free energies of formation of $CaZrO_3$ from CaO and ZrO_2 .	658-662B	Wear-resistant coatings produced by shock-wave compaction of powders.	2297-2304A
Activities in $CaO-SiO_2-Al_2O_3$ slags and deoxidation equilibria of silicon and aluminum.	943-953B	Low alloy steels, Corrosion	
Thermodynamics of calcium and oxygen in molten titanium and titanium-aluminum alloy.	967-972B	Influence of titanium and carbon contents on the hydrogen trapping of microalloyed steels.	3773-3780A
Lime, Ternary systems		Low alloy steels, Heat treatment	
Chemical potentials of components of the system $CaO-P_2O_5-Fe_2O_3$ at 1673K.	595-603B	Modeling recovery and recrystallization kinetics in cold-rolled Ti-Nb stabilized interstitial-free steel.	3410-3423A
Liquid metals, Physical properties		Low alloy steels, Mechanical properties	
Prediction of liquid metal viscosities using an adjustable hard sphere radial distribution curve.	29-34B	A comparison of fracture behavior of low alloy steel with different sizes of carbide particles.	1909-1917A
Liquid metals, Sorption		Low alloy steels, Phase transformations	
Effects of oxygen, selenium, and tellurium on the rate of nitrogen dissolution in molten iron.	846-851B	The driving force for martensitic transformations in low alloy steels.	1127-1132A
Liquid metals, Surface properties		Low carbon steels, Casting	
Studies of interface deformations in single- and multi-layered liquid baths due to an impinging gas jet.	911-920B	Prediction of dendrite arm spacing for low alloy steel casting processes.	689-693B
Liquid phase sintering		Modeling of the peritectic reaction and macro-segregation in casting of low carbon steel.	999-1014B
Solid-state contributions to densification during liquid-phase sintering.	901-909B	Low carbon steels, Coating	
Abnormal growth of faceted (WC) grains in a (Co) liquid matrix.	2809-2819A	Correlation of microstructure and fracture toughness in high-chromium white iron hardfacing alloys.	3881-3891A
Liquid phase sintering, Alloying effects		Low carbon steels, Composite materials	
The effect of Mo addition on the liquid-phase sintering of W heavy alloy.	3120-3125A	Nanoscale brass/steel multilayer composites produced by cold rolling.	2383-2385A
Liquid phases		Low carbon steels, Crystal growth	
Dynamic behavior of a liquid/liquid interface at an oscillating wall.	305-314B	An analysis of static recrystallization during continuous, rapid heat treatment.	2051-2053A
Effects of flow on morphological stability during directional solidification.	583-593A	Austenite grain growth kinetics in Al-killed plain carbon steels.	3399-3409A
Interface attachment kinetics in alloy solidification.	671-686A	Low carbon steels, Heat treatment	
An adaptive mesh refinement scheme for solidification problems.	707-717A	Surface morphology and compound layer pores of plasma nitrocarburized low carbon steel.	135-143A
Real time x-ray transmission microscopy of solidifying Al-In alloys.	801-808A	Transmission electron microscopy study on the cross-sectional microstructure of an ion-nitriding layer.	1347-1352A
Microstructural development in NiAl/Ni-Si-B/Ni transient liquid phase bonds.	1925-1931A	Low carbon steels, Mechanical properties	
The Rayleigh instability and the origin of rows of droplets in the monotectic microstructure of zinc-bismuth alloys.	2053-2057A	Plastic anisotropy of sheets with continuously varying anisotropic parameters and flow stress.	317-326A
Transient liquid-phase bonding in the NiAl/Cu/Ni system—a microstructural investigation.	3621-3629A	The influence of aqueous environments on low ΔK and high ΔK fatigue crack propagation behavior in low carbon structural steels.	2678-2685A
Liquid phases, Cooling effects			
Vacuum evaporation of KCl-NaCl salts. II. Vaporization-rate model and experimental results.	433-443B		
Liquid phases, Field effects			
On the reaction between Fe-Ti and Fe-C liquids under microgravity.	407-414A		

Low carbon steels, Metal working		
The influence of niobium supersaturation in austenite on the static recrystallization behavior of low carbon microalloyed steels.		
Low carbon steels, Microstructure		
Modeling texture change during the static recrystallization of interstitial free steels.	951-960A	Magnetostriction Development of a magnetoelastic resonant sensor using iron-rich, nonzero magnetostrictive amorphous alloys. 3203-3213A
The role of coincident site lattice boundaries during selective growth in interstitial-free steels.	155-164A	Manganese, Alloying additive Effects of alloy modification and thermomechanical processing on recrystallization of Al-Mg-Mn alloys. 2947-2957A
Low carbon steels, Oxidation	2178-2186A	Manganese, Alloying elements The effect of iron and manganese on the recrystallization behavior of hot-rolled and solution-heat-treated aluminum alloy 6013. 19-27A
Real-time observations of the oxidation of mild steel at high temperature by neutron diffraction.	993-997B	Manganese, Binary systems Inverse melting in binary systems: morphology and microscopy of catactic alloys. 979-986B
Low cycle fatigue	2239-2251A	Manganese, Composite materials Effect of manganese dispersoid on the fatigue crack propagation of Al-Zn-Mg alloys. 490-493A
High-temperature low-cycle fatigue of a gamma titanium aluminide alloy Ti-46Al-2Nb-2Cr.	353-361A	Manganese, Phases (state of matter) Stable and metastable ordered phases in microcrystalline alloys Ni (Fe, Mn, Ti). 2045-2046A
Low cycle fatigue, Coating effects		Manganese, Quaternary systems An isothermal section at 550°C in the Al-rich corner of the Al-Fe-Mn-Si system. 3357-3361A
Isothermal fatigue of an aluminide-coated single-crystal superalloy.	490-493A	Manganese, Ternary systems Experimental study of the phase equilibria in the Fe-Mn-Al system. Martensitic transformations in NiMnAl β phase alloys. 2429-2435A 4153-4162A
Low cycle fatigue, Composition effects		Manganese base alloys, Phases (state of matter) Nucleation controlled solidification kinetics. 533-547A
Effect of manganese dispersoid on the fatigue crack propagation of Al-Zn-Mg alloys.	1273-1281A	Manganese base alloys, Refining Thermodynamics of sulfur in the BaO-MnO-SiO ₂ flux system. 652-657B
Low cycle fatigue, Microstructural effects		Maraging steels, Mechanical properties Effect of thermal cycling on the mechanical properties of 350 grade maraging steel. 757-761A
The normalized Coffin-Manson plot in terms of a new damage function based on grain boundary cavitation under creep-fatigue condition.	2663-2672A	Martensite The effects of microstructure, strength level, and crack propagation mode on stress corrosion cracking behavior of 4135 steel. 281-290A
Low cycle fatigue, Radiation effects		Microstructure and tensile behavior of nitrogen-alloyed, dual-phase stainless steels. 1845-1859A
Effects of nitrogen implantation on low cycle fatigue behavior of ferritic Fe-24Cr-4Al stainless alloy.	851-861A	Microstructural development in NiAl/NI-Si-B/NI transient liquid phase bonds. 1925-1931A
Low cycle fatigue, Stress effects		Mössbauer spectroscopy study of the aging and tempering of high nitrogen quenched Fe-N alloys: kinetics of formation of Fe ₁₈ N ₂ nitride by interstitial ordering in martensite. 2160-2177A
Temperature and strain-rate effects on low-cycle fatigue behavior of alloy 800H.	255-267A	Martensite, Alloying effects A study on morphology and plate mean dimensions in Fe-Ni and Fe-Ni-Cr alloys. 973-980A
Mechanisms of high-temperature fatigue failure in alloy 800H.	851-861A	Martensite, Composition effects Structural characterization of martensitic iron-carbon alloy films electrodeposited from an iron(II) sulfate solution. 483-486A
Magnesium, Alloying additive		Martensite, Cooling effects Bainite in the light of rapid continuous cooling information. 1499-1510A
Effect of magnesium on the aging behavior of Al-Zn-Mg-Cu/Al ₂ O ₃ metal matrix composites.	2005-2012A	Austenite decomposition during continuous cooling of an HSLA-80 plate steel. 1554-1568A
Magnesium, Binary systems		Martensite, Deformation effects Experimental investigation of the transformation texture in hot-rolled ferritic stainless steel using single orientation determination. 49-57A
Critical evaluation and optimization of the thermodynamic properties of liquid tin solutions.	808-826B	Martensite, Heating effects Microstructural stability on aging of an α - β titanium alloy: Ti-6Al-1.6Zr-3.3Mo-0.3Si. 1167-1173A
Thermodynamic studies and the phase diagram of the Li-Mg system.	2419-2428A	Martensite, High temperature effects Carbide diagrams and precipitation of alloying elements during aging of low-alloy steels. 498-502A
Magnesium, Chemical analysis		Martensite, Temperature effects The driving force for martensitic transformations in low alloy steels. 1127-1132A
Formation of aluminum-silicon alloys from feldspars—determination of silicon, light, and heavy elements in alumin by scanning electron microscopy.	604-609B	Martensitic stainless steels, Mechanical properties Observations of secondary carbide precipitation and its relation to high-temperature flow and fracture in HT-9 stainless steel. 467-469A
Magnesium, Forming		Martensitic stainless steels, Phase transformations Splitting phenomena occurring in the martensitic transformation of Cr13 and CrMoV14 stainless steels in the absence of carbide precipitation. 1799-1805A
Reply: Dynamic materials model. Basis and principles.	235-236A	Martensitic transformations NiTi and NiTi-TiC composites. II. Compressive mechanical properties. 183-191A
Magnesium base alloys, Forming		A comprehensive dynamical study of nucleation and growth in a one-dimensional shear martensitic transition. 1203-1216A
Reply: Dynamic materials model. Basis and principles.	235-236A	Temperature dependent deformation of polydomain phases in an In-22.5 at.% Ti shape memory alloy. 1687-1692A
Magnesium base alloys, Mechanical properties		
Rapid solidification processing of a Mg-Li-Si-Ag alloy.	1363-1370A	
Magnesium base alloys, Microstructure		
On the stable Mg-Zn-Y quasicrystals.	1779-1784A	
Magnetic fields		
Effects of forced electromagnetic vibrations during the solidification of aluminum alloys. I. Solidification in the presence of crossed alternating electric fields and stationary magnetic fields.	445-455B	
Effects of forced electromagnetic vibrations during the solidification of aluminum alloys. II. Solidification in the presence of collinear variable and stationary magnetic fields.	457-464B	
Convection during thermally unstable solidification of Pb-Sn in a magnetic field.	1095-1110A	
Magnetic measurements		
Alloy phase analysis from measurements of bulk magnetic properties.	2958-2965A	
Magnetic permeability		
Alloy phase analysis from measurements of bulk magnetic properties.	2958-2965A	
Magnetic permeability, Heating effects		
Effects of low-temperature aging on the microstructure and soft magnetic properties of rapidly quenched Fe-Si-B alloys.	2454-2460A	
Magnetic testing		
Alloy phase analysis from measurements of bulk magnetic properties.	2958-2965A	
Magnetization		
Development of a magnetoelastic resonant sensor using iron-rich, nonzero magnetostrictive amorphous alloys.	3203-3213A	
Magnetoelastic effect		
Development of a magnetoelastic resonant sensor using iron-rich, nonzero magnetostrictive amorphous alloys.	3203-3213A	

Splitting phenomena occurring in the martensitic transformation of Cr13 and CrMoV14 stainless steels in the absence of carbide precipitation.	1799-1805A	Heat transfer and pressure drop considerations in the design of Siros melt lances.	221-230B
Thermoelastic martensite and shape memory effect in ductile Cu-Al-Mn alloys.	2187-2195A	Communication: Mechanical deformation of dendrites by fluid flow.	229-232A
NiTi and NiTi-TiC composites. IV. Neutron diffraction study of twinning and shape-memory recovery.	2820-2836A	Communication: Discussion of "Modeling of dynamic materials behavior. A critical evaluation of the dissipator power content approach".	232-235A
The effect of substrate constraint on the martensitic transformation of Ni-Ti thin films.	2858-2860A	Applicability of Butler's equation in interpreting the thermodynamic behavior of surfaces and adsorption in Fe-S-O melts.	241-253B
Influence of training time and temperature on shape memory effect in Cu-Zn-Al alloys.	3108-3111A	A strain-based fracture model for stress corrosion cracking of low-alloy steels.	291-304A
High-resolution transmission electron microscopy investigation of the face-centered cubic/hexagonal close-packed martensite transformation in Co-31.8 wt.% Ni alloy. I. Plate interfaces and growth ledges.	3362-3370A	An extended two-dimensional mathematical model of vertical ring furnaces.	297-304B
High-resolution transmission electron microscopy investigation of the face-centered cubic/hexagonal close-packed martensite transformation in Co-31.8 wt.% Ni alloy. II. Plate intersections, extended defects, and nucleation mechanisms.	3371-3380A	Dynamic behavior of a liquid/liquid interface at an oscillating wall.	305-314B
Martensitic transformations in NiMnAl β phase alloys.	4153-4162A	Interdissolution kinetics in oxide powder mixture using high temperature x-ray diffraction technique.	318-322B
Martensitic transformations, Alloying effects		Thermal decomposition of silicon carbides: discussion of "the effect of an electric field on self sustaining combustion synthesis, I and II", and author's reply.	322-325B
A study on morphology and plate mean dimensions in Fe-Ni and Fe-Ni-Cr alloys.	973-980A	Discussion of "Derivation and consistency of the partial functions of the ternary system involving interaction coefficients" and author's reply.	325-327B
Effect of alloying elements on martensitic transformation in the binary NiAl(β) phase alloys.	2445-2453A	Vacuum evaporation of KCl-NaCl salts. II. Vaporization-rate model and experimental results.	433-443B
Martensitic transformations, Cooling effects		Theoretical modeling of densification during activated solid-state sintering.	441-450A
NiTi and NiTi-TiC composites. III. Shape-memory recovery. Bainite in the light of rapid continuous cooling information.	193-203A	The effect of bulk flow concentration on diffusion coupling between dendrites.	477-480A
1499-1510A	Dilution in single pass arc welds.	481-489B	
Martensitic transformations, Heating effects		A process model for on-line quenching of aluminum extrusions. The x-ray diffraction study of deformation in the composite matrix of Al-Mg-Zn and SiC.	501-508B
Effect of aging on shape memory behavior of Ti-51.3 at.% Ni thin films.	3753-3759A	Transient thermal model of the continuous single-wheel thin-strip casting process.	503-505A
Influence of reinforcement volume fraction and size on the microstructure and abrasion wear resistance of hot isostatic pressed white iron matrix composites.	4171-4181A	Rafting in superalloys.	509-525B
Influence of matrix structure on the abrasion wear resistance and toughness of a hot isostatic pressed white iron matrix composites.	4183-4191A	Some consequences of thermosolutal convection: the grain structure of castings.	513-530A
Martensitic transformations, Stress effects		Numerical modeling of cellular/dendritic array growth: spacing and structure predictions.	569-581A
Predicting the orientation-dependent stress-induced transformation and detwinning response of shape memory alloy single crystals.	269-279A	Intermixing model of continuous casting during a grade transition.	611-623A
Computer simulation of reversible martensitic transformations. Molecular dynamics simulation of martensitic transformations in NiAl.	1187-1201A	Banded solidification microstructures.	617-632B
Effect of stress state on the stress-induced martensitic transformation in polycrystalline Ni-Ti alloy.	1476-1488A	The phase field method: simulation of alloy dendritic solidification during recalescence.	625-634A
Martensitic transformations, Temperature effects		Effects of shear flow and anisotropic kinetics on the morphological stability of a binary alloy.	657-669A
The driving force for martensitic transformations in low alloy steels.	3066-3073A	Prediction of dendrite arm spacing for low alloy steel casting processes.	687-694A
Mass transfer	1127-1132A	An adaptive mesh refinement scheme for solidification problems.	689-693B
Control of iron nitride layers growth kinetics in the binary Fe-N system.	1823-1835A	A study of typical yields of metals.	707-717A
Mathematical analysis		Mathematical modeling of tundish operation and flow control to reduce transition slabs.	731-736A
Van der Waals approximation for potassium bubbles in tungsten.	987-992B	A water model study of the flow asymmetry inside a continuous slab casting mold.	745-756B
Analysis of the stress-strain curves of a modified 9Cr-1Mo steel by the Voce equation.	3340-3343A	Model study of bubble and liquid-flow characteristics in a bottom blown bath under reduced pressure.	757-764B
Temperature dependence of the rate sensitivity and its effect on the activation energy for high-temperature flow.	3346-3348A	The production of nickel-zinc alloys by powder injection.	765-772B
An analysis of the flow stress of a two-phase alloy system, Ti-6Al-4V.	3957-3962A	Modeling and experimental study of gaseous oxidation of liquid iron alloys.	780-787B
Mathematical models		Generalized enthalpy method for multicomponent phase change.	852-862B
Physical modeling studies of electrolyte flow due to gas evolution and some aspects of bubble behavior in advanced Hall cells. III. Predicting the performance of advanced Hall cells.	19-27B	Solid-state contributions to densification during liquid-phase sintering.	869-879B
Hydride formation and decomposition in electrolytically charged metastable austenitic stainless steels.	29-40A	Bridge toughening enhancement in double-notched MoSi ₂ /Nb model composites.	901-909B
Prediction of liquid metal viscosities using an adjustable hard sphere radial distribution curve.	29-34B	Studies of interface deformations in single- and multi-layered liquid baths due to an impinging gas jet.	909-921A
Solubility of carbon in CaO-Al ₂ O ₃ melts.	57-64B	Ostwald ripening in ternary alloys.	911-920B
Representation of mixed reactive gases on free energy (Ellingsham-Richardson) diagrams.	65-69B	A thermodynamic evaluation of the Ti-Mo-C system.	937-943A
Thermomechanics of the cooling stage in casting processes: three-dimensional finite element analysis and experimental validation.	81-99B	Modeling of the peritectic reaction and macro-segregation in casting of low carbon steel.	955-966B
Scaling of intragranular dendritic microstructure in ingot solidification.	101-113B	A one-phase model of the mixing of Al-SiC composite melt.	999-1014B
Vacuum evaporation of KCl-NaCl salts. I. Thermodynamic modeling of vapor pressures of solid and liquid solutions.	141-146B	Theoretical analysis of the particle gradient distribution in centrifugal field during solidification.	1015-1023B
Modeling texture change during the static recrystallization of interstitial free steels.	155-164A	Thermodynamics and long-range order of nitrogen in γ -Fe ₂ N.	1025-1029B
Effective elastic moduli of fiber-matrix interphases in high-temperature composites.	165-182A	^x Theoretical treatment of nitriding and nitrocarburizing of iron.	1055-1061A
A multiphase fluid mechanics approach to gas holdup in bath smelting processes.	195-201B	Modeling iron enrichment in hot-dip galvanneal coatings on interstitial-free steels.	1073-1080A
Dispersed phase holdup in liquid-liquid emulsions generated by high strength bottom gas injection.	213-219B	Computer simulation of reversible martensitic transformations. A comprehensive dynamical study of nucleation and growth in a one-dimensional shear martensitic transition.	1132-1134A
		The normalized Coffin-Manson plot in terms of a new damage function based on grain boundary cavitation under creep-fatigue condition.	1187-1201A
		Theory of nucleation with cluster loss and injection: application to plastic deformation and irradiation.	1203-1216A
		Effect of uniaxial stress on coarsening of precipitate clusters.	1273-1281A
		Characterization of a massive transformation by microstructural analysis.	1441-1448A
			1460-1475A
			1511-1516A

Heterogeneous nucleation of 8 on dislocations in a dilute aluminum-lithium alloy.	1595-1605A	Kinetics of phase evolution of Zn-Fe intermetallics.	2904-2910A
Analysis on the amplitude of serrated flow associated with the Portevin-LeChâtelier effect of substitutional fcc alloys.	1683-1686A	Incipient chemical instabilities of nanophasic Fe-Cu alloys prepared by mechanical alloying.	2934-2946A
Control of iron nitride layers growth kinetics in the binary Fe-N system.	1823-1835A	Microstructure and tensile properties of compacted, mechanically alloyed, nanocrystalline Fe-Al.	3126-3134A
Modeling of microsegregation in macrosegregation computations.	2314-2327A	Thermally assisted and mechanically driven solid-state reactions for formation of amorphous Al ₃₃ Ta ₆₇ alloy powders.	3267-3278A
Theoretical calculation of the stress-strain behavior of dual-phase metals with randomly oriented spheroidal inclusions. Average effective interdiffusion coefficients and the Matano plane composition.	2359-2365A	Microstructural changes in a mechanically alloyed Al-6.22Ni-2.5Mg-1.7Cu alloy (7010) with and without particulate SiC reinforcement.	3718-3726A
A model for macrosegregation and its application to Al-Cu castings.	2504-2509A	Medium carbon steels, Casting	
Determination of the solidification curves of commercial aluminum alloys.	2708-2721A	Analysis of shell thickness irregularity in continuously cast middle carbon steel slabs using mold thermocouple data.	1045-1056B
Equiaxed dendritic solidification with convection. I. Multiscale/multiphase modeling.	2722-2726A	Medium carbon steels, Heat treatment	
Equiaxed dendritic solidification with convection. II. Numerical simulations for an Al-4 wt.% Cu alloy.	2754-2764A	Quenching C60 fullerene into diamond in the Fe-C alloy system by laser treatment.	2293-2296A
Equiaxed dendritic solidification with convection. III. Comparisons with NH ₄ Cl-H ₂ O experiments.	2765-2783A	Medium carbon steels, Phase transformations	
A thermodynamic evaluation of the nickel-silicon system.	2784-2795A	Precipitation behavior in a medium carbon, Ti-V-N microalloyed steel.	1149-1165A
Constitutive behavior of tantalum and tantalum-tungsten alloys.	2897-2903A	Melting	
Control of superplastic deformation rate during uniaxial tensile tests.	2994-3006A	The effect of bulk flow concentration on diffusion coupling between dendrites.	477-480A
Prediction of creep-rupture life of unidirectional titanium matrix composites subjected to transverse loading.	3030-3042A	Analysis and Modeling of Solidification.	509-824A
Tension characteristics of notched specimens for Al-Li-Cu-Zr alloys sheets with various cerium contents.	3074-3080A	Microstructural aspects of the dissolution and melting of Al ₂ Cu phase in Al-Si alloys during solution heat treatment.	1785-1798A
Simulation of the hot-tension test under cavitating conditions.	3089-3094A	Modeling of microsegregation in macrosegregation computations.	2314-2327A
Modeling of ingot distortions during direct chill casting of aluminum alloys.	3112-3119A	Melting points	
A model describing neutron irradiation-induced segregation to grain boundaries in dilute alloys.	3214-3225A	Vacuum evaporation of KCl-NaCl salts. II. Vaporization-rate model and experimental results.	433-443B
Analysis of mean square penetration depth in grain boundary diffusion.	3381-3390A	Melts	
The plastic anisotropy of an Al-Li-Cu-Zr alloy extrusion in unidirectional deformation.	3473-3477A	The separation of the solids from the carrier gas during submerged powder injection.	773-779B
A model for coupled growth of reaction layers in reactive brazing of ZrO ₂ -toughened Al ₂ O ₃ .	3503-3512A	Melts, Chemical analysis	
Plastic zone and pileup around large indentations.	3630-3638A	Reference electrode of simple galvanic cells for developing sodium sensors for use in molten aluminum.	794-800B
Shear ligament phenomena in Fe ₃ Al intermetallics and micro-mechanics of shear ligament toughening.	3793-3800A	Melts, Oxidation	
Evidence of fracture surface interference for cracks loaded in shear detected by phase-shifted speckle interferometry.	3817-3825A	Modeling and experimental study of gaseous oxidation of liquid iron alloys.	852-862B
Creep lifetime prediction of oxide-dispersion-strengthened nickel-base superalloys: a micromechanically based approach.	3853-3860A	Metal powders, Synthesis	
Elevated temperature deformation behavior of a dispersion-strengthened Al-Fe, V, Si alloy.	3861-3870A	Preparation of fine copper powders from organic media by reaction with hydrogen under pressure. I. Experimental study.	577-584B
Flow and fracture of bimaterial systems based on aluminum alloys.	3913-3923A	Preparation of fine copper powders from organic media by reaction with hydrogen under pressure. II. The kinetics of particle nucleation, growth, and dispersion.	585-594B
Measurement of friction under sheet forming conditions.	3937-3947A	Metallic glasses, Atomic properties	
High-temperature oxidation of Ti ₃ Al-based titanium aluminides in oxygen.	3971-3981A	Effects of low-temperature aging on the microstructure and soft magnetic properties of rapidly quenched Fe-Si-B alloys.	2454-2460A
Infrared transient-liquid-phase joining of SCS-6/β21S titanium matrix composite.	3993-4002A	Metallic glasses, Crystal growth	
Nonuniform distribution of carbonitride particles and its effect on prior austenite grain size in the simulated coarse-grained heat-affected zone of thermomechanical control-processed steels.	4011-4018A	Crystallization of amorphous phase in sputter-deposited Ti-Al alloy thin films.	2047-2050A
Macrotransport-solidification kinetics modeling of equiaxed dendritic growth. I. Model development and discussion.	4031-4038A	The effect of metallic elements on the crystallization behavior of amorphous Fe-Si-B alloys.	3424-3430A
Macrotransport-solidification kinetics modeling of equiaxed dendritic growth. II. Computation problems and validation on Inconel 718 superalloy casting.	4061-4074A	Metallic glasses, Magnetic properties	
Modeling of primary and secondary dendrites in a Cu-6 wt.% tin alloy.	4075-4083A	Development of a magnetoelastic resonant sensor using iron-rich, nonzero magnetostrictive amorphous alloys.	3203-3213A
Mathematical modeling of the extrusion of 6061/Al ₂ O ₃ /20p composite.	4085-4093A	Metallic glasses, Powder technology	
Modeling particle fracture during the extrusion of aluminum/alumina composites.	4095-4111A	Thermally assisted and mechanically driven solid-state reactions for formation of amorphous Al ₃₃ Ta ₆₇ alloy powders.	3267-3278A
Modeling recrystallization kinetics, grain sizes, and textures during multipass hot rolling.	4113-4120A	Metallizing	
Lamellar growth of eutectic equiaxed grains.	4133-4144A	Characterization of titanium thin films prepared by bias assisted magnetron sputtering.	1057-1060B
Mechanical alloying	4205-4210A	Metastable phases	
Mechanical alloying of Nb-Al powders.	41-48A	Interface attachment kinetics in alloy solidification.	671-686A
Effect of primary grain size on the secondary recrystallization of mechanically alloyed oxide dispersion strengthened nickel-based superalloy.	493-496A	Stable and metastable ordered phases in microcrystalline alloys Ni (Fe, Mn, Ti).	2045-2048A
Identification of precipitate phases in a mechanically alloyed rapidly solidified Al-Fe-Ce alloy.	1033-1041A	Microstructural development of a gas-atomized and hot-pressed super- α_2 alloy.	2221-2228A
Tensile properties of mechanically alloyed/milled ODS-Ni-based alloys.	1371-1377A	Kinetics of phase evolution of Zn-Fe intermetallics.	2904-2910A
Recrystallization in oxide-dispersion strengthened mechanically alloyed sheet steel.	1963-1978A	High-resolution electron microscopy analysis of structural defects in a (2/1, 5/3)-type approximant of a decagonal quasicrystal of an Al-Pd-Mn alloy.	2911-2915A
Milling dynamics. II. Dynamics of a SPEX mill and a one-dimensional mill.	1991-1997A	Solidification of undercooled Fe-Cr-Ni alloys. II. Microstructural evolution.	3226-3240A
Milling dynamics. III. Integration of local and global modeling of mechanical alloying devices.	1999-2004A	An isothermal section at 550°C in the Al-rich corner of the Al-Fe-Mn-Si system.	3357-3361A
		Microstructure of Cu-Co alloys solidified at various supercoolings.	4049-4059A
		Metastable phases, Alloying effects	
		Identification of precipitate phases in a mechanically alloyed rapidly solidified Al-Fe-Ce alloy.	1033-1041A

Metastable phases, Composition effects		
Hydride formation and decomposition in electrochemically charged metastable austenitic stainless steels.	29-40A	Modulus of elasticity, High temperature effects
		Effective elastic moduli of fiber-matrix interphases in high-temperature composites.
		165-182A
Metastable phases, Temperature effects		Modulus of elasticity, Microstructural effects
Nucleation controlled solidification kinetics.	533-547A	NiTi and NiTi-TiC composites. II. Compressive mechanical properties.
Eutectoid decomposition in Ag-Ga.	1676-1682A	Effect of bainite transformation and retained austenite on mechanical properties of austempered spheroidal graphite cast steel.
		1585-1594A
Microalloying		Temperature dependent deformation of polydomain phases in an In-22.5 at.% Ti shape memory alloy.
Influence of microalloying on the corrosion resistance of steel in saturated calcium hydroxide.	1693-1699A	
Microhardness		Modulus of elasticity, Stress effects
The control of grain size and distribution of particles in a (6061 alloy) _m /(Al ₂ O ₃) _n composite by solutionizing treatment.	2023-2034A	Subcritical crack growth at bimaterial interfaces. I. Flexural peel technique.
		205-211A
Microhardness, Coating effects		Temperature dependence of the intrinsic small fatigue crack growth behavior in nickel-base superalloys based on measurement of crack closure.
Microstructural analysis and oxidation behavior of laser-processed Fe-Cr-Al-Y alloy coatings.	381-390A	
Microhardness, Cooling effects		Modulus of elasticity, Temperature effects
Rapid solidification processing of a Mg-Li-Si-Ag alloy.	1363-1370A	Observations of secondary carbide precipitation and its relation to high-temperature flow and fracture in HT-9 stainless steel.
		467-469A
Microhardness, Heating effects		Modulus of rupture in bending, Stress effects
Mechanical properties and 95°C aging characteristics of zircon reinforced Zn-4Al-3Cu alloy.	809-818A	Subcritical crack growth at bimaterial interfaces. I. Flexural peel technique.
Influence of long term annealing on tensile properties and fracture of near-eut. titanium alloy Ti-6Al-2.75Sn-4Zr-0.4Mo-0.45Si.	1700-1708A	Subcritical crack growth at bimaterial interfaces. III. Shear-enhanced fatigue crack growth resistance at polymer/metal interface.
		221-228A
Microhardness, Microstructural effects		Molds
Mechanical behavior of the <i>in situ</i> composite alloys in the Al-Ni-Ti system near the L ₁ phase field.	71-79A	A water model study of the flow asymmetry inside a continuous slab casting mold.
Precipitation in lead-calcium alloys containing tin.	1668-1675A	757-764B
		Molybdenum, Alloying additive
Microhardness, Welding effects		The effect of Mo addition on the liquid-phase sintering of W heavy alloy.
Cleavage initiation in the intercritically reheated coarse-grained heat affected zone. II. Failure criteria and statistical effects.	3019-3029A	3120-3125A
Effect of postweld treatment on the fatigue crack growth rate of electron-beam-welded AISI 4130 steel.	3162-3169A	
		Molybdenum, Binary systems
Microporosity		Critical evaluation and optimization of the thermodynamic properties of liquid tin solutions.
Permeability of microporous carbon preforms.	3669-3674A	808-826B
		Molybdenum, Composite materials
Microscopy		Investigation of the reaction zone between TiAl and molybdenum.
Quantitative characterization of the surface topography of rolled sheets by laser scanning microscopy and Fourier transformation.	2338-2346A	2285-2292A
		Molybdenum, Extraction
Microstructure		Zinc reduction of MoO ₃ in a self propagating high temperature synthesis process.
The effect of thermal cycle on the microstructural development of a powder metallurgy superalloy braze material.	145-153A	315-318B
Comparative study of pore structure evolution during solvent and thermal debinding of powder injection molded parts.	245-253A	
Characterization and mechanical properties of ultrahigh boron steels produced by powder metallurgy.	1861-1867A	3793-3800A
On the role of magnesium and silicon in the formation of alumina from aluminum alloys by means of DILOX processing.	2094-2099A	
Microstructure and properties of Al ₂ O ₃ -Al(Si) and Al ₂ O ₃ -Al(Si)-Si composites formed by <i>in situ</i> reaction of aluminum with aluminosilicate ceramics.	2122-2129A	2869-2880A
		Molybdenum, Ternary systems
Microstructure, Heating effects		A thermodynamic evaluation of the Ti-Mo-C system.
Evolution of microstructures in the nickel modified titanium tri-aluminides near the L ₁ phase field.	5-17A	955-966B
		Molybdenum compounds, Composite materials
Microstructure, High temperature effects		Bridge toughening enhancement in double-notched MoSi ₂ /Nb model composites.
Phase relations of a silicide/silica reaction couple at 2273K.	271-276B	909-921A
		Fracture and fatigue-crack growth behavior in ductile-phase toughened molybdenum disilicide: effects of niobium wire vs. particulate reinforcements.
		3781-3792A
Mischmetal, Alloying additive		Molybdenum compounds, Reactions (chemical)
A study of the influence of mischmetal additions to Al-7Si-0.3Mg (IM 25/356) alloy.	1283-1292A	Modeling of sequential reactions during micropyrolytic synthesis.
		961-972A
Miscibility		Molybdenum steels, Mechanical properties
Retrograde solubility in semiconductors.	2704-2707A	Effect of alloying additions on fracture behavior of molybdenum-containing secondary hardening steels.
		3343-3346A
Mixing		Monitoring
Intermixing model of continuous casting during a grade transition.	617-632B	The measurement of hydrogen activities in molten copper using an oxide protonic conductor.
		929-935B
Modulus of elasticity		Mossbauer spectroscopy
Communication: On the <i>in situ</i> formation of TiC and Ti ₂ C reinforcements in combustion-assisted synthesis of titanium matrix composites.	237-240A	Incipient chemical instabilities of nanophasic Fe-Cu alloys prepared by mechanical alloying.
		2934-2946A
Thermal stability of SIC-SCS-6 fiber-reinforced IMI834 alloys.	1403-1405A	Multilayers, Rolling
Microstructure and properties of Al ₂ O ₃ -Al(Si) and Al ₂ O ₃ -Al(Si)-Si composites formed by <i>in situ</i> reaction of aluminum with aluminosilicate ceramics.	2122-2129A	Nanoscale brass/steel multilayer composites produced by cold rolling.
		2383-2385A
The effects on fracture toughness of ductile-phase composition and morphology in Nb-Cr-Ti and Nb-Si <i>in situ</i> composites.	3007-3018A	Nanomaterials, Microstructure
The balance of mechanical and environmental properties of a multielement niobium-niobium silicide-based <i>in situ</i> composite.	3801-3808A	Microstructure and tensile properties of compacted, mechanically alloyed, nanocrystalline Fe-Al.
		3126-3134A
Modulus of elasticity, Alloying effects		Nanomaterials, Synthesis
Tension characteristics of notched specimens for Al-Li-Cu-Zr alloy sheets with various cerium contents.	3089-3094A	Synthesis of full-density nanocrystalline tungsten carbide by reduction of tungsten oxide at room temperature.
Elastic moduli of titanium-hydrogen alloys in the temperature range 20°C to 1100°C.	3963-3970A	Synthesis of nanocrystalline Ni ₃ Cu by sol-gel route.
		4210-4213A
		4213-4216A
		Near net shaping
		Optimization of cold and warm workability in 304 stainless steel using instability maps.
		Liquid state infrared processing of SCS-6/Ti-6Al-4V composites.
		527-532B

Phase transformations in condensed systems revisited: Industrial applications.	2397-2418A	Nickel, Oxidation	The growth and structure of thin oxide films on cerium ion-implanted nickel.	3649-3661A
<i>The plastic anisotropy of an Al-Li-Cu-Zr alloy extrusion in unidirectional deformation.</i>	3503-3512A			
<i>The squeeze casting of hypoeutectic binary Al-Cu.</i>	4121-4132A	Nickel, Ternary systems	<i>Evolution of microstructures in the nickel modified titanium tri-aluminides near the L₁ phase field.</i>	5-17A
Necking			<i>Mechanical behavior of the in situ composite alloys in the Al-Ni-Ti system near the L₁ phase field.</i>	71-79A
<i>Simulation of the hot-tension test under cavitating conditions.</i>	3112-3119A		<i>Mechanical properties of Ru-Ni-Al alloys.</i>	1395-1400A
<i>High-temperature deformation and failure of an orthorhombic titanium aluminide sheet material.</i>	3675-3681A	Thermodynamic and kinetic study of diffusion paths in the system Cu-Fe-Ni.		2229-2238A
Necking, Deformation effects			<i>Thermodynamic activities and phase boundaries for the alloys of the Ni₃Al-Ni₃Ti pseudobinary section in the Ni-Al-Ti system.</i>	2673-2677A
<i>Micronecking and fracture in cavitated superplastic materials.</i>	1043-1046A		<i>Solidification of undercooled Fe-Cr-Ni alloys. II. Microstructural evolution.</i>	3226-3240A
Necking, Microstructural effects			<i>Thermodynamic activities and partial enthalpies of mixing in the solid solution of Fe in Ni₃Al.</i>	3569-3575A
<i>Bridge toughening enhancement in double-notched MoSi₂/Nb model composites.</i>	909-921A		<i>Martensitic transformations in NiMnAl β phase alloys.</i>	4153-4162A
Necking, Stress effects		Nickel base alloys		
<i>Reinforcement stresses during deformation of sphere- and particulate-reinforced aluminum-matrix composites.</i>	486-490A	<i>Recrystallization in oxide-dispersion strengthened mechanically alloyed sheet steel.</i>		1963-1978A
Neodymium, Binary systems		Nickel base alloys, Casting	<i>Viscosity of superalloy 718 by the oscillating vessel technique.</i>	698-701B
<i>Inverse melting in binary systems: morphology and microscopy of cataclysmic alloys.</i>	979-986B			
Neutron activation analysis		Nickel base alloys, Claddings	<i>Solidification of an alloy 625 weld overlay.</i>	3612-3620A
<i>Determination of hydrogen in titanium alloys by cold neutron prompt gamma activation analysis.</i>	3682-3687A		<i>The wear behavior between hardfacing materials.</i>	3639-3648A
Neutron diffraction		Nickel base alloys, Coating		
<i>Neutron diffraction study of austempered ductile iron.</i>	923-928A	<i>Isothermal fatigue of an aluminide-coated single-crystal superalloy. I.</i>		353-361A
<i>Real-time observations of the oxidation of mild steel at high temperature by neutron diffraction.</i>	993-997B		<i>Isothermal fatigue of an aluminide-coated single-crystal superalloy. II. Effects of brittle precracking.</i>	363-369A
Neutron scattering		Nickel base alloys, Composite materials		
<i>Incipient chemical instabilities of nanoparticle Fe-Cu alloys prepared by mechanical alloying.</i>	2934-2946A	<i>Microstructure of bonding zones in laser-clad nickel-alloy-based composite coatings reinforced with various ceramic powders.</i>		391-400A
New technology		<i>Microstructure of Al₂O₃ fiber-reinforced superalloy (Inconel 718) composites.</i>		451-458A
<i>Alternative technologies in iron and steelmaking.</i>	541-553B	<i>Effect of primary grain size on the secondary recrystallization of mechanically alloyed oxide dispersion strengthened nickel-based superalloy.</i>		493-498A
Nickel, Alloying additive		<i>Tensile properties of mechanically alloyed/milled ODS-Ni-based alloys.</i>		1371-1377A
<i>Solid-state contributions to densification during liquid-phase sintering.</i>	901-909B	Nickel base alloys, Corrosion		
Nickel, Alloying elements		<i>Structure, chemistry, and stress corrosion cracking of grain boundaries in alloys 600 and 690.</i>		327-341A
<i>Effects of nickel on the sintering behavior of Fe-Ni compacts made from composite and elemental powders.</i>	203-211B	Nickel base alloys, Crystal growth		
<i>The production of nickel-zinc alloys by powder injection.</i>	780-787B	<i>Macrotransport-solidification kinetics modeling of equiaxed dendritic growth. I. Model development and discussion.</i>		4061-4074A
<i>A study on morphology and plate mean dimensions in Fe-Ni and Fe-Ni-Cr alloys.</i>	973-980A	<i>Macrotransport-solidification kinetics modeling of equiaxed dendritic growth. II. Computation problems and validation on Inconel 718 superalloy casting.</i>		4075-4083A
Nickel, Atomic properties		Nickel base alloys, Crystal lattices		
<i>Sputter-induced pits on (100) nickel surfaces.</i>	981-993A	<i>Lattice misfits in four binary Ni-base γ/γ' alloys at ambient and elevated temperatures.</i>		2888-2896A
Nickel, Binary systems		Nickel base alloys, Forming		
<i>Standard enthalpies of formation of dysprosium alloys, Dy+Me (Me=Ni, Ru, Rh, Pd, Ir, and Pt), by high-temperature direct synthesis calorimetry.</i>	417-422B	<i>Reply: Dynamic materials model. Basis and principles.</i>		235-236A
<i>Critical evaluation and optimization of the thermodynamic properties of liquid tin solutions.</i>	808-826B	Nickel base alloys, Heat treatment		
<i>Generalized enthalpy method for multicomponent phase change.</i>	868-879B	<i>High-temperature nitridation of Ni-Cr alloys</i>		59-69A
<i>A thermodynamic evaluation of the nickel-silicon system.</i>	2897-2903A	<i>Effect of homogenization heat treatment on the microstructure and heat affected zone microfissuring in welded cast alloy 718.</i>		785-790A
<i>Thermochemistry of the Ni-Hf system—intermetallic phases.</i>	3578-3590A	<i>Transition between internal and external nitridation of Ni-Ti alloys.</i>		1606-1617A
Nickel, Bonding		Nickel base alloys, Joining		
<i>Microstructural development in NiAl/Ni-Si-B/Ni transient liquid phase bonds.</i>	1925-1931A	<i>Transient liquid-phase bonding in the NiAl/Cu/Ni system—a microstructural investigation.</i>		3621-3629A
Nickel, Crystal growth		Nickel base alloys, Mechanical properties		
<i>High-speed imaging and analysis of the solidification of undercooled nickel melts.</i>	863-868B	<i>The effect of hydrogen on the fracture of alloy X-750.</i>		101-110A
Nickel, Diffusion		<i>Predicting the orientation-dependent stress-induced transformation and detwinning response of shape memory alloy single crystals.</i>		269-279A
<i>Hydrogen trapping and permeation in nickel thoria.</i>	2495-2503A	<i>Creep deformation and crack growth behavior of a single-crystal nickel-base superalloy.</i>		829-837A
Nickel, Extraction		<i>On the influence of grain morphology on creep deformation and damage mechanisms in directionally solidified and oxide dispersion strengthened superalloys.</i>		879-890A
<i>Bioleaching of lateritic nickel ore by ultrasound.</i>	351-354B	<i>High-temperature measurements of lattice parameters and internal stresses of a creep-deformed monocrystalline nickel-base superalloy.</i>		1003-1014A
<i>A study of solid-aqueous equilibria by the speciation approach in the hydronium alunite-sulfuric acid-water system at high temperatures.</i>	555-566B	<i>Temperature dependence of the intrinsic small fatigue crack growth behavior in nickel-base superalloys based on measurement of crack closure.</i>		1021-1031A
<i>Experimental study of splash generation in a flash smelting furnace.</i>	633-646B			
<i>Phase equilibria in the metal-sulfur-oxygen system and selective reduction of metal oxides and sulfides. I. The carbothermic reduction and calcination of complex mineral sulfides.</i>	827-838B			
Nickel, Forming				
<i>Reply: Dynamic materials model. Basis and principles.</i>	235-236A			
Nickel, Joining				
<i>Transient liquid-phase bonding in the NiAl/Cu/Ni system—a microstructural investigation.</i>	3621-3629A			
Nickel, Metallography				
<i>An optical method for determining the surface orientation of crystals.</i>	2057-2061A			

Nickel base alloys, Metal working		
Flow stress and microstructural evolution during hot working of alloy 22Cr-13Ni-5Mn-0.3N austenitic stainless steel.	1251-1268A	
Nickel base alloys, Microstructure		
Prediction of grain structures in various solidification processes.	695-705A	
Characterization of constitutional liquid film migration in nickel-base alloy 718.	2692-2703A	
Nickel base alloys, Phase transformations		
Effect of alloying elements on martensitic transformation in the binary NiAl(B) phase alloys.	2445-2453A	
The effect of substrate constraint on the martensitic transformation of Ni-Ti thin films.	2858-2860A	
Effect of stress state on the stress-induced martensitic transformation in polycrystalline Ni-Ti alloy.	3066-3073A	
Effect of aging on shape memory behavior of Ti-51.3 at. % Ni thin films.	3753-3759A	
Martensitic transformations in NiMnAl β phase alloys.	4153-4162A	
Nickel base alloys, Phases (state of matter)		
Nucleation controlled solidification kinetics.	533-547A	
The phase field method: simulation of alloy dendritic solidification during recalescence.	657-669A	
The breakdown of single-crystal solidification in high refractory nickel-base alloys.	1081-1094A	
Nickel base alloys, Powder technology		
The effect of thermal cycle on the microstructural development of a powder metallurgy superalloy braze material.	145-153A	
Nickel base alloys, Structural hardening		
A study on coherency strain and precipitate morphology via a discrete atom method.	1449-1459A	
Bauschinger effect in Haynes 230 alloy: influence of strain rate and temperature.	1739-1748A	
Preferential coarsening of γ' precipitates in Inconel 718 during creep.	3391-3398A	
Manifestations of dynamic strain aging in soft-oriented NiAl single crystals.	3542-3557A	
Creep lifetime prediction of oxide-dispersion-strengthened nickel-base superalloys: a micromechanically based approach.	3861-3870A	
Nickel chromium molybdenum steels, Cladding		
Ballistic impact behavior of multilayered armor plates processed by hardfacing.	3335-3340A	
Nickel chromium molybdenum steels, Heat treatment		
The dependence of complex alloyed steel properties on quenching and tempering conditions.	2852-2858A	
Nickel chromium molybdenum steels, Mechanical properties		
On the transition of fatigue crack growth from stage I to stage II in a corrosive environment.	471-476A	
High cycle fatigue behavior of gas-carburized medium carbon Cr-Mo steel.	2557-2564A	
Effect of alloying additions on fracture behavior of molybdenum-containing secondary hardening steels.	3343-3346A	
Conditioning monitoring by microstructural evaluation of cumulative fatigue damage.	3841-3851A	
Nickel chromium molybdenum steels, Phases (state of matter)		
Copper precipitation during continuous cooling and isothermal aging of A710 type steels.	1569-1584A	
Nickel compounds		
Martensitic transformations in NiMnAl β phase alloys.	4153-4162A	
Nickel compounds, Bonding		
Microstructural development in NiAl/Ni-Si-B/Ni transient liquid phase bonds.	1925-1931A	
Nickel compounds, Composite materials		
NiTi and NiTi-TiC composites. II. Compressive mechanical properties.	183-191A	
NiTi and NiTi-TiC composites. III. Shape-memory recovery.	193-203A	
Formation of structural intermetallics by reactive metal penetration of titanium and nickel oxides and aluminides.	2100-2104A	
Ni ₃ Al intermetallic particles as wear-resistant reinforcement for Al-base composites processed by powder metallurgy.	3259-3266A	
Nickel compounds, Joining		
Transient liquid-phase bonding in the NiAl/Cu/Ni system—a microstructural investigation.	3621-3629A	
Nickel compounds, Mechanical properties		
Non-Schmid effects on the behavior of polycrystals, with applications to Ni ₃ Al.	81-99A	
Rating superalloys.	513-530A	
High-temperature deformation properties of NiAl single crystals.	1229-1240A	
Elevated temperature compressive properties of zirconium-modified NiAl.	2628-2641A	
Elevated temperature compressive properties of N-doped NiAl.	3170-3180A	
Nickel compounds, Phase transformations		
Molecular dynamics simulation of martensitic transformations in NiAl.	1476-1488A	
Effect of alloying elements on martensitic transformation in the binary NiAl(B) phase alloys.	2445-2453A	
NiTi and NiTi-TiC composites. IV. Neutron diffraction study of twinning and shape-memory recovery.	2820-2836A	
The effect of substrate constraint on the martensitic transformation of Ni-Ti thin films.	2858-2860A	
Nickel compounds, Phases (state of matter)		
Stable and metastable ordered phases in microcrystalline alloys Ni (Fe, Mn, Ti).	2045-2046A	
Nickel compounds, Structural hardening		
Manifestations of dynamic strain aging in soft-oriented NiAl single crystals.	3542-3557A	
Nickel compounds, Synthesis		
Synthesis of nanocrystalline Ni ₃ Cu by sol-gel route.	4213-4216A	
Nickel compounds, Thermal properties		
Thermodynamic activities and partial enthalpies of mixing in the solid solution of Fe in Ni ₃ Al.	3569-3575A	
Nickel ores		
Bioleaching of lateritic nickel ore by ultrasound.	351-354B	
Niobium, Alloying additive		
The effect of metallic elements on the crystallization behavior of amorphous Fe-Si-B alloys.	3424-3430A	
Niobium, Alloying elements		
Mechanical alloying of Nb-Al powders.	41-48A	
The influence of niobium supersaturation in austenite on the static recrystallization behavior of low carbon microalloyed steels.	951-960A	
The effects on fracture toughness of ductile-phase composition and morphology in Nb-Cr-Ti and Nb-Si in situ composites.	3007-3018A	
Niobium, Binary systems		
Thermodynamic assessment of the Nb-N system.	3591-3600A	
Niobium, Composite materials		
Loading rate and test temperature effects on fracture of in situ niobium silicide-niobium composites.	3292-3306A	
Fracture and fatigue-crack growth behavior in ductile-phase toughened molybdenum disilicide: effects of niobium wire vs. particulate reinforcements.	3781-3792A	
Niobium, Diffusion		
Analysis of mean square penetration depth in grain boundary diffusion.	3473-3477A	
Niobium, Dopants		
High-temperature oxidation of Ti ₃ Al-based titanium aluminides in oxygen.	3993-4002A	
Niobium, Heat treatment		
Improved oxidation resistance of group VB refractory metals by Al ⁺ ion implantation.	491-500B	
Niobium, Mechanical properties		
Influence of interstitials on the mechanical properties of metallic materials.	3524-3529A	
Niobium, Powder technology		
Milling dynamics. III. Integration of local and global modeling of mechanical alloying devices.	1999-2004A	
Niobium base alloys, Composite materials		
The fracture toughness of niobium-based, in situ composites.	2518-2531A	
The effects on fracture toughness of ductile-phase composition and morphology in Nb-Cr-Ti and Nb-Si in situ composites.	3007-3018A	
The balance of mechanical and environmental properties of a multielement niobium-niobium silicide-based in situ composite.	3801-3808A	
Niobium base alloys, Phases (state of matter)		
Phase transformations in Nb-Al-Ti alloys.	1642-1654A	
Niobium compounds, Composite materials		
Loading rate and test temperature effects on fracture of in situ niobium silicide-niobium composites.	3292-3306A	
The balance of mechanical and environmental properties of a multielement niobium-niobium silicide-based in situ composite.	3801-3808A	
Nitrides		
Microstructure and tensile behavior of nitrogen-alloyed, dual-phase stainless steels.	1845-1859A	
Mössbauer spectroscopy study of the aging and tempering of high nitrogen quenched Fe-N alloys: kinetics of formation of Fe _{1-x} N _x nitride by interstitial ordering in martensite.	2160-2177A	
Nitriding		
High-temperature nitridation of Ni-Cr alloys	59-69A	
Theoretical treatment of nitriding and nitrocarburizing of iron. Transition between internal and external nitridation of Ni-Ti alloys.	1073-1080A	
	1606-1617A	

Control of iron nitride layers growth kinetics in the binary Fe-N system.	1823-1835A	Crystallography of grain boundary α precipitates in a β titanium alloy.	1630-1641A
Nitrogen, Alloying additive		The mechanism of formation of a fine duplex microstructure in Ti-48Al-2Mn-2Nb alloys.	1655-1667A
Elevated temperature compressive properties of N-doped NiAl.	3170-3180A	On the role of magnesium and silicon in the formation of alumina from aluminum alloys by means of DIMOX processing.	2094-2099A
Nitrogen, Alloying elements		The role of coincident site lattice boundaries during selective growth in interstitial-free steels.	2178-2186A
Thermodynamics and long-range order of nitrogen in γ -Fe ₃ N.	1055-1061A	Modeling recrystallization kinetics, grain sizes, and textures during multipass hot rolling.	4133-4144A
^x An evaluation of the Fe-N phase diagram considering long-range order of nitrogen atoms in γ -Fe ₃ N _{1-x} and ϵ -Fe ₂ N _{1-x} .	1063-1071A	Nucleation, Cooling effects	480-483A
Electron microscopic study of Cr ₂ N formation in thermally aged 316LN austenitic stainless steels.	1175-1186A	The role of grain corners in nucleation.	695-705A
Nitrogen, Binary systems		Prediction of grain structures in various solidification processes.	
Control of iron nitride layers growth kinetics in the binary Fe-N system.	1823-1835A	Nucleation, Heating effects	
Thermodynamic assessment of the Nb-N system.	3591-3600A	Effect of superheat on the solidification structures of AISI 310S austenitic stainless steel.	287-296B
Nitrogen, Environment		Effect of primary grain size on the secondary recrystallization of mechanically alloyed oxide dispersion strengthened nickel-based superalloy.	493-496A
Effect of nitrogen on the oxidation behavior of Ti ₃ Al-based intermetallic alloys.	4003-4010A	Characterization of the formation of α_1 plates from the β_3 phase in a Cu-Zn-Au alloy.	719-724A
Nitrogen, Impurities		Heterogeneous nucleation of δ on dislocations in a dilute aluminum-lithium alloy.	1595-1605A
Physical chemistry of the powder metallurgy of beryllium: chemical characterization of the powder in relation to its granularity.	371-379A	Nucleation, Radiation effects	
Nitrogen, Quaternary systems		Theory of nucleation with cluster loss and injection: application to plastic deformation and irradiation.	1441-1448A
An experimental study and thermodynamic calculations of phase equilibria in the Fe-Mo-C-N system.	2869-2880A	Nucleation, Stress effects	
Nitrogen, Reactions (chemical)		On the effect of stress on nucleation and growth of precipitates in an Al-Cu-Mg-Ag alloy.	3431-3444A
Modeling and experimental study of gaseous oxidation of liquid iron alloys.	852-862B	Nucleation, Temperature effects	
Nitrogen, Solubility		RAFTing in superalloys.	513-530A
Effects of oxygen, selenium, and tellurium on the rate of nitrogen dissolution in molten iron.	846-851B	Nucleation controlled solidification kinetics.	533-547A
Nodular iron		Banded solidification microstructures.	625-634A
Modeling of ferrite growth in nodular cast iron.	2209-2220A	Morphological instabilities of lamellar eutectics.	635-656A
Nodular iron, Crystal growth		The formation mechanism(s), morphology, and crystallography of ferrite sideplates.	1517-1532A
Modeling of ferrite growth in nodular cast iron.	2209-2220A	Numerical analysis	
Nodular iron, Mechanical properties		Interface effects on the micromechanical response of a transversely loaded single fiber SCS-6/Ti-6Al-4V composite.	2035-2043A
Effect of holding time in the (α - γ) temperature range on toughness of specially austempered ductile iron.	1979-1989A	A model for macrosegregation and its application to Al-Cu castings.	2708-2721A
Nodular iron, Microstructure		Equiaxed dendritic solidification with convection. II. Numerical simulations for an Al-4 wt.% Cu alloy.	2765-2783A
Neutron diffraction study of austempered ductile iron.	923-928A	Equiaxed dendritic solidification with convection. III. Comparisons with NH ₄ CH ₂ O experiments.	2784-2795A
Nonferrous metals, Extraction		Modeling of ingot distortions during direct chill casting of aluminum alloys.	3214-3225A
The separation of the solids from the carrier gas during submerged powder injection.	773-779B	Evidence of fracture surface interference for cracks loaded in shear detected by phase-shifted speckle interferometry.	3853-3860A
Notch sensitivity		Modeling of primary and secondary dendrites in a Cu-6 wt.% tin alloy.	4085-4093A
A comparison of fracture behavior of low alloy steel with different sizes of carbide particles.	1909-1917A	Oils, Environment	
Notch strength		Hydrogen-induced cleavage fracture of Fe ₃ Al-based intermetallics.	3949-3956A
Notch fracture in γ -titanium aluminides.	3903-3912A	Optical microscopy	
Notch strength, Alloying effects		Inverse melting in binary systems: morphology and microscopy of catastrophic alloys.	979-986B
Tension characteristics of notched specimens for Al-Li-Cu-Zr alloys sheets with various cerium contents.	3089-3094A	An optical method for determining the surface orientation of crystals.	2057-2061A
Notch strength, Welding effects		Thermally assisted and mechanically driven solid-state reactions for formation of amorphous Al ₃₃ Te ₆₇ alloy powders.	3267-3278A
Cleavage initiation in the intercritically reheated coarse-grained heat affected zone. II. Failure criteria and statistical effects.	3019-3029A	Infrared transient-liquid-phase joining of SCS-6/B21S titanium matrix composite.	4011-4018A
Nuclear fusion reactors, Irradiation		Microstructural features of friction welded MA 956 superalloy material.	4019-4029A
Theory of nucleation with cluster loss and injection: application to plastic deformation and irradiation.	1441-1448A	Creep deformation and damage in a continuous fiber-reinforced Ti-6Al-4V composite.	4193-4204A
Nuclear power generation		Order disorder	
Gibbs energies of formation of chromium carbides.	1919-1924A	Mössbauer spectroscopy study of the aging and tempering of high nitrogen quenched Fe-N alloys: kinetics of formation of Fe ₁₈ N ₂ nitride by interstitial ordering in martensite.	2160-2177A
Nuclear reactor components, Corrosion		Thermoelastic martensite and shape memory effect in ductile Cu-Al-Mn alloys.	2187-2195A
Structure, chemistry, and stress corrosion cracking of grain boundaries in alloys 600 and 690.	327-341A	Microstructural development of a gas-atomized and hot-pressed super- α_2 alloy.	2221-2228A
Influence of thermal aging on the intergranular corrosion resistance of types 304LN and 316LN stainless steels.	2881-2887A	A thermodynamic evaluation of the nickel-silicon system.	2897-2903A
Nuclear reactor components, Extrusion		Order disorder, Heating effects	
Microsegregation of oxygen in Zr-2.5Nb alloy materials.	431-440A	Characterization of the formation of α_1 plates from the β_3 phase in a Cu-Zn-Au alloy.	719-724A
Nucleation		Order disorder, Temperature effects	
Atomistic Mechanisms of Nucleation and Growth in Solids. Modeling texture change during the static recrystallization of interstitial free steels.	155-164A	Rafting in superalloys.	513-530A
Preparation of fine copper powders from organic media by reaction with hydrogen under pressure. II. The kinetics of particle nucleation, growth, and dispersion.	585-594B	Organic compounds	
High-speed imaging and analysis of the solidification of under-cooled nickel melts.	863-868B	Preparation of fine copper powders from organic media by reaction with hydrogen under pressure. I. Experimental study.	577-584B
Creep deformation of dispersion-strengthened copper.	1217-1227A		
Characterization of a massive transformation by microstructural analysis.	1511-1516A		
Formation of bainite in ferrous and nonferrous alloys through sympathetic nucleation and ledgewise growth mechanism.	1533-1543A		

Preparation of fine copper powders from organic media by reaction with hydrogen under pressure. II. The kinetics of particle nucleation, growth, and dispersion.	585-594B	Oxygen, Alloying additive Effects of oxygen, selenium, and tellurium on the rate of nitrogen dissolution in molten iron.	846-851B
Orientation An optical method for determining the surface orientation of crystals.	2057-2061A	Oxygen, Binary systems Critical evaluation and optimization of the thermodynamic properties of liquid tin solutions.	808-826B
Oscillations Viscosity of superalloy 718 by the oscillating vessel technique.	698-701B	Oxygen, Impurities Physical chemistry of the powder metallurgy of beryllium: chemical characterization of the powder in relation to its granularity.	371-379A
Ostwald ripening Ostwald ripening in ternary alloys.	937-943A	Microsegregation of oxygen in Zr-2.5Nb alloy materials.	431-440A
Ostwald ripening of solid-liquid Pb-Sn dispersions.	2470-2478A	Thermodynamic properties of oxygen in yttrium-oxygen solid solutions.	839-845B
Precipitation behaviors in Al-Cu-Mg and 2024 aluminum alloys.	2479-2494A		
Preferential coarsening of γ' precipitates in Inconel 718 during creep.	3391-3398A	Oxygen, Quaternary systems Thermodynamic properties of complex oxides in the Sm-Ba-Cu-O system.	973-978B
M_2C precipitates in isothermal tempering of high Co-Ni secondary hardening steel.	3466-3472A	Oxygen, Ternary systems Applicability of Butler's equation in interpreting the thermodynamic behavior of surfaces and adsorption in Fe-S-O melts.	241-253B
Oxidation Probing the initial stage of synthesis of Al_2O_3/Al composites by directed oxidation of Al-Mg alloys.	43-50B	Pack cementation The deposition of aluminide and silicide castings on γ -TiAl using the halide-activated pack cementation method.	3761-3772A
Representation of mixed reactive gases on free energy (Ellingham-Richardson) diagrams.	65-69B	Pack siliconizing The deposition of aluminide and silicide castings on γ -TiAl using the halide-activated pack cementation method.	3761-3772A
Reoxidation of aluminum in Fe-Al-M (M=C, Mn, and Ti) melts with $CaO-Al_2O_3-FeO$ (3 mass%) slags.	423-431B		
On the stable Mg-Zn-Y quasicrystals.	1779-1784A	Palladium, Binary systems Standard enthalpies of formation of dysprosium alloys, Dy+Me (Me=Ni, Ru, Rh, Pd, Ir, and Pt), by high-temperature direct synthesis calorimetry.	417-422B
The balance of mechanical and environmental properties of a multielement niobium-niobium silicide-based <i>in situ</i> composite.	3801-3808A	Partial pressure Thermodynamics of sulfur in the $BaO-MnO-SiO_2$ flux system.	652-657B
Effects of the alumina scale on the room-temperature tensile behavior of preoxidized MA 956.	3809-3816A	Particle shape Preparation of fine copper powders from organic media by reaction with hydrogen under pressure. I. Experimental study.	577-584B
Oxidation, Alloying effects Influence of microalloying on the corrosion resistance of steel in saturated calcium hydroxide.	1693-1699A	Preparation of fine copper powders from organic media by reaction with hydrogen under pressure. II. The kinetics of particle nucleation, growth, and dispersion.	585-594B
Oxidation, Composition effects On the role of magnesium and silicon in the formation of alumina from aluminum alloys by means of DIMOX processing.	2094-2099A	Reinforcement shape effects on the fracture behavior and ductility of particulate-reinforced 6061-Al matrix composites.	3739-3746A
Oxidation, Environmental effects Oxidation-reduction equilibrium of Cu^{2+}/Cu^+ in binary alkaline sulfate melts.	385-392B	Particle size A one-phase model of the mixing of Al-SiC composite melt.	1015-1023B
Oxidation, High temperature effects Phase relations of a silicide/silica reaction couple at 2273K.	271-276B	A comparison of fracture behavior of low alloy steel with different sizes of carbide particles.	1909-1917A
Oxidation rate Probing the initial stage of synthesis of Al_2O_3/Al composites by directed oxidation of Al-Mg alloys.	43-50B	The effect of volume percent and morphology of phases on the damping behavior of epoxy-aluminum composites.	2366-2373A
Oxidation rate, High temperature effects Kinetics of cyclic oxidation and cracking and finite element analysis of MA956 and sapphire/MA956 composite system.	3279-3291A	The effects on fracture toughness of ductile-phase composition and morphology in Nb-Cr-Ti and Nb-Si <i>in situ</i> composites.	3007-3018A
Oxidation rate, Radiation effects The growth and structure of thin oxide films on cerium ion-implanted nickel.	3649-3661A	Microstructure and fracture of SiC-particulate-reinforced cast A356 aluminum alloy composites.	3893-3901A
Oxidation resistance The balance of mechanical and environmental properties of a multielement niobium-niobium silicide-based <i>in situ</i> composite.	3801-3808A	Modeling of primary and secondary dendrites in a Cu-6 wt.% tin alloy.	4085-4093A
Effects of the alumina scale on the room-temperature tensile behavior of preoxidized MA 956.	3809-3816A	Synthesis of nanocrystalline Ni_3Cu by sol-gel route.	4213-4216A
Oxidation resistance, Alloying effects High-temperature oxidation of Ti_3Al -based titanium aluminides in oxygen.	3993-4002A	Particle size, High temperature effects Creep lifetime prediction of oxide-dispersion-strengthened nickel-base superalloys: a micromechanically based approach.	3861-3870A
Oxidation resistance, Coating effects Microstructural analysis and oxidation behavior of laser-processed Fe-Cr-Al-Y alloy coatings.	381-390A	Particle size, Welding effects Microstructural features of friction welded MA 956 superalloy material.	4019-4029A
Oxidation resistance, Environmental effects Effect of nitrogen on the oxidation behavior of Ti_3Al -based intermetallic alloys.	4003-4010A	Particle size distribution Preparation of fine copper powders from organic media by reaction with hydrogen under pressure. I. Experimental study.	577-584B
Oxidation resistance, Radiation effects Improved oxidation resistance of group VB refractory metals by Al^+ ion implantation.	491-500B	A one-phase model of the mixing of Al-SiC composite melt.	1015-1023B
Oxides, Composite materials Effect of primary grain size on the secondary recrystallization of mechanically alloyed oxide dispersion strengthened nickel-based superalloy.	493-496A	Theoretical analysis of the particle gradient distribution in centrifugal field during solidification.	1025-1029B
Tensile properties of mechanically alloyed/milled ODS-Ni-based alloys.	1371-1377A	Microstructure and fracture of SiC-particulate-reinforced cast A356 aluminum alloy composites.	3893-3901A
Oxides, Reactions (chemical) Thermodynamic properties of complex oxides in the Sm-Ba-Cu-O system.	973-978B	Modeling of primary and secondary dendrites in a Cu-6 wt.% tin alloy.	4085-4093A
Oxides, Reduction (chemical) Discussion of "Representation of mixed reactive gases on free energy (Ellingham-Richardson) diagrams" and reply.	693-694B	Modeling particle fracture during the extrusion of aluminum/alumina composites.	4113-4120A
Oxidizing atmospheres Oxidation-reduction equilibrium of Cu^{2+}/Cu^+ in binary alkaline sulfate melts.	385-392B	Synthesis of nanocrystalline Ni_3Cu by sol-gel route.	4213-4216A
		Particle size distribution, Heating effects The control of grain size and distribution of particles in a (6061 alloy) _m /(Al_2O_3) _p composite by solutionizing treatment.	2023-2034A
		Particle size distribution, Welding effects Microstructural features of friction welded MA 956 superalloy material.	4019-4029A
		Nonuniform distribution of carbonitride particles and its effect on prior austenite grain size in the simulated coarse-grained heat-affected zone of thermomechanical control-processed steels.	4031-4038A

Particulate composites, Brazing A model for coupled growth of reaction layers in reactive brazing of ZrO_2 -toughened Al_2O_3 .	3630-3638A	Communication: On the in situ formation of TiC and Ti_2C reinforcements in combustion-assisted synthesis of titanium matrix composites.	237-240A
Particulate composites, Casting Transient thermal analysis of solidification in a centrifugal casting for composite materials containing particle segregation. Solidification of particle-reinforced metal-matrix composites. A one-phase model of the mixing of Al - SiC composite melt.	277-285B 663-671B 1015-1023B	On the role of magnesium and silicon in the formation of alumina from aluminum alloys by means of DIMOX processing. Formation of structure intermetallics by reactive metal penetration of titanium and nickel oxides and aluminates.	2094-2099A 2100-2104A
Particulate composites, Coatings Microstructure of bonding zones in laser-clad nickel-alloy-based composite coatings reinforced with various ceramic powders.	391-400A	Passivation Fundamental studies of copper anode passivation during electropolishing. I. Development of techniques. Fundamental studies of copper anode passivation during electropolishing. II. Surface morphology.	393-398B 610-616B
Particulate composites, Extrusion Mathematical modeling of the extrusion of $6061/Al_2O_3/20p$ composite. Modeling particle fracture during the extrusion of aluminum/alumina composites.	4095-4111A 4113-4120A	Pearlite Effect of holding time in the $(\alpha+\gamma)$ temperature range on toughness of specially austempered ductile iron.	1979-1989A
Particulate composites, Heat treatment The control of grain size and distribution of particles in a $(6061$ alloy) $_m/(Al_2O_3)_p$ composite by solutionizing treatment.	2023-2034A	Pearlite, Deformation effects Analysis and prevention of vertical cracking phenomena during deep drawing of hot-rolled SG295 steel strips.	1241-1250A
Particulate composites, Mechanical properties NiTi and NiTi-TiC composites. II. Compressive mechanical properties. NiTi and NiTi-TiC composites. III. Shape-memory recovery. Subcritical crack growth at bimaterial interfaces. II. Microstructural effects on fracture resistance of metal/ceramic interfaces. Effect of a solid solution on the steady-state creep behavior of an aluminum matrix composite. Reinforcement stresses during deformation of sphere- and particulate-reinforced aluminum-matrix composites. Effect of manganese dispersoid on the fatigue crack propagation of Al - Zn - Mg alloys. Mechanical properties and 95°C aging characteristics of zircon reinforced Zn - $4Al$ - $3Cu$ alloy. Creep deformation of dispersion-strengthened copper. Tensile properties of mechanically alloyed/milled ODS-Ni-based alloys. The effect of volume percent and morphology of phases on the damping behavior of epoxy-aluminum composites. Analysis of damping in particle-reinforced superplastic zinc composites. Corrosive wear of SiC whisker- and particulate-reinforced 6061 aluminum alloy composites. Tensile ductility and fracture of superplastic aluminum-SiC composites under thermal cycling conditions. Failure characteristics of $6061/Al_2O_3/15p$ and $2014/Al_2O_3/15p$ composites as a function of loading rate. High-temperature wear and deformation processes in metal matrix composites. Ni_3Al intermetallic particles as wear-resistant reinforcement for Al -base composites processed by powder metallurgy. Reinforcement shape effects on the fracture behavior and ductility of particulate-reinforced 6061-Al matrix composites. Microstructure and fracture of SiC -particulate-reinforced cast A356 aluminum alloy composites. Analysis of thermal residual stress in a thick-walled ring of Dur-alcan-base Al-SiC functionally graded material. Influence of reinforcement volume fraction and size on the microstructure and abrasion wear resistance of hot isostatic pressed white iron matrix composites. Influence of matrix structure on the abrasion wear resistance and toughness of a hot isostatic pressed white iron matrix composites.	183-191A 193-203A 213-219A 305-316A 486-490A 490-493A 809-818A 1217-1227A 1371-1377A 2368-2373A 2565-2573A 2653-2662A 2837-2842A 3095-3107A 3135-3148A 3259-3266A 3739-3746A 3893-3901A 4145-4151A 4171-4181A 4183-4191A 459-465A 493-496A 503-505A 3700-3717A 3718-3726A 1025-1029B 43-50B	Pearlite, Heating effects Pearlite in ultrahigh carbon steels: heat treatments and mechanical properties. Pearlite, Temperature effects Eutectoid decomposition in Ag - Ge . Peel strength, Stress effects Subcritical crack growth at bimaterial interfaces. I. Flexural peel technique. Subcritical crack growth at bimaterial interfaces. III. Shear-enhanced fatigue crack growth resistance at polymer/metal interface. Penetration Analysis of mean square penetration depth in grain boundary diffusion. Influence of titanium and carbon contents on the hydrogen trapping of microalloyed steels. Peritectic reactions Generalized enthalpy method for multicomponent phase change. Peritectic reactions, Alloying effects Electron microscope study of Al - Fe - Si intermetallics in 6201 aluminum alloy. Peritectic reactions, Cooling effects Modeling of the peritectic reaction and macro-segregation in casting of low carbon steel. Permanent mold casting Microstructure and fracture of SiC -particulate-reinforced cast A356 aluminum alloy composites. Permeability Hydrogen trapping and permeation in nickel thoria. Permeability, Microstructural effects Permeability of microporous carbon preforms. Petroleum pipelines, Corrosion Microstructural aspects of sulfide stress cracking in an API X-80 pipeline steel. Phase boundary Kinetics of sulfation of chalcocite with steam and oxygen in the presence of ferric oxide. Thermodynamic activities and partial enthalpies of mixing in the solid solution of Fe in Ni_3Al . Phase boundary, Composition effects An evaluation of the Fe - Ni phase diagram considering long-range order of nitrogen atoms in γ - Fe_2N_{1-x} and ϵ - Fe_2N_{1-x} . Phase boundary, Cooling effects Ferrite nucleation and growth during continuous cooling. Phase boundary, Heating effects Analysis of heat affected zone phase transformations using in situ spatially resolved x-ray diffraction with synchrotron radiation. Phase boundary, Temperature effects Overview of geometric effects on coarsening of mushy zones. A new characterization method of the microstructure using the macroscopic composition gradient in alloys. Phase decomposition Microstructural development of a gas-atomized and hot-pressed super- c_2 alloy. Phase transformations in condensed systems revisited: industrial applications. A thermodynamic evaluation of the nickel-silicon system. Alloy phase analysis from measurements of bulk magnetic properties. A high-resolution transmission electron microscopy study of the precipitation process in a dilute Ti - N alloy.	111-118A 1676-1682A 205-211A 221-228A 3473-3477A 3773-3780A 869-879B 929-936A 999-1014B 3893-3901A 2495-2503A 3689-3674A 3601-3611A 465-474B 3569-3575A 1083-1071A 1544-1553A 775-783A 557-567A 945-949A 2221-2228A 2397-2418A 2897-2903A 2958-2965A 2966-2977A

Phase decomposition, Alloying effects			
Electron microscope study of Al-Fe-Si intermetallics in 6201 aluminum alloy.	929-936A	An adaptive mesh refinement scheme for solidification problems.	707-717A
Retardation of intermetallic phase formation in experimental superferritic stainless steels.	2436-2444A	Real time x-ray transmission microscopy of solidifying Al-In alloys.	801-808A
Phase decomposition, Cooling effects		Generalized enthalpy method for multicomponent phase change.	869-879B
Ferrite nucleation and growth during continuous cooling.	1544-1553A	Ostwald ripening in ternary alloys.	937-943A
Austenite decomposition during continuous cooling of an HSLA-80 plate steel.	1554-1568A	Crystal shapes and phase equilibria: a common mathematical basis.	1431-1440A
Phase decomposition, Heating effects		Characterization of a massive transformation by microstructural analysis.	1511-1516A
Phase transformations in Nb-Al-Ti alloys.	1642-1654A	The mechanism of formation of a fine duplex microstructure in Ti-48Al-2Mn-2Nb alloys.	1655-1667A
Phase decomposition, Radiation effects		Kinetics of phase evolution of Zn-Fe intermetallics.	2904-2910A
The effect of high-energy electron-beam irradiation on microstructural modification of a high-speed steel roll.	3149-3161A	Solidification of undercooled Fe-Cr-Ni alloys. II. Microstructural evolution.	3226-3240A
Phase decomposition, Temperature effects		Phase transformations, Alloying effects	
A study of the thermal decomposition of BaCO_3 .	409-416B	Effects of nickel on the sintering behavior of Fe-Ni compacts made from composite and elemental powders.	203-211B
Phase diagrams		Electron microscope study of Al-Fe-Si intermetallics in 6201 aluminum alloy.	929-936A
Liquidus temperatures for primary crystallization of cryolite in molten salt systems of interest for aluminum electrolysis.	739-744B	The breakdown of single-crystal solidification in high refractory nickel-base alloys.	1081-1094A
Critical evaluation and optimization of the thermodynamic properties of liquid tin solutions.	808-826B	Effect of strain rate and temperature on the flow stress of β -phase titanium-hydrogen alloys.	1303-1312A
Generalized enthalpy method for multicomponent phase change.	869-879B	Precipitation in lead-calcium alloys containing tin.	1668-1675A
A thermodynamic evaluation of the Ti-Mo-C system.	955-966B	Phase transformations, Composition effects	
Inverse melting in binary systems: morphology and microscopy of catactic alloys.	979-986B	Hydride formation and decomposition in electrochemically charged metastable austenitic stainless steels.	29-40A
Thermodynamic studies and the phase diagram of the Li-Mg system.	2419-2428A	Phase transformations, Cooling effects	
Experimental study of the phase equilibria in the Fe-Mn-Al system.	2429-2435A	The role of grain corners in nucleation.	480-483A
An experimental study and thermodynamic calculations of phase equilibria in the Fe-Mo-C-N system.	2869-2880A	Ferrite nucleation and growth during continuous cooling.	1544-1553A
A thermodynamic evaluation of the nickel-silicon system.	2897-2903A	Austenite decomposition during continuous cooling of an HSLA-80 plate steel.	1554-1568A
An isothermal section at 550°C in the Al-rich corner of the Al-Fe-Mn-Si system.	3357-3361A	Phase transformations, Deformation effects	
Thermochemistry of the Ni-Hf system—intermetallic phases.	3576-3590A	Experimental investigation of the transformation texture in hot-rolled ferritic stainless steel using single orientation determination.	49-57A
Thermodynamic assessment of the Nb-N system.	3591-3600A	Phase transformations, Field effects	
Synthesis of RuAl by reactive powder processing.	3688-3699A	On the reaction between Fe-Ti and Fe-C liquids under microgravity.	407-414A
The deposition of aluminide and silicide castings on γ -TiAl using the halide-activated pack cementation method.	3761-3772A	Phase transformations, Heating effects	
Martensitic transformations in NiMnAl β phase alloys.	4153-4162A	Characterization of the formation of α_1 plates from the β_0 phase in a Cu-Zn-Au alloy.	719-724A
Phase stability		Analysis of heat affected zone phase transformations using in situ spatially resolved x-ray diffraction with synchrotron radiation.	775-783A
Thermal decomposition of silicon carbides: discussion of "the effect of an electric field on self sustaining combustion synthesis, I and II", and author's reply.	322-325B	Bainitic microstructures formed by split isothermal transformation in an Fe-C-Si-Mn-Mo steel.	1141-1147A
Effects of flow on morphological stability during directional solidification.	583-593A	Effect of bainite transformation and retained austenite on mechanical properties of austempered spheroidal graphite cast steel.	1585-1594A
A thermodynamic evaluation of the Ti-Mo-C system.	955-966B	Phase transformations in Nb-Al-Ti alloys.	1642-1654A
A high resolution transmission electron microscopy study of interfaces between the γ , B2, and α_2 phases in a Ti-Al-Mo alloy.	1618-1629A	Phase transformations, Stress effects	
On the stable Mg-Zn-Y quasicrystals.	1779-1784A	Computer simulation of ledge migration under elastic interaction.	1489-1498A
Microstructural aspects of the dissolution and melting of Al_2Cu phase in Al-Si alloys during solution heat treatment.	1785-1798A	Phase transformations, Temperature effects	
Stable and metastable ordered phases in microcrystalline alloys Ni (Fe, Mn, Ti).	2045-2046A	A study of the thermal decomposition of BaCO_3 .	409-416B
Thermoelastic martensite and shape memory effect in ductile Cu-Al-Mn alloys.	2187-2195A	Overview of geometric effects on coarsening of mushy zones.	557-567A
Structural stability of super duplex stainless steel weld metals and its dependence on tungsten and copper.	2196-2208A	Banded solidification microstructures.	625-634A
Alloy phase analysis from measurements of bulk magnetic properties.	2958-2965A	Phase stability and atom probe field ion microscopy of type 308 CRE stainless steel weld metal.	763-774A
An isothermal section at 550°C in the Al-rich corner of the Al-Fe-Mn-Si system.	3357-3361A	A new characterization method of the microstructure using the macroscopic composition gradient in alloys.	945-949A
Phase stability, Alloying effects		The formation mechanism(s), morphology, and crystallography of ferrite sideplates.	1517-1532A
Mechanical alloying of Nb-Al powders.	41-48A	Eutectoid decomposition in Ag-Ga.	1676-1682A
Effect of alloying elements on martensitic transformation in the binary NiAl(B) phase alloys.	2445-2453A	Phases (state of matter)	
Phase stability, Environmental effects		The mineralogical deposit of germanium in the Clarksville electrolytic zinc plant of Savage Zinc Inc.	567-576B
Oxidation-reduction equilibrium of $\text{Cu}^{2+}/\text{Cu}^+$ in binary alkaline sulfate melts.	385-392B	M_{23}C_6 carbide equilibria in the Fe-Cr-C system.	701-704B
Phase stability, Heating effects		Microstructure and phase relations in a powder-processed Ti-22Al-12Nb alloy.	1121-1128A
Evolution of microstructures in the nickel modified titanium tri-aluminides near the L_1 phase field.	5-17A	Crystal shapes and phase equilibria: a common mathematical basis.	1431-1440A
Phase stability, Temperature effects		Control of iron nitride layers growth kinetics in the binary Fe-N system.	1823-1835A
Phase stability and atom probe field ion microscopy of type 308 CRE stainless steel weld metal.	763-774A	Phases (state of matter), Composition effects	
Phase transformations		An evaluation of the Fe-N phase diagram considering long-range order of nitrogen atoms in $\gamma\text{-Fe}_2\text{N}_{1-x}$ and $\epsilon\text{-Fe}_2\text{N}_{1-x}$.	1063-1071A
Dynamic behavior of a liquid/liquid interface at an oscillating wall.	305-314B	Electron microscopic study of Cr_2N formation in thermally aged 316LN austenitic stainless steels.	1175-1186A
Thermal decomposition of silicon carbides: discussion of "the effect of an electric field on self sustaining combustion synthesis, I and II", and author's reply.	322-325B	Phases (state of matter), Deformation effects	
Effects of flow on morphological stability during directional solidification.	583-593A	Reply: Dynamic materials model. Basis and principles.	235-236A
Thermodynamics of sulfur in the $\text{BaO}-\text{MnO}-\text{SiO}_2$ flux system. Interface attachment kinetics in alloy solidification.	652-657B		
	671-686A		

Phases (state of matter), Radiation effects		
Transmission electron microscopy study on the cross-sectional microstructure of an ion-nitriding layer.	1347-1352A	
Phosphorus, Alloying additive		
Influence of phosphorus addition on the surface tension of liquid iron and segregation of phosphorus on the surface of Fe-P alloy.	71-79B	
Phosphorus, Binary systems		
Critical evaluation and optimization of the thermodynamic properties of liquid tin solutions.	808-826B	
Phosphorus, Impurities		
Thermodynamics of phosphorus in molten silicon.	937-941B	
Phosphorus compounds, Ternary systems		
Chemical potentials of components of the system $\text{CaO}+\text{P}_2\text{O}_5+\text{Fe}_2\text{O}_3$ at 1673K.	595-603B	
Photoelectron spectroscopy		
Physical chemistry of the powder metallurgy of beryllium: chemical characterization of the powder in relation to its granularity.	371-379A	
Pistons, Materials selection		
Structure of phases in the $\delta\text{-Al}_2\text{O}_3$ fiber studied by convergent beam electron diffraction.	3318-3329A	
Pitting (corrosion), Heating effects		
Corrosion fatigue in nitrocarburized quenched and tempered steels.	1333-1346A	
Pitting (corrosion), Microstructural effects		
Retardation of intermetallic phase formation in experimental superferitic stainless steels.	2436-2444A	
Plasma arc welding		
Dilution in single pass arc welds.	481-489B	
The wear behavior between hardfacing materials.	3639-3648A	
Plastic deformation		
Non-Schmid effects on the behavior of polycrystals, with applications to Ni_3Al .	81-89A	
Communication: Discussion of "Modeling of dynamic materials behavior. A critical evaluation of the dissipator power component approach".	232-235A	
A study of typical yields of metals.	731-736A	
High-temperature deformation processing of Ti-24Al-20Nb.	2593-2604A	
The relationship between microstructural and plastic instability in Al-4.0 wt. % Cu alloy.	2916-2922A	
Plastic zones and fatigue-crack closure under plane-strain double slip.	3491-3502A	
The plastic anisotropy of an Al-Li-Cu-Zr alloy extrusion in unidirectional deformation.	3503-3512A	
Influence of plastic deformation upon the half-width of engineering metallic materials in hard state.	3662-3668A	
High-temperature deformation and failure of an orthorhombic titanium aluminide sheet material.	3675-3681A	
Plastic zone and plateaus around large indentations.	3793-3800A	
Microstructural evolution and superplastic deformation behavior of fine grain 5083Al.	3827-3839A	
Plastic deformation, Composition effects		
Mechanical properties of Ru-Ni-Al alloys.	1395-1400A	
Plastic deformation, Diffusion effects		
Hydrogen-induced cleavage fracture of Fe_3Al -based intermetallics.	3949-3956A	
Plastic deformation, High temperature effects		
High-temperature measurements of lattice parameters and internal stresses of a creep-deformed monocrystalline nickel-base superalloy.	1003-1014A	
Plastic deformation, Impurity effects		
The effect of hydrogen on the fracture of alloy X-750.	101-110A	
Plastic deformation, Microstructural effects		
NiTi and NiTi-TiC composites. II. Compressive mechanical properties.	183-191A	
Plastic deformation, Radiation effects		
Theory of nucleation with cluster loss and injection: application to plastic deformation and irradiation.	1441-1448A	
Plastic deformation, Stress effects		
Plastic anisotropy of sheets with continuously varying anisotropic parameters and flow stress.	317-326A	
Reinforcement stresses during deformation of sphere- and particulate-reinforced aluminum-matrix composites.	486-490A	
RAFTing in superalloys.	513-530A	
Discussion of a fully plastic microcracking model for transgranular stress corrosion cracking in planar slip materials" and reply.	819-821A	
Plastic deformation, Temperature effects		
Manifestations of dynamic strain aging in soft-oriented NiAl single crystals.	3542-3557A	
Plastic flow		
Aspects of dynamic recrystallization in shaped charge and explosively formed projectile devices.	1773-1778A	
Control of superplastic deformation rate during uniaxial tensile tests.	3030-3042A	
Flow and fracture of bimaterial systems based on aluminum alloys.	3937-3947A	
Plastic flow, Temperature effects		
Influence of temperature transients on the hot workability of a two-phase gamma titanium aluminide alloy.	1933-1950A	
Temperature dependence of the rate sensitivity and its effect on the activation energy for high-temperature flow.	3346-3348A	
Plasticity		
High-temperature deformation processing of Ti-24Al-20Nb.	2593-2604A	
Plastic zones and fatigue-crack closure under plane-strain double slip.	3491-3502A	
Plasticity, Composition effects		
A statistical analysis of the effect of a mixture component on the rheology of alumina feedstocks.	399-406B	
Plasticity, Environmental effects		
On the transition of fatigue crack growth from stage I to stage II in a corrosive environment.	471-476A	
Plasticity, Heating effects		
The plastic anisotropy of an Al-Li-Cu-Zr alloy extrusion in unidirectional deformation.	3503-3512A	
Plasticity, Impurity effects		
The effect of hydrogen on the fracture of alloy X-750.	101-110A	
Plasticity, Microstructural effects		
The use of microstructural gradients in hot gas-pressure forming of Zn-Al sheet.	3250-3258A	
Plate metal, Coating		
Correlation of microstructure and fracture toughness in high-chromium white iron hardfacing alloys.	3881-3891A	
Plate metal, Mechanical properties		
Conditioning monitoring by microstructural evaluation of cumulative fatigue damage.	3841-3851A	
Plate metal, Phase transformations		
A study on morphology and plate mean dimensions in Fe-Ni and Fe-Ni-Cr alloys.	973-980A	
Plate metal, Phases (state of matter)		
Characterization of the formation of α_1 plates from the β_2 phase in a Cu-Zn-Al alloy.	719-724A	
Austenite decomposition during continuous cooling of an HSLA-80 plate steel.	1554-1568A	
Platinum, Binary systems		
Standard enthalpies of formation of dysprosium alloys, Dy-Me (Me=Ni, Ru, Rh, Pd, Ir, and Pt), by high-temperature direct synthesis calorimetry.	417-422B	
Plutonium, Extraction		
Vacuum evaporation of KCl-NaCl salts. I. Thermodynamic modeling of vapor pressures of solid and liquid solutions.	141-146B	
Point defects, Radiation effects		
Sputter-induced pits on {100} nickel surfaces.	981-993A	
Positrons ratio, Alloying effects		
Elastic moduli of titanium-hydrogen alloys in the temperature range 20°C to 1100°C.	3963-3970A	
Pole figures		
Crystallographic preferred orientation induced by cyclic rolling contact loading.	3445-3465A	
Pollution abatement		
Eco-techno-economic synthesis of process routes for the production of zinc using combinatorial optimization.	1031-1044B	
Porosity		
Comparative study of pore structure evolution during solvent and thermal debinding of powder injection molded parts.	245-253A	
Characterization and mechanical properties of ultrahigh boron steels produced by powder metallurgy.	1861-1867A	
A model for macrosegregation and its application to Al-Cu castings.	2708-2721A	
The effect of Mo addition on the liquid-phase sintering of W heavy alloy.	3120-3125A	
Porosity, Cooling effects		
Porosity formation in Al-9 wt. % Si-3 wt. % Cu alloy systems: metallographic observations.	415-429A	
Porous materials, Physical properties		
Permeability of microporous carbon preforms.	3669-3674A	
Potassium, Chemical analysis		
Formation of aluminum-silicon alloys from feldspars—determination of silicon, light, and heavy elements in alumin by scanning electron microscopy.	604-609B	

Potassium, Dopants	
Van der Waals approximation for potassium bubbles in tungsten.	987-992B
Powder coating	
Kinetics of phase evolution of Zn-Fe intermetallics.	2904-2910A
Powder coatings, Materials selection	
Kinetics of phase evolution of Zn-Fe intermetallics.	2904-2910A
Powder compacts, Mechanical properties	
Microstructure and tensile properties of compacted, mechanically alloyed, nanocrystalline Fe-Al.	3126-3134A
Powder metallurgy	
The effect of thermal cycle on the microstructural development of a powder metallurgy superalloy braze material.	145-153A
Physical chemistry of the powder metallurgy of beryllium: chemical characterization of the powder in relation to its granularity.	371-379A
Powder metallurgy parts, Machining	
Active wear and failure mechanisms of titanium nitride-coated high speed steel and titanium nitride-coated cemented carbide tools when machining powder metallurgically made stainless steels.	2796-2808A
Powder technology	
A statistical analysis of the effect of a mixture component on the rheology of alumina feedstocks.	399-408B
Precious metal alloys, Mechanical properties	
High-temperature behavior of precious metal base composites.	2042-2052A
Precipitates	
Structural stability of super duplex stainless steel weld metals and its dependence on tungsten and copper.	2196-2208A
Lattice misfits in four binary Ni-base γ / γ ' alloys at ambient and elevated temperatures.	2888-2896A
The relationship between microstructural and plastic instability in Al-4.0 wt.% Cu alloy.	2916-2922A
A high-resolution transmission electron microscopy study of the precipitation process in a dilute Ti-N alloy.	2966-2977A
Internal sulfide precipitation in low Cr-Fe alloys.	3192-3202A
Influence of titanium and carbon contents on the hydrogen trapping of microalloyed steels.	3773-3780A
An evaluation of the creep properties of two Al-Si alloys produced by rapid solidification processing.	3871-3879A
Correlation of microstructure and fracture toughness in high-chromium white iron hardfacing alloys.	3881-3891A
Precipitates, Crystal growth	
Ostwald ripening of solid-liquid Pb-Sn dispersions.	2470-2478A
Precipitation behaviors in Al-Cu-Mg and 2024 aluminum alloys.	2479-2494A
Preferential coarsening of γ ' precipitates in Inconel 718 during creep.	3391-3398A
On the effect of stress on nucleation and growth of precipitates in an Al-Cu-Mg-Ag alloy.	3431-3444A
M_2C precipitates in isothermal tempering of high Co-Ni secondary hardening steel.	3466-3472A
Precipitation	
Mechanical behavior of the in situ composite alloys in the Al-Ni-Ti system near the L_1 phase field.	71-79A
The effects of microstructure, strength level, and crack propagation mode on stress corrosion cracking behavior of 4135 steel.	281-290A
Structure, chemistry, and stress corrosion cracking of grain boundaries in alloys 600 and 690.	327-341A
Preparation of fine copper powders from organic media by reaction with hydrogen under pressure. I. Experimental study.	577-584B
Preparation of fine copper powders from organic media by reaction with hydrogen under pressure. II. The kinetics of particle nucleation, growth, and dispersion.	585-594B
Crystallography of grain boundary α precipitates in a β titanium alloy.	1630-1641A
Splitting phenomena occurring in the martensitic transformation of Cr13 and CrMoV14 stainless steels in the absence of carbide precipitation.	1799-1805A
Microstructural development in NiAl/Ni-Si-B/NI transient liquid phase bonds.	1925-1931A
Modeling of microsegregation in macrosegregation computations.	2314-2327A
Internal sulfide precipitation in low Cr-Fe alloys.	3192-3202A
Precipitation, Alloying effects	
The effect of iron and manganese on the recrystallization behavior of hot-rolled and solution-heat-treated aluminum alloy 6013.	19-27A
The influence of niobium supersaturation in austenite on the static recrystallization behavior of low carbon microalloyed steels.	951-960A
Identification of precipitate phases in a mechanically alloyed rapidly solidified Al-Fe-Ce alloy.	1033-1041A
Precipitation in lead-calcium alloys containing tin.	1668-1675A
Precipitation, Composition effects	
Electron microscopic study of Cr ₂ N formation in thermally aged 316LN austenitic stainless steels.	1175-1186A
Precipitation, Cooling effects	
Porosity formation in Al-9 wt.% Si-3 wt.% Cu alloy systems: metallographic observations.	415-429A
Copper precipitation during continuous cooling and isothermal aging of A710 type steels.	1589-1584A
Precipitation, Deformation effects	
Reply: Dynamic materials model. Basis and principles.	235-236A
Precipitation behavior in a medium carbon, Ti-V-N microalloyed steel.	1149-1165A
Precipitation, Field effects	
On the reaction between Fe-Ti and Fe-C liquids under microgravity.	407-414A
Precipitation, Heating effects	
Evolution of microstructures in the nickel modified titanium tri-aluminides near the L_1 phase field.	5-17A
High-temperature nitridation of Ni-Cr alloys	59-69A
Mechanical properties and 95°C aging characteristics of zircon reinforced Zn-4Al-3Cu alloy.	809-818A
Microstructural stability on aging of an α - β titanium alloy: Ti-6Al-1.6Zr-3.3Mo-0.3Si.	1167-1173A
Transition between internal and external nitridation of Ni-Ti alloys.	1606-1617A
Phase transformations in Nb-Al-Ti alloys.	1642-1654A
M_2C precipitates in isothermal tempering of high Co-Ni secondary hardening steel.	3466-3472A
Precipitation, High temperature effects	
Phase relations of a silicide/silica reaction couple at 2273K.	271-276B
Carbide diagrams and precipitation of alloying elements during aging of low-alloy steels.	498-502A
Precipitation, Radiation effects	
Transmission electron microscopy study on the cross-sectional microstructure of an ion-nitrided layer.	1347-1352A
Precipitation, Stress effects	
Temperature and strain-rate effects on low-cycle fatigue behavior of alloy 800H.	255-267A
Effect of carbide precipitation on the creep behavior of alloy 800HT in the temperature range 700-900°C.	747-756A
A study on coherency strain and precipitate morphology via a discrete atom method.	1449-1459A
Effect of uniaxial stress on coarsening of precipitate clusters.	1460-1475A
On the effect of stress on nucleation and growth of precipitates in an Al-Cu-Mg-Ag alloy.	3431-3444A
Precipitation, Temperature effects	
Phase stability and atom probe field ion microscopy of type 308 CRE stainless steel weld metal.	763-774A
A new characterization method of the microstructure using the macroscopic composition gradient in alloys.	945-949A
The formation mechanism(s), morphology, and crystallography of ferrite sideplates.	1517-1532A
Precipitation hardening	
Bauschinger effect in Haynes 230 alloy: influence of strain rate and temperature.	1739-1748A
Phase transformations in condensed systems revisited: Industrial applications.	2397-2418A
Precipitation behaviors in Al-Cu-Mg and 2024 aluminum alloys.	2479-2494A
Low quench sensitivity of superplastic 8090 Al-Li thin sheets.	2923-2933A
Alloy phase analysis from measurements of bulk magnetic properties.	2958-2965A
A high-resolution transmission electron microscopy study of the precipitation process in a dilute Ti-N alloy.	2966-2977A
On the effect of stress on nucleation and growth of precipitates in an Al-Cu-Mg-Ag alloy.	3431-3444A
Creep lifetime prediction of oxide-dispersion-strengthened nickel-base superalloys: a micromechanically based approach.	3861-3870A
Precipitation hardening, Alloying effects	
Effect of magnesium on the aging behavior of Al-Zn-Mg-Cu/ Al_2O_3 metal matrix composites.	2005-2012A
Precipitation hardening, Stress effects	
A study on coherency strain and precipitate morphology via a discrete atom method.	1449-1459A
An evaluation of the creep properties of two Al-Si alloys produced by rapid solidification processing.	3871-3879A
Precipitation hardening alloys, Mechanical properties	
Microstructure and mechanical behavior of Cr-Cr ₂ Hf in situ intermetallic composites.	2583-2592A
Intergranular fracture in some precipitation-hardened aluminum alloys at low temperatures.	3081-3088A
Precipitation hardening steels, Mechanical properties	
Microstructural basis for the effect of chromium on the strength and toughness of AF1410-based high performance steels.	2510-2517A

Precision forming		
Comparative study of pore structure evolution during solvent and thermal debinding of powder injection molded parts.	245-253A	High-resolution electron microscopy analysis of structural defects in a (2/1, 5/3)-type approximant of a decagonal quasicrystal of an Al-Pd-Mn alloy. 2911-2915A
Preferred orientation, Stress effects		
Crystallographic preferred orientation induced by cyclic rolling contact loading.	3445-3465A	Quaternary systems, Phases (state of matter)
Preforming		Thermodynamic properties of complex oxides in the Sm-Ba-Cu-O system. 973-978B
Permeability of microporous carbon preforms.	3669-3674A	An experimental study and thermodynamic calculations of phase equilibria in the Fe-Mo-C-N system. 2869-2880A
Press forming		
Forming of tailor-welded blanks.	2605-2616A	Quenching (cooling)
Pressure		Quenching C60 fullerene into diamond in the Fe-C alloy system by laser treatment. 2293-2296A
Pressure dependence of anomalous diffusion of zirconium in β -titanium.	1807-1814A	High cycle fatigue behavior of gas-carburized medium carbon Cr-Mo steel. 2557-2564A
Pressure castings, Microstructure		Low quench sensitivity of superplastic 8090 Al-Li thin sheets. 2923-2933A
The squeeze casting of hypoeutectic binary Al-Cu.	4121-4132A	The quench sensitivity of cast Al-7 wt.% Si-0.4 wt.% Mg alloy. 3983-3991A
Pressure vessels, Corrosion		
Stress corrosion cracking of pressure vessel steels in high-temperature caustic aluminate solutions.	1327-1331A	Quenching and tempering
Pressure vessels, Extrusion		Corrosion fatigue in nitrocarburized quenched and tempered steels. 1333-1346A
Microsegregation of oxygen in Zr-2.5Nb alloy materials.	431-440A	The dependence of complex alloyed steel properties on quenching and tempering conditions. 2852-2858A
Pressure vessels, Irradiation		
Theory of nucleation with cluster loss and injection: application to plastic deformation and irradiation.	1441-1448A	Radiation damage
Pressure vessels, Materials selection		Theory of nucleation with cluster loss and injection: application to plastic deformation and irradiation. 1441-1448A
Conditioning monitoring by microstructural evaluation of cumulative fatigue damage.	3841-3851A	
Pressure vessels, Metal working		
Analysis and prevention of vertical cracking phenomena during deep drawing of hot-rolled SG295 steel strips.	1241-1250A	Radioactive waste
Probes, Development		Preparation of glass-forming materials from granulated blast furnace slag. 801-807B
The measurement of hydrogen activities in molten copper using an oxide protonic conductor.	929-935B	Microstructure and phase identification in type 304 stainless steel-zirconium alloys. 2151-2159A
Process control		
The measurement of hydrogen activities in molten copper using an oxide protonic conductor.	929-935B	Rapid solidification
Eco-techno-economic synthesis of process routes for the production of zinc using combinatorial optimization.	1031-1044B	Interface attachment kinetics in alloy solidification. 671-686A
Projectiles		High-speed imaging and analysis of the solidification of under-cooled nickel melts. 863-868B
Aspects of dynamic recrystallization in shaped charge and explosively formed projectile devices.	1773-1778A	Identification of precipitate phases in a mechanically alloyed rapidly solidified Al-Fe-Ce alloy. 1033-1041A
Proof stress, Composition effects		Rapid solidification processing of a Mg-Li-Si-Ag alloy. 1363-1370A
High-temperature behavior of precious metal base composites.	2642-2652A	Characterization and mechanical properties of ultrahigh boron steels produced by powder metallurgy. 1861-1867A
Proof stress, Microstructural effects		An evaluation of the creep properties of two Al-Si alloys produced by rapid solidification processing. 3871-3879A
Fracture characteristics, microstructure, and tissue reaction of Ti-5Al-2.5Fe for orthopedic surgery.	3925-3935A	Elevated temperature deformation behavior of a dispersion-strengthened Al-Fe, V, Si alloy. 3913-3923A
Prosthetics, Materials selection		
Fracture characteristics, microstructure, and tissue reaction of Ti-5Al-2.5Fe for orthopedic surgery.	3925-3935A	Reaction kinetics
Protective coatings, Heat treatment		Kinetics of sulfation of chalcopyrite with steam and oxygen in the presence of ferric oxide. 465-474B
Quenching C60 fullerene into diamond in the Fe-C alloy system by laser treatment.	2293-2296A	Preparation of fine copper powders from organic media by reaction with hydrogen under pressure. II. The kinetics of particle nucleation, growth, and dispersion. 585-594B
Protective coatings, Melting		Reduction of FeO in smelting slags by solid carbon: experimental results. 717-730B
The production of nickel-zinc alloys by powder injection.	780-787B	Formation of structural intermetallics by reactive metal penetration of titanium and nickel oxides and aluminates. 2100-2104A
Purification		Mössbauer spectroscopy study of the aging and tempering of high nitrogen quenched Fe-N alloys: kinetics of formation of $Fe_{1-x}N_x$ nitride by interstitial ordering in martensite. 2160-2177A
Thermodynamics of phosphorus in molten silicon.	937-941B	
Pyrometallurgy		Reaction kinetics, Composition effects
Vacuum evaporation of KCl-NaCl salts. I. Thermodynamic modeling of vapor pressures of solid and liquid solutions.	141-146B	On the role of magnesium and silicon in the formation of alumina from aluminum alloys by means of DIMOX processing. 2094-2099A
Electrical conductivity of molten cryolite based mixtures obtained with a tube type cell made of pyrolytic boron nitride.	255-261B	
Zinc reduction of MoO_3 in a self propagating high temperature synthesis process.	315-318B	Reactions (chemical)
A kinetic study of the reaction of zinc oxide with iron powder.	363-374B	Symposium on In Situ Reactions for Synthesis of Composites, Ceramics, and Intermetallics. II. 555-566B
Chemical potentials of oxygen for mixtures of $CaO(s) + Ca_2P_2O_7(s) + (CaO + P_2O_5 + Fe_2O_3)$ melts and $Ca_4P_2O_9(s) + Ca_2P_2O_8(s) + CaO + P_2O_5 + Fe_2O_3$ melts.	375-378B	A study of solid-aqueous equilibria by the speciation approach in the hydronium alunite-sulfuric acid-water system at high temperatures. 155-164A
Oxidation-reduction equilibrium of Cu^{2+}/Cu^{+} in binary alkaline sulfate melts.	385-392B	
The separation of the solids from the carrier gas during submerged powder injection.	773-779B	Recovery, Alloying effects
Qualitative analysis		Modeling recovery and recrystallization kinetics in cold-rolled Ti-Nb stabilized interstitial-free steel. 3410-3423A
Determination of hydrogen in titanium alloys by cold neutron prompt gamma activation analysis.	3682-3687A	
Quantitative analysis		Recrystallization
Physical chemistry of the powder metallurgy of beryllium: chemical characterization of the powder in relation to its granularity.	371-379A	Mechanical behavior of the in situ composite alloys in the Al-Ni-Ti system near the L_1 phase field. 71-79A
Quasicrystalline structure		Modeling texture change during the static recrystallization of interstitial-free steels. 155-164A
On the stable Mg-Zn-Y quasicrystals.	1779-1784A	Recrystallization in oxide-dispersion strengthened mechanically alloyed sheet steel. 1963-1978A
		The role of coincident site lattice boundaries during selective growth in interstitial-free steels. 2178-2186A
		Orientation selective recrystallization of nonoriented electrical steels. 2347-2358A
		Effects of alloy modification and thermomechanical processing on recrystallization of Al-Mg-Mn alloys. 2947-2957A
		Modeling recrystallization kinetics, grain sizes, and textures during multipass hot rolling. 4133-4144A
		Recrystallization, Alloying effects
		The effect of iron and manganese on the recrystallization behavior of hot-rolled and solution-heat-treated aluminum alloy 8013. 19-27A

The influence of niobium supersaturation in austenite on the static recrystallization behavior of low carbon microalloyed steels.	951-960A	Rhodium, Binary systems Standard enthalpies of formation of dysprosium alloys, Dy+Me (Me=Ni, Ru, Rh, Pd, Ir, and Pt), by high-temperature direct synthesis calorimetry.	417-422B
Modeling recovery and recrystallization kinetics in cold-rolled Ti-Nb stabilized interstitial-free steel.	3410-3423A	Roasting Kinetics of sulfation of chalcopyrite with steam and oxygen in the presence of ferric oxide.	465-474B
Recrystallization, Deformation effects		Rockwell hardness Quenching C60 fullerene into diamond in the Fe-C alloy system by laser treatment.	2293-2296A
Experimental investigation of the transformation texture in hot-rolled ferritic stainless steel using single orientation determination.	49-57A	Rockwell hardness, Alloying effects Effect of magnesium on the aging behavior of Al-Zn-Mg-Cu/ Al_2O_3 metal matrix composites.	2005-2012A
Aspects of dynamic recrystallization in shaped charge and explosively formed projectile devices.	1773-1778A	Rod milling Thermally assisted and mechanically driven solid-state reactions for formation of amorphous $Al_{33}Ta_{67}$ alloy powders.	3267-3278A
Recrystallization, Heating effects		Rolling contact Crystallographic preferred orientation induced by cyclic rolling contact loading.	3445-3465A
Effect of primary grain size on the secondary recrystallization of mechanically alloyed oxide dispersion strengthened nickel-based superalloy.	493-496A	Rolling texture Modeling recrystallization kinetics, grain size, and textures during multipass hot rolling.	4133-4144A
An analysis of static recrystallization during continuous, rapid heat treatment.	2051-2053A	Rolls, Irradiation The effect of high-energy electron-beam irradiation on microstructural modification of a high-speed steel roll.	3149-3161A
Reduction (chemical), Environmental effects		Roughness Quantitative characterization of the surface topography of rolled sheets by laser scanning microscopy and Fourier transformation.	2338-2346A
Oxidation-reduction equilibrium of Cu^{2+}/Cu^+ in binary alkaline sulfide melts.	385-392B	Ruthenium, Binary systems Standard enthalpies of formation of dysprosium alloys, Dy+Me (Me=Ni, Ru, Rh, Pd, Ir, and Pt), by high-temperature direct synthesis calorimetry.	417-422B
Relaxation		Ruthenium, Ternary systems Mechanical properties of Ru-Ni-Al alloys.	1395-1400A
Internal friction in hydrogen-charged CrNi and CrNiMn austenitic stainless steels.	1815-1821A	Ruthenium base alloys, Powder technology Synthesis of RuAl by reactive powder processing.	3688-3699A
Residual stress		Ruthenium compounds, Powder technology Synthesis of RuAl by reactive powder processing.	3688-3699A
The Bauschinger effect in a SiC/Al composite.	995-1001A	Rutile, Reduction (chemical) Preoxidation and hydrogen reduction of ilmenite in a fluidized bed reactor.	731-738B
High-temperature measurements of lattice parameters and internal stresses of a creep-deformed monocrystalline nickel-base superalloy.	1003-1014A	S-N diagrams Fracture characteristics, microstructure, and tissue reaction of Ti-5Al-2.5Fe for orthopedic surgery.	3925-3935A
Recrystallization in oxide-dispersion strengthened mechanically alloyed sheet steel.	1963-1978A	Sag Van der Waals approximation for potassium bubbles in tungsten.	987-992B
Thermal residual stresses in functionally graded and layered 6061 Al/SiC materials.	3241-3249A	Salt water, Environment Corrosive wear of SiC whisker- and particulate-reinforced 6061 aluminum alloy composites.	2653-2662A
Residual stress, Cooling effects		The influence of aqueous environments on low ΔK and high ΔK fatigue crack propagation behavior in low carbon structural steels.	2678-2685A
Analysis of thermal residual stress in a thick-walled ring of Dur-alcan-base Al-SiC functionally graded material.	4145-4151A	Samarium, Binary systems Inverse melting in binary systems: morphology and microscopy of catactic alloys.	979-986B
Residual stress, Corrosion effects		Samarium, Quaternary systems Thermodynamic properties of complex oxides in the Sm-Ba-Cu-O system.	973-978B
Effects of the alumina scale on the room-temperature tensile behavior of preoxidized MA 956.	3809-3816A	Sapphire, Composite materials Kinetics of cyclic oxidation and cracking and finite element analysis of MA956 and sapphire/MA956 composite system.	3279-3291A
Residual stress, Field effects		Scale (corrosion) A study of solid-aqueous equilibria by the speciation approach in the hydronium alunite-sulfuric acid-water system at high temperatures.	555-566B
Characterization of titanium thin films prepared by bias assisted magnetron sputtering.	1057-1060B	Kinetics of cyclic oxidation and cracking and finite element analysis of MA956 and sapphire/MA956 composite system.	3279-3291A
Residual stress, Microstructural effects		Effects of the alumina scale on the room-temperature tensile behavior of preoxidized MA 956.	3809-3816A
Influence of interstitials on the mechanical properties of metallic materials.	3524-3529A	Scale (corrosion), Metallography Real-time observations of the oxidation of mild steel at high temperature by neutron diffraction.	993-997B
Residual stress, Welding effects		Scanning electron microscopy Formation of aluminum-silicon alloys from feldspars—determination of silicon, light, and heavy elements in silicon by scanning electron microscopy.	604-609B
Effect of postweld treatment on the fatigue crack growth rate of electron-beam-welded AISI 4130 steel.	3162-3169A	Inverse melting in binary systems: morphology and microscopy of catactic alloys.	979-986B
Residues			
The mineralogical department of germanium in the Clarksville electrolytic zinc plant of Savage Zinc Inc.	567-576B		
Resistivity			
Physical modeling studies of electrolyte flow due to gas evolution and some aspects of bubble behavior in advanced Hall cells. III. Predicting the performance of advanced Hall cells.	19-27B		
Resistivity, Composition effects			
A study of the influence of mischmetal additions to Al-7Si-0.3Mg (LM 25/356) alloy.	1283-1292A		
Resistivity, Microstructural effects			
Precipitation in lead-calcium alloys containing tin.	1668-1675A		
Resistivity, Temperature effects			
Electrical conductivity of molten cryolite based mixtures obtained with a tube type cell made of pyrolytic boron nitride.	255-261B		
Retained austenite, Crystal lattices			
Nonuniform distribution of carbonitride particles and its effect on prior austenite grain size in the simulated coarse-grained heat-affected zone of thermomechanical control-processed steels.	4031-4038A		
Retained austenite, Heating effects			
Influence of reinforcement volume fraction and size on the microstructure and abrasion wear resistance of hot isostatic pressed white iron matrix composites.	4171-4181A		
Influence of matrix structure on the abrasion wear resistance and toughness of a hot isostatic pressed white iron matrix composites.	4183-4191A		
Rhenium, Alloying elements			
The breakdown of single-crystal solidification in high refractory nickel-base alloys.	1081-1094A		
Rheological properties, Composition effects			
A statistical analysis of the effect of a mixture component on the rheology of alumina feedstocks.	399-408B		

Real-time observations of the oxidation of mild steel at high temperature by neutron diffraction.	993-997B	Selenium, Alloying additive Effects of oxygen, selenium, and tellurium on the rate of nitrogen dissolution in molten iron.	846-851B
The formation mechanism(s), morphology, and crystallography of ferrite sideplates.	1517-1532A	Selenium, Binary systems Critical evaluation and optimization of the thermodynamic properties of liquid tin solutions.	808-826B
The relationship between microstructural and plastic instability in Al-4.0 wt.% Cu alloy.	2916-2922A	Self-propagating synthesis Synthesis of RuAl by reactive powder processing.	3688-3699A
Thermally assisted and mechanically driven solid-state reactions for formation of amorphous Al ₃₃ Ta ₆₇ alloy powders.	3267-3278A	Self-propagating synthesis, Pressure effects Pressure-assisted reactive synthesis of titanium aluminides from dense 50Al-50Ti elemental powder blends.	2130-2139A
Discussion of "Effects of tensile stress on microstructural change of eutectoid Zn-Al alloy" and authors' reply.	3330-3335A	Semiconductors Retrograde solubility in semiconductors.	2704-2707A
Shear ligament phenomena in Fe ₃ Al intermetallics and micro-mechanics of shear ligament toughening.	3817-3825A	Sensitizing Influence of thermal aging on the intergranular corrosion resistance of types 304LN and 316LN stainless steels.	2881-2887A
Correlation of microstructure and fracture toughness in high-chromium white iron hardfacing alloys.	3881-3891A	Sensors Reference electrode of simple galvanic cells for developing sodium sensors for use in molten aluminum.	794-800B
Microstructure and fracture of SiC-particulate-reinforced cast A356 aluminum alloy composites.	3893-3901A	Sensors, Development The measurement of hydrogen activities in molten copper using an oxide protonic conductor.	929-935B
Notch fracture in γ -tinum aluminides.	3903-3912A	Sensors, Materials selection Development of a magnetoelastic resonant sensor using iron-rich, nonzero magnetostrictive amorphous alloys.	3203-3213A
High-temperature oxidation of Ti ₃ Al-based titanium aluminides in oxygen.	3993-4002A	Serrated yielding, Temperature effects Manifestations of dynamic strain aging in soft-oriented NiAl single crystals.	3542-3557A
Effect of nitrogen on the oxidation behavior of Ti ₃ Al-based intermetallic alloys.	4003-4010A	Service life, Composition effects Carbide diagrams and precipitation of alloying elements during aging of low-alloy steels.	498-502A
Infrared transient-liquid-phase joining of SCS-6/B21S titanium matrix composite.	4011-4018A	Shaft furnaces Modeling and experimental study of gaseous oxidation of liquid iron alloys.	852-862B
Nonuniform distribution of carbonitride particles and its effect on prior austenite grain size in the simulated coarse-grained heat-affected zone of thermomechanical control-processed steels.	4031-4038A	Shape, Pressure effects Studies of interface deformations in single- and multi-layered liquid baths due to an impinging gas jet.	911-920B
Modeling of primary and secondary dendrites in a Cu-6 wt.% tin alloy.	4085-4093A	Shape memory The effect of substrate constraint on the martensitic transformation of Ni-Ti thin films.	2858-2860A
Creep deformation and damage in a continuous fiber-reinforced Ti-6Al-4V composite.	4193-4204A	Shape memory, Cooling effects NiTi and NiTi-TiC composites. III. Shape-memory recovery.	193-203A
Secondary hardening Effect of alloying additions on fracture behavior of molybdenum-containing secondary hardening steels.	3343-3346A	Shape memory, Heating effects Effect of aging on shape memory behavior of Ti-51.3 at.% Ni thin films.	3753-3759A
M ₂ C precipitates in isothermal tempering of high Co-Ni secondary hardening steel.	3466-3472A	Shape memory, Microstructural effects Temperature dependent deformation of polydomain phases in an In-22.5 at.% Ti shape memory alloy.	1687-1692A
Segregations Theoretical modeling of densification during activated solid-state sintering.	441-450A	Shape memory, Stress effects Predicting the orientation-dependent stress-induced transformation and detwinning response of shape memory alloy single crystals.	269-279A
The embrittlement and de-embrittlement of grain boundaries in an Fe-Mn-Ni alloy due to grain boundary segregation of manganese.	1015-1020A	Shape memory, Temperature effects Influence of training time and temperature on shape memory effect in Cu-Zn-Al alloys.	3108-3111A
Modeling of microsegregation in macrosegregation computations.	2314-2327A	Shape memory alloys, Heat treatment Effect of aging on shape memory behavior of Ti-51.3 at.% Ni thin films.	3753-3759A
A model for macrosegregation and its application to Al-Cu castings.	2708-2721A	Shape memory alloys, Phase transformations Predicting the orientation-dependent stress-induced transformation and detwinning response of shape memory alloy single crystals.	269-279A
Equiaxed dendritic solidification with convection. II. Numerical simulations for an Al-4 wt.% Cu alloy.	2765-2783A	Thermoelastic martensite and shape memory effect in ductile Cu-Al-Mn alloys.	2187-2195A
Equiaxed dendritic solidification with convection. III. Comparisons with NH ₄ Cl-H ₂ O experiments.	2784-2795A	Effect of stress state on the stress-induced martensitic transformation in polycrystalline Ni-Ti alloy.	3066-3073A
Incipient chemical instabilities of nanophase Fe-Cu alloys prepared by mechanical alloying.	2934-2946A	Influence of training time and temperature on shape memory effect in Cu-Zn-Al alloys.	3108-3111A
Nonequilibrium grain-boundary segregation and ductile-brittle-ductile transition in Fe-Mn-Ni-Ti age-hardening alloy.	3059-3065A	Martensitic transformations in NiMnAl β phase alloys.	4153-4162A
Macrotransport-solidification kinetics modeling of equiaxed dendritic growth. II. Computation problems and validation on Inconel 718 superalloy casting.	4075-4083A	Shear modulus Communication: On the in situ formation of TiC and Ti ₂ C reinforcements in combustion-assisted synthesis of titanium matrix composites.	237-240A
Segregations, Alloying effects Influence of phosphorus addition on the surface tension of liquid iron and segregation of phosphorus on the surface of Fe-P alloy.	71-79B	Shear modulus, Alloying effects Elastic moduli of titanium-hydrogen alloys in the temperature range 20°C to 1100°C.	3963-3970A
Segregations, Cooling effects Transient thermal analysis of solidification in a centrifugal casting for composite materials containing particle segregation.	277-285B	Shear modulus, Properties A comprehensive dynamical study of nucleation and growth in a one-dimensional shear martensitic transition.	1203-1216A
Modeling of the peritectic reaction and macro-segregation in casting of low carbon steel.	999-1014B		
Macrosegregation during dendritic arrayed growth of hypoeutectic Pb-Sn alloys: Influence of primary arm spacing and mushy zone length.	1353-1362A		
The squeeze casting of hypoeutectic binary Al-Cu.	4121-4132A		
Segregations, Field effects Convection during thermally unstable solidification of Pb-Sn in a magnetic field.	1095-1110A		
Segregations, Heating effects Effect of homogenization heat treatment on the microstructure and heat affected zone microfissuring in welded cast alloy 718.	785-790A		
Neutron diffraction study of austempered ductile iron.	923-928A		
Segregations, Impurity effects Microsegregation of oxygen in Zr-2.5Nb alloy materials.	431-440A		
Segregations, Radiation effects A model describing neutron irradiation-induced segregation to grain boundaries in dilute alloys.	3381-3390A		
Seizing, Composition effects Characterization of the wear response of a modified zinc-based alloy vis-à-vis a conventional zinc-based alloy and a bearing bronze at a high sliding speed.	3513-3523A		

Shear properties, Composition effects			
Effects of shear flow and anisotropic kinetics on the morphological stability of a binary alloy.	687-694A		
Shear properties, Microstructural effects			
Bridge toughening enhancement in double-notched MoSi_2/Nb model composites.	909-921A		
Shear strength			
Interface effects on the micromechanical response of a transversely loaded single fiber SCS-6/Ti-6Al-4V composite.	2035-2043A		
Wear-resistant coatings produced by shock-wave compaction of powders.	2297-2304A		
Shear stress			
Water model experiment on the liquid flow behavior in a bottom blown bath with top layer.	35-41B		
Subcritical crack growth at bimaterial interfaces. I. Flexural peel technique.	205-211A		
Interface effects on the micromechanical response of a transversely loaded single fiber SCS-6/Ti-6Al-4V composite.	2035-2043A		
Evidence of fracture surface interference for cracks loaded in shear detected by phase-shifted speckle interferometry.	3853-3860A		
Shear stress, Temperature effects			
Manifestations of dynamic strain aging in soft-oriented NiAl single crystals.	3542-3557A		
Sheet metal, Heat treatment			
Low quench sensitivity of superplastic 8090 Al-Li thin sheets.	2923-2933A		
Sheet metal, Mechanical properties			
Plastic anisotropy of sheets with continuously varying anisotropic parameters and flow stress.	317-326A		
Tension characteristics of notched specimens for Al-Li-Cu-Zr alloys sheets with various cerium contents.	3089-3094A		
High-temperature deformation and failure of an orthorhombic titanium aluminide sheet material.	3675-3681A		
Sheet metal, Rolling			
Quantitative characterization of the surface topography of rolled sheets by laser scanning microscopy and Fourier transformation.	2338-2346A		
Sheet metal, Surface properties			
Measurement of friction under sheet forming conditions.	3971-3981A		
Sheet metal, Welding			
Forming of tailor-welded blanks.	2605-2616A		
Shielded metal arc welding			
Structural stability of super duplex stainless weld metals and its dependence on tungsten and copper.	2196-2208A		
Shock loading			
Mechanistic processes influencing shock chemistry in powder mixtures of the Ti-Si, Ti-Al, and Ti-B systems.	1761-1771A		
Shock waves			
Aspects of dynamic recrystallization in shaped charge and explosively formed projectile devices.	1773-1778A		
Short range order			
Stable and metastable ordered phases in microcrystalline alloys Ni (Fe, Mn, Ti).	2045-2046A		
Shot peening			
Influence of plastic deformation upon the half-width of engineering metallic materials in hard state.	3662-3668A		
Shrinkage, Cooling effects			
Thermomechanics of the cooling stage in casting processes: three-dimensional finite element analysis and experimental validation.	81-99B		
Shrinkage, Radiation effects			
Sputter-induced pits on {100} nickel surfaces.	981-993A		
Silicides, Coatings			
The deposition of aluminide and silicide castings on γ -TiAl using the halide-activated pack cementation method.	3761-3772A		
Silicides, Composite materials			
Bridge toughening enhancement in double-notched MoSi_2/Nb model composites.	909-921A		
Loading rate and test temperature effects on fracture of in situ niobium silicide-niobium composites.	3292-3306A		
Fracture and fatigue-crack growth behavior in ductile-phase toughened molybdenum disilicide: effects of niobium wire vs. particulate reinforcements.	3781-3792A		
The balance of mechanical and environmental properties of a multielement niobium-niobium silicide-based <i>in situ</i> composite.	3801-3808A		
Silicides, Oxidation			
Phase relations of a silicide/silica reaction couple at 2273K.	271-276B		
Silicides, Powder technology			
Mechanistic processes influencing shock chemistry in powder mixtures of the Ti-Si, Ti-Al, and Ti-B systems.	1761-1771A		
Silicides, Reactions (chemical)			
Modeling of sequential reactions during micropyretic synthesis.		961-972A	
Silicon, Alloying elements			
The effects on fracture toughness of ductile-phase composition and morphology in Nb-Cr-Ti and Nb-Si <i>in situ</i> composites.		3007-3018A	
The cracking mechanism of silicon particles in an A357 aluminum alloy.		3558-3568A	
Silicon, Binary systems			
Thermal decomposition of silicon carbides: discussion of "the effect of an electric field on self-sustaining combustion synthesis, I and II", and author's reply.		322-325B	
Effects of shear flow and anisotropic kinetics on the morphological stability of a binary alloy.		687-694A	
Critical evaluation and optimization of the thermodynamic properties of liquid tin solutions.		808-826B	
Mechanistic processes influencing shock chemistry in powder mixtures of the Ti-Si, Ti-Al, and Ti-B systems.		1761-1771A	
A thermodynamic evaluation of the nickel-silicon system.		2897-2903A	
Silicon, Chemical analysis			
Formation of aluminum-silicon alloys from feldspars—determination of silicon, light, and heavy elements in silumin by scanning electron microscopy.		604-609B	
Silicon, Extraction			
Preparation of pure silicon by electrowinning in a bytownite-cryolite melt.		895-900B	
Silicon, Impurities			
Influence of chromium and impurities on the grain refining behavior of aluminum.		791-800A	
Silicon, Quaternary systems			
An isothermal section at 550°C in the Al-rich corner of the Al-Fe-Mn-Si system.		3357-3361A	
Silicon, Refining			
Thermodynamics of phosphorus in molten silicon.		937-941B	
Silicon carbide, Coatings			
Investigation of the temperature field developed by a spinning beam in laser processing.		4039-4047A	
Silicon carbide, Composite materials			
Effective elastic moduli of fiber-matrix interphases in high-temperature composites.		165-182A	
Transient thermal analysis of solidification in a centrifugal casting for composite materials containing particle segregation.		277-285B	
Effect of a solid solution on the steady-state creep behavior of an aluminum matrix composite.		305-316A	
Stacking faults in SiC particles and their effect on the fracture behavior of a 15 vol.-% SiC/6061-Al matrix composite.		459-465A	
The x-ray diffraction study of deformation in the composite matrix of Al-Mg-Zn and SiC.		503-505A	
Liquid state infrared processing of SCS-6/Ti-6Al-4V composites.		527-532B	
Solidification of particle-reinforced metal-matrix composites.		663-671B	
The Bauschinger effect in a SiC/Al composite.		995-1001A	
A one-phase model of the mixing of Al-SiC composite melt.		1015-1023B	
Theoretical analysis of the particle gradient distribution in centrifugal field during solidification.		1025-1029B	
Interface characterization of ceramic fiber-reinforced titanium alloy composites manufactured by infrared processing.		1379-1394A	
Thermal stability of SiC-SCS-6 fiber-reinforced IM834 alloys.		1403-1405A	
An experimental and theoretical investigation of the rapid consolidation of continuously reinforced, metal-matrix composites.		1709-1720A	
Multiple matrix cracking in a fiber-reinforced titanium matrix composite under high-cycle fatigue.		1899-1907A	
Growth behavior of microstructurally short cracks in the 6061 aluminum alloy with and without 22 vol.-% SiC whiskers.		2013-2021A	
Interface effects on the micromechanical response of a transversely loaded single fiber SCS-6/Ti-6Al-4V composite.		2035-2043A	
Corrosive wear of SiC whisker- and particulate-reinforced 6061 aluminum alloy composites.		2653-2662A	
Tensile ductility and fracture of superplastic aluminum-SiC composites under thermal cycling conditions.		2837-2842A	
Observation of short fatigue crack-growth process in SiC-fiber-reinforced Ti-15-3 alloy composite.		2843-2851A	
Prediction of creep-rupture life of unidirectional titanium matrix composites subjected to transverse loading.		3074-3080A	
Thermal residual stresses in functionally graded and layered 6061 Al/SiC materials.		3241-3249A	
Thermal expansion of metals reinforced with ceramic particles and microcellular foams.		3700-3717A	
Microstructural changes in a mechanically alloyed Al-6.2Zn-2.5Mg-1.7Cu alloy (7010) with and without particulate SiC reinforcement.		3718-3726A	
Microstructure and fracture of SiC-particulate-reinforced cast A356 aluminum alloy composites.		3893-3901A	
Infrared transient-liquid-phase joining of SCS-6/B21S titanium matrix composite.		4011-4018A	
Analysis of thermal residual stress in a thick-walled ring of Dur-alcan-base Al-SiC functionally graded material.		4145-4151A	

Creep deformation and damage in a continuous fiber-reinforced Ti-6Al-4V composite.	4193-4204A	Slags, Surface properties	Studies of interface deformations in single- and multi-layered liquid baths due to an impinging gas jet.	911-920B
Silicon dioxide, Reactions (chemical) Activities in $\text{CaO-SiO}_2\text{-Al}_2\text{O}_3$ slags and deoxidation equilibria of silicon and aluminum.	943-953B	Slaked lime, Environment	Influence of microalloying on the corrosion resistance of steel in saturated calcium hydroxide.	1693-1699A
Silver, Binary systems Generalized enthalpy method for multicomponent phase change.	869-879B	Sliding friction	High-temperature wear and deformation processes in metal matrix composites.	3135-3148A
Silver, Diffusion Analysis of mean square penetration depth in grain boundary diffusion.	3473-3477A		Ni_3Al intermetallic particles as wear-resistant reinforcement for Al-base composites processed by powder metallurgy.	3259-3268A
Silver, Extraction Electrochemical behavior of the dissolution of gold-silver alloys in cyanide solutions.	355-361B		Characterization of the wear response of a modified zinc-based alloy vis-à-vis a conventional zinc-based alloy and a bearing bronze at a high sliding speed.	3513-3523A
Silver, Recovering Influence of gold content on copper oxidation from silver-gold-copper alloys.	3187-3191A		The wear behavior between hardfacing materials.	3639-3648A
Silver base alloys, Brazing A model for coupled growth of reaction layers in reactive brazing of ZrO_2 -toughened Al_2O_3 .	3630-3638A	Slip	NiTi and NiTi-TiC composites. II. Compressive mechanical properties.	183-191A
Silver base alloys, Phase transformations Characterization of a massive transformation by microstructural analysis.	1511-1516A		Crystallography of grain boundary α precipitates in a β titanium alloy.	1630-1641A
Silver base alloys, Phases (state of matter) Eutectoid decomposition in Ag-Ga.	1678-1682A		Bauschinger effect in Haynes 230 alloy: influence of strain rate and temperature.	1739-1748A
Simulation Cold model study of the surface profile in a continuous slab casting mold: effect of second phase.	695-697B	Slip, Composition effects	Effect of manganese dispersoids on the fatigue crack propagation of Al-Zn-Mg alloys.	490-493A
Eco-techno-economic synthesis of process routes for the production of zinc using combinatorial optimization.	1031-1044B	Slip, Environmental effects	On the transition of fatigue crack growth from stage I to stage II in a corrosive environment.	471-476A
Thermal expansion of metals reinforced with ceramic particles and microcellular foams.	3700-3717A	Slip, Stress effects	Discussion of "a fully plastic microcracking model for transgranular stress corrosion cracking in planar slip materials" and reply.	819-821A
Evidence of fracture surface interference for cracks loaded in shear detected by phase-shifted speckle interferometry.	3853-3860A	Slip planes	Plastic zones and fatigue-crack closure under plane-strain double slip.	3491-3502A
Measurement of friction under sheet forming conditions.	3971-3981A	Smelting	A multiphase fluid mechanics approach to gas holdup in bath smelting processes.	195-201B
Sinterability, Alloying effects The effect of Mo addition on the liquid-phase sintering of W heavy alloy.	3120-3125A		Heat transfer and pressure drop considerations in the design of Sirosmelit lances.	221-230B
Sintered compacts, Physical properties The effect of Mo addition on the liquid-phase sintering of W heavy alloy.	3120-3125A		Influence of gold content on copper oxidation from silver-gold-copper alloys.	3187-3191A
Sintering (powder metallurgy) Effects of nickel on the sintering behavior of Fe-Ni compacts made from composite and elemental powders.	203-211B	Snoek effect	Influence of interstitials on the mechanical properties of metallic materials.	3524-3529A
Comparative study of pore structure evolution during solvent and thermal debinding of powder injection molded parts.	245-253A	Sodium, Binary systems	Critical evaluation and optimization of the thermodynamic properties of liquid tin solutions.	808-826B
Theoretical modeling of densification during activated solid-state sintering.	441-450A	Sodium, Chemical analysis	Formation of aluminum-silicon alloys from feldspars—determination of silicon, light, and heavy elements in silumin by scanning electron microscopy.	604-609B
Microstructure and phase relations in a powder-processed Ti-22Al-12Nb alloy.	1121-1126A		Reference electrode of simple galvanic cells for developing sodium sensors for use in molten aluminum.	794-800B
Slab casting Flow and thermal behavior of the top surface flux/powder layers in continuous casting molds.	672-685B	Sodium, Thermal properties	The transported entropy of Na^+ in solid state cryolite.	788-793B
Cold model study of the surface profile in a continuous slab casting mold: effect of second phase.	695-697B	Sodium chloride, Environment	Studies on the influence of metallurgical variables on the stress corrosion behavior of AISI 304 stainless steel in sodium chloride solution using the fracture mechanics approach.	1313-1325A
Analysis of shell thickness irregularity in continuously cast mid-size carbon steel slabs using mold thermocouple data.	1045-1056B	Sol gel process	Preparation of glass-forming materials from granulated blast furnace slag.	801-807B
Slabs, Casting A water model study of the flow asymmetry inside a continuous slab casting mold.	757-764B		Synthesis of nanocrystalline Ni_3Cu by sol-gel route.	4213-4216A
Slag disposal Preparation of glass-forming materials from granulated blast furnace slag.	801-807B	Solar generators	Thermodynamics of phosphorus in molten silicon.	937-941B
Slags A multiphase fluid mechanics approach to gas holdup in bath smelting processes.	195-201B	Solid phases	Interdissolution kinetics in oxide powder mixture using high temperature x-ray diffraction technique.	318-322B
Activities in $\text{MnO-SiO}_2\text{-Al}_2\text{O}_3$ slags and deoxidation equilibria of manganese and silicon.	263-270B		Effects of flow on morphological stability during directional solidification.	583-593A
Controversy on the free energy of formation of CaO —additional evidence in support of thermochemical data.	647-651B		Interface attachment kinetics in alloy solidification.	671-686A
Cold model study of the surface profile in a continuous slab casting mold: effect of second phase.	695-697B		An adaptive mesh refinement scheme for solidification problems.	707-717A
Slags, Reactions (chemical) Chemical potentials of components of the system $\text{CaO-P}_2\text{O}_5\text{-Fe}_2\text{O}_3$ at 1673K.	595-603B		Real time x-ray transmission microscopy of solidifying Al-In alloys.	801-808A
Reduction of FeO smelting slags by solid carbon: experimental results.	717-730B		Inverse melting in binary systems: morphology and microscopy of eutectic alloys.	979-986B
Activities in $\text{CaO-SiO}_2\text{-Al}_2\text{O}_3$ slags and deoxidation equilibria of silicon and aluminum.	943-953B	Solid phases, Alloying effects	Characterization of a massive transformation by microstructural analysis.	1511-1516A
Slags, Solubility Solubility of carbon in $\text{CaO-Al}_2\text{O}_3$ melts.	57-64B		Precipitation in lead-calcium alloys containing tin.	1668-1675A

Solid phases, Heating effects		
High-temperature nitridation of Ni-Cr alloys	59-69A	Macrotransport-solidification kinetics modeling of equiaxed dendritic growth. II. Computation problems and validation on Inconel 718 superalloy casting.
Pearlite in ultrahigh carbon steels: heat treatments and mechanical properties.	111-118A	Modeling of primary and secondary dendrites in a Cu-6 wt.% tin alloy.
Solid phases, Pressure effects		
Vacuum evaporation of KCl-NaCl salts. I. Thermodynamic modeling of vapor pressures of solid and liquid solutions.	141-146B	Solidification, Alloying effects The breakdown of single-crystal solidification in high refractory nickel-base alloys.
Solid phases, Temperature effects		
A study of the thermal decomposition of BaCO ₃ .	409-416B	Solidification, Cooling effects Numerical modeling of cellular/dendritic array growth: spacing and structure predictions.
Overview of geometric effects on coarsening of mushy zones. The phase field method: simulation of alloy dendritic solidification during recalescence.	557-567A	Solidification, Field effects On the reaction between Fe-Ti and Fe-C liquids under microgravity.
Solid solubility		
The production of nickel-zinc alloys by powder injection.	657-669A	Solidification, Pressure effects The squeeze casting of hypoeutectic binary Al-Cu.
Solid-state contributions to densification during liquid-phase sintering.	780-787B	Solidification, Temperature effects
Retrograde solubility in semiconductors.	901-909B	Nucleation controlled solidification kinetics.
Thermodynamic activities and partial enthalpies of mixing in the solid solution of Fe in Ni ₃ Al.	2704-2707A	Overview of geometric effects on coarsening of mushy zones.
Solid solubility, Alloying effects		Banded solidification microstructures.
Mechanical alloying of Nb-Al powders.	3569-3575A	The phase field method: simulation of alloy dendritic solidification during recalescence.
Solid solubility, Composition effects		
Microstructural changes in a mechanically alloyed Al-6.2Zn-2.5Mg-1.7Cu alloy (7010) with and without particulate SiC reinforcement.	3718-3726A	Solidification point
Solid solutions, Mechanical properties		Solidification of an alloy 625 weld overlay.
Influence of interstitials on the mechanical properties of metallic materials.	3524-3529A	Solubility, Alloying effects
Solid state		Solubility of carbon in CaO-Al ₂ O ₃ melts.
Dense CoAl-based alloys with improved ductility: solid-state synthesis and microstructure control.	2140-2150A	Effects of oxygen, selenium, and tellurium on the rate of nitrogen dissolution in molten iron.
Solidification		Solutes
Thermomechanics of the cooling stage in casting processes: three-dimensional finite element analysis and experimental validation.	81-99B	Modeling of microsegregation in macrosegregation computations.
Scaling of intragranular dendritic microstructure in ingot solidification.	101-113B	Solution heat treatment
Transient thermal analysis of solidification in a centrifugal casting for composite materials containing particle segregation.	277-285B	Microstructural aspects of the dissolution and melting of Al ₂ Cu phase in Al-Si alloys during solution heat treatment.
Effect of superheat on the solidification structures of AISI 310S austenitic stainless steel.	287-296B	The control of grain size and distribution of particles in a (6061 alloy) _m (Al ₂ O ₃) _n composite by solutionizing treatment.
Porosity formation in Al-9 wt.% Si-3 wt.% Cu alloy systems: metallographic observations.	415-429A	Dense CoAl-based alloys with improved ductility: solid-state synthesis and microstructure control.
Effects of forced electromagnetic vibrations during the solidification of aluminum alloys. I. Solidification in the presence of crossed alternating electric fields and stationary magnetic fields.	445-455B	Hot deformation mechanisms of a solution-treated Al-Li-Cu-Mg-Zr alloy.
Microstructure of Al ₂ O ₃ fiber-reinforced superalloy (Inconel 718) composites.	451-458A	Sour gas, Environment
Effects of forced electromagnetic vibrations during the solidification of aluminum alloys. II. Solidification in the presence of collinear variable and stationary magnetic fields.	457-464B	Microstructural aspects of sulfide stress cracking in an API X-80 pipeline steel.
The effect of bulk flow concentration on diffusion coupling between dendrites.	477-480A	Spalling
Analysis and Modeling of Solidification.	509-824A	Kinetics of cyclic oxidation and cracking and finite element analysis of MA956 and sapphire/MA956 composite system.
Intermixing model of continuous casting during a grade transition.	617-632B	Effects of the alumina scale on the room-temperature tensile behavior of preoxidized MA 956.
Solidification of particle-reinforced metal-matrix composites.	663-671B	Specific heat
Radioscopic visualization of isothermal solidification of eutectic Ga-In alloy.	686-689B	Modeling of ingot distortions during direct chill casting of aluminum alloys.
An adaptive mesh refinement scheme for solidification problems.	707-717A	Spheroidal structure, Deformation effects
Inverse melting in binary systems: morphology and microscopy of catactic alloys.	979-986B	Effect of creep strain on microstructural stability and creep resistance of a TiAl/Ti ₃ Al lamellar alloy.
Modeling of the peritectic reaction and macro-segregation in casting of low carbon steel.	999-1014B	Spheroidal structure, Heating effects
Theoretical analysis of the particle gradient distribution in centrifugal field during solidification.	1025-1029B	Pearlite in ultrahigh carbon steels: heat treatments and mechanical properties.
Analysis of shell thickness irregularity in continuously cast middle carbon steel slabs using mold thermocouple data.	1045-1056B	Effect of bainite transformation and retained austenite on mechanical properties of austempered spheroidal graphite cast steel.
Modeling of ferrite growth in nodular cast iron.	2209-2220A	Spheroidizing
Modeling of microsegregation in macrosegregation computations.	2314-2327A	Bainitic microstructures formed by split isothermal transformation in an Fe-C-Si-Mn-Mo steel.
A model for macrosegregation and its application to Al-Cu castings.	2708-2721A	Spinodal decomposition, Stress effects
Determination of the solidification curves of commercial aluminum alloys.	2722-2726A	Molecular dynamics simulation of martensitic transformations in NiAl.
Orientation dependence of primary dendrite spacing.	2727-2739A	Splitting
Equiaxed dendritic solidification with convection. I. Multiscale/multiphase modeling.	2754-2764A	Splitting phenomena occurring in the martensitic transformation of Cr13 and CrMoV14 stainless steels in the absence of carbide precipitation.
Equiaxed dendritic solidification with convection. II. Numerical simulations for an Al-4 wt.% Cu alloy.	2765-2783A	Squeeze casting
Equiaxed dendritic solidification with convection. III. Comparisons with NH ₄ Cl-H ₂ O experiments.	2784-2795A	Microstructure and fracture of SiC-particulate-reinforced cast A356 aluminum alloy composites.
Solidification of an alloy 625 weld overlay.	3612-3620A	The squeeze casting of hypoeutectic binary Al-Cu.
Macrotransport-solidification kinetics modeling of equiaxed dendritic growth. I. Model development and discussion.	4061-4074A	Stability
		The relationship between microstructural and plastic instability in Al-40 wt.% Cu alloy.
		Stacking fault energy
		Reply: Dynamic materials model. Basis and principles.

Stacking faults		
The mechanism of formation of a fine duplex microstructure in Ti-4Al-2Mn-2Nb alloys.	1655-1867A	
High-resolution transmission electron microscopy investigation of the face-centered cubic/hexagonal close-packed martensite transformation in Co-31.8 wt.% Ni alloy. II. Plate intersections, extended defects, and nucleation mechanisms.	3371-3380A	
Stacking faults, Deformation effects		
The x-ray diffraction study of deformation in the composite matrix of Al-Mg-Zn and SiC.	503-505A	
Stacking faults, Radiation effects		
Transmission electron microscopy study on the cross-sectional microstructure of an ion-nitriding layer.	1347-1352A	
Stacking faults, Stress effects		
Stacking faults in SiC particles and their effect on the fracture behavior of a 15 vol.-% SiC/6061-Al matrix composite.	459-465A	
Stainless steels, Casting		
Intermixing model of continuous casting during a grade transition.	617-632B	
Stainless steels, Forming		
Reply: Dynamic materials model. Basis and principles.	235-236A	
Stainless steels, Microstructure		
Prediction of grain structures in various solidification processes.	695-705A	
Statistical analysis		
A statistical analysis of the effect of a mixture component on the rheology of alumina feedstocks.	399-408B	
Steam turbines, Service life		
Carbide diagrams and precipitation of alloying elements during aging of low-alloy steels.	498-502A	
Steel making		
Representation of mixed reactive gases on free energy (Ellingham-Richardson) diagrams.	65-69B	
Dispersed phase holdup in liquid-liquid emulsions generated by high strength bottom gas injection.	213-219B	
Characteristics of eccentric bubble plumes in liquids.	231-239B	
The use of blast furnace slag and derived materials in the vitrification of electric arc furnace dust.	379-384B	
A study of the thermal decomposition of BaCO ₃ .	409-416B	
Reoxidation of aluminum in Fe-Al-M (M=C, Mn, and Ti) melts with CaO-Al ₂ O ₃ -FeO (3 mass%) slags.	423-431B	
Transient thermal model of the continuous single-wheel thin-strip casting process.	509-525B	
Alternative technologies in iron and steelmaking.	541-553B	
Model study of bubble and liquid-flow characteristics in a bottom blown bath under reduced pressure.	765-772B	
Activities in CaO-SiO ₂ -Al ₂ O ₃ slags and deoxidation equilibria of silicon and aluminum.	943-953B	
Steels, Casting		
Transient thermal model of the continuous single-wheel thin-strip casting process.	509-525B	
Flow and thermal behavior of the top surface flux/powder layers in continuous casting molds.	672-685B	
Mathematical modeling of tundish operation and flow control to reduce transition slabs.	745-756B	
Steels, Coating		
Discussion of "The effect of steel chemistry on the formation of Fe-Zn intermetallic compounds of galvannealed-coated steel sheets" and authors' reply.	146-148B	
Microstructure of bonding zones in laser-clad nickel-alloy-based composite coatings reinforced with various ceramic powders.	391-400A	
The production of nickel-zinc alloys by powder injection.	780-787B	
Kinetics of phase evolution of Zn-Fe intermetallics.	2904-2910A	
Steels, Corrosion		
Stress corrosion cracking of pressure vessel steels in high-temperature caustic aluminate solutions.	1327-1331A	
Steels, Diffusion		
Annealing and aging of interstitial C in α -Fe, as measured by internal friction.	2461-2469A	
Steels, Heat treatment		
Effect of bainite transformation and retained austenite on mechanical properties of austempered spheroidal graphite cast steel.	1585-1594A	
Steels, Irradiation		
Theory of nucleation with cluster loss and injection: application to plastic deformation and irradiation.	1441-1448A	
Steels, Mechanical properties		
Detecting stable crack onset at ductile-brittle transition in steels.	469-471A	
Steels, Melting		
Studies of interface deformations in single- and multi-layered liquid baths due to an impinging gas jet.		911-920B
Steels, Phase transformations		
On the reaction between Fe-Ti and Fe-C liquids under microgravity.		407-414A
Bainitic microstructures formed by split isothermal transformation in an Fe-C-Si-Mn-Mo steel.		1141-1147A
Steels, Quality control		
Effects of oxygen, selenium, and tellurium on the rate of nitrogen dissolution in molten iron.		846-851B
Steels, Refining		
Thermodynamics of sulfur in the BaO-MnO-SiO ₂ flux system. Use of solid-electrolyte galvanic cells to determine the activity of CaO in the CaO-ZrO ₂ system and the standard Gibbs free energies of formation of CaZrO ₃ from CaO and ZrO ₂ .		652-657B
Model study of bubble and liquid-flow characteristics in a bottom blown bath under reduced pressure.		658-662B
Steels, Steel making		
Water model experiment on the liquid flow behavior in a bottom blown bath with top layer.		765-772B
Steels, Surface finishing		
Influence of plastic deformation upon the half-width of engineering metallic materials in hard state.		3662-3668A
Stiffness		
Microstructure and properties of Al ₂ O ₃ -Al(Si) and Al ₂ O ₃ -Al(Si)-Si composites formed by in situ reaction of aluminum with aluminosilicate ceramics.		2122-2129A
The effect of volume percent and morphology of phases on the damping behavior of epoxy-aluminum composites.		2366-2373A
Stiffness, High temperature effects		
Effective elastic moduli of fiber-matrix interphases in high-temperature composites.		165-182A
Stirring		
A unified representation of the two-phase plume characteristics in gas-stirred ladle systems.		704-708B
Stochiometry		
Formation of structural intermetallics by reactive metal penetration of titanium and nickel oxides and aluminates.		2100-2104A
Dense CoAl-based alloys with improved ductility: solid-state synthesis and microstructure control.		2140-2150A
Strain		
Effect of creep strain on microstructural stability and creep resistance of a TiAl/Ti ₃ Al lamellar alloy.		127-134A
Mechanisms of high-temperature fatigue failure in alloy 800H.		851-861A
The influence of niobium supersaturation in austenite on the static recrystallization behavior of low carbon microalloyed steels.		951-960A
The Bauschinger effect in a SiC/Al composite.		995-1001A
Increased ductility in high velocity electromagnetic ring expansion.		1837-1844A
The effects on fracture toughness of ductile-phase composition and morphology in Nb-Cr-Ti and Nb-Si in situ composites.		3007-3018A
Analysis of the stress-strain curves of a modified 9Cr-1Mo steel by the Voce equation.		3340-3343A
Strain, Cooling effects		
NiTi and NiTi-TiC composites. III. Shape-memory recovery.		193-203A
Strain, Environmental effects		
On the transition of fatigue crack growth from stage I to stage II in a corrosive environment.		471-476A
Strain, Heating effects		
Heterogeneous nucleation of δ on dislocations in a dilute aluminum-lithium alloy.		1595-1605A
Strain, Stress effects		
Computer simulation of reversible martensitic transformations. A study on coherency strain and precipitate morphology via a discrete atom method.		1187-1201A
Effect of uniaxial stress on coarsening of precipitate clusters.		1449-1459A
Strain aging		
Temperature and strain-rate effects on low-cycle fatigue behavior of alloy 800H.		1460-1475A
Dynamic strain aging and hydrogen-induced softening in alpha titanium.		255-267A
The relationship between microstructural and plastic instability in Al-4.0 wt.-% Cu alloy.		1877-1887A
Strain aging, Microstructural effects		
Influence of interstitials on the mechanical properties of metallic materials.		2916-2922A
Strain aging, Temperature effects		
Manifestations of dynamic strain aging in soft-oriented NiAl single crystals.		3524-3529A
		3542-3557A

Strain hardenability		
Constitutive behavior of tantalum and tantalum-tungsten alloys.	2994-3006A	Manifestations of dynamic strain aging in soft-oriented NiAl single crystals.
Strain hardening		3542-3557A
NiTi and NiTi-TiC composites. II. Compressive mechanical properties.	183-191A	Strain softening
Constitutive behavior of tantalum and tantalum-tungsten alloys.	2994-3006A	Dynamic strain aging and hydrogen-induced softening in alpha titanium.
Influence of interstitials on the mechanical properties of metallic materials.	3524-3529A	1877-1887A
Strain hardening, Alloying effects		Strain softening, Alloying effects
Effect of phase composition and hydrogen level on the deformation behavior of titanium-hydrogen alloys.	1869-1876A	Effect of phase composition and hydrogen level on the deformation behavior of titanium-hydrogen alloys.
Dynamic strain aging and hydrogen-induced softening in alpha titanium.	1877-1887A	1869-1876A
Strain hardening, Deformation effects		Stress analysis
Non-Schmid effects on the behavior of polycrystals, with applications to Ni ₃ Al.	81-99A	Evidence of fracture surface interference for cracks loaded in shear detected by phase-shifted speckle interferometry.
The x-ray diffraction study of deformation in the composite matrix of Al-Mg-Zn and SiC.	503-505A	Creep lifetime prediction of oxide-dispersion-strengthened nickel-base superalloys: a micromechanically based approach.
Strain hardening, Microstructural effects		Elevated temperature deformation behavior of a dispersion-strengthened Al-Fe, V, Si alloy.
Reinforcement shape effects on the fracture behavior and ductility of particulate-reinforced 6061-Al matrix composites.	3739-3746A	Analysis of thermal residual stress in a thick-walled ring of Dur-alcan-base Al-SiC functionally graded material.
Strain hardening, Temperature effects		4145-4151A
Enhanced ductility in coarse-grained Al-Mg alloys.	343-352A	Stress concentration
Manifestations of dynamic strain aging in soft-oriented NiAl single crystals.	3542-3557A	Interface effects on the micromechanical response of a transversely loaded single fiber SCS-6/Ti-6Al-4V composite.
Strain rate		The effect of volume percent and morphology of phases on the damping behavior of epoxy-aluminum composites.
Bauschinger effect in Haynes 230 alloy: influence of strain rate and temperature.	1739-1748A	Tension characteristics of notched specimens for Al-Li-Cu-Zr alloys sheets with various cerium contents.
Characterization and mechanical properties of ultrahigh boron steels produced by powder metallurgy.	1861-1867A	Stress concentration, Stress effects
Deformation behavior of an Al-3.37 wt. % Li alloy.	2274-2284A	Evidence of fracture surface interference for cracks loaded in shear detected by phase-shifted speckle interferometry.
Constitutive behavior of tantalum and tantalum-tungsten alloys.	2994-3006A	3853-3860A
Control of superplastic deformation rate during uniaxial tensile tests.	3030-3042A	Stress corrosion cracking
Effect of stress state on the stress-induced martensitic transformation polycrystalline Ni-Ti alloy.	3066-3073A	Discussion of "a fully plastic microcracking model for transgranular stress corrosion cracking in planar slip materials" and reply.
Failure characteristics of 6061/Al ₂ O ₃ /15 _p and 2014/Al ₂ O ₃ /15 _p composites as a function of loading rate.	3095-3107A	819-821A
High-temperature deformation and failure of an orthorhombic titanium aluminide sheet material.	3675-3681A	Initiation of stress corrosion cracking for pipeline steels in a carbonate-bicarbonate solution.
Hydrogen-induced cleavage fracture of Fe ₃ Al-based intermetallics.	3949-3956A	2686-2691A
An analysis of the flow stress of a two-phase alloy system, Ti-6Al-4V.	3957-3962A	Stress corrosion cracking, Environmental effects
Microstructural features of friction welded MA 956 superalloy material.	4019-4029A	Studies on the influence of metallurgical variables on the stress corrosion behavior of AISI 304 stainless steel in sodium chloride solution using the fracture mechanics approach.
Mathematical modeling of the extrusion of 6061/Al ₂ O ₃ /20 _p composite.	4095-4111A	Stress corrosion cracking of pressure vessel steels in high-temperature caustic aluminate solutions.
Strain rate, Alloying effects		Microstructural aspects of sulfide stress cracking in an API X-80 pipeline steel.
Effect of strain rate and temperature on the flow stress of β -phase titanium-hydrogen alloys.	1303-1312A	Stress corrosion cracking, Heating effects
Dynamic strain aging and hydrogen-induced softening in alpha titanium.	1877-1887A	A strain-based fracture model for stress corrosion cracking of low-alloy steels.
Strain rate, Corrosion effects		Atmospheric stress corrosion cracking of a superplastic 7475 aluminum alloy.
Effects of the alumina scale on the room-temperature tensile behavior of preoxidized MA 956.	3809-3818A	Influence of thermal aging on the intergranular corrosion resistance of types 304LN and 316LN stainless steels.
Strain rate, Deformation effects		291-304A
Optimization of cold and warm workability in 304 stainless steel using instability maps.	119-126A	Stress corrosion cracking, Microstructural effects
Flow stress and microstructural evolution during hot working of alloy 22Cr-13Ni-5Mn-0.3N austenitic stainless steel.	1251-1266A	The effects of microstructure, strength level, and crack propagation mode on stress corrosion cracking behavior of 4135 steel.
Analysis on the amplitude of serrated flow associated with the Portevin-LeChatelier effect of substitutional fcc alloys.	1683-1686A	281-290A
Strain rate, High temperature effects		Structure, chemistry, and stress corrosion cracking of grain boundaries in alloys 600 and 690.
High-temperature deformation properties of NiAl single crystals.	1229-1240A	327-341A
Strain rate, Impurity effects		Stress cycle
The effect of hydrogen on the fracture of alloy X-750.	101-110A	Temperature and strain-rate effects on low-cycle fatigue behavior of alloy 800H.
Strain rate, Microstructural effects		Effect of thermal cycling on the mechanical properties of 350 grade maraging steel.
Effect of iron on ductility and cavitation in the superplastic An-22% Al eutectoid.	863-872A	255-267A
The inter-relationship between grain boundary sliding and cavitation during creep of polycrystalline copper.	901-907A	757-761A
Creep deformation of dispersion-strengthened copper.	1217-1227A	Stress Intensity
Influence of interstitials on the mechanical properties of metallic materials.	3524-3529A	Effect of creep strain on microstructural stability and creep resistance of a TiAl/Ti ₂ Al lamellar alloy.
Strain rate, Temperature effects		Effect of a solid solution on the steady-state creep behavior of an aluminum matrix composite.
Temperature and strain-rate effects on low-cycle fatigue behavior of alloy 800H.	255-267A	513-530A
Enhanced ductility in coarse-grained Al-Mg alloys.	343-352A	Effect of carbide precipitation on the creep behavior of alloy 800HT in the temperature range 700-900°C.
Temperature dependence of the rate sensitivity and its effect on the activation energy for high-temperature flow.	3348-3348A	Creep deformation and crack growth behavior of a single-crystal nickel-base superalloy.
		Time-dependent, environmentally assisted crack growth in Nicalon-fiber-reinforced SiC composites at elevated temperatures.
		Temperature dependence of the intrinsic small fatigue crack growth behavior in nickel-base superalloys based on measurement of crack closure.
		Analysis on the amplitude of serrated flow associated with the Portevin-LeChatelier effect of substitutional fcc alloys.
		1021-1031A
		1683-1686A
		Stress relaxation
		Influence of interstitials on the mechanical properties of metallic materials.
		3524-3529A
		Stress strain curves
		Mechanical behavior of the in situ composite alloys in the Al-Ni-Ti system near the L ₂ phase field.
		71-79A

Optimization of cold and warm workability in 304 stainless steel using instability maps.	119-126A	Sulfides, Crystal growth Internal sulfide precipitation in low Cr-Fe alloys.	3192-3202A
NI Ti and NI Ti-C composites. II. Compressive mechanical properties.	183-191A	Sulfides, Reduction (chemical) Phase equilibria in the metal-sulfur-oxygen system and selective reduction of metal oxides and sulfides. I. The carbothermic reduction and calcination of complex mineral sulfides.	827-838B
Subcritical crack growth at bimaterial interfaces. III. Shear-enhanced fatigue crack growth resistance at polymer/metal interface.	221-228A	Sulfur, Binary systems Critical evaluation and optimization of the thermodynamic properties of liquid tin solutions.	808-826B
Temperature and strain-rate effects on low-cycle fatigue behavior of alloy 800H.	255-267A	Sulfur, Physical properties Thermodynamics of sulfur in the BaO-MnO-SiO ₂ flux system.	652-657B
Predicting the orientation-dependent stress-induced transformation and detwinning response of shape memory alloy single crystals.	269-279A	Sulfur, Ternary systems Applicability of Butler's equation in interpreting the thermodynamic behavior of surfaces and adsorption in Fe-S-O melts.	241-253B
Plastic anisotropy of sheets with continuously varying anisotropic parameters and flow stress.	317-326A	Internal sulfide precipitation in low Cr-Fe alloys.	3192-3202A
Reinforcement stresses during deformation of sphere- and particulate-reinforced aluminum-matrix composites.	486-490A	Sulfuric acid leaching A study of solid-aqueous equilibria by the speciation approach in the hydronium alunite-sulfuric acid-water system at high temperatures.	555-566B
The characteristics of cavitation in superplastic metals and ceramics.	873-878A	Sulfurization Internal sulfide precipitation in low Cr-Fe alloys.	3192-3202A
Characterization of superplastic deformation behavior of a fine grain 5083 Al alloy sheet.	1889-1898A	Superalloys Recrystallization in oxide-dispersion strengthened mechanically alloyed sheet steel.	1963-1978A
Influence of temperature transients on the hot workability of a two-phase gamma titanium aluminide alloy.	1933-1950A	Superalloys, Casting Viscosity of superalloy 718 by the oscillating vessel technique.	698-701B
Interface effects on the micromechanical response of a transversely loaded single fiber SCS-6/Ti-6Al-4V composite.	2035-2043A	Superalloys, Claddings Solidification of an alloy 625 weld overlay.	3612-3620A
High-temperature deformation processing of Ti-24Al-20Nb.	2593-2604A	The wear behavior between hardfacing materials.	3639-3648A
The relationship between microstructural and plastic instability in Al-4.0 wt.% Cu alloy.	2916-2922A	Superalloys, Coating Isothermal fatigue of an aluminide-coated single-crystal superalloy. I.	353-361A
Effect of thermomechanical treatments on the room-temperature mechanical behavior of iron aluminide Fe ₃ Al.	2985-2993A	Isothermal fatigue of an aluminide-coated single-crystal superalloy. II. Effects of brittle precracking.	363-369A
Constitutive behavior of tantalum and tantalum-tungsten alloys.	2994-3006A	Superalloys, Composite materials Microstructure of Al ₂ O ₃ fiber-reinforced superalloy (Inconel 718) composites.	451-458A
Control of superplastic deformation rate during uniaxial tensile tests.	3030-3042A	Effect of primary grain size on the secondary recrystallization of mechanically alloyed oxide dispersion strengthened nickel-based superalloy.	493-496A
Effect of stress state on the stress-induced martensitic transformation in polycrystalline Ni-Ti alloy.	3066-3073A	Kinetics of cyclic oxidation and cracking and finite element analysis of MA956 and sapphire/MA956 composite system.	3279-3291A
Simulation of the hot-tension test under cavitating conditions.	3112-3119A	Superalloys, Corrosion Structure, chemistry, and stress corrosion cracking of grain boundaries in alloys 600 and 690.	327-341A
Elevated temperature compressive properties of N-doped NiAl.	3170-3180A	Superalloys, Crystal growth Recrystallization in oxide-dispersion strengthened mechanically alloyed sheet steel.	1963-1978A
Thermal residual stresses in functionally graded and layered 6061 Al/SiC materials.	3241-3249A	Macrotransport-solidification kinetics modeling of equiaxed dendritic growth. I. Model development and discussion.	4061-4074A
The use of microstructural gradients in hot gas-pressure forming of Zn-Al sheet.	3250-3258A	Macrotransport-solidification kinetics modeling of equiaxed dendritic growth. II. Computation problems and validation on Inconel 718 superalloy casting.	4075-4083A
Analysis of the stress-strain curves of a modified 9Cr-1Mo steel by the Voce equation.	3340-3343A	Superalloys, Forming Reply: Dynamic materials model. Basis and principles.	235-236A
Hot deformation mechanisms of a solution-treated Al-Li-Cu-Mg-Zr alloy.	3478-3490A	Superalloys, Heat treatment Effect of homogenization heat treatment on the microstructure and heat affected zone microfissuring in welded cast alloy 718.	785-790A
Plastic zones and fatigue-crack closure under plane-strain double slip.	3491-3502A	Superalloys, Joining Transient liquid-phase bonding in the NiAl/Cu/Ni system—a microstructural investigation.	3621-3629A
Manifestations of dynamic strain aging in soft-oriented NiAl single crystals.	3542-3557A	Superalloys, Mechanical properties The effect of hydrogen on the fracture of alloy X-750.	101-110A
High-temperature deformation and failure of an orthorhombic titanium aluminide sheet material.	3675-3681A	Rafting in superalloys.	513-530A
Plastic zone and pileup around large indentations.	3793-3800A	Effect of carbide precipitation on the creep behavior of alloy 800HT in the temperature range 700-900°C.	747-756A
Effects of the alumina scale on the room-temperature tensile behavior of preoxidized MA 956.	3809-3816A	Creep deformation and crack growth behavior of a single-crystal nickel-base superalloy.	829-837A
Microstructural evolution and superplastic deformation behavior of fine grain 5083Al.	3827-3839A	Mechanisms of high-temperature fatigue failure in alloy 800H.	851-861A
Creep lifetime prediction of oxide-dispersion-strengthened nickel-base superalloys: a micromechanically based approach.	3861-3870A	On the influence of grain morphology on creep deformation and damage mechanisms in directionally solidified and oxide dispersion strengthened superalloys.	879-890A
Notch fracture in γ -titanium aluminides.	3903-3912A	High-temperature measurements of lattice parameters and internal stresses of a creep-deformed monocrystalline nickel-base superalloy.	1003-1014A
Creep deformation and damage in a continuous fiber-reinforced Ti-6Al-4V composite.	4193-4204A	Temperature dependence of the intrinsic small fatigue crack growth behavior in nickel-base superalloys based on measurement of crack closure.	1021-1031A
Stress strain curves, Alloying effects		Effects of the alumina scale on the room-temperature tensile behavior of preoxidized MA 956.	3809-3816A
Elevated temperature compressive properties of zirconium-modified NiAl.	2628-2641A		
Stress strain curves, Microstructural effects			
Theoretical calculation of the stress-strain behavior of dual-phase metals with randomly oriented spheroidal inclusions.	2359-2365A		
Stresses			
Multiple matrix cracking in a fiber-reinforced titanium matrix composite under high-cycle fatigue.	1899-1907A		
Strip casting			
Transient thermal model of the continuous single-wheel thin-strip casting process.	509-525B		
Strip steel, Metal working			
Analysis and prevention of vertical cracking phenomena during deep drawing of hot-rolled SG295 steel strips.	1241-1250A		
Strontium, Alloying elements			
Electron microscope study of Al-Fe-Si intermetallics in 6201 aluminum alloy.	929-936A		
Effect of strontium modification on near-threshold fatigue crack growth in an Al-Si-Cu die cast alloy.	1293-1302A		
Submerged arc welding			
Dilution in single pass arc welds.	481-489B		
Sulfation			
Kinetics of sulfation of chalcopyrite with steam and oxygen in the presence of ferric oxide.	465-474B		

Superalloys, Metal working		
Flow stress and microstructural evolution during hot working of alloy 22Cr-13Ni-5Mn-0.3N austenitic stainless steel.	1251-1266A	
Superalloys, Microstructure		
Prediction of grain structures in various solidification processes.	695-705A	
Characterization of constitutional liquid film migration in nickel-base alloy 718.	2692-2703A	
Superalloys, Phases (state of matter)		
The breakdown of single-crystal solidification in high refractory nickel-base alloys.	1081-1094A	
Superalloys, Powder technology		
The effect of thermal cycle on the microstructural development of a powder metallurgy superalloy braze material.	145-153A	
Superalloys, Structural hardening		
A study on coherency strain and precipitate morphology via a discrete atom method.	1449-1459A	
Bauschinger effect in Haynes 230 alloy: influence of strain rate and temperature.	1739-1745A	
Preferential coarsening of γ' precipitates in Inconel 718 during creep.	3391-3398A	
Creep lifetime prediction of oxide-dispersion-strengthened nickel-base superalloys: a micromechanically based approach.	3861-3870A	
Superalloys, Welding		
Microstructural features of friction welded MA 956 superalloy material.	4019-4029A	
Superconductors		
A thermodynamic evaluation of the Ti-Mo-C system.	955-966B	
Supercooling		
The role of grain corners in nucleation.	480-483A	
High-speed imaging and analysis of the solidification of undercooled nickel melts.	863-868B	
Solidification of undercooled Fe-Cr-Ni alloys. II. Microstructural evolution.	3226-3240A	
Microstructure of Cu-Co alloys solidified at various supercoolings.	4049-4059A	
Superlattices		
Stable and metastable ordered phases in microcrystalline alloys Ni (Fe, Mn, Ti).	2045-2046A	
Superplastic forming		
Effects of alloy modification and thermomechanical processing on recrystallization of Al-Mg-Mn alloys.	2947-2957A	
Microstructural evolution and superplastic deformation behavior of fine grain 5083Al.	3827-3839A	
Superplasticity		
Characterization of superplastic deformation behavior of a fine grain 5083 Al alloy sheet.	1889-1898A	
Pressure-assisted reactive synthesis of titanium aluminides from dense 50Al-50Ti elemental powder blends.	2130-2139A	
An investigation by interactive electron backscatter pattern analysis of processing and superplasticity in an aluminum-magnesium alloy.	2252-2262A	
A model study of cavity growth in superplasticity using single premachined holes.	2532-2539A	
Tensile ductility and fracture of superplastic aluminum-SiC composites under thermal cycling conditions.	2837-2842A	
Control of superplastic deformation rate during uniaxial tensile tests.	3030-3042A	
The behavior of internal markers in Ti-6Al-4V deformed in superplastic tension.	3747-3748A	
Superplasticity, Deformation effects		
Micronecking and fracture in cavitated superplastic materials.	1043-1046A	
Superplasticity, Heating effects		
Low quench sensitivity of superplastic 8090 Al-Li thin sheets.	2923-2933A	
Superplasticity, Mechanical properties		
The characteristics of cavitation in superplastic metals and ceramics.	873-878A	
Superplasticity, Microstructural effects		
Effect of iron on ductility and cavitation in the superplastic An-22% Al eutectoid.	863-872A	
On microsuperplasticity in AA7475 domes.	1400-1403A	
Microstructural evolution and superplastic deformation behavior of fine grain 5083Al.	3827-3839A	
Superplasticity, Stress effects		
Predicting the orientation-dependent stress-induced transformation and detwinning response of shape memory alloy single crystals.	269-279A	
Supersaturation		
Incipient chemical instabilities of nanophase Fe-Cu alloys prepared by mechanical alloying.	2934-2946A	
Surface chemistry		
Studies on the corrosion and the behavior of inert anodes in aluminum electrolysis.		185-193B
Physical chemistry of the powder metallurgy of beryllium: chemical characterization of the powder in relation to its granularity.		371-379A
Fundamental studies of copper anode passivation during electrotrefining. II. Surface morphology.		610-616B
Surface chemistry, Temperature effects		
Variation of contact angles with temperature and time in the Al-Al ₂ O ₃ system.		51-55B
Surface hardening		
Quenching C60 fullerene into diamond in the Fe-C alloy system by laser treatment.		2293-2298A
Surface hardness, Deformation effects		
Influence of plastic deformation upon the half-width of engineering metallic materials in hard state.		3662-3668A
Surface hardness, Radiation effects		
Simultaneous plasma treatment for carburizing and carbonitriding using hollow cathode discharge.		401-405A
Surface layer		
Flow and thermal behavior of the top surface flux/powder layers in continuous casting molds.		672-685B
Control of iron nitride layers growth kinetics in the binary Fe-N system.		1823-1835A
Surface structure		
Physical chemistry of the powder metallurgy of beryllium: chemical characterization of the powder in relation to its granularity.		371-379A
Bridge toughening enhancement in double-notched MoSi ₂ /Nb model composites.		909-921A
Interface characterization of ceramic fiber-reinforced titanium alloy composites manufactured by infrared processing.		1379-1394A
On microsuperplasticity in AA7475 domes.		1400-1403A
Formation of bainite in ferrous and nonferrous alloys through sympathetic nucleation and ledgewise growth mechanism.		1533-1543A
A high resolution transmission electron microscopy study of interfaces between the γ , B2, and α_2 phases in a Ti-Al-Mo alloy.		1618-1629A
Surface structure, Alloying effects		
Effects of nickel on the sintering behavior of Fe-Ni compacts made from composite and elemental powders.		203-211B
Surface structure, Deformation effects		
Quantitative characterization of the surface topography of rolled sheets by laser scanning microscopy and Fourier transformation.		2338-2346A
Surface structure, Environmental effects		
On the transition of fatigue crack growth from stage I to stage II in a corrosive environment.		471-476A
Surface structure, Heating effects		
Surface morphology and compound layer pores of plasma nitrocarburized low carbon steel.		135-143A
Transition between internal and external nitridation of Ni-Ti alloys.		1608-1617A
Surface structure, Temperature effects		
Overview of geometric effects on coarsening of mushy zones.		557-567A
Surface temperature		
Heat-flow-based analysis of surface crack formation during the start-up of the direct chill casting process. I. Development of the inverse heat-transfer model.		119-127B
Surface tension, Alloying effects		
Influence of phosphorus addition on the surface tension of liquid iron and segregation of phosphorus on the surface of Fe-P alloy.		71-79B
Surface tension, Pressure effects		
The influence of oxygen pressure and P ₂ O ₅ on the surface tension of liquid iron oxide at 1435°C.		139-141B
Surface tension, Temperature effects		
Applicability of Butler's equation in interpreting the thermodynamic behavior of surfaces and adsorption in Fe-S-O melts.		241-253B
Surgical implants, Materials selection		
Fracture characteristics, microstructure, and tissue reaction of Ti-5Al-2.5Fe for orthopedic surgery.		3925-3935A
Synthesis		
Symposium on In Situ Reactions for Synthesis of Composites, Ceramics, and Intermetallics. II.		
Modeling of sequential reactions during micropyretic synthesis.		961-972A
Formation of structural intermetallics by reactive metal penetration of titanium and nickel oxides and aluminates.		2100-2104A
Tantalum, Alloying elements		
The breakdown of single-crystal solidification in high refractory nickel-base alloys.		1081-1094A

Tantalum, Crystal growth		
Aspects of dynamic recrystallization in shaped charge and explosively formed projectile devices.	1773-1778A	The embrittlement and de-embrittlement of grain boundaries in an Fe-Mn-Ni alloy due to grain boundary segregation of manganese.
Tantalum, Heat treatment		1015-1020A
Improved oxidation resistance of group VB refractory metals by Al ⁺ ion implantation.	491-500B	Tensile properties of mechanically alloyed/milled ODS-Ni-based alloys.
Tantalum, Structural hardening		1371-1377A
Constitutive behavior of tantalum and tantalum-tungsten alloys.	2994-3006A	Effect of bainite transformation and retained austenite on mechanical properties of austempered spheroidal graphite cast steel.
Tantalum base alloys, Powder technology		1585-1594A
Thermally assisted and mechanically driven solid-state reactions for formation of amorphous Al ₃₃ Ta ₆₇ alloy powders.	3267-3278A	Microstructural aspects of the dissolution and melting of Al ₂ Cu phase in Al-Si alloys during solution heat treatment.
Tantalum base alloys, Structural hardening		1785-1798A
Constitutive behavior of tantalum and tantalum-tungsten alloys.	2994-3006A	Fracture characteristics, microstructure, and tissue reaction of Ti-5Al-2.5Fe for orthopedic surgery.
Tellurium, Alloying additive		3925-3935A
Effects of oxygen, selenium, and tellurium on the rate of nitrogen dissolution in molten iron.	846-851B	Tensile strength, Pressure effects
Tellurium, Dopants		Synthesis of Ru/Ib by reactive powder processing.
Hydrogen effects on directional solidification of tellurium-doped cast irons.	496-498A	3688-3699A
Temperature		Tensile strength, Stress effects
Influence of temperature transients on the hot workability of a two-phase gamma titanium aluminide alloy.	1933-1950A	Temperature and strain-rate effects on low-cycle fatigue behavior of alloy 800H.
Mathematical modeling of the extrusion of 6061/Al ₂ O ₃ /20p composite.	4095-4111A	255-267A
Temperature distribution		Rafting in superalloys.
Flow and thermal behavior of the top surface flux/powder layers in continuous casting molds.	672-685B	513-530A
Tempering		Effect of thermal cycling on the mechanical properties of 350 grade maraging steel.
A strain-based fracture model for stress corrosion cracking of low-alloy steels.	291-304A	757-761A
Mössbauer spectroscopy study of the aging and tempering of high nitrogen quenched Fe-N alloys: kinetics of formation of Fe ₁₉ N ₂ nitride by interstitial ordering in martensite.	2160-2177A	Effect of uniaxial stress on coarsening of precipitate clusters.
Microstructural basis for the effect of chromium on the strength and toughness of AF1410-based high performance steels.	2510-2517A	1460-1475A
Atmospheric stress corrosion cracking of a superplastic 7475 aluminum alloy.	2617-2627A	Tensile strength, Temperature effects
M ₂ C precipitates in isothermal tempering of high Co-Ni secondary hardening steel.	3466-3472A	Observations of secondary carbide precipitation and its relation to high-temperature flow and fracture in HT-9 stainless steel.
Tensile properties, Heating effects		467-469A
The dependence of complex alloyed steel properties on quenching and tempering conditions.	2852-2858A	Tensile stress
Tensile properties, Microstructural effects		Subcritical crack growth at bimaterial interfaces. I. Flexural peel technique.
Microstructure and tensile behavior of nitrogen-alloyed, dual-phase stainless steels.	1845-1859A	205-211A
A comparison of fracture behavior of low alloy steel with different sizes of carbide particles.	1909-1917A	Subcritical crack growth at bimaterial interfaces. III. Shear-enhanced fatigue crack growth resistance at polymer/metal interface.
Tensile strength		221-228A
Thermal stability of SiC-SCS-6 fiber-reinforced IMI834 alloys. Characterization and mechanical properties of ultrahigh boron steels produced by powder metallurgy.	1403-1405A	Mechanisms of high-temperature fatigue failure in alloy 800H. The Bauschinger effect in a SiC/Al composite.
Tensile ductility and fracture of superplastic aluminum-SiC composites under thermal cycling conditions.	1881-1887A	995-1001A
Microstructure and tensile properties of compacted, mechanically alloyed, nanocrystalline Fe-Al.	2837-2842A	Tension tests
Analysis of the stress-strain curves of a modified 9Cr-1Mo steel by the Voce equation.	3126-3134A	Control of superplastic deformation rate during uniaxial tensile tests.
The balance of mechanical and environmental properties of a multielement niobium-niobium silicide-based in situ composite.	3340-3343A	3030-3042A
Tensile strength, Alloying effects		Simulation of the hot-tension test under cavitating conditions.
Effect of strontium modification on near-threshold fatigue crack growth in an Al-Si-Cu die cast alloy.	3801-3808A	3112-3119A
Tension characteristics of notched specimens for Al-Li-Cu-Zr alloys sheets with various cerium contents.	3801-3808A	Effect of postweld treatment on the fatigue crack growth rate of electron-beam-welded AISI 4130 steel.
Tensile strength, Cooling effects		3162-3169A
The quench sensitivity of cast Al-7 wt% Si-0.4 wt% Mg alloy.	3809-3911A	The use of microstructural gradients in hot gas-pressure forming of Zn-Al sheet.
Tensile strength, Corrosion effects		3250-3258A
Effects of the alumina scale on the room-temperature tensile behavior of preoxidized MA 956.	3809-3816A	An evaluation of the creep properties of two Al-Si alloys produced by rapid solidification processing.
Tensile strength, Heating effects		3871-3879A
Influence of long term annealing on tensile properties and fracture of near- α titanium alloy Ti-6Al-2.75Sn-4Zr-0.4Mo-0.4SSi.	1700-1708A	Tension tests, Development
Microstructural basis for the effect of chromium on the strength and toughness of AF1410-based high performance steels.	2510-2517A	Measurement of friction under sheet forming conditions.
Low quench sensitivity of superplastic 8090 Al-Li thin sheets.	2923-2933A	3971-3981A
Tensile strength, Impurity effects		Ternary systems
Microsegregation of oxygen in Zr-2.5Nb alloy materials.	431-440A	Discussion of "derivation and consistency of the partial functions of the ternary system involving interaction coefficients" and author's reply.
Tensile strength, Microstructural effects		325-327B
Pearlite in ultrahigh carbon steels: heat treatments and mechanical properties.	111-118A	Ternary systems, Diffusion
		Thermodynamic and kinetic study of diffusion paths in the system Cu-Fe-Ni.
		2229-2238A
		Ternary systems, Mechanical properties
		Mechanical behavior of the in situ composite alloys in the Al-Ni-Ti system near the L ₁ ₂ phase field.
		71-79A
		Mechanical properties of Ru-Ni-Al alloys.
		1395-1400A
		Ternary systems, Phases (state of matter)
		Evolution of microstructures in the nickel modified titanium tri-aluminides near the L ₁ ₂ phase field.
		5-17A
		M ₂₃ C ₆ carbide equilibria in the Fe-Cr-C system.
		701-704B
		Critical evaluation and optimization of the thermodynamic properties of liquid tin solutions.
		808-826B
		Thermodynamic investigations of the ternary Au-Sn-Zn system.
		921-927B
		A thermodynamic evaluation of the Ti-Mo-C system.
		955-966B
		Experimental study of the phase equilibria in the Fe-Mn-Al system.
		2429-2435A
		Thermodynamic activities and phase boundaries for the alloys of the Ni ₃ Al-Ni ₃ Ti pseudobinary section in the Ni-Al-Ti system.
		2673-2677A
		Internal sulfide precipitation in low Cr-Fe alloys.
		3192-3202A
		Solidification of undercooled Fe-Cr-Ni alloys. II. Microstructural evolution.
		3226-3240A
		Thermodynamic activities and partial enthalpies of mixing in the solid solution of Fe in Ni ₃ Al.
		3569-3575A
		Martensitic transformations in NiMnAl β phase alloys.
		4153-4162A
		Ternary systems, Reactions (chemical)
		Chemical potentials of components of the system CaO+P ₂ O ₅ +Fe ₂ O ₃ at 1673K.
		595-603B
		Ternary systems, Surface properties
		Applicability of Butler's equation in interpreting the thermodynamic behavior of surfaces and adsorption in Fe-S-O melts.
		241-253B
		Texture
		Modeling texture change during the static recrystallization of interstitial free steels.
		155-164A

Recrystallization in oxide-dispersion strengthened mechanically alloyed sheet steel.	1963-1978A	Activities in $\text{CaO}-\text{SiO}_2-\text{Al}_2\text{O}_3$ slags and deoxidation equilibria of silicon and aluminum.	943-953B
The role of coincident site lattice boundaries during selective growth in interstitial-free steels.	2178-2186A	A thermodynamic evaluation of the Ti-Mo-C system.	955-966B
An investigation by interactive electron backscatter pattern analysis of processing and superplasticity in an aluminum-magnesium alloy.	2252-2262A	Thermodynamics of calcium and oxygen in molten titanium and titanium-aluminum alloy.	967-972B
Orientation selective recrystallization of nonoriented electrical steels.	2347-2358A	Thermodynamic properties of complex oxides in the Sm-Ba-Cu-O system.	973-978B
Nanoscale brass/steel multilayer composites produced by cold rolling.	2383-2385A	Thermodynamics and long-range order of nitrogen in $\gamma\text{-Fe}_4\text{N}_1$.	1055-1061A
Texture, Deformation effects		Crystal shapes and phase equilibria: a common mathematical basis.	1431-1440A
Experimental investigation of the transformation texture in hot-rolled ferritic stainless steel using single orientation determination.	49-57A	Thermodynamic and kinetic study of diffusion paths in the system Cu-Fe-Ni.	2229-2238A
Non-Schmid effects on the behavior of polycrystals, with applications to Ni_3Al .	81-99A	Thermodynamic studies and the phase diagram of the Li-Mg system.	2419-2428A
Aspects of dynamic recrystallization in shaped charge and explosively formed projectile devices.	1773-1778A	Thermodynamic activities and phase boundaries for the alloys of the $\text{Ni}_3\text{Al}-\text{Ni}_3\text{Ti}$ pseudobinary section in the Ni-Al-Ti system.	2673-2677A
Texture, Stress effects		An experimental study and thermodynamic calculations of phase equilibria in the Fe-Mo-C-N system.	2869-2880A
Plastic anisotropy of sheets with continuously varying anisotropic parameters and flow stress.	317-326A	A thermodynamic evaluation of the nickel-silicon system.	2897-2903A
Crystallographic preferred orientation induced by cyclic rolling contact loading.	3445-3465A	Kinetics of phase evolution of Zn-Fe intermetallics.	2904-2910A
Thermal conductivity		Incipient chemical instabilities of nanophasic Fe-Cu alloys prepared by mechanical alloying.	2934-2946A
Solidification of particle-reinforced metal-matrix composites.	663-671B	An isothermal section at 550°C in the Al-rich corner of the Al-Fe-Mn-Si system.	3357-3361A
Modeling of ingot distortions during direct chill casting of aluminum alloys.	3214-3225A	Thermodynamic activities and partial enthalpies of mixing in the solid solution of Fe in Ni_3Al .	3569-3575A
Thermal conductivity, Temperature effects		Thermochemistry of the Ni-Hf system—intermetallic phases.	3576-3590A
Heat-flow-based analysis of surface crack formation during the start-up of the direct chill casting process. II. Experimental study of an AA5182 rolling ingot.	129-137B	Thermodynamic assessment of the Nb-N system.	3591-3600A
Thermal cycling		Thermoelastic properties	3214-3225A
The effect of thermal cycle on the microstructural development of a powder metallurgy superalloy braze material.	145-153A	Modeling of ingot distortions during direct chill casting of aluminum alloys.	
Thermal expansion		Thermoelastic properties, Cooling effects	
Microstructure and properties of Al_2O_3 -Al(Si) and Al_2O_3 -Al(Si)-Si composites formed by in situ reaction of aluminum with aluminosilicate ceramics.	2122-2129A	Thermomechanics of the cooling stage in casting processes: three-dimensional finite element analysis and experimental validation.	81-99B
The balance of mechanical and environmental properties of a multielement niobium-niobium silicide-based in situ composite.	3801-3808A	Thermoelastic properties, Temperature effects	
Thermal expansion, Microstructural effects		Observations of secondary carbide precipitation and its relation to high-temperature flow and fracture in HT-9 stainless steel.	467-469A
Thermal expansion of metals reinforced with ceramic particles and microcellular foams.	3700-3717A	Thermogravimetric analysis	
Thermal fatigue, Temperature effects		A study of the thermal decomposition of BaCO_3 . High-temperature oxidation of Ti_3Al -based titanium aluminides in oxygen.	409-416B
Isothermal fatigue of an aluminide-coated single-crystal superalloy. II. Effects of brittle precracking.	363-369A	Effect of nitrogen on the oxidation behavior of Ti_3Al -based intermetallic alloys.	3993-4002A
Thermal stability		Thermomechanical treatment	
Thermal stability of SiC-SCS-6 fiber-reinforced IMI834 alloys.	1403-1405A	The influence of niobium supersaturation in austenite on the static recrystallization behavior of low carbon microalloyed steels.	4003-4010A
Thermal stability, Cooling effects		An investigation by interactive electron backscatter pattern analysis of processing and superplasticity in an aluminum-magnesium alloy.	2252-2262A
Rapid solidification processing of a Mg-Li-Si-Ag alloy.	1363-1370A	Effects of alloy modification and thermomechanical processing on recrystallization of Al-Mg-Mn alloys.	2947-2957A
Thermal stresses		Effect of thermomechanical treatments on the room-temperature mechanical behavior of iron aluminide Fe_3Al .	2985-2993A
Effect of carbide precipitation on the creep behavior of alloy 800HT in the temperature range 700-900°C.	747-756A	Nonuniform distribution of carbonitride particles and its effect on prior austenite grain size in the simulated coarse-grained heat-affected zone of thermomechanical control-processed steels.	4031-4038A
Effect of thermal cycling on the mechanical properties of 350 grade maraging steel.	757-761A	Thickness	
Thermal residual stresses in functionally graded and layered 6061 Al/SiC materials.	3241-3249A	Analysis of shell thickness irregularity in continuously cast middle carbon steel slabs using mold thermocouple data.	1045-1056B
Thermit brazing		Thin films	
A model for coupled growth of reaction layers in reactive brazing of ZrO_2 -toughened Al_2O_3 .	3630-3638A	Crystallization of amorphous phase in sputter-deposited Ti-Al alloy thin films.	2047-2050A
Thermochemistry		Thin films, Microstructure	
Thermochemistry of the Ni-Hf system—intermetallic phases.	3576-3590A	Morphological instabilities of lamellar eutectics.	635-656A
Thermocouples		Microstructural stability on aging of an $\alpha+\beta$ titanium alloy: $\text{Ti}-\text{Al}-1.6\text{Zr}-3.3\text{Mo}-0.3\text{Si}$.	1167-1173A
Analysis of shell thickness irregularity in continuously cast middle carbon steel slabs using mold thermocouple data.	1045-1056B	Tin, Alloying elements	
Thermodynamics		Precipitation in lead-calcium alloys containing tin.	1668-1675A
Vacuum evaporation of KCl-NaCl salts. I. Thermodynamic modeling of vapor pressures of solid and liquid solutions.	141-146B	Tin, Binary systems	
Applicability of Butler's equation in interpreting the thermodynamic behavior of surfaces and adsorption in Fe-S-O melts.	241-253B	Critical evaluation and optimization of the thermodynamic properties of liquid tin solutions.	808-826B
Discussion of "derivation and consistency of the partial functions of the ternary system involving interaction coefficients" and author's reply.	325-327B	Tin, Ternary systems	
Kinetics of sulfation of chalcopyrite with steam and oxygen in the presence of ferric oxide.	465-474B	Thermodynamic investigations of the ternary Au-Sn-Zn system.	921-927B
Overview of geometric effects on coarsening of mushy zones.	557-567A	Tin base alloys, Phases (state of matter)	
Thermodynamics of sulfur in the Ba-C-MnO-SiO_2 flux system.	652-657B	Overview of geometric effects on coarsening of mushy zones.	557-567A
Discussion of "Representation of mixed reactive gases on free energy (Ellingham-Richardson) diagrams" and reply.	693-694B	Titanium, Alloying additive	
Thermodynamic investigations of the ternary Au-Sn-Zn system.	921-927B	The effects on fracture toughness of ductile-phase composition and morphology in Nb-Cr-Ti and Nb-Si in situ composites.	3007-3018A
Thermodynamics of phosphorus in molten silicon.	937-941B		

Titanium, Alloying elements

Influence of microalloying on the corrosion resistance of steel in saturated calcium hydroxide.

Influence of titanium and carbon contents on the hydrogen trapping of microalloyed steels.

Titanium, Binary systems

Critical evaluation and optimization of the thermodynamic properties of liquid tin solutions.

Mechanistic processes influencing shock chemistry in powder mixtures of the Ti-Si, Ti-Al, and Ti-B systems.

Titanium, Chemical analysis

Formation of aluminum-silicon alloys from feldspars—determination of silicon, light, and heavy elements in alumin by scanning electron microscopy.

Titanium, Coatings

Characterization of titanium thin films prepared by bias assisted magnetron sputtering.

Titanium, Composite materialsCommunication: On the in situ formation of TiC and Ti_2C reinforcements in combustion-assisted synthesis of titanium matrix composites.

Interface characterization of ceramic fiber-reinforced titanium alloy composites manufactured by infrared processing.

Titanium, Crystal growth

An analysis of static recrystallization during continuous, rapid heat treatment.

Titanium, DiffusionPressure dependence of anomalous diffusion of zirconium in β -titanium.**Titanium, Extraction**

Preoxidation and hydrogen reduction of ilmenite in a fluidized bed reactor.

Titanium, Mechanical properties

Temperature dependence of the rate sensitivity and its effect on the activation energy for high-temperature flow.

Plastic zone and pileup around large indentations.

Titanium, Phases (state of matter)

Stable and metastable ordered phases in microcrystalline alloys Ni (Fe, Mn, Ti).

Titanium, Reactions (chemical)

Thermodynamics of calcium and oxygen in molten titanium and titanium-aluminum alloy.

Titanium, Ternary systemsEvolution of microstructures in the nickel modified titanium tri-aluminides near the L_12 phase field.Mechanical behavior of the in situ composite alloys in the Al-Ni-Ti system near the L_12 phase field.

A thermodynamic evaluation of the Ti-Mo-C system.

Thermodynamic activities and phase boundaries for the alloys of the Ni_3Al-Ni_3Ti pseudobinary section in the Ni-Al-Ti system.**Titanium, Welding**

Analysis of heat affected zone phase transformations using in situ spatially resolved x-ray diffraction with synchrotron radiation.

Titanium base alloysEffect of nitrogen on the oxidation behavior of Ti_3Al -based intermetallic alloys.**Titanium base alloys, Chemical analysis**

Determination of hydrogen in titanium alloys by cold neutron prompt gamma activation analysis.

Titanium base alloys, Composite materials

Liquid state infrared processing of SCS-6/Ti-6Al-4V composites.

Thermal stability of SiC-SCS-6 fiber-reinforced IMI834 alloys.

An experimental and theoretical investigation of the rapid consolidation of continuously reinforced, metal-matrix composites.

Multiple matrix cracking in a fiber-reinforced titanium matrix composite under high-cycle fatigue.

Interface effects on the micromechanical response of a transversely loaded single fiber SCS-6/Ti-6Al-4V composite.

Observation of short fatigue crack-growth process in SiC-fiber-reinforced Ti-15-3 alloy composite.

Prediction of creep-rupture life of unidirectional titanium matrix composites subjected to transverse loading.

Infrared transient-liquid-phase joining of SCS-6/B21S titanium matrix composite.

Creep deformation and damage in a continuous fiber-reinforced Ti-6Al-4V composite.

Titanium base alloys, Forming

Reply: Dynamic materials model. Basis and principles.

Titanium base alloys, Heat treatmentInfluence of long term annealing on tensile properties and fracture of near- α titanium alloy Ti-6Al-2.75Sn-4Zr-0.4Mo-0.45Si.

1700-1708A

Titanium base alloys, Mechanical propertiesEffect of strain rate and temperature on the flow stress of β -phase titanium-hydrogen alloys.

1303-1312A

High-temperature deformation processing of Ti-24Al-20Nb.

2593-2604A

The influence of stress triaxiality on the damage mechanisms in an equiaxed α/β Ti-6Al-4V alloy.

3043-3058A

High-temperature deformation and failure of an orthorhombic titanium aluminide sheet material.

3675-3681A

The behavior of internal markers in Ti-6Al-4V deformed in superplastic tension.

3747-3748A

Plastic zone and pileup around large indentations.

3793-3800A

Notch fracture in γ -titanium aluminides.

3903-3912A

Fracture characteristics, microstructure, and tissue reaction of Ti-5Al-2.5Fe for orthopedic surgery.

3925-3935A

An analysis of the flow stress of a two-phase alloy system, Ti-6Al-4V.

3957-3962A

Elastic moduli of titanium-hydrogen alloys in the temperature range 20°C to 1100°C.

3963-3970A

Titanium base alloys, MicrostructureMicrostructural stability on aging of an $\alpha+\beta$ titanium alloy: Ti-6Al-1.8Zr-3.3Mo-0.3Si.

1167-1173A

Crystallography of grain boundary α precipitates in a β titanium alloy.

1630-1641A

The mechanism of formation of a fine duplex microstructure in Ti-48Al-2Mn-2Nb alloys.

1655-1667A

Microstructural development of a gas-atomized and hot-pressed super- α_2 alloy.

2221-2228A

Titanium base alloys, OxidationHigh-temperature oxidation of Ti_3Al -based titanium aluminides in oxygen.

3993-4002A

Titanium base alloys, Phase transformations

A high-resolution transmission electron microscopy study of the precipitation process in a dilute Ti-N alloy.

2966-2977A

Effect of stress state on the stress-induced martensitic transformation in polycrystalline Ni-Ti alloy.

3066-3073A

Titanium base alloys, Powder technology

Microstructure and phase relations in a powder-processed Ti-22Al-12Nb alloy.

1121-1128A

Titanium base alloys, Reactions (chemical)

Thermodynamics of calcium and oxygen in molten titanium and titanium-aluminum alloy.

967-972B

Titanium base alloys, Structural hardening

Effect of phase composition and hydrogen level on the deformation behavior of titanium-hydrogen alloys.

1869-1876A

Dynamic strain aging and hydrogen-induced softening in alpha titanium.

1877-1887A

Titanium base alloys, Surface finishing

Investigation of the temperature field developed by a spinning beam in laser processing.

4039-4047A

Titanium carbide, Composite materials

NiTi and NiTi-TiC composites. II. Compressive mechanical properties.

183-191A

NiTi and NiTi-TiC composites. III. Shape-memory recovery. Communication: On the in situ formation of TiC and Ti_2C reinforcements in combustion-assisted synthesis of titanium matrix composites.

193-203A

Analysis of damping in particle-reinforced superplastic zinc composites.

237-240A

NiTi and NiTi-TiC composites. IV. Neutron diffraction study of twinning and shape-memory recovery.

2565-2573A

Influence of reinforcement volume fraction and size on the microstructure and abrasion wear resistance of hot isostatic pressed white iron matrix composites.

2820-2836A

Influence of matrix structure on the abrasion wear resistance and toughness of a hot isostatic pressed white iron matrix composites.

4171-4181A

Titanium compounds, Alloying elementsNotch fracture in γ -titanium aluminides.

3903-3912A

Titanium compounds, CoatingThe deposition of aluminide and silicide castings on γ -TiAl using the halide-activated pack cementation method.

3761-3772A

Titanium compounds, Composite materials

NiTi and NiTi-TiC composites. II. Compressive mechanical properties.

183-191A

NiTi and NiTi-TiC composites. III. Shape-memory recovery. Formation of structural intermetallics by reactive metal penetration of titanium and nickel oxides and aluminates.

193-203A

Investigation of the reaction zone between TiAl and molybdenum.

2100-2104A

Titanium compounds, Crystal growth

Crystallization of amorphous phase in sputter-deposited Ti-Al alloy thin films.

2285-2292A

Titanium compounds, Crystal growth

Crystallization of amorphous phase in sputter-deposited Ti-Al alloy thin films.

2047-2050A

Titanium compounds, Mechanical properties	
Effect of creep strain on microstructural stability and creep resistance of a TiAl/Ti ₃ Al lamellar alloy.	127-134A
Influence of temperature transients on the hot workability of a two-phase gamma titanium aluminide alloy.	1933-1950A
High-temperature low-cycle fatigue of a gamma titanium aluminide alloy Ti-46Al-2Nb-2Cr.	2239-2251A
High-temperature deformation processing of Ti-24Al-20Nb.	2593-2604A
High-temperature deformation and failure of an orthorhombic titanium aluminide sheet material.	3675-3681A
Titanium compounds, Oxidation	
High-temperature oxidation of Ti ₃ Al-based titanium aluminides in oxygen.	3993-4002A
Effect of nitrogen on the oxidation behavior of Ti ₃ Al-based intermetallic alloys.	4003-4010A
Titanium compounds, Phase transformations	
NiTi and NiTi-TiC composites. IV. Neutron diffraction study of twinning and shape-memory recovery.	2820-2836A
The effect of substrate constraint on the martensitic transformation of Ni-Ti thin films.	2858-2860A
Titanium compounds, Powder technology	
Mechanistic processes influencing shock chemistry in powder mixtures of the Ti-Si, Ti-Al, and Ti-B systems.	1761-1771A
Pressure-assisted reactive synthesis of titanium aluminides from dense 50Al-50Ti elemental powder blends.	2130-2139A
Titanium compounds, Reactions (chemical)	
Thermodynamics of calcium and oxygen in molten titanium and titanium-aluminum alloy.	967-972B
Titanium nitride, Coatings	
Active wear and failure mechanisms of titanium nitride-coated high speed steel and titanium nitride-coated cemented carbide tools when machining powder metallurgically made stainless steels.	2796-2808A
Tool life, Coating effects	
Active wear and failure mechanisms of titanium nitride-coated high speed steel and titanium nitride-coated cemented carbide tools when machining powder metallurgically made stainless steels.	2796-2808A
Tool steels, Coating	
Wear-resistant coatings produced by shock-wave compaction of powders.	2297-2304A
Topography	
Quantitative characterization of the surface topography of rolled sheets by laser scanning microscopy and Fourier transformation.	2338-2346A
Toughness	
Failure characteristics of 6061/Al ₂ O ₃ /15 _p and 2014/Al ₂ O ₃ /15 _p composites as a function of loading rate.	3095-3107A
Toughness, Composition effects	
Mechanical properties of Ru-Ni-Al alloys.	1395-1400A
Toughness, Heating effects	
Effect of holding time in the (α+γ) temperature range on toughness of specialty austempered ductile iron.	1979-1989A
Toughness, Microstructural effects	
Mechanical behavior and properties of mechanically alloyed aluminum alloys.	737-745A
Toxicology	
The use of blast furnace slag and derived materials in the vitrification of electric arc furnace dust.	379-384B
Transgranular corrosion, Stress effects	
Discussion of "a fully plastic microcracking model for transgranular stress corrosion cracking in planar slip materials" and reply.	1845-1859A
Transgranular fracture	
Microstructure and tensile behavior of nitrogen-alloyed, dual-phase stainless steels.	3043-3058A
The influence of stress triaxiality on the damage mechanisms in an equiaxed α/β Ti-6Al-4V alloy.	291-304A
Transgranular fracture, Heating effects	
A strain-based fracture model for stress corrosion cracking of low-alloy steels.	2445-2453A
Transition metals, Alloying additive	
Effect of alloying elements on martensitic transformation in the binary NiAl(β) phase alloys.	1347-1352A
Transmission electron microscopy	
Real time x-ray transmission microscopy of solidifying Al-In alloys.	801-808A
Characterization of titanium thin films prepared by bias assisted magnetron sputtering.	1057-1060B
Transmission electron microscopy study on the cross-sectional microstructure of an ion-nitriding layer.	1347-1352A
The formation mechanism(s), morphology, and crystallography	
The relationship between microstructural and plastic instability in Al-4 wt.% Cu alloy.	2916-2922A
A high-resolution transmission electron microscopy study of the precipitation process in a dilute Ti-N alloy.	2966-2977A
Thermally assisted and mechanically driven solid-state reactions for formation of amorphous Al ₃ Ta ₇ alloy powders.	3267-3278A
High-resolution transmission electron microscopy investigation of the face-centered cubic/hexagonal close-packed martensite transformation in Co-31.8 wt.% Ni alloy. I. Plate interfaces and growth ledges.	3362-3370A
High-resolution transmission electron microscopy investigation of the face-centered cubic/hexagonal close-packed martensite transformation in Co-31.8 wt.% Ni alloy. II. Plate intersections, extended defects, and nucleation mechanisms.	3371-3380A
Effect of aging on shape memory behavior of Ti-51.3 at.% Ni thin films.	3753-3759A
Influence of titanium and carbon contents on the hydrogen trapping of microalloyed steels.	3773-3780A
Creep lifetime prediction of oxide-dispersion-strengthened nickel-base superalloys: a micromechanically based approach.	3861-3870A
Elevated temperature deformation behavior of a dispersion-strengthened Al-Fe, V, Si alloy.	3913-3923A
Hydrogen-induced cleavage fracture of Fe ₃ Al-based intermetallics.	3949-3956A
The quench sensitivity of cast Al-7 wt.% Si-0.4 wt.% Mg alloy.	3983-3991A
Microstructural features of friction welded MA 956 superalloy material.	4019-4029A
Nonuniform distribution of carbonitride particles and its effect on prior austenite grain size in the simulated coarse-grained heat-affected zone of thermomechanical control-processed steels.	4031-4038A
Martensitic transformations in NiMnAl β phase alloys.	4153-4162A
Tribology	
Ni ₃ Al intermetallic particles as wear-resistant reinforcement for Al-base composites processed by powder metallurgy.	3259-3266A
Tribology, Radiation effects	
Simultaneous plasma treatment for carburizing and carbonitrating using hollow cathode discharge.	401-405A
Tundishes	
Intermixing model of continuous casting during a grade transition.	617-632B
Mathematical modeling of tundish operation and flow control to reduce transition slabs.	745-756B

Tungsten, Alloying elements

The breakdown of single-crystal solidification in high refractory nickel-base alloys.

1081-1094A

Constitutive behavior of tantalum and tantalum-tungsten alloys.

2994-3006A

Tungsten, Powder technology

Theoretical modeling of densification during activated solid-state sintering.

441-450A

Tungsten, Solubility

Solid-state contributions to densification during liquid-phase sintering.

901-909B

Tungsten, Structural hardening

Van der Waals approximation for potassium bubbles in tungsten.

987-992B

Tungsten base alloys, Powder technology

Solid-state contributions to densification during liquid-phase sintering.

901-909B

The effect of Mo addition on the liquid-phase sintering of W heavy alloy.

3120-3125A

Tungsten carbide, Synthesis

Synthesis of full-density nanocrystalline tungsten carbide by reduction of tungstic oxide at room temperature.

4210-4213A

Turbine blades, Microstructure

Prediction of grain structures in various solidification processes.

695-705A

Turbine blades, Service life

Creep lifetime prediction of oxide-dispersion-strengthened nickel-base superalloys: a micromechanically based approach.

3861-3870A

Turbulence

Experimental study of splash generation in a flash smelting furnace.

633-646B

A unified representation of the two-phase plume characteristics in gas-stirred ladle systems.

704-708B

Twin roll casting

Quantitative characterization of the surface topography of rolled sheets by laser scanning microscopy and Fourier

Twinning

NiTi and NiTi-TiC composites. II. Compressive mechanical properties.
An optical method for determining the surface orientation of crystals.

183-191A

Twinning, Cooling effects

The role of grain corners in nucleation.

2057-2061A

480-483A

Twinning, Deformation effects

The x-ray diffraction study of deformation in the composite matrix of Al-Mg-Zn and SiC.

503-505A

Twinning, Stress effects

Predicting the orientation-dependent stress-induced transformation and detwinning response of shape memory alloy single crystals.

269-279A

Ultrasonic testing

Elastic moduli of titanium-hydrogen alloys in the temperature range 20°C to 1100°C.

3963-3970A

Vacuum refining

Thermodynamics of phosphorus in molten silicon.

937-941B

Vanadium, Alloying additive

The effect of metallic elements on the crystallization behavior of amorphous Fe-Si-B alloys.

3424-3430A

Vanadium, Alloying elements

Influence of microalloying on the corrosion resistance of steel in saturated calcium hydroxide.

1693-1699A

Vanadium, Heat treatment

Improved oxidation resistance of group VB refractory metals by Al⁺ ion implantation.

491-500B

Vapor pressure

Vacuum evaporation of KCl-NaCl salts. I. Thermodynamic modeling of vapor pressures of solid and liquid solutions.

141-146B

Vaporizing, Cooling effects

Vacuum evaporation of KCl-NaCl salts. II. Vaporization-rate model and experimental results.

433-443B

Velocity

Increased ductility in high velocity electromagnetic ring expansion.

1837-1844A

Vertical shaft furnaces

An extended two-dimensional mathematical model of vertical ring furnaces.

297-304B

Video

Experimental study of splash generation in a flash smelting furnace.

633-646B

Viscoplasticity, Cooling effects

Thermomechanics of the cooling stage in casting processes: three-dimensional finite element analysis and experimental validation.

81-99B

Viscoplasticity, Deformation effects

Non-Schmid effects on the behavior of polycrystals, with applications to Ni₃Al.

81-99A

Communication: Discussion of "Modeling of dynamic materials behavior. A critical evaluation of the dissipator power content approach".

232-235A

Viscosity

Water model experiment on the liquid flow behavior in a bottom blown bath with top layer.

35-41B

Viscosity of superalloy 718 by the oscillating vessel technique. Effect of grain refinement on the fluidity of two commercial Al-Si foundry alloys.

698-701B

2305-2313A

Viscosity, Composition effects

A statistical analysis of the effect of a mixture component on the rheology of alumina feedstocks.

399-408B

Viscosity, Temperature effects

Prediction of liquid metal viscosities using an adjustable hard sphere radial distribution curve.

29-34B

Vitrification

Preparation of glass-forming materials from granulated blast furnace slag.

801-807B

Void ratio, Deformation effects

Microstructural evolution and superplastic deformation behavior of fine grain 5083Al.

3827-3839A

Voids

The measurement of hydrogen activities in molten copper using an oxide protonic conductor.

929-935B

Thermal expansion of metals reinforced with ceramic particles and microcellular foams.

3700-3717A

Voids, Radiation effects

Sputter-induced pits on {100} nickel surfaces.

981-993A

Theory of nucleation with cluster bias and injection: application

Voids, Stress effects

The influence of stress triaxiality on the damage mechanisms in an equiaxed α/β Ti-6Al-4V alloy.

3043-3058A

Warp working

Optimization of cold and warm workability in 304 stainless steel using instability maps.

119-126A

Waste disposal

Oxidation-reduction equilibrium of $\text{Cu}^{2+}/\text{Cu}^+$ in binary alkaline sulfate melts.

385-392B

Vacuum evaporation of KCl-NaCl salts. II. Vaporization-rate model and experimental results.

433-443B

Preparation of glass-forming materials from granulated blast furnace slag.

801-807B

Microstructure and phase identification in type 304 stainless steel-zirconium alloys.

2151-2159A

Wastes

Eco-techno-economic synthesis of process routes for the production of zinc using combinatorial optimization.

1031-1044B

Water

A water model study of the flow asymmetry inside a continuous slab casting mold.

757-764B

Water cooling

The improved microstructures and properties of 7075 alloys produced by a water-cooling centrifugal casting method.

1951-1962A

Water quenching

A process model for on-line quenching of aluminum extrusions.

501-508B

Wear particles

Ni₃Al intermetallic particles as wear-resistant reinforcement for Al-base composites processed by powder metallurgy.

3259-3266A

Wear rate

High-temperature wear and deformation processes in metal matrix composites.

3135-3148A

Wear rate, Coating effects

Active wear and failure mechanisms of titanium nitride-coated high speed steel and titanium nitride-coated cemented carbide tools when machining powder metallurgically made stainless steels.

2796-2808A

Wear rate, Composition effects

Characterization of the wear response of a modified zinc-based alloy vis-à-vis a conventional zinc-based alloy and a bearing bronze at a high sliding speed.

3513-3523A

Wear resistance

Corrosive wear of SiC whisker- and particulate-reinforced 6061 aluminum alloy composites.

263-2662A

High-temperature wear and deformation processes in metal matrix composites.

3135-3148A

The wear behavior between hardfacing materials.

3639-3648A

Wear and friction behavior of metal impregnated microporous carbon composites.

3727-3738A

Wear resistance, Coating effects

Wear-resistant coatings produced by shock-wave compaction of powders.

2297-2304A

Wear resistance, Composition effects

Wear behavior of aluminum-based metal matrix composites reinforced with a preform of aluminosilicate fiber.

2385-2389A

Wear resistance, Heating effects

Mechanical properties and 95°C aging characteristics of zircon reinforced Zn-4Al-3Cu alloy.

809-818A

Wear resistance, Microstructural effects

Correlation of microstructure and fracture toughness in high-chromium white iron hardfacing alloys.

3881-3891A

Influence of reinforcement volume fraction and size on the microstructure and abrasion wear resistance of hot isostatic pressed white iron matrix composites.

4171-4181A

Influence of matrix structure on the abrasion wear resistance and toughness of a hot isostatic pressed white iron matrix composites.

4183-4191A

Wear tests

High-temperature wear and deformation processes in metal matrix composites.

3135-3148A

Weld cladding

Ballistic impact behavior of multilayered armor plates processed by hardfacing.

3335-3340A

Solidification of an alloy 625 weld overlay.

3612-3620A

The wear behavior between hardfacing materials.

3639-3648A

Weld defects

Solidification of an alloy 625 weld overlay.

3612-3620A

Weld deposited coatings, Crystal growth

Solidification of an alloy 625 weld overlay.

3612-3620A

Weld deposited coatings, Mechanical properties

Solidification of an alloy 625 weld overlay.

3612-3620A

Weld metal, Microstructure		
Structural stability of super duplex stainless weld metals and its dependence on tungsten and copper.	2196-2208A	801-808A
Welded joints, Heat treatment		
Effect of homogenization heat treatment on the microstructure and heat affected zone microfissuring in welded cast alloy 718.	785-790A	577-584B 937-941B
Welded joints, Mechanical properties		
Effect of multiaxial stresses on creep damage of 316 stainless steel weldments.	891-900A	237-240A 731-736A
Microstructures relevant to brittle fracture initiation at the heat-affected zone of weldment of a low carbon steel.	2574-2582A	1709-1720A
Forming of tailor-welded blanks.	2605-2616A	1739-1748A 2274-2284A
Effect of postweld treatment on the fatigue crack growth rate of electron-beam-welded AISI 4130 steel.	3162-3169A	3007-3018A 3793-3800A 3903-3912A
Welded joints, Microstructure		
Microstructural features of friction welded MA 956 superalloy material.	4019-4029A	1869-1876A 1877-1887A
Welded joints, Phase transformations		
Analysis of heat affected zone phase transformations using in situ spatially resolved x-ray diffraction with synchrotron radiation.	775-783A	490-493A
Welded joints, Phases (state of matter)		
Phase stability and atom probe field ion microscopy of type 308 CRE stainless steel weld metal.	783-774A	3983-3991A
Wetting, Temperature effects		
Variation of contact angles with temperature and time in the Al-Al ₂ O ₃ system.	51-55B	3809-3816A
Whisker composites, Mechanical properties		
Growth behavior of microstructurally short cracks in the 6061 aluminum alloy with and without 22 vol.% SiC whiskers.	2013-2021A	81-99A
Corrosive wear of SiC whisker and particulate-reinforced 6061 aluminum alloy composites.	2653-2662A	1251-1266A
White iron, Casting		
Hydrogen effects on directional solidification of tellurium-doped cast irons.	496-498A	2994-3006A
White iron, Claddings		
Ballistic impact behavior of multilayered armor plates processed by hardfacing.	3335-3340A	3662-3668A
White iron, Coatings		
Correlation of microstructure and fracture toughness in high-chromium white iron hardfacing alloys.	3881-3891A	3478-3490A
White iron, Composite materials		
Influence of reinforcement volume fraction and size on the microstructure and abrasion wear resistance of hot isostatic pressed white iron matrix composites.	4171-4181A	3503-3512A
Influence of matrix structure on the abrasion wear resistance and toughness of a hot isostatic pressed white iron matrix composites.	4183-4191A	1700-1708A 2923-2933A
White iron, Crystal growth		
Directional solidification of white cast iron.	2328-2337A	101-110A
Widmanstatten structure		
Dense Co-Al-based alloys with improved ductility: solid-state synthesis and microstructure control.	2140-2150A	111-118A
Fracture characteristics, microstructure, and tissue reaction of Ti-5Al-2.5Fe for orthopedic surgery.	3925-3935A	183-191A
Workability		
High-temperature deformation and failure of an orthorhombic titanium aluminide sheet material.	3675-3681A	213-219A
X ray analysis		
Radioscopic visualization of isothermal solidification of eutectic Ga-In alloy.	688-689B	1785-1798A
X ray diffraction		
Interdissolution kinetics in oxide powder mixture using high temperature x-ray diffraction technique.	318-322B	2359-2365A
Analysis of heat affected zone phase transformations using in situ spatially resolved x-ray diffraction with synchrotron radiation.	775-783A	3250-3258A
Characterization of titanium thin films prepared by bias assisted magnetron sputtering.	1057-1060B	3524-3529A
Lattice misfits in four binary Ni-base γ/γ' alloys at ambient and elevated temperatures.	2888-2896A	3558-3568A
Incipient chemical instabilities of nanophasic Fe-Cu alloys prepared by mechanical alloying.	2934-2946A	3739-3748A
Thermally assisted and mechanically driven solid-state reactions for formation of amorphous Al ₃ Ta ₂ alloy powders.	3287-3278A	3747-3748A
Discussion of "Effects of tensile stress on microstructural change of eutectoid Zn-Al alloy" and authors' reply.	3330-3335A	3773-3780A
Effect of aging on shape memory behavior of Ti-51.3 at.% Ni thin films.	3753-3759A	317-326A
High-temperature oxidation of Ti ₃ Al-based titanium aluminides in oxygen.	3993-4002A	469-471A
Martensitic transformations in NiMnAl β phase alloys.	4153-4162A	
X ray microscopy		
Real time x-ray transmission microscopy of solidifying Al-In alloys.		
Yield		
Preparation of fine copper powders from organic media by reaction with hydrogen under pressure. I. Experimental study.		
Thermodynamics of phosphorus in molten silicon.		
Yield strength		
Communication: On the in situ formation of TiC and Ti ₂ C reinforcements in combustion-assisted synthesis of titanium matrix composites.		
A study of typical yields of metals.		
An experimental and theoretical investigation of the rapid consolidation of continuously reinforced, metal-matrix composites.		
Bauschinger effect in Haynes 230 alloy: influence of strain rate and temperature.		
Deformation behavior of an Al-3.37 wt.% Li alloy.		
The effects on fracture toughness of ductile-phase composition and morphology in Nb-Cr-Ti and Nb-Si in situ composites.		
Plastic zone and pileup around large indentations.		
Notch fracture in γ-titanium aluminides.		
Yield strength, Alloying effects		
Effect of strain rate and temperature on the flow stress of β-phase titanium-hydrogen alloys.		
Effect of phase composition and hydrogen level on the deformation behavior of titanium-hydrogen alloys.		
Dynamic strain aging and hydrogen-induced softening in alpha titanium.		
Yield strength, Composition effects		
Effect of manganese dispersoid on the fatigue crack propagation of Al-Zn-Mg alloys.		
Yield strength, Cooling effects		
The quench sensitivity of cast Al-7 wt.% Si-0.4 wt.% Mg alloy.		
Yield strength, Corrosion effects		
Effects of the alumina scale on the room-temperature tensile behavior of preoxidized MA 956.		
Yield strength, Deformation effects		
Non-Schmid effects on the behavior of polycrystals, with applications to Ni ₃ Al.		
Flow stress and microstructural evolution during hot working of alloy 22Cr-13Ni-5Mn-0.3N austenitic stainless steel.		
Constitutive behavior of tantalum and tantalum-tungsten alloys.		
Influence of plastic deformation upon the half-width of engineering metallic materials in hard state.		
Yield strength, Heating effects		
Influence of long term annealing on tensile properties and fracture of near-α titanium alloy Ti-6Al-2.75Sn-4Zr-0.4Mo-0.45Si.		
Low quench sensitivity of superplastic 8090 Al-Li thin sheets.		
Hot deformation mechanisms of a solution-treated Al-Li-Cu-Mg-Zr alloy.		
The plastic anisotropy of an Al-Li-Cu-Zr alloy extrusion in unidirectional deformation.		
Yield strength, Impurity effects		
The effect of hydrogen on the fracture of alloy X-750.		
Yield strength, Microstructural effects		
Pearlite in ultrahigh carbon steels: heat treatments and mechanical properties.		
NiTi and NiTi-TiC composites. II. Compressive mechanical properties.		
Subcritical crack growth at bimaterial interfaces. II. Microstructural effects on fracture resistance of metal/ceramic interfaces.		
Microstructural aspects of the dissolution and melting of Al ₂ Cu phase in Al-Si alloys during solution heat treatment.		
Theoretical calculation of the stress-strain behavior of dual-phase metals with randomly oriented spheroidal inclusions.		
The use of microstructural gradients in hot gas-pressure forming of Zn-Al sheet.		
Influence of interstitials on the mechanical properties of metallic materials.		
The cracking mechanism of silicon particles in an A357 aluminum alloy.		
Reinforcement shape effects on the fracture behavior and ductility of particulate-reinforced 6061-Al matrix composites.		
The behavior of internal markers in Ti-6Al-4V deformed in superplastic tension.		
Influence of titanium and carbon contents on the hydrogen trapping of microalloyed steels.		
Yield strength, Stress effects		
Plastic anisotropy of sheets with continuously varying anisotropic parameters and flow stress.		
Detecting stable crack onset at ductile-brittle transition in steels.		

Effect of thermal cycling on the mechanical properties of 350 grade maraging steel.	757-761A	Zinc base alloys, Microstructure	The Rayleigh instability and the origin of rows of droplets in the monotectic microstructure of zinc-bismuth alloys.	2053-2057A
The Bauschinger effect in a SiC/Al composite.	995-1001A	Zinc base alloys, Phase transformations	Discussion of "Effects of tensile stress on microstructural change of eutectoid Zn-Al alloy" and authors' reply.	3330-3335A
Yield strength, Temperature effects		Zinc base alloys, Powder technology	Kinetics of phase evolution of Zn-Fe intermetallics.	2904-2910A
Observations of secondary carbide precipitation and its relation to high-temperature flow and fracture in HT-9 stainless steel.	467-469A	Zinc compounds, Powder technology	Kinetics of phase evolution of Zn-Fe intermetallics.	2904-2910A
High-temperature wear and deformation processes in metal matrix composites.	3135-3148A	Zinc dust, Recovering	A kinetic study of the reaction of zinc oxide with iron powder.	363-374B
Manifestations of dynamic strain aging in soft-oriented NiAl single crystals.	3542-3557A	Zircon, Composite materials	Mechanical properties and 95°C aging characteristics of zircon reinforced Zn-4Al-3Cu alloy.	809-818A
An analysis of the flow stress of a two-phase alloy system, Ti-6Al-4V.	3957-3962A	Zirconium, Alloying additive	Microstructure and phase identification in type 304 stainless steel-zirconium alloys.	2151-2159A
Yttrium, Refining			Elevated temperature compressive properties of zirconium-modified NiAl.	2628-2641A
Thermodynamic properties of oxygen in yttrium-oxygen solid solutions.	839-845B		Effects of alloy modification and thermomechanical processing on recrystallization of Al-Mg-Mn alloys.	2947-2957A
Zinc, Composite materials			The effect of metallic elements on the crystallization behavior of amorphous Fe-Si-B alloys.	3424-3430A
Analysis of damping in particle-reinforced superplastic zinc composites.	2585-2573A	Zirconium, Diffusion	Pressure dependence of anomalous diffusion of zirconium in β -titanium.	1807-1814A
Zinc, Extraction		Zirconium, Mechanical properties	Influence of interstitials on the mechanical properties of metallic materials.	3524-3529A
The mineralogical department of germanium in the Clarksville electrolytic zinc plant of Savage Zinc Inc.	567-576B	Zirconium base alloys, Extrusion	Microsegregation of oxygen in Zr-2.5Nb alloy materials.	431-440A
Application of centrifugal fields in fused salt electrowinning with a view to reducing electrolytic energy consumption.	889-894B	Zirconium base alloys, Forming	Reply: Dynamic materials model. Basis and principles.	235-236A
Eco-techno-economic synthesis of process routes for the production of zinc using combinatorial optimization.	1031-1044B	Zirconium base alloys, Phases (state of matter)	Microstructure and phase identification in type 304 stainless steel-zirconium alloys.	2151-2159A
Zinc, Recovering		Zirconium compounds, Composite materials	A model for coupled growth of reaction layers in reactive brazing of ZrO_2 -toughened Al_2O_3 .	3630-3638A
A kinetic study of the reaction of zinc oxide with iron powder.	363-374B	Zirconium compounds, Oxidation	Phase relations of a silicide/silica reaction couple at 2273K.	271-276B
Zinc, Ternary systems				
Thermodynamic investigations of the ternary Au-Sn-Zn system.	921-927B			
Zinc base alloys, Casting				
The design of feed systems for thin-walled zinc high-pressure die castings.	115-118B			
Zinc base alloys, Composite materials				
Mechanical properties and 95°C aging characteristics of zircon reinforced Zn-4Al-3Cu alloy.	809-818A			
Zinc base alloys, Forming				
The use of microstructural gradients in hot gas-pressure forming of Zn-Al sheet.	3250-3258A			
Zinc base alloys, Mechanical properties				
Effect of iron on ductility and cavitation in the superplastic An-22% Al eutectoid.	863-872A			
Characterization of the wear response of a modified zinc-based alloy vis-à-vis a conventional zinc-based alloy and a bearing bronze at a high sliding speed.	3513-3523A			
Zinc base alloys, Melting				
The production of nickel-zinc alloys by powder injection.	780-787B			